Numerical modeling of geomechanical processes related to CO_2 injection within generic reservoirs

Final Scientific/Technical Report: DE-FE0001836

PI: Andreas Eckert

On behalf of

Missouri University of Science and Technology

1870 Miner Circle, Rolla, MO 65409

Project period: December 2009 to May 2013

Rolla, August 12, 2013

DISCLAIMER

ABSTRACT

In this project generic anticline structures have been used for numerical modeling analyses to study the influence of geometrical parameters, fluid flow boundary conditions, in situ stress regime and inter-bedding friction coefficient on geomechanical risks such as fracture reactivation and fracture generation. The resulting stress states for these structures are also used to determine safe drilling directions and a methodology for wellbore trajection optimization is developed that is applicable for non-Andersonian stress states.

The results of the fluid flow simulation show that the type of fluid flow boundary condition is of utmost importance and has significant impact on all injection related parameters. It is recommended that further research is conducted to establish a method to quantify the fluid flow boundary conditions for injection applications.

The results of the geomechanical simulation show that in situ stress regime is a crucial, if not the most important, factor determining geomechanical risks. For extension and strike slip stress regimes anticline structures should be favored over horizontally layered basin as they feature higher ΔP_c magnitudes. If sedimentary basins are tectonically relaxed and their state of stress is characterized by the uni-axial strain model the basin is in exact frictional equilibrium and fluids should not be injected. The results also show that low inter bedding friction coefficients effectively decouple layers resulting in lower ΔP_c magnitudes, especially for the compressional stress regime.

Table of Contents

EXECUTIVE SUMMARY

Preventing environmental damages from CO_2 release into the atmosphere, underground storage of liquefied CO_2 has become a goal in recent research projects. The successful sequestration of the CO_2 depends on minimizing the risk of leakage through cap rock and fracture networks. Assessment of cap rock stability, fracture generation and reactivation due to injection related pore pressure increase as well as wellbore integrity thus becomes of major interest and successful modeling of these parameters will help to find suitable conditions for possible CO_2 sequestration sites. The main objective of this ARRA training project was to properly train graduate students to develop multi-scale Finite Element (FE) models of different geological settings for sequestration sites and compare the results concerning geomechanical processes, such as how fluid pressure induces rock deformation, as well as critical wellbore placement and wellbore integrity to each other. This shall give a more thorough understanding of how reservoir geometry affects wellbore stability, formation and cap rock stability and thus shall facilitate future site selection.

In order to analyze and evaluate these geomechanical risks the numerical modeling methods employed in this project focus on two different spatial scales. 1) the reservoir system scale to study fluid flow boundary conditions and geometrical influences of anticline structures on the state of stress and to analyze the risk of fracture generation and reactivation and 2) the borehole scale system to determine stable drilling directions and wellbore trajectory optimization. The numerical models employed in this project focus on generic anticline structures as these geologic scenarios represent prime targets for CO2 sequestration sites. It is important to note that the results showcase the relative importance of the modeling parameters investigated and the methodology developed can readily be applied to real case scenarios.

The fluid flow simulation on the reservoir scale investigates the influence of geometrical parameters such as wavelength, amplitude and thickness as well as the influence of the fluid flow boundary conditions on safe injection limits. The results show that higher wavelengths, lower amplitudes and relatively thick layers provide the best conditions for safe CO_2 sequestration. A major and not surprising conclusion is that the lateral fluid flow boundary condition of an aquifer system has the most significant influence on the CO_2 sequestration parameters. The assumption of an open system requires gigantic aquifers (~100 km) that may be very difficult, if not impossible, to locate in the vicinity of many CO_2 producers. A more realistic approach of semi-

open fluid flow boundaries yields similar if not better results than the open system case. However, this approach seems only applicable if the total magnitude of the lateral flow boundary condition of an aquifer system can be determined e.g. by water drawdown tests similar to conventional pressure transient testing and production data analysis of the oil and gas wells. Our results show that for such a system, the anticline wavelength, amplitude and thickness have a pronounced influence on CO_2 sequestration parameters. However, unless extensive field tests permit the application of semi-open or open aquifer, this study shows that the safest approach for a sustainable CO_2 sequestration project should be the assumption of closed fluid flow boundaries.

On the reservoir scale a 3D finite element (FE) model is employed to assess maximum sustainable pore pressures prior to injection. The FE results of the stress state are used for analytical estimates based on the pore pressure - stress coupling principle. Based on these estimates the strike-slip regime results in the highest sustainable pore pressure differences. The generic anticline geometries investigated in this study have also shown that in addition to the in-situ state of stress the stress heterogeneities associated to the geometry of such structures result in significant differences with respect to sustainable pore pressure magnitudes (ΔP_c). For extension and strike slip stress regimes anticline structures should be favored over horizontally layered basin as they feature higher ΔP_c magnitudes. If sedimentary basins are tectonically relaxed and their state of stress is characterized by the uni-axial strain model the basin is in exact frictional equilibrium and fluids should not be injected.

The analytical pre-injection estimates together with the coupled simulations have shown and confirmed that the in-situ stress regime is a crucial, if not the most important, factor determining geomechanical risks, for fluid injection applications such as CO_2 sequestration. It is therefore strongly recommended that every case study is based on in-situ stress measurements for a thorough calibration of numerical models used to analyze geomechanical risks. The coupled simulations for the generic anticline structures have shown that the extensional stress regime represents the overall safest scenario, however is considered the most unlikely as anticlines are compressional structures.

Another important observation from the generic models is the influence of geological parameters such as the inter-bedding friction coefficient. Whilst the influence of this parameter is not important for horizontally layered structures, the geometry of anticline structures results in stress heterogeneities and the coefficient of friction on bedding planes determines the mechanical coupling between different layers. The results have shown that low friction coefficients effectively decouple layers resulting in lower ΔP_c magnitudes, especially for the compressional stress regime.

On the borehole scale a methodology has been established to setup and optimize numerical models in order to minimize errors. The results of the FE models on the reservoir scale have been used to perform a wellbore stability analysis and to find stable drilling directions for the anticline structures. While vertical wells have proven to be stable for all three stress regimes, a procedure has been developed that can be readily applied to prospective case studies with more complex material models and geometries. The procedure developed provides mud pressure window calculation for inclined wellbores of type I wells. These wellbore types, especially type I wellbores with a horizontal hold section, are relevant for CO_2 sequestration applications, as horizontal wells have an increased surface area inside the reservoir and thus feature increased injectivity. As predicted by Kirsch's analytical solution the in-situ stress regime has significant impact on stable drilling directions, whereby the direction of the intermediate principal stress represents the least stable direction. This procedure developed becomes of relevance when applied to case studies where the principal stresses are not given by σ_V, and $\sigma_{h,H}$. In order to further improve the resulting wellbore stability analysis a wellbore trajectory optimization procedure is necessary to account for scenarios where the vertical stress is not a principal stress.

The methodology developed represents a process to optimize wellbore trajectories in the planning stage of a well. Assumptions on the state of stress are not necessary as the 3D FEM provides the complete stress tensor at any point in the model. The methodology is based on the general mathematical description and thus enables all possible scenarios of azimuth, inclination and surface rig location for multiple well types along the entire trajectory of the well path. The case study results show that if applied to a scenario with a highly varying state of stress a significant improvement of wellbore stability conditions can be achieved. In comparison to a vertical well the proposed well trajectory has a significantly wider mud pressure window also resulting in a reduction of casing points.

1. Reservoir Scale Model

For the reservoir scale models of the generic anticline structures 3 different analyses have been performed:

a) Fluid Flow Simulation
b) Geomechanical Analysis:
   a. Pre-injection Geomechanical Assessment of Maximum Sustainable Pore Pressures
   b. Coupled Analysis

1.1. Fluid Flow Simulation

1.1.1. Introduction

Often numerical CO2 injection scenarios are based on the simplified assumption of a horizontally layered sedimentary basin [Settari and Mourits, 1998; Thomas et al., 2003; Dean et al., 2006; Pettersen, 2006; Zhou et al., 2008; Inoue, 2009; Taberner et al., 2009; Tran et al., 2009; Ehlig-Economides And Economides, 2010; Cappa and Rutqvist, 2011; Graupner et al., 2011]. While this scenario serves well to study the impact of different parameters (such as permeability, injection rate, fluid flow boundary conditions and seal efficiency) on CO2 flow and pressurization [Zhou et al., 2008; Inoue, 2009; Taberner et al., 2009; Ehlig-Economides And Economides, 2010; Cappa and Rutqvist, 2011], for a geomechanical risk analysis a model geometry reflecting the actual geologic scenario, which exhibits a heterogeneous state of stress is required. The geomechanical risks accompanying aquifer pressurization due to the CO2 injection have been investigated by several authors [Settari and Mourits, 1998; Thomas et al., 2003; Pettersen, 2006; Van der Meer et al., 2006; Rutqvist et al., 2007; Schembre-McCabe et al., 2007; Zhou et al., 2008; Inoue, 2009; Taberner et al., 2009; Tran et al., 2009; Ehlig-Economides And Economides, 2010; Cappa and Rutqvist, 2011; Graupner et al., 2011] with one of the most important being the reactivation of existing faults or fracture sets which can result in induced seismicity [Van der Meer et al., 2006; Rutqvist et al., 2007; Schembre-McCabe et al., 2007;Loizzo et al., 2009] and potential leakage pathways. [Rutqvist et al., 2007; Zhou et al., 2008] have shown that the pressure build-up in models representing horizontally layered sedimentary basins is strongly dependent, amongst others, on the fluid flow boundary conditions.

A closed system, reflecting a compartmentalized reservoir, results in a much higher and faster pressure increase than open-flow boundary conditions. This influence of the fluid flow boundary conditions on the pressure build-up becomes increasingly relevant for geomechanical risk analyses of storage sites exhibiting a heterogeneous state of stress [Paradeis et al., 2012]. Possible geologic scenarios may represent an aquifer being trapped in a closed system bounded by faults or an anticline structure which may have existing fracture sets along the hinge. Anticline/Antiform structures as an example of folded sedimentary layers are among the most common structural traps for hydrocarbon reservoirs and thus become a prime target of the emerging challenge of safe geologic sequestration of CO2 [Metz et al., 2005].

One reason for the utilization of simple geometries for generic fluid flow simulation studies is due to the lack of flexible pre-processors, which can generate finite difference grids of more complex geometries. Preprocessors for the finite element method have the ability to generate complex structures but do not yield discretization formats which can be used in finite difference based reservoir simulations [Amirlatifi et al., 2011a; Amirlatifi et al., 2011b]. In this paper we address this limitation by using a commercial finite element pre-processor (Altair® Hypermesh®) and use the Coupled Geomechanical Reservoir Simulator, CGRS, a coupling module for geomechanical reservoir simulation developed at Missouri University of Science and Technology [Amirlatifi et al., 2011a; Amirlatifi et al., 2011b] to convert several synthetic reservoir geometries from the finite element file format to the reservoir simulation grid file format. We then study the effects of anticline geometry on CO2 injection parameters. We use the commercial fluid flow simulation package Schlumberger® Eclipse® to investigate the effects of different amplitudes, wavelengths and height of generic anticline structures on the storability of CO2 in these reservoirs at different depths and under different injection rates. The results of this study may finally serve as a guideline for possible injection sites and scenarios resembling the cases presented here. The methodology presented in this paper further enables coupling between the reservoir simulation and the geomechanical analysis whereby both simulations use the same discretization minimizing the use of interpolation algorithms.

1.1.2. Modeling Approach

Numerical modeling studies in the oil and gas industry assume a realistic reservoir geometry which is obtained by seismic data, well logs and surface mapping. The data collection may result in quite complex reservoir geometries. Although most state of the art commercial simulators are capable of handling unstructured grids that can accommodate these complex structural features, the computational cost of aforementioned simulators limits their applicability. This feature is not commonly employed and finite difference discretization is still the prominent practice. However, the limitation of finite difference discretization algorithms [Amirlatifi et al., 2011a; Amirlatifi et al., 2011b] for reservoir simulation studies requires up-scaling and simplification of the complex geometry. As a result, most of the preprocessors in the oil and gas industry are based on discretizing an existing geometry and it is very difficult, if not impossible, to use them for building parametric study models that incorporate anticlines, for example. This limitation has resulted in the implementation of simplified horizontal basin models in most of the literature, unless real field data are present. As part of our efforts to couple the finite element (FE) analysis package Abaqus® with Eclipse® in the Coupled Geomechanical Reservoir Simulator, CGRS, we have created a file convertor and grid mapper in Java® that converts geometries created in the Abaqus 3D file format to the grid file format of Eclipse®. The FE pre-processor Altair® Hypermesh® is used to generate 3D anticline models of different amplitude, wavelengths and heights. Due to the requirements of finite difference grids, all grid blocks in the 3D FE model need to be hexahedral in columns sharing the same coordinates in horizontal directions albeit variable depth. Once the geometry is created in the FEA preprocessor, it is exported to the Abaqus® 3D file format and is transferred into the CGRS file convertor. The initial step of the file conversion routine stores the nodal coordinates and the corresponding elements into the memory and organizes them into arrays of nodes and elements. In the next step, the nodes are sorted by their coordinates and the closest node to the origin is selected as the starting point of the finite difference grid. The nodes are then sorted by their X-coordinates for an initial constant y-coordinate. Once all nodes having the same Y-coordinates are identified, the next row in the Y direction is examined and so forth, until all elements and nodes in the first layer are determined and the process continues with the elements and nodes in the second and the following layers (z-coordinates). At each step, the number of rows, columns and layers are determined as the maximum number of nodes in any row, column and layer. Once all nodes and elements in the finite element mesh are analyzed, the corresponding Eclipse® grid is generated. The coordinates of the nodes in the first layer are reported by the COORD keyword in the generated Eclipse® grid data file, followed by the vertical location of each node, reported under the ZCORN keyword. This efficient method enables us to generate highly flexible generic geometries for reservoir simulation studies with the ease of finite element analysis pre-processors.

1.1.3. Model Description

Sinusoidal curves with different amplitudes and wavelengths are used as the framework of the anticlines and synclines to be modeled. As it is shown in Fig. 1, the general layout of the anticline structures used throughout this modeling study comprises seven layers where all layers are assumed to be fully saturated with water. The thickness of shale and sandstone layers together with the base layer stay the same, while the thickness of the overburden is increased or decreased during the study of the effect of depth. The pseudo 3D model employed here (Fig. 1) is part of a direct line CO2 sequestration scheme with a lateral extension of 76 meters where the injection well is placed at the crest of the anticline and two brine production wells are placed at the sides to keep the hydrostatic pressure under open boundary conditions. No flow boundary condition along the longitudinal extension of the model results in the direct line sequestration configuration flow regime, with image wells acting as parallel well sets (Fig.1).

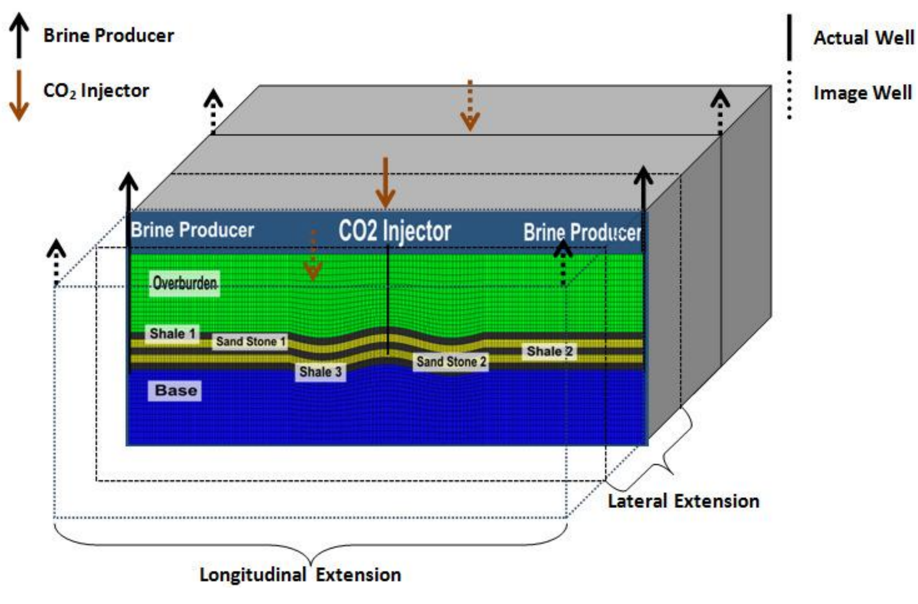

Figure 1: General layout of the anticline structure used in this study.

Two sandstone layers are contained between three shale layers, which act as sealing caprock for each sandstone reservoir. Table 1 lists the intrinsic rock properties, thickness and the order of different layers used in this study. The “Sand Stone 2” layer is taken as the main aquifer in this study and the CO2 is injected in this layer.

Table 1. Properties of layers used in the parametric study.

Layer Name	ρ (Kg/m^3)	E (MPa)	ν	ϕ (%)	k (10^{-16}m^2)	S_w (%)
Overburden	2210	1500	0.25	0.01	0.098	100
Shale 1	2130	1500	0.25	0.01	0.0009	100
Sand Stone 1	2210	2000	0.25	20	986.9	100
Shale 2	2130	1500	0.25	0.01	0.0009	100
Sand Stone 2	2210	2000	0.25	20	986.9	100
Shale 3	2130	1500	0.25	0.01	0.0009	100
Base	2245	1500	0.25	0.01	0.098	100

Table 2 lists the range of geometrical and operational parameters that were used in this study. Wavelengths of 750, 1500 and 3000 meters and an infinite wavelength, resembling the horizontally layered basin are used (section 2.4). Reservoir thicknesses of 25, 50 and 100 meters are considered (section 2.5). In order to investigate effect of amplitude variation, anticlines with amplitudes of 50, 100 and 150 meters are modeled (section 2.6). The simultaneous variation of wavelength, thickness and amplitude is examined as described in section 2.7 and Table 7. Effect of boundary condition is examined through modeling of the closed, Semi-Open and Open boundary conditions as described in section 2.8. Depth of the model is varied between 500 to 3000 meters as described in section 2.9 which has resulted in different maximum allowable pore pressures. The lateral extent of the model is varied between 6, 23 and 103 Km as described in the discussion. As a reference base case of this study we consider a reservoir at the depth of 1250 meters with an anticline of a wavelength of 1500 m, an amplitude of 150 m and a height of 100 meters. The injection well is located at the crest of the anticline and the boundaries are assumed to be closed. In order to evaluate the validity of the simplified horizontally layered basin models, a simple horizontally layered basin model is created and is compared to the base model. Simulations reflecting open boundary fluid flow conditions are carried out by placing water production wells at the boundaries that maintain hydrostatic pore pressure. An initial CO_2 injection rate of 20.7 KTons/year (1798.71 lbs/MWhr) is based on the 50% reinjection of CO_2 emission rate of a common 495 MW capacity coal fired power plant [18] with 75% efficiency over 100 years period and CO_2 density of 1.98 Kg/m3 and formation properties are based on the geology of common sedimentary rocks.

Table 2: Range of parameters used in the parametric study.

	Units							

Values / Attribute								
Depth	m	500	1000	1250	1500	2000	2500	3000
Maximum Allowable Pore Pressure	MPa	26.3	34.1	36.0	41.8	49.5	56.5	62.4
Wave Length	m	1500	750					
Amplitude	m	150	100	50				
Reservoir Thickness	m	100	50	25				
Well Location		Crest						
Boundary Type		Open	Closed					
Injection Rate	m^3/sec	0.33194						
Model Size	Km	3	23	103				
Number of Anticlines		0	1	3				

Table 3: The base simulation case and its simulation results.

Attribute	Units	Value
Anticline Wavelength	m	1500
Anticline Amplitude	m	150
Anticline Height	m	100
Depth	m	1250
Reservoir Volume	m^3	9129120
Boundary		Closed
CO_2 Injection Rate	m^3/sec	0.33194
Fault Present		No
Well Location		Crest of Anticline
Number of Anticlines		1
Critical Pore Pressure	MPa	36.0
Safe Injection Limit	Years	6.35
CO_2 Saturation at SIL	%	53
Average Pressure at SIL	MPa	32.45
Mass of Injected CO_2	10^3Tons	117.583
Occupancy	%	1.62

1.1.4. Results

For the injection simulations we use a maximum allowable pore pressure before failure of intact rock is initiated as a threshold value before injection is stopped. These critical pore pressure values are determined by geomechanical finite element analysis for each geometry assuming a compressional stress regime, as described in [Rutqvist et al., 2007; Paradeis et al., 2012]. Based on these results the reservoir simulation analyses are conducted, thus a one way coupling procedure is followed here. Simulations results are checked on a monthly basis until the pore pressure in any grid block of the reservoir layer or the surrounding shale layers reaches the maximum allowable pore pressure. The time to reach the maximum allowable pore pressure is identified as the Safe Injection Limit, SIL. The ratio of the reservoir volume of CO_2 at the SIL to the total pore volume, which is also equal to the average gas saturation, is considered as the degree of occupancy, an indication of how well the reservoir volume is utilized. Unless maximum allowable pore pressure is reached, the simulation is continued for 50 years. The simulation results of the base anticline model of this study, Fig. 1 and Table 3, are taken as the basis for benchmarking the other simulation runs. Fig. 2 shows the pressure distribution in the base model after the safe injection limit is passed. The black regions in the syncline show the parts of the syncline that will experience pressures exceeding the critical pressure limit.

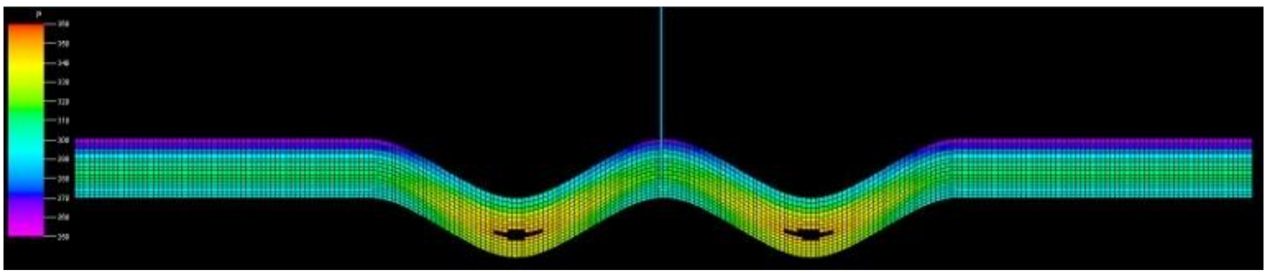

Figure 2: Pressure distribution in base model after 7 years of injection, showing the failed regions.

For the sake of comparison, we have not investigated the escape of injected fluid in this study and when the maximum allowable pore pressure is violated, the well is shut in and simulation is continued for the remainder of ten years, so that the average reservoir pressure at the end of the ten year interval can be determined.

1.1.4.1.Effect of Wavelength Variation

The effect of wave length is investigated by varying the wavelength from one half of the base case to two times of the base case and the horizontally layered basin which has an infinite wavelength. Results (Table 4) of this simulation show that the higher the wavelength of the anticline, the longer the SIL, the higher reservoir occupancy and finally the higher the CO2 storage capacity of the reservoir becomes.

Table 4: Effect of wavelength on CO2 storage capacity.

Wavelength (m)	SIL (Years)	Occupancy (%)	Average Reservoir Pressure (MPa)	Mass of Injected CO_2 10^3Tons
750	6.34	1.62	32.4	117.40

1500	6.35	1.62	32.5	117.58
3000	7.15	1.79	34.8	132.54
∞	7.80	1.93	35.1	144.59

1.1.4.2.Effect of Reservoir Layer Thickness Variation

The reservoir height directly controls CO2 storage capacity through variation of accessible pore volume. Eq. (1) shows the pore volume for a simple case of a cubic reservoir of constant height, h, porosity, ϕ, and area, A.

$$"V=Ah\emptyset" \tag{1}$$

An immediate conclusion from Eq. (1) is that the higher the reservoir thickness, the more pore space is available for CO2 sequestration, assuming that we have a connected pore network. Table 5 shows the effect of variation in height on the CO2 storage capacity on the base model.

Table 5: Effect of height on CO2 storage capacity.

Height (m)	SIL (Years)	Occupancy (%)	Average Reservoir Pressure (MPa)	Mass of Injected CO_2 10^3Tons
25	1.65	1.6	31.8	30.56
50	3.29	1.6	32.5	60.95
100	6.35	1.6	32.4	117.58

The simulation results confirm that the increased volume of the reservoir results in increased safe injection limits and consequently an increase in injected gas volume is achieved, but the overall occupancy stays the same.

1.1.4.3.Effect of Amplitude Variation

Three different amplitude variations of the base case, presented in Table 3, are considered, ranging from 50 meters to 150 meters in the closed system. The simulation results of such variations are presented in Table 6.

Table 6: Effect of amplitude on CO2 storage capacity.

Amplitude (m)	SIL (Years)	Occupancy (%)	Average Reservoir Pressure (MPa)	Mass of Injected CO_2 10^3Tons

50	7.32	1.83	34.2	135.56
100	6.82	1.72	33.3	126.39
150	6.35	1.62	32.4	117.58

As the results suggest, the lower amplitude anticline gives the highest CO_2 storage capacity of 135.56 kilo Tons. Assuming that the most favorable case is to increase the average reservoir pressure up to the maximum allowable pore pressure, an anticline with the low amplitude of 50 meters yields the best average reservoir pressure of 34.2 MPa.

1.1.4.4. Simultaneous variation of Wavelength, Amplitude and Height

Simultaneous variation of wavelength, amplitude and reservoir height are studied through 15 simulations where the wavelength is varied between 750 meters and 1500 meters, the amplitude is varied between 50 meters, 100 meters and 150 meters and the height is varied between 25 meters, 50 meters and 100 meters. Results of these simulations are presented in Table 7.

Table 7: Simultaneous variation of wavelength, amplitude and height.

Wavelength (m)	Amplitude (m)	Height (m)	SIL (Years)	Occupancy (%)	Mass of Injected CO_2 10^3Tons
750	50				
		25	1.81	1.75	32.54
		50	3.71	1.84	68.14
		100	7.23	1.82	134.66
	100				
		25	1.73	1.67	30.92
		50	3.46	1.73	63.46
		100	6.82	1.74	126.93
1500	50				
		25	1.9	1.82	33.98
		50	3.79	1.87	69.58
		100	7.32	1.83	136.10
	100				
		25	1.73	1.68	30.92
		50	3.57	1.76	64.90
		100	6.82	1.72	126.93
	150				
		25	1.65	1.6	30.56
		50	3.29	1.65	60.95
		100	6.35	1.62	117.58

The results show that the highest storage capacity is observed for the high wavelength of 1500 meters, the low amplitude of 50 meters and the thick reservoir of 100 meters thickness. As previously shown in Table 5 and confirmed in Table 7, height or net thickness of the reservoir has a direct effect on the CO2 storage capacity.

1.1.4.5. Effect of Boundary Conditions

Three types of fluid flow boundary conditions can be thought for the aquifer systems, namely Open, Semi-Open and Closed boundaries [Ehlig-Economides and Economides, 2010; Zhou et al., 2008]. Many scholars have assumed fully open boundaries where the pressure at the boundary remains hydrostatic. These studies show very promising results on the storage capacity and the safety of the project. We have considered 3 cases where storage under open boundary condition is compared to the closed and semi-open boundaries. In order to simulate open boundary conditions per definition, two brine production wells are placed at the sides of the aquifer and the constraints are set such that the well flowing pressure, P_{wf}, remains at the hydrostatic pore pressure. The limit for the injection period is set equal to the CO2 breakthrough time. In the semi-open model, the production rate of the brine producers is reduced by half and the pressure is allowed to increase at the boundaries until the safe sequestration pressure limit is reached, or until the CO2 breaks through the production wells, which was the case here. Table 8 presents the simulation results of the base case under different boundary conditions.

Table 8: Effect of Boundary Conditions on CO2 Storage Capacity of the base case.

Boundary Type	SIL (Years)	Occupancy (%)	Average Reservoir Pressure (MPa)	Mass of Injected CO_2 10^3Tons
Closed	6.35	1.62	32.4	117.58
Open	50	25.13	13.1	942.10
Semi-Open	80	25.96	20.4	1506.65

The results show the significant influence of the fluid flow boundary condition. Whilst a Closed system (resembling a compartmentalized reservoir) yields a SIL of only 6.35 years and an occupancy of only 1.62%, Open and Semi-Open systems yield much higher SIL (50-80 years) and much higher occupancies (25-26%). The Semi-Open system yields overall safer conditions and more CO2 can be injected by allowing partial pressure increase in the reservoir, resulting in compression of CO2 and contained spread of the plume. The contained spreading gives higher sweep efficiency and continuous flow of fluids in the system, which itself results in increased contact between the two fluids and dissolution of CO2 in the brine. While open systems benefit from the favorable pressure gradient that makes it possible for CO2 to quickly spread in the system, mix with the brine as it spreads and dissolve in it, unconstrained spreading of the plume results in lower sweep efficiency than that of the Semi-Open system.

1.1.4.6.Effect of Depth

The depth of the reservoir determines the state of the stress, the resulting maximum allowable pore pressure as well as the CO2 density and phase (Fig. 3), which in turn determines its compressibility and viscosity. The resulting effects on CO2 storage capacity are studied through 7 simulations where the depth of the base case, as described in Table 3, is varied from 500 meters to 3000 meters. A compressional stress regime is assumed for the calculation of the maximum allowable pore pressure. Table 9 presents the simulation results for the base case at different depths.

Table 9: Effect of Depth variation on CO2 Storage Limit.

Reservoir Depth (m)	Maximum Allowable Pore Pressure (MPa)	SIL (Years)	Occupancy (%)	Mass of Injected CO_2 10^3Tons
500	26.3	5.266	1.57	97.45
1000	34.1	6.28	1.60	116.41
1250	36.0	6.35	1.62	117.58
1500	41.8	7.73	1.88	143.86
2000	49.5	8.877	2.04	165.52
2500	56.5	9.619	2.13	179.44
3000	62.4	9.78	2.10	182.53

The results show that CO2 sequestration in deep formations results in longer safe CO2 injection periods and consequently higher CO2 storage capacity. The highest occupancy is observed in 2500 meters depth with a value of 2.13% and the deepest model at a depth of 3000 meters has the longest injection period of 9.78 years. Comparison between the increase in injection period and the increase in depth and the occupancy suggests that 2500 meters is the most favorable depth of all cases under closed boundary conditions.

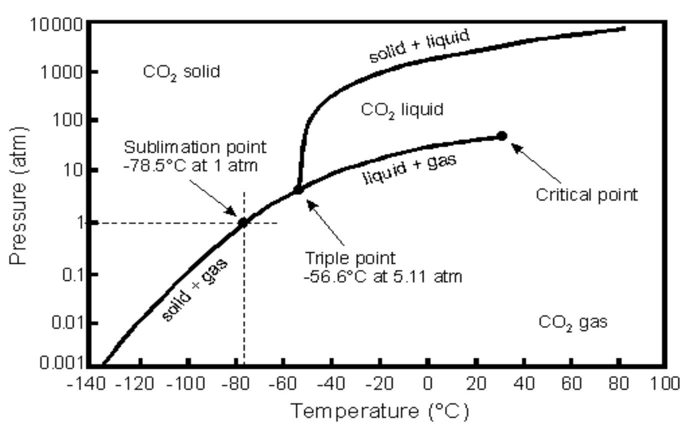

Figure 3: Phase Diagram of CO2.

1.1.5. Discussion

CO2 sequestration based fluid flow simulations utilizing simplified horizontally layered basins show promising results regarding the amount of CO2 that can be safely injected over long periods of time [Zhou et al., 2008; Birkholzer et al., 2009]. The assumption of a horizontally layered basin, however, neglects the requirement of a structural trap system to store the fluids. A prime example of such trap systems are anticline structures. The results presented in this study show that once realistic structural geometries for CO2 sequestration projects are considered, geometrical parameters such as anticline wavelength, anticline amplitude and respective aquifer depth influence the SIL, the occupancy and the total amount of injected CO2.The results presented in Table 4, Table 6 & Table 7 suggest that the anticline wavelength and amplitude have direct influence on the CO2 storage capacity. The larger the wavelength and the lower the amplitude, the longer it takes to get to the maximum allowable pore pressure in a closed system and thus the more CO2 can be injected into the anticline. Comparison with the horizontally layered basin shows that the horizontally layered basins have more storage capacity than the actual capacity of an anticline structure. This suggests that the existence of anticline structures should not be ignored by simplifying the model with horizontally layered basins. Using simplified model geometries can result in the prediction of Safe Injection Limits that are longer than the actual tolerance of the medium. When comparing the influence of the geometrical parameters on the CO2 occupancy in closed systems, the results only show slight variations. However, once other fluid flow boundary conditions are considered the effects of the geometrical parameters become significantly more pronounced. Table 10 shows the effect of reservoir height and boundary condition variation on CO2 storage capacity.

Table 10: Effect of reservoir height and boundary condition variation on CO2 storage capacity

Height (m)	Boundary Type	SIL (Years)	Occupancy (%)	Average Reservoir Pressure (MPa)	Mass of Injected CO_2 10^3Tons
50	Closed	3.29	1.65	32.1	60.95
	Open	30.72	28.95	13.9	577.13
100	Closed	6.35	1.62	32.4	117.58
	Open	50	25.13	13.1	942.10

Although the occupancy of the two models in a closed system is the same, the thinner reservoir of 50 meter thickness shows a better sweep and occupancy of 28.95% under the open conditions, compared to the 25.13% of the 100 meter thick reservoir. While the difference in the volume of the two reservoirs controls the mass of injected CO2 and SIL, the difference in occupancy can show the influence of geometrical parameters that may be masked out otherwise by the influence of the fluid flow boundary conditions.

The simulation results confirm previous studies [Ehlig-Economides and Economides, 2010; Zhou et al., 2008] showing that the type of fluid flow boundary condition has a huge impact on the result parameters. CO2occupancy in closed systems is a function of total compressibility. When more pore space is available, assuming that the total compressibility stays the same, more CO2 volume can be injected into the reservoir, but the overall occupancy of the reservoir stays the same regardless of the volume or the height, as shown in Table 5. Our results of maximum occupancy of 1.6%-2% compare well with results from [Zhou et al., 2008] of 0.5% and [Ehlig-Economides and Economides, 2010] of ~1% for closed systems.

The effect of the lateral fluid flow boundary conditions on CO2 storage capacity for the base anticline was presented in Table 8. These results suggest that the assumption of open boundary condition can significantly increase the CO2 storage capacity but a semi-open boundary serves the purpose even better, as long as the pressure stays in the safe injection limit. The question, however, is whether the open boundary condition case can be observed in real life. One way of achieving open boundary conditions is through the use of pore volume multipliers [Samier et al., 2007] which, in the authors' opinion, are only applicable to reservoir simulation studies, where exact knowledge about the size and water flux of the aquifer is not available. Under these circumstances one may use the pore volume multipliers on the aquifer grid blocks to achieve a history match. However, this is not the case in studies concerning CO2 sequestration in saline formations where the aquifer is the most important part of the fluid system. Another way of achieving open boundary conditions, as presented previously, is to drill brine production wells at the boundaries and control the pressure through these production wells. While drilling of these wells is possible, a question that needs to be addressed is where to dispose of the produced brine. Another possibility is to have such large aquifers that the compressibility of the liquids in place doesn't result in the increased pore pressure. In order to investigate the typical size needed for such an aquifer, we have made two extensions of the base case where the boundaries are extended 10km and 50km on each side of the 3km wide anticline structure, resulting in reservoirs that are 23 and 103 km long respectively. As it is shown in Table 11, the large reservoir of 23 km width fails to replicate the results of the fully open boundary and the gigantic reservoir of 103km size is the minimum reservoir size capable of replicating such results. This conclusion leaves us with some fundamental questions that need to be answered before one can make the fully open boundaries assumption:

1. What is the likelihood of finding such gigantic reservoirs in the immediate vicinity of CO2 producers?

2. Provided that such a reservoir is available, are there any faults/inhomogenities or stress anomalies that influence the maximum allowable pore pressure?

3. What is the probability that no one else is injecting in the same aquifer of interest which would otherwise result in pressure interference in the premises of the well(s) that are planned for the CO2 sequestration?

Table 11: Comparison of Different Model Sizes and Boundary Conditions.

Reservoir Size (km)	Reservoir Volume (10^6m)	SIL (Years)	Boundary Type	Mass of Injected CO_2 10^3Tons
6	9.13	6.35	Closed	117.58
6	9.13	50	Open	942.11
23	35.0	22.46	Closed	420.71
103	156.7	50	Closed	942.10

The presented results show that the lateral fluid flow boundary conditions have a significant influence on CO2 sequestration parameters. Although huge aquifers such as Sleipner [Kongsjorden et al., 1998] exist throughout the world that have high potential for CO2 sequestration, they may not be in the vicinity of the power plant(s) of interest or meet the salinity level requirements set forward by federal or state regulations; thus an important step in CO2 sequestration feasibility study of a candidate aquifer should be determination of its size. This can be achieved by analogy between the existing and well established practices in petroleum engineering for well testing and estimation of the size/drainage radius of an oil well. Without knowing the exact size of the aquifer and matching boundary type, care should be taken before suggesting safe sequestration limits. In the authors' opinion, it is better to take the more conservative practice and assume semi-open or closed boundaries to stay within the safe sequestration limit, instead of assuming that the aquifer has fully open boundaries and face the otherwise high risk of exceeding the maximum allowable pore pressure and causing the rock to fail. Note should be taken that the maximum allowable pore pressure used throughout this study is the pressure that will result in failure of intact rock, which is obviously greater than the critical pore pressure needed for reactivation of favorably oriented existing failed structures.

1.1.6. Conclusions

While the assumption of using horizontally layered basins for CO2 sequestration studies may be valid for most cases, the need for an actual trap system requires a more realistic geometry for parametric studies and simulations. The geometry should be flexible enough to include faults or fractures and any unconformities that may exist. Our study shows that by using finite element analysis pre-processor geometries resembling structural trap systems can be generated and successfully converted into native fluid flow simulation formats. This novel approach enables us to study the influence of geometric parameters such as anticline wavelength, amplitude and thickness.

The results of our study show that higher wavelengths, lower amplitudes and relatively thick layers provide the best conditions for safe CO2 sequestration. Further, the depth of the sequestration site also plays an important role. Our results conclude that for aquifer depths of 2500m and 3000m (for a closed system) the maximum occupancy and SIL can be obtained, respectively. If the economic costs of drilling to the deeper aquifers and compression of CO2 for injection into such reservoirs can be justified, deep CO2 sequestration results in higher storage capacity.

A major and not surprising conclusion is that the lateral fluid flow boundary condition of an aquifer system has the most significant influence on the CO2 sequestration parameters. The assumption of an open system requires gigantic aquifers (~100 km) that may be very difficult, if not impossible, to locate in the vicinity of many CO2 producers. The open system assumption might also lead to over-simplified cases, unless brine production wells are included. A more realistic approach of semi-open fluid flow boundaries yields similar if not better results than the open system case. However, this approach seems only applicable if the total magnitude of the lateral flow boundary condition of an aquifer system can be determined e.g. by water drawdown tests similar to conventional pressure transient testing and production data analysis of the oil and gas wells. Our results show that for such a system, the anticline wavelength, amplitude and thickness have a pronounced influence on CO2 sequestration parameters. However, unless extensive field tests permit the application of semi-open or open aquifer, this study shows that the safest approach for a sustainable CO2 sequestration project should be the assumption of closed fluid flow boundaries.

1.2. Geomechanical Analysis

1.2.1. Introduction

Geologic CO2 sequestration in deep saline aquifers, depleted oil and gas fields and unmineable coal seams has been identified as a possibility to reduce CO2 emissions from coal fired power plants and production facilities (Metz et al., 2007), provided that a thorough understanding of the storage site is conducted. The selection of suitable injection sites depends critically on the assessment of geomechanical risks such as fracture reactivation associated to the pore pressure increase (e.g. Streit and Hillis, 2004; Li et al., 2006; Rutquist et al., 2007; Rutquist et al., 2008; Vidal-Gilbert et al., 2009; Cappa and Rutqvist, 2011). Sibson (2003) shows that hydraulic extensional fractures are only critical for intact rock at low differential stress and that the reactivation of cohesion-less, optimally oriented shear fractures determines the lower limit of sustainable reservoir overpressures. These fractures, if critically stressed, represent fluid flow pathways (Barton et al., 1995) along which dissolved CO2 may escape into the atmosphere or into freshwater aquifers. If such fractures are reactivated due to fluid injection applications induced seismicity with moment magnitudes ranging from -3 to 5 can be observed (e.g. Gibbs et al., 1973; Wesson and Nicholson, 1987; Cappa and Rutquist, 2011; Verdon et al., 2011). In order to assess these geomechanical risks a thorough understanding of the state of stress at potential sequestration sites is necessary.

Numerical simulations provide excellent tools for a critical assessment of reservoir pressurization and the associated geomechanical risks. A thorough and most realistic representation of the in-situ effective stress conditions requires the coupling of a fluid flow simulation through porous media with a geoemchanical analysis (e.g. Settari and Mouritis, 1998; Rutqvist et al., 2002; Dean et al., 2006; Vidal-Gilbert et al., 2009). As a major conclusion from such studies, the prevailing stress regime (Rutqvist et al., 2007; Rutqvist et al., 2008; Paradeis et al., 2012) and the fluid flow boundary conditions (Zhou et al., 2008; Rutqvist et al., 2007) are the most critical parameters. Often such numerical modeling studies of CO2 injection scenarios are simplified to a horizontally layered sedimentary basin (Li et al., 2006; Rutquist et al., 2007; Rutquist et al., 2008; Zhou et al., 2008; Cappa and Rutqvist, 2011). These simplified model geometries are valuable to study the influence of parameters such as permeability, injection rate, fluid flow boundary conditions and seal efficiency on CO2 plume spreading and pressurization (e.g. Zhou et al., 2008; Inoue, 2009; Taberner et al., 2009; Ehlig-Economides and Economides, 2010; Cappa and Rutqvist, 2011). A geomechanical risk assessment simulating an accurate representation of the often heterogeneous in-situ state of stress requires model geometries reflecting the actual geologic scenario and thus considering the mechanical contribution arising from geometrical heterogeneities (Rutqvist et al., 2008; Amirlatifi et al., 2012; Paradeis et al., 2012). In this regard anticline structures are among the most common structural traps for hydrocarbon reservoirs and thus become a prime target of the emerging challenge of safe geologic sequestration of CO2 (Metz et al., 2007). CO2 sequestration in anticline structures has been investigated by Paradeis et al. (2012) and Amirlatifi et al. (2012). Amirlatifi et al. (2012) perform a fluid flow simulation analysis based on generic anticline geometries and show that low amplitude, large wavelength anticline structures provide the best conditions for CO2 sequestration. They also conclude that the fluid flow boundary conditions are of utmost importance when evaluating geomechanical risks due to fluid injection. Paradeis et al. (2012) utilize the same generic model geometries and perform a finite element based pre-injection risk assessment by calculating the critical pore pressure increase based on the geometrical factors of anticline wavelength and amplitude and the prevailing stress regime. Using a simplified analytical solution neglecting pore pressure - stress coupling they conclude that the stress regime is the most critical factor and that for extensional and strike slip stress regimes anticline structures provide safer conditions than horizontally layered basins.

In this paper the generic anticline model geometries used in Paradeis et al. (2012) and Amirlatifi et al. (2012) are used to further evaluate critical geologic parameters and to perform a pseudo-3D coupled geomechanical analysis to assess the fault reactivation risk within generic anticline structures. Of particular interest in this study is the coefficient of friction between bedding layers and its impact on critical sustainable pore pressures and the resulting risk of fault reactivation.

Flexural slip between sedimentary layers accommodates the strain during multi-layer folding and it has been shown that the presence or absence of interlayer slip strongly controls the distribution and evolution of strain within folded strata (Smart et al., 2009) and thus has a significant impact on fracture reactivation (Sanz et al., 2008; Smart et al., 2009). The coefficient of friction between bedding planes effectively describes the coupling between different layers, whereby a low coefficient of friction represents a weak coupling and a high competence contrast between adjacent layers is produced (Twiss and Moores, 2002). A large coefficient of friction represents a strong coupling and hence different friction values should result in different stress and strain distributions across adjacent bedding layers.

In order to study the influence of the inter-bedding coefficient of friction for extensional, strike-slip and compressional stress regimes this study first presents a pre-injection geomechanical risk assessment based on simplified analytical solutions including the pore pressure - stress coupling effect (Altmann et al., 2010) and then the results of a pseudo-3D partially coupled fluid flow - geomechanical analysis are presented to show the interplay of friction coefficient and stress regime and their influence on fault reactivation probability and the safe injection limits within anticline structures.

1.2.2. Modeling Approach

The numerical modeling analysis comprises a finite element analysis based on the prevailing stress regime that is used for a pre-injection assessment of critical sustainable pore pressures, and a partially coupled fluid flow - geomechanical analysis for analysis of the CO_2 injection related risk of fracture reactivation for different stress regimes and inter-bedding friction coefficients.

It is important to note that the modeling approach is based on the assumption that the anticline structure is pre-existing and that static displacement boundary conditions can be used to simulate the different far-field stress regimes. The modeling approach does not consider the structural development of the anticline over geologic time scales. Different geologic strain rates result in different states of stress of an anticline. However, this represents an extensive sensitivity study by itself which was outside the scope of this paper. A static state of stress using displacement boundary conditions is considered sufficient to enable the study of the model parameters of the anticline and represents the most common approach to simulate in-situ stress states for geomechanical studies.

1.2.3. Finite Element Model

1.2.3.1. Geometry and Boundary Conditions

The geometry for the generic anticline structures used in this study is shown in Figure 4a. The models are 6000m (x-direction) by 1500m (y-direction) by 2500m (vertical direction). In order to minimize the boundary effects of the numerical model, the anticline is positioned in the center of the model with 1500m of horizontally layered material on both sides of the anticline. The models comprise rock layers of four different materials: a sandstone and shale sequence (Figure 4b) in the middle of the model is covered by an overburden layer and supported from beneath by a basement layer. The total thickness of the shale and sandstone sequence is 500m with the top shale, top sandstone, and caprock each being 100m for all of the models. The interface between each layer is modeled as a frictional contact surface enabling in-plane displacements.

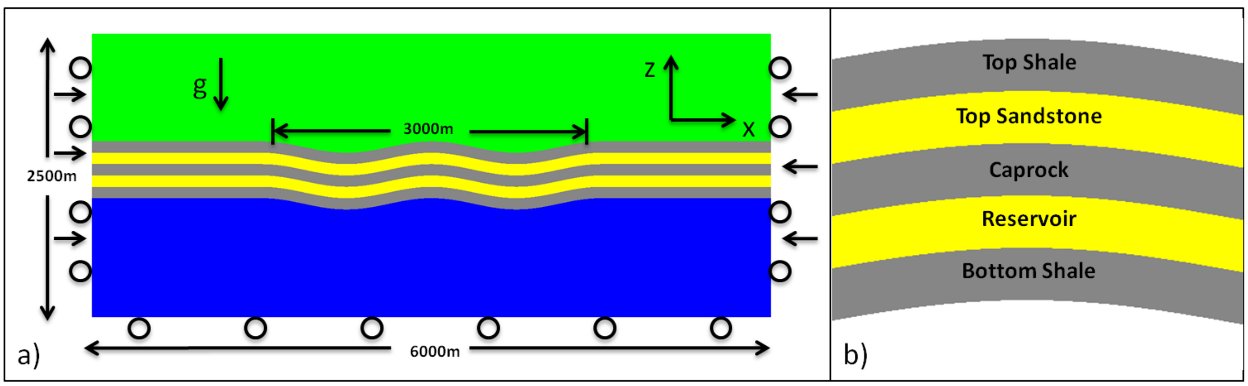

Figure 4: a) FE model geometry and boundary conditions. b) Shale-sandstone sequence of the anticline layer. The second sandstone layer represents the injection layer.

The finite element analyses are run in two consecutives steps. The first step serves to equilibrate the gravitational body force over the complete model domain. In the second step displacement boundary conditions are used to generate the strains simulating the different stress regimes in 3D. The corresponding equations of linear poro-elasticity were used to calculate the displacements (Jaeger et al., 2007). For the extensional stress regime, we assume that the sedimentary layers are tectonically relieved and thus the uni-axial strain assumption to calculate the resulting horizontal stresses applies (Engelder, 1993).

$$\sigma_h = \frac{\nu}{1-\nu}\sigma_V + \frac{(1-2\nu)}{(1-\nu)}\alpha P \tag{2}$$

For strike-slip and compressional regimes, the three-dimensional boundary conditions are calculated using the relative stress ratios. For both of these regimes, the vertical stress is given by the integration of overburden density. In a strike-slip regime, the minimum principle stress is the minimum horizontal stress which is given by $\sigma_h = 0.8 * \sigma_v$, the vertical stress is the intermediate principle stress and the maximum principle stress is $\sigma_H = 1.2\sigma_v$. For the compressional regime, the vertical stress is the minimum principle stress, the intermediate stress is $\sigma_h = 1.25\sigma_v$ and the maximum principle stress is $\sigma_H = 1.5\sigma_v$.

1.2.3.2.Pore Pressure – Stress Coupling

Simplified analytical techniques can be used as a pre-injection risk estimate for fault reactivation. The principle of pore pressure – stress coupling (Engelder and Fischer, 1994; Hillis, 2001) can be used to estimate the maximum sustainable pore pressure, P_c, (e.g. Wiprut and Zoback, 2000; Streit and Hillis, 2004; Rutqvist et al., 2008) for sites where limited geological knowledge exists. Pore pressure – stress coupling is based on the observation that the total minimum horizontal stress changes with a change in pore pressure (Teufel et al., 1991). However, as recent studies by Mueller et al. (2010) and Altmann et al. (2010) show, pore pressure stress coupling does not only affect the minimum horizontal stress but affects all components of the principal stress tensor and is a complex function of space and time. Altmann (2010) shows that pore pressure stress coupling is therefore different for each stress regime. For the pre-injection risk assessment the principle of pore pressure - stress coupling, based on the long term limits given by Altmann et al. (2010), is utilized to determine the maximum sustainable pore pressure, P_c, for fault reactivation in extensional, strike-slip and compressional stress regimes. The simplification to the long term limits becomes especially relevant for subsurface engineering applications such as CO_2 sequestrations which are interested in how much pore pressure change is sustainable over long times. The following simplified analytical solutions are based on the Mohr Coulomb failure criterion and the detailed derivations for these equations can be found in the Appendix.

1.2.3.3.Results

As the state of stress in an anticline displays the largest variations on a vertical cross section at the crest of the structure (Paradeis et al., 2012), for the determination of the maximum sustainable pore pressure, P_c, the stress changes associated to pore pressure – stress coupling along the σ_V-direction are considered for the various stress regimes. Assuming a friction coefficient of μ=0.577, α=1 and using the model parameter of ν=0.25 in equations 3-5 (see Appendix 1), the critical pore pressures for the various stress regimes can be determined.

For the compressional regime:

$$P_c = 9\sigma_V - 3\sigma_H - 5P \tag{3}$$

For the strike-slip regime:

$$P_c = \frac{9}{4}\sigma_h - \frac{3}{4}\sigma_H - \frac{1}{2}P \tag{4}$$

For the extensional regime:

$$P_c = \frac{9}{5}\sigma_h - \frac{3}{5}\sigma_V - \frac{1}{5}P \tag{5}$$

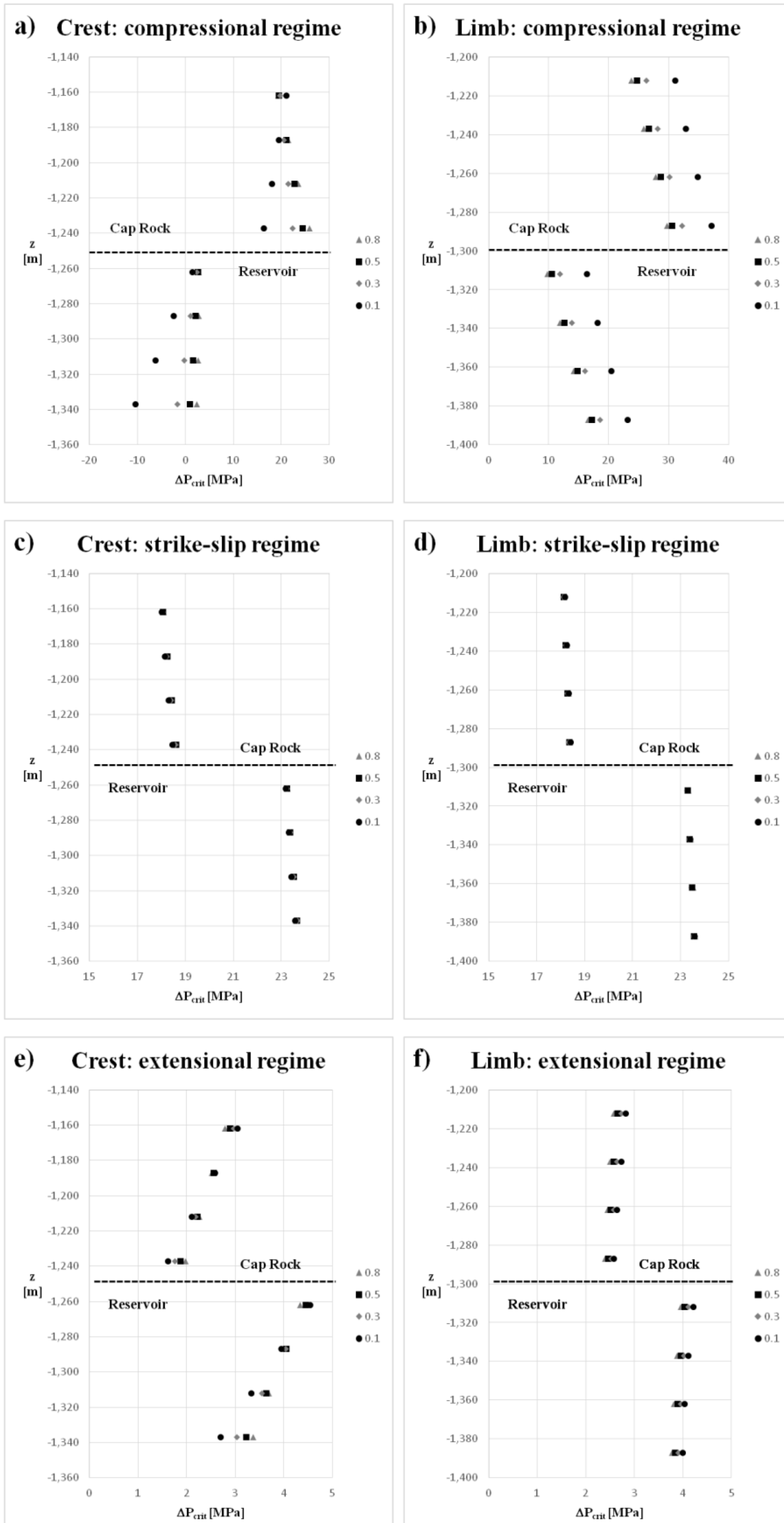

a) Crest: compressional regime
b) Limb: compressional regime
c) Crest: strike-slip regime
d) Limb: strike-slip regime
e) Crest: extensional regime
f) Limb: extensional regime
Cap Rock
Reservoir
z [m]
ΔP_{crit} [MPa]
0.8
0.5
0.3
0.1

Figure 5: Critical pore pressure difference for the various stress regimes at the crest and limb of the anticline structure. For the compressional stress regime the cap rock can sustain higher ΔP_c magnitudes than the reservoir layer. Fo the extensional and strike-slip regime the cap rock is able to sustain lower ΔP_c magnitudes than the reservoir layer and seal integrity (in terms of the permeability contrast) is more crucial.

Using equations 3, 4, and 5 the maximum sustainable pore pressure change, $\Delta P_c=P_c-P$, based on the initial effective state of stress can be calculated for the various stress regimes. Figure 5a-f show ΔP_c along the vertical direction for the reservoir and cap rock layers. For each stress regime the coefficient of friction between the bedding planes is given values of μ=0.1, 0.3, 0.5 and 0.8 to study the influence of inter-bedding coupling.

The results show that for the compressional stress regime in the reservoir layer ΔP_c is close to 0 MPa and fracture reactivation is very likely. However, across the interface to the cap rock ΔP_c increases to 16.4 MPa for m=0.1 and 25.8 MPa for m=0.8. As Figure 5a shows, higher friction coefficients result in a higher sustainable pore pressure across the interface.

For the strike-slip stress regime (Figure 5c) ΔP_c is slightly higher with 23.2 MPa in the reservoir layer than in the cap rock (18.6 MPa). The influence of the inter-layer friction coefficient is minimized as the vertical stress is a principal stress included in equation (4).

For the extensional stress regime (Figure 5e) displays the overall lowest critical pore pressure magnitudes of ~4.5 MPa in the reservoir layer and 1.5-2 MPa in the cap rock. Hereby, lower friction coefficients result in lower ΔP_c magnitudes in the cap rock. The extensional stress regime shows how critical the seal integrity (in terms of permeability) is.

1.2.4. Coupled Model

1.2.4.1. Model Setup and Boundary Conditions

The realistic assessment of the geomechanical risks due to CO_2 injection related pore pressure increases requires the utilization of a modeling approach that that involves multiphase and multi-component fluid flow in a geologic system. The study of mechanical deformations under such conditions is achieved by numerical modeling of fluid flow through porous medium coupled with a geomechanical analysis of the medium at different pore pressure distributions (Rutqvist et al., 2002; Settari and Mourits, 1998; Settari and Walters, 1999; Thomas et al., 2003; Vidal-Gilbert et al., 2009). For this purpose an implicit partially coupled fluid flow-geomechanical analysis coupling ECLIPSE™ and ABAQUS™ developed at Missouri S&T (Amirlatifi et al., 2011a,b; project: DE-FE0001132) is utilized. Amirlatifi et al.'s (2012) coupling approach enables coupling between the reservoir simulation and the geomechanical analysis whereby both simulations use the same discretization minimizing the use of interpolation algorithms.

The pseudo 3D model employed here is part of a direct line CO_2 sequestration scheme with a lateral extension of 76 meters where the injection well is placed at the crest of the anticline. No flow boundary condition along the longitudinal extension of the model results in the direct line sequestration configuration flow regime, with image wells acting as parallel well sets (Figure 6). A CO_2 injection well is placed at the crest of the anticline in the bottom reservoir layer. The well is perforated all the way in the reservoir layer. The lateral fluid flow boundary conditions reflect a closed system. Furthermore, the simulations are based on 1 year injection time-steps to minimize computational costs. The relevant simulation and injection parameters are given by Table 12.

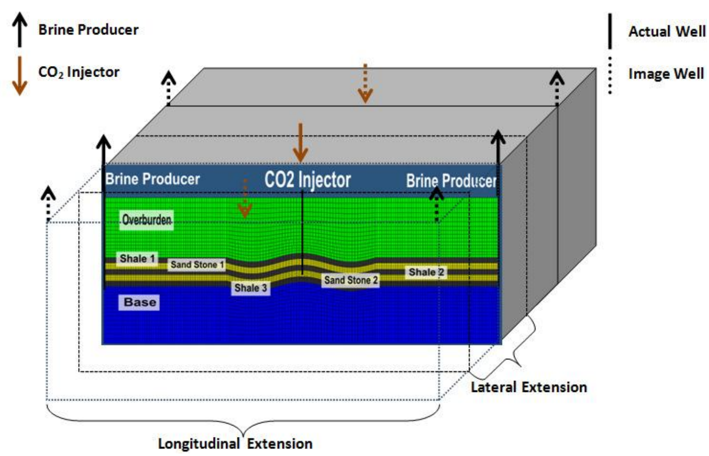

Figure 6: Model geometry and CO2 injection setup as a direct line scheme with image wells. In order to utilize partially coupled modeling approach for the anticline models the model geometry of Figure x has been slightly altered. Instead of 1500m in the y-direction the model dimension had to be decreased to 76m. The reduction of the model dimension in y-direction is due to the computational requirements of the coupling procedure. Due to license availability the simulation had to be run on a high performance desktop PC. Larger model dimensions would have increased the simulation time manifold without producing significantly different results.

Table 12: Boundary Conditions and model paramters

Parameter	Units	Assumed values
Stress Regimes	[ ]	Extensional
		Compressional

		Strike Slip
Coefficient of Friction(μ)	[ ]	0.1
		0.8
Well Location	[ ]	Crest
Boundary type	[ ]	Closed
CO_2 Injection rate (STD)	kTons/Year	20 (28680 m3/day)
Reservoir Thickness	m	100
Wavelength	m	1500
Amplitude	m	100
FP: cohesion	[MPa]	15
FP: friction angle	deg	33
FP: tensile strength	[MPa]	7.5

1.2.4.2.Results

Note: Due to licensing problems for the reservoir simulation software ECLIPSE at Missouri S&T, during the project period, only the results for fracture generation can be presented.

In order to show the occurrence of fault generation due to the CO_2 related pore pressure increase this study utilizes the concept of Fracture Potential (Eckert and Connolly, 2007; Verdon et al., 2010). Fracture Potential (FP) describes the ratio between the actual differential stress and the differential stress at failure, and thus, if FP=1 can be used to indicate regions in a numerical model where fault generation occurs. The concept of Fracture Potential to assess the likelihood of fracture occurrence is chosen to overcome convergence problems of the numerical models once appropriate plasticity models are applied in ABAQUS™. Whilst such plasticity models are a standard procedure and can be readily included, a coupled effective stress – displacement analysis including contact surfaces has resulted in severe convergence problems and stable solutions could not be obtained. As a suitable alternative solution, FP represents a post-processing failure criterion which is automatically calculated after each time iteration modeled. The various CO_2 injection scenarios are halted when the FP in the cap rock reaches 1 and the achieved injection time is termed Safe Injection Limit (SIL). For the various stress regimes, CO2 injection scenarios are analyzed for inter-bedding friction coefficients of 0.1. and 0.8.

Before the CO2 injection stages an in initial hydrostatic pore pressure distribution is applied throughout the model as shown in Figure 7.

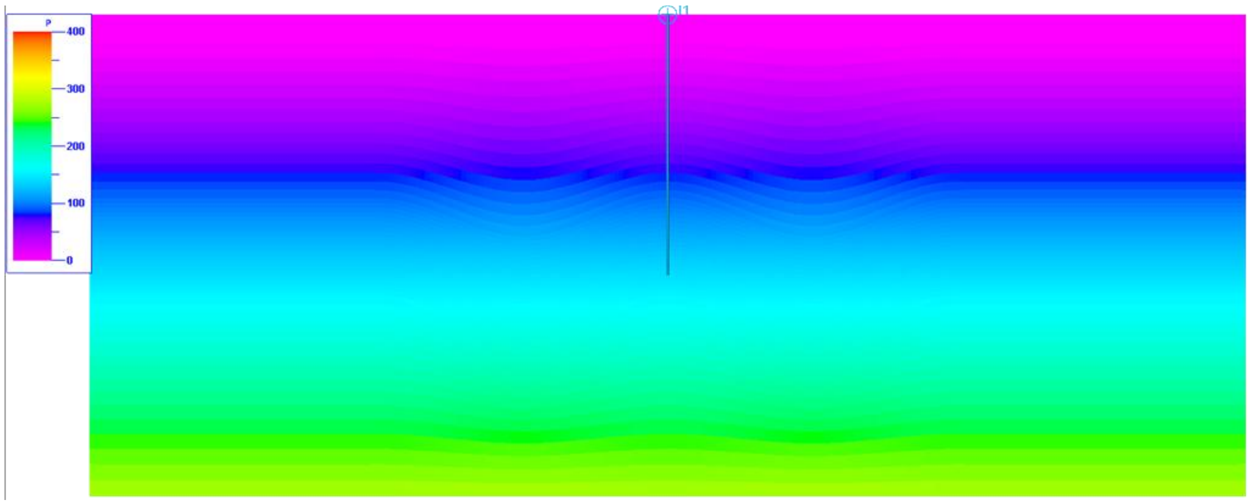

Figure 7 - Hydrostatic Pore Pressure Distribution in bar in the model.

1.2.4.2.1. Compressional Stress Regime

For the compressional regime in this study, the vertical stress is the minimum principle stress, the intermediate stress is given by $\sigma_h = 1.25\sigma_v$ and the maximum principle stress is given by $\sigma_H = 1.5\sigma_v$.

Figure 8 and Figure 9 show the initial shear fracture potential for the anticline with the coefficient of friction of 0.1 and 0.8 between the layers under the compressional regime respectively.

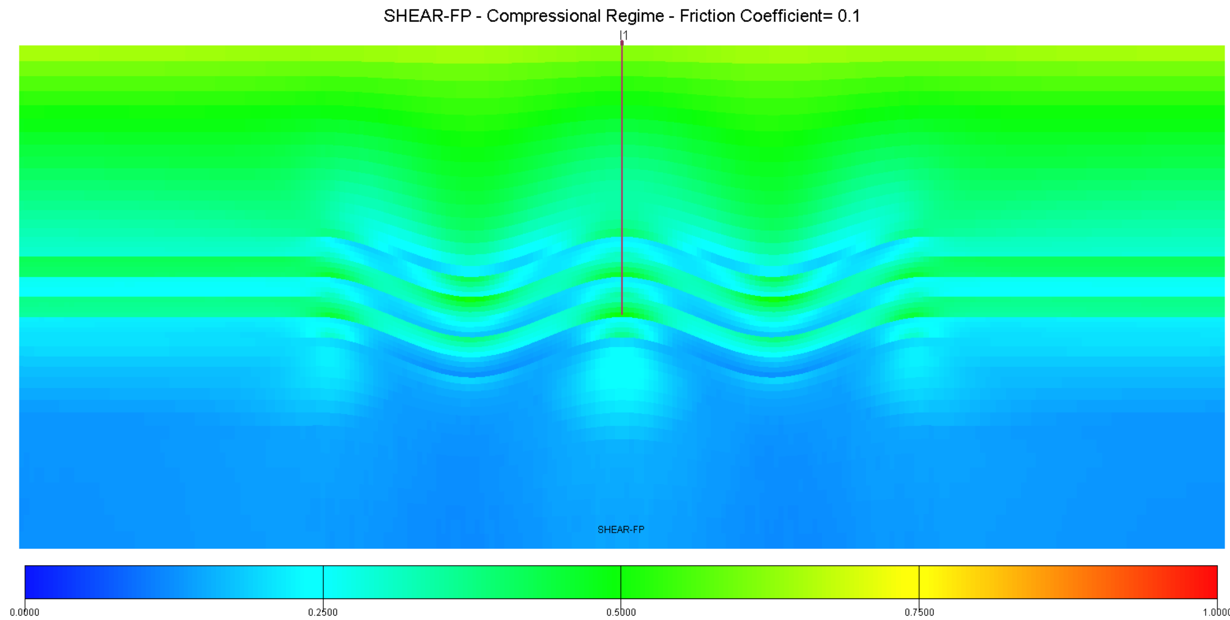

Figure 8 - Initial Shear Fracture Potential - Coefficient of friction = 0.1 – Compressional Model

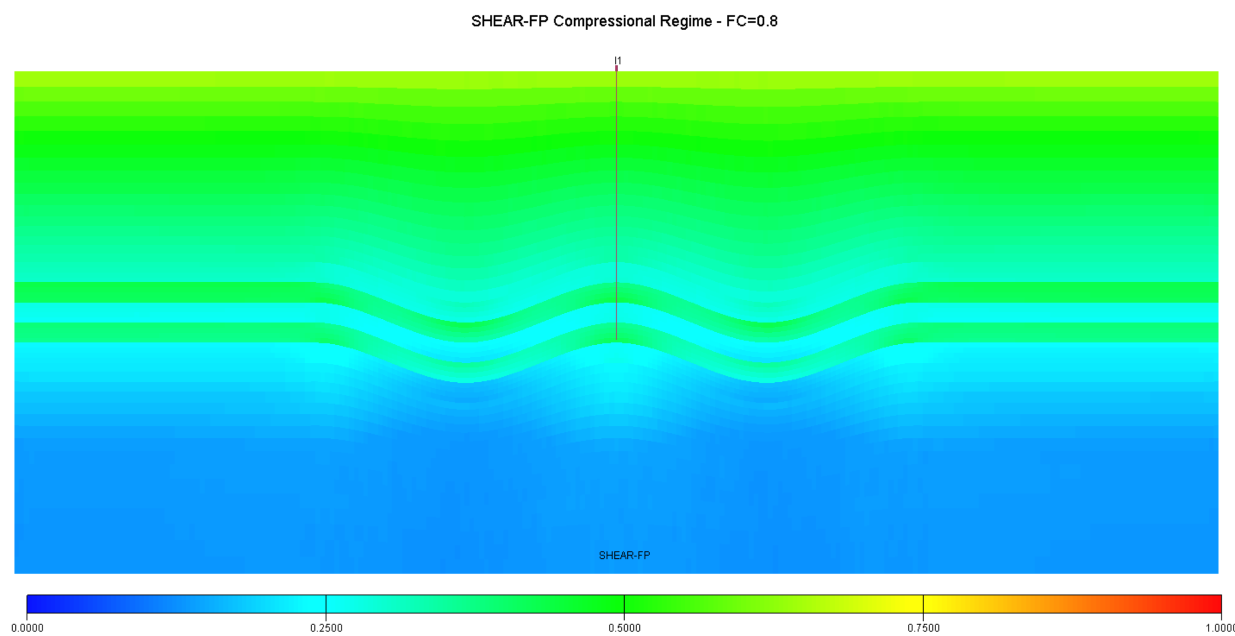

Figure 9 - Initial Shear Fracture Potential - Coefficient of friction = 0.8 – Compressional Model

As shown in these two figures, the initial shear fracture potential in the two models is similar in the overburden and base of the model, but the two models behave differently in the shale-sand layers. While the μ=0.8 model is initially at an elevated FP state, compared to the μ=0.1 model, it is speculated that this model will tolerate the increase in pore pressure better, since the differential stresses occurring across model layers is reduced.

The two models show the same pore pressure distribution after five years of CO_2 injection at the rate of 20kTons/year, which is depicted in Figure 10.

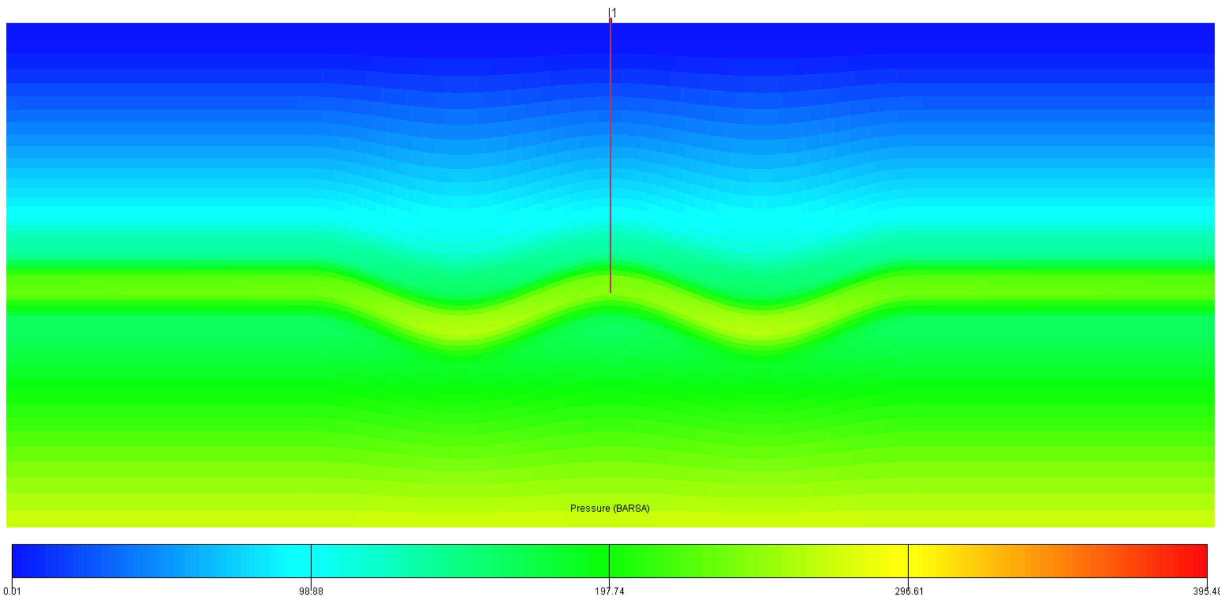

Figure 10 - Pore pressure distribution in bar in the model after 5 years of injection

The increase in pore pressure will result in new states of stress in the model models as shown in Figure 11 and Figure 12. As expected, the μ=0.1 shows a significant increase in the shear fracture potential, with sFP at the well bore vicinity increasing from an initial value of 0.5 to 0.75 after five years of injection, while the μ=0.8 model goes from an initial sFP value of 0.41 to 0.63 after the same period of injection.

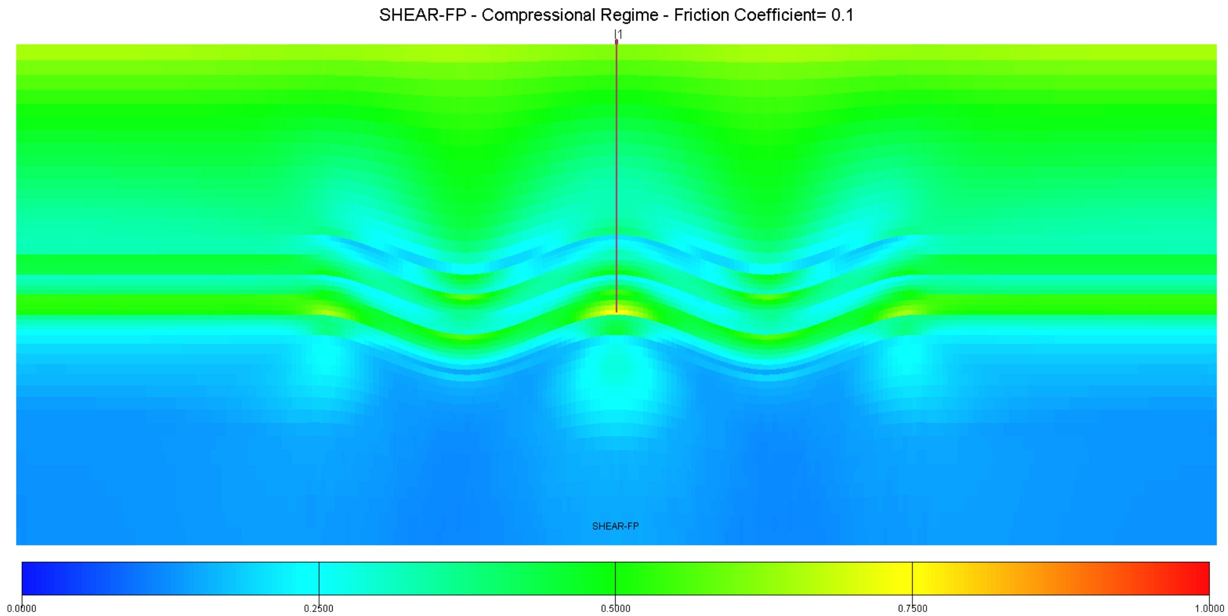

Figure 11 - Shear Fracture Potential after 5 years of injection- Coefficient of friction = 0.1 – Compressional Model

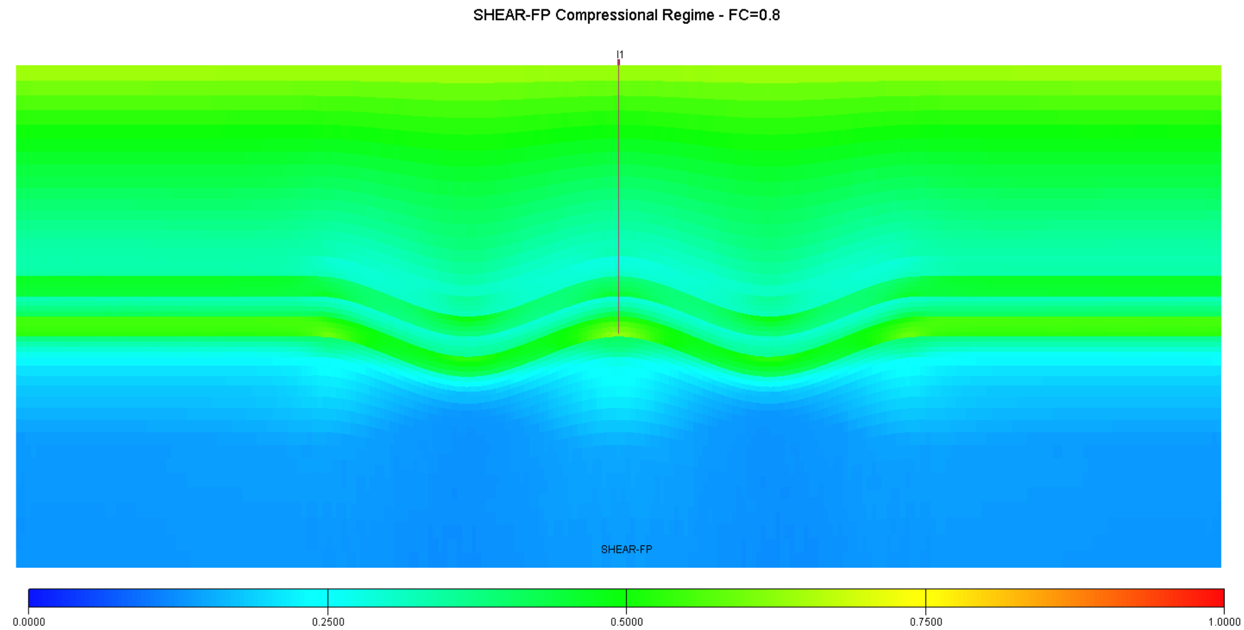

Figure 12- Shear Fracture Potential after 5 years of injection - Coefficient of friction = 0.8 – Compressional Model

The two models show the same overall pore pressure increase after 10 years of injection, as shown in Figure 13. The final CO_2 saturation distribution under closed boundary conditions after 10 years of injection is shown in Figure 14. The overall occupancy of the two models is 1.4%. At this point hydraulic fractures are created in the vicinity of the well which can be considered good for the overall performance of the model.

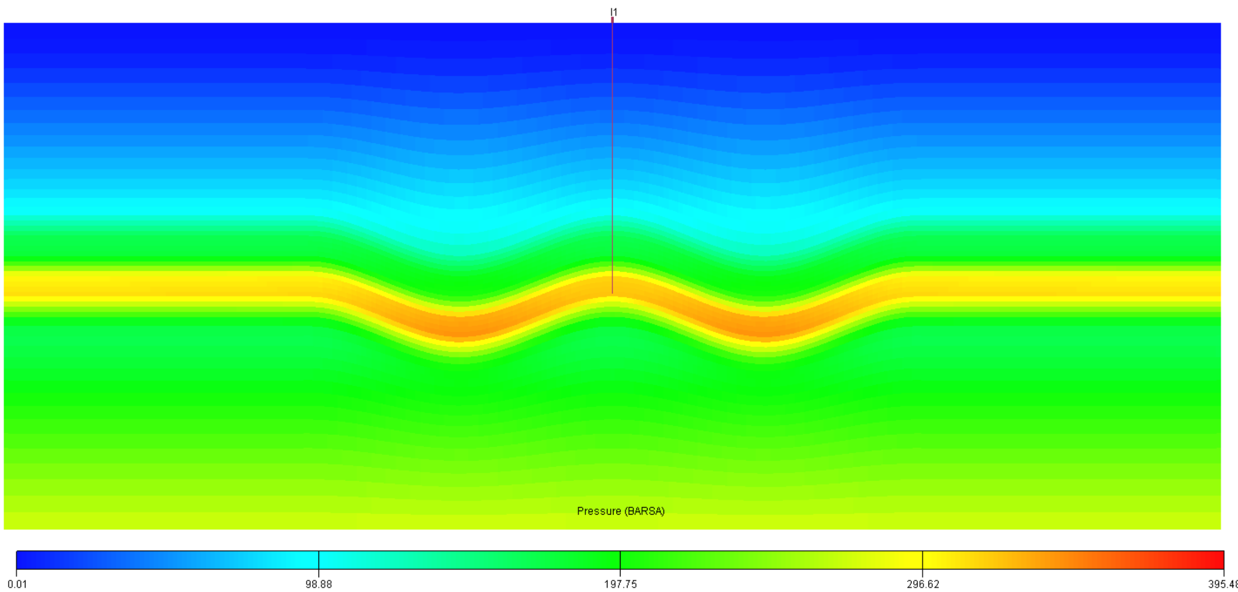

Figure 13- Pore pressure distribution in bar in the model after 10 years of injection

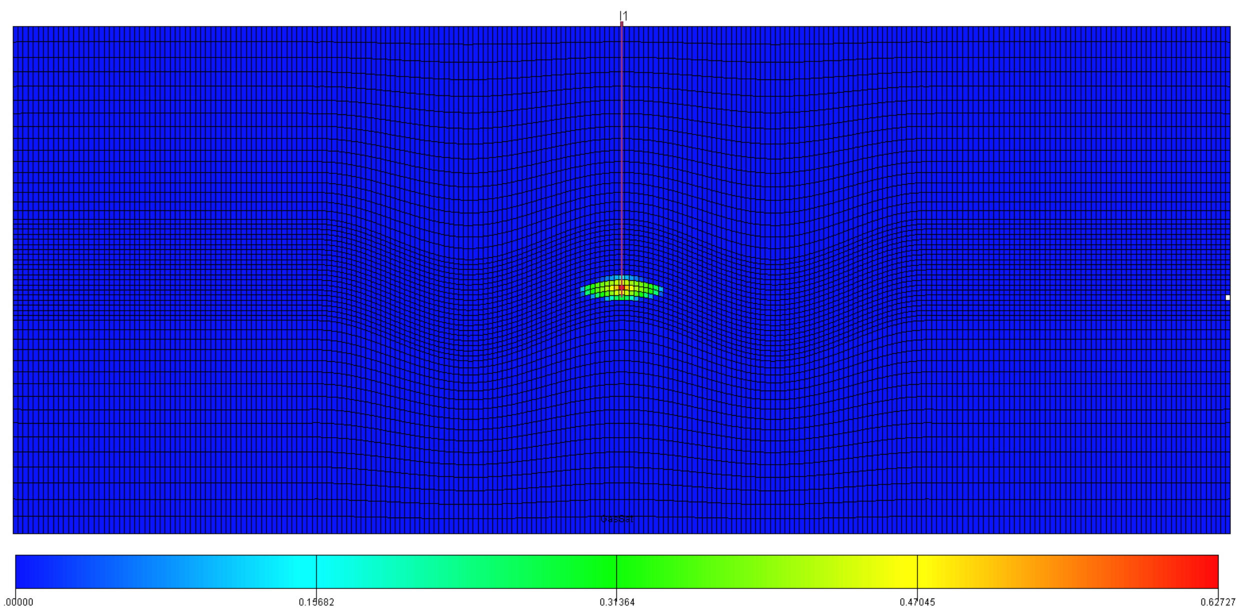

Figure 14 - Saturation of CO2 in the model after 10 years of injection

The two models, however, show different behaviors in terms of the shear fracture potential. While the μ=0.8 is still at a safe state of stress, but close to shear failure at the well bore vicinity after 10 years of injection, the μ=0.1 has already failed at this stage at the wellbore and the edges of the anticline are prone to failure. The sFP distribution for each model is shown in Figure 15 and Figure 6. The failure in the vicinity of the wellbore is considered positive as the overall performance of CO2 injection will be increased. It should be noted that the caprock integrity remains intact for both models.

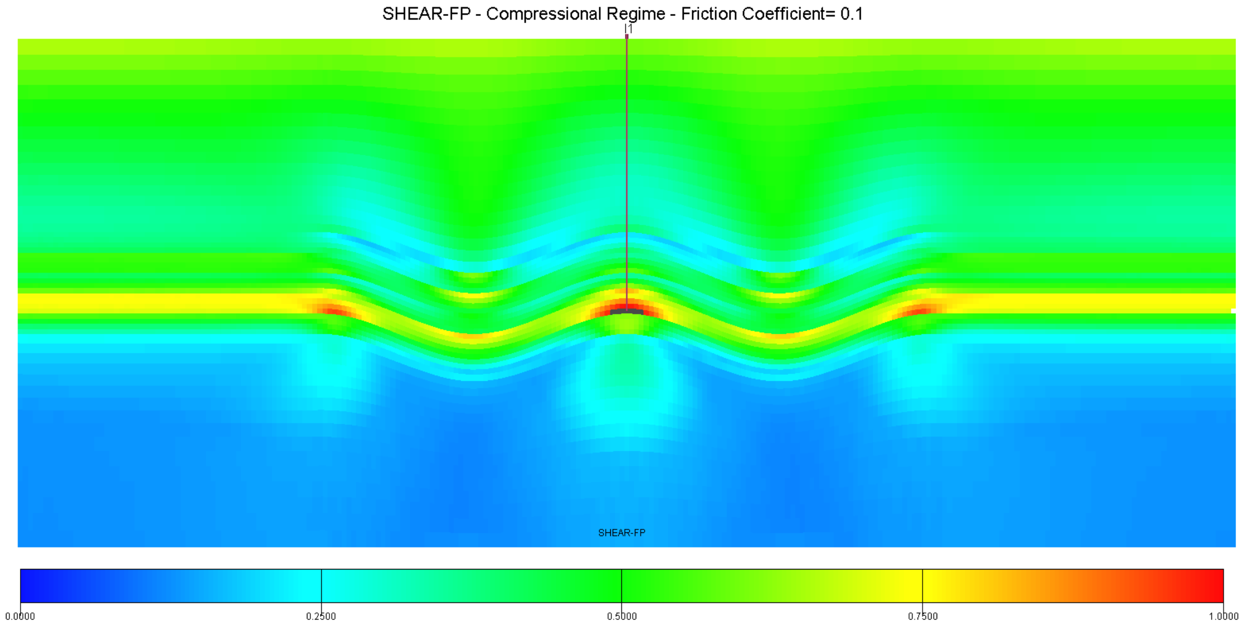

Figure 15 - Shear Fracture Potential After 10 years of injection- Coefficient of friction = 0.1 – Compressional Model

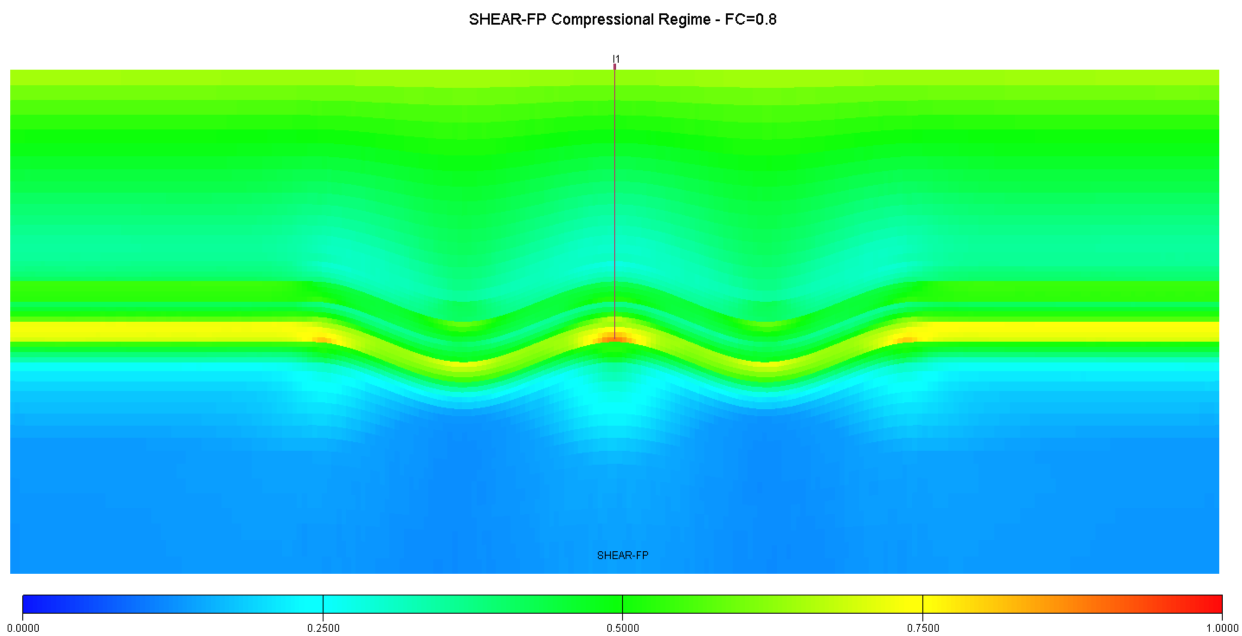

Figure 16 - Shear Fracture Potential After 10 years of injection- Coefficient of friction = 0.8 – Compressional Model

If the injection in the μ=0.1 model is continued for 10 more years, the basement shale will also fail but the overlying shale caprock is still safe. sFP corresponding to the extended simulation run in the two models are shown in Figure 7 and Figure 8. Failure of the caprock is taken as the limit for safe injection, which means that that the safe injection limit (SIL) for the μ=0.1 model is not reached after 20 years. The overall occupancy in the model after 20 years of injection is 1.8% which is in good agreement with results from other studies for CO_2 sequestration under closed boundary conditions. The μ=0.8 model is still at safe sequestration limits and does not undergo shear or tensile fracture in the caprock but it undergoes hydraulic fractures in the wellbore vicinity, the syncline and at the edges of the anticline, all in the reservoir layer. At the caprock level, this model is at sFP=0.93 which is close to the failure, but still it is safe.

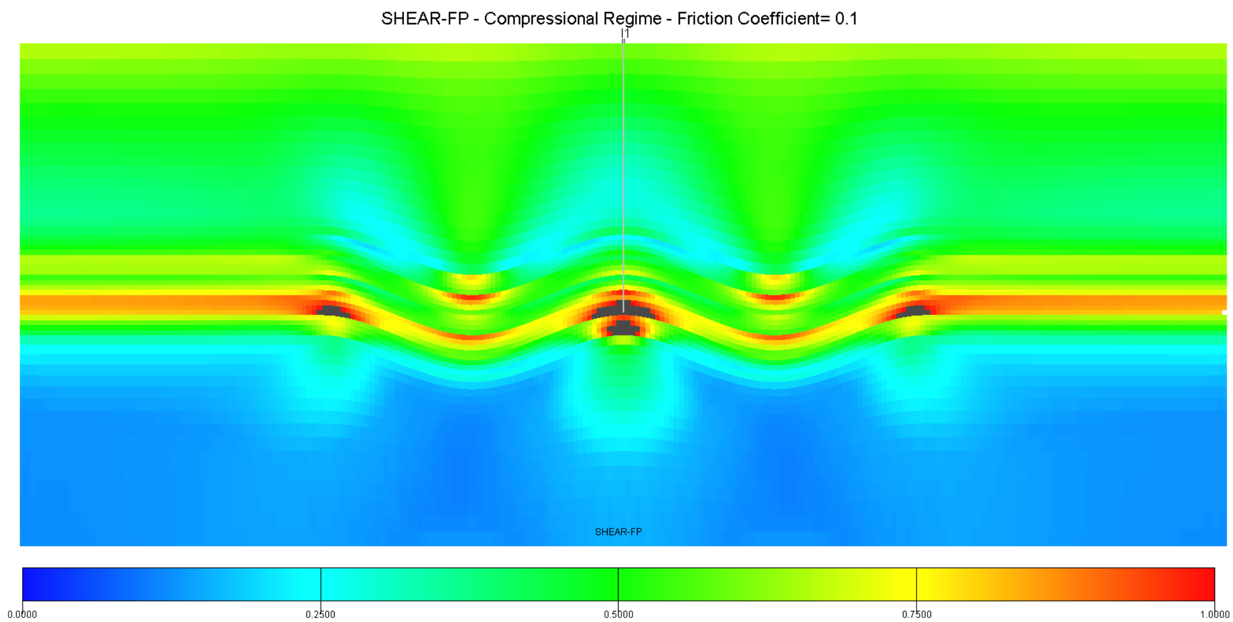

Figure 17 - Shear Fracture Potential After 20 years of injection- Coefficient of friction = 0.1 – Compressional Model

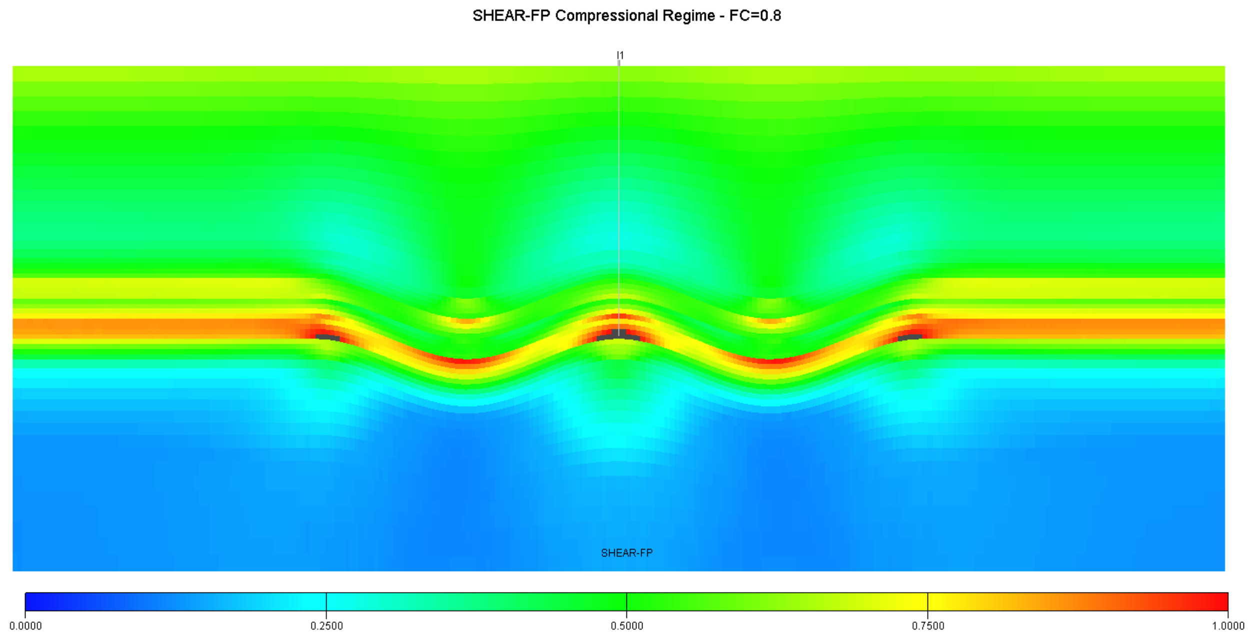

Figure 18 - Shear Fracture Potential After 20 years of injection- Coefficient of friction = 0.8 – Compressional Model

The evolution of sFP for the two models at wellbore vicinity, caprock and the far field over the course of 20 years of injection are illustrated in Figure 21. The graphs show that the 0.1 model shows a more rapid increase in sFP and shear fractures in the reservoir are generated after 10 years, 3 years earlier than for the 0.8 model. The sFP in the caprock remains under 1 and thus the SIL has not been reached yet. Extended injection periods are in progress and will be investigated in conjunction with a sensitivity analysis of the injection rate to find the safest (i.e. optimal) scenario.

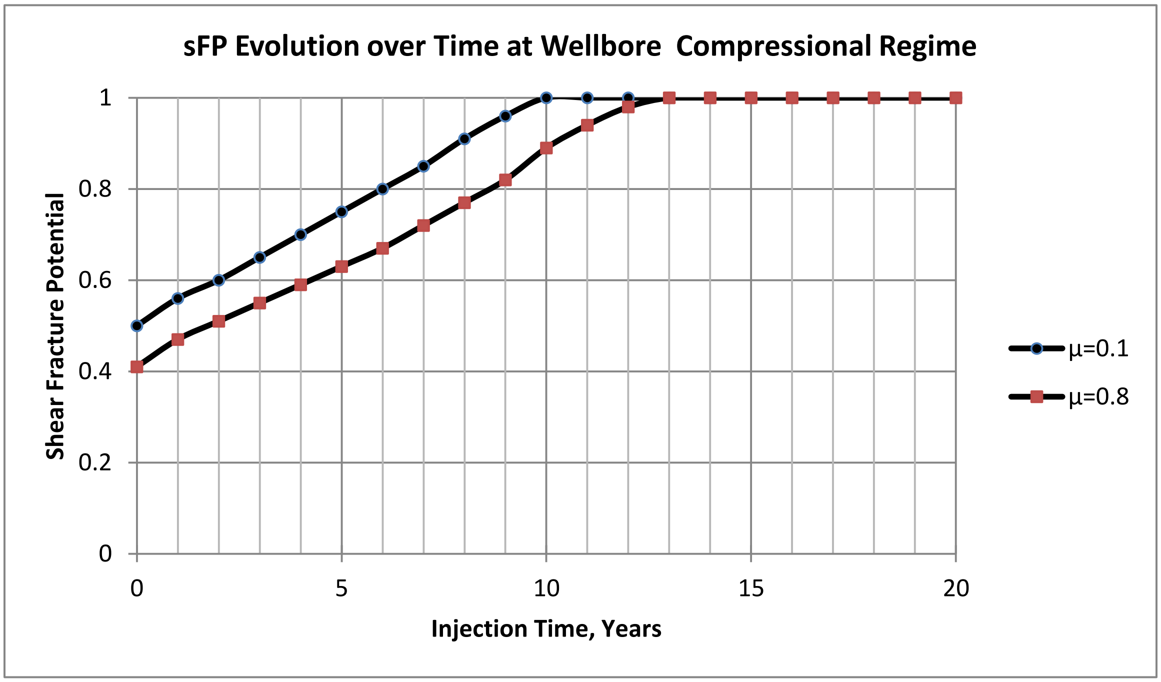

Figure 19 - sFP Evolution over Time at Wellbore - Compressional Regime

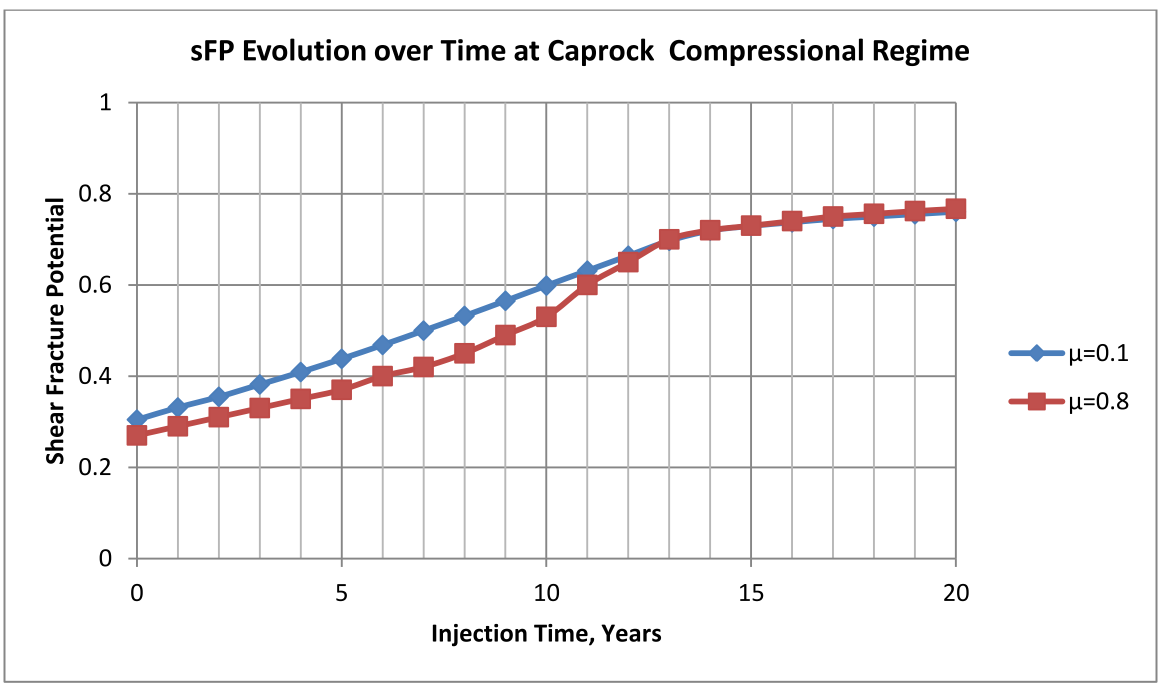

Figure 20 - sFP Evolution over Time at Far Field - Compressional Regime

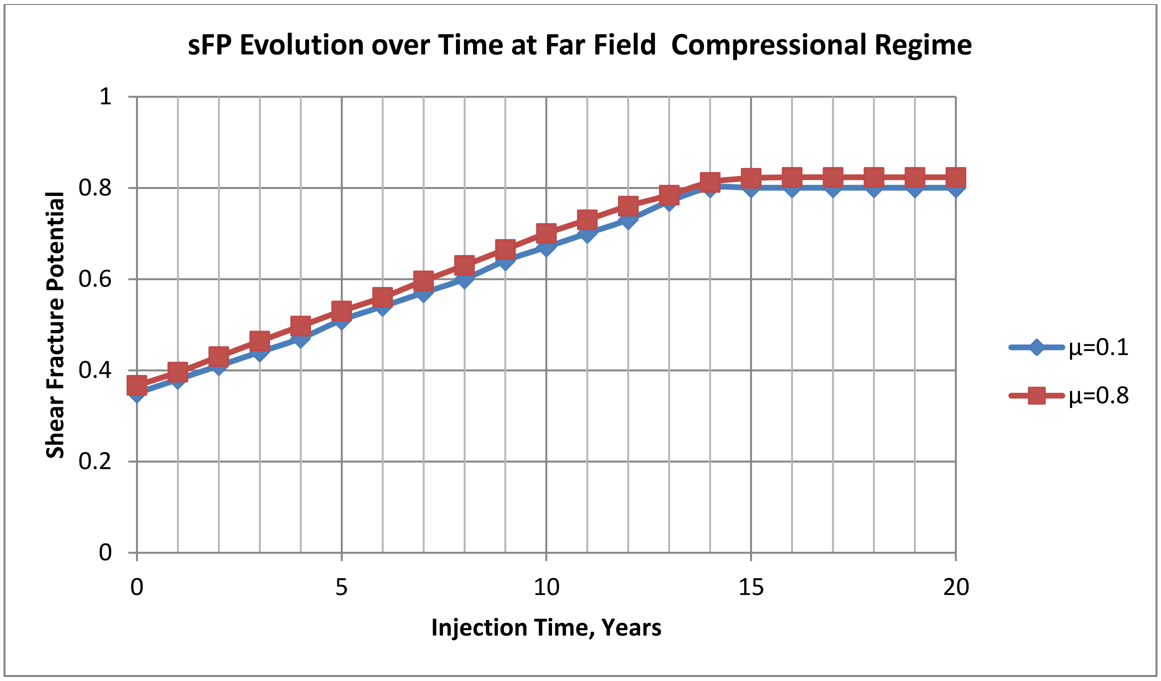

Figure 21 - sFP Evolution over Time at Far Field - Compressional Regime

1.2.4.2.2. Extensional Stress Regime

In the extensional regime, vertical stress is taken as the maximum principal stress and maximum horizontal stress is considered the intermediate principal stress with minimum horizontal stress being the minimum principal stress.

Figure 2 and Figure 3 show the initial shear fracture potential for the anticline with the coefficient of friction of 0.1 and 0.8 between the layers under the Extensional regime respectively.

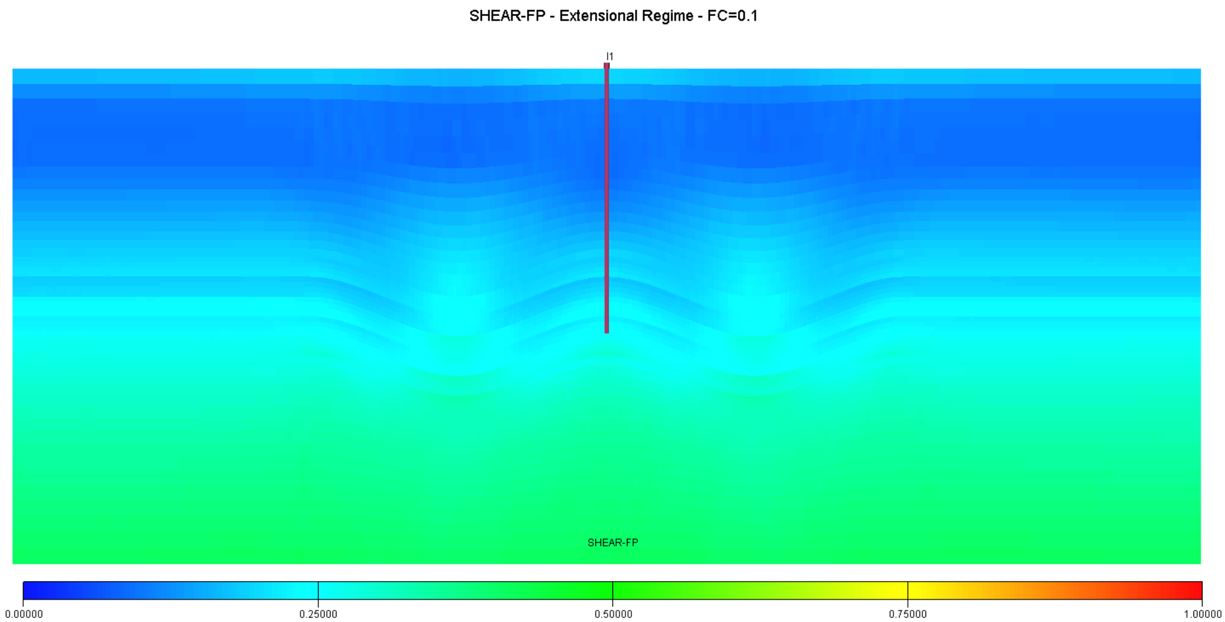

Figure 22 - Initial Shear Fracture Potential - Coefficient of friction = 0.1 – Extensional Model

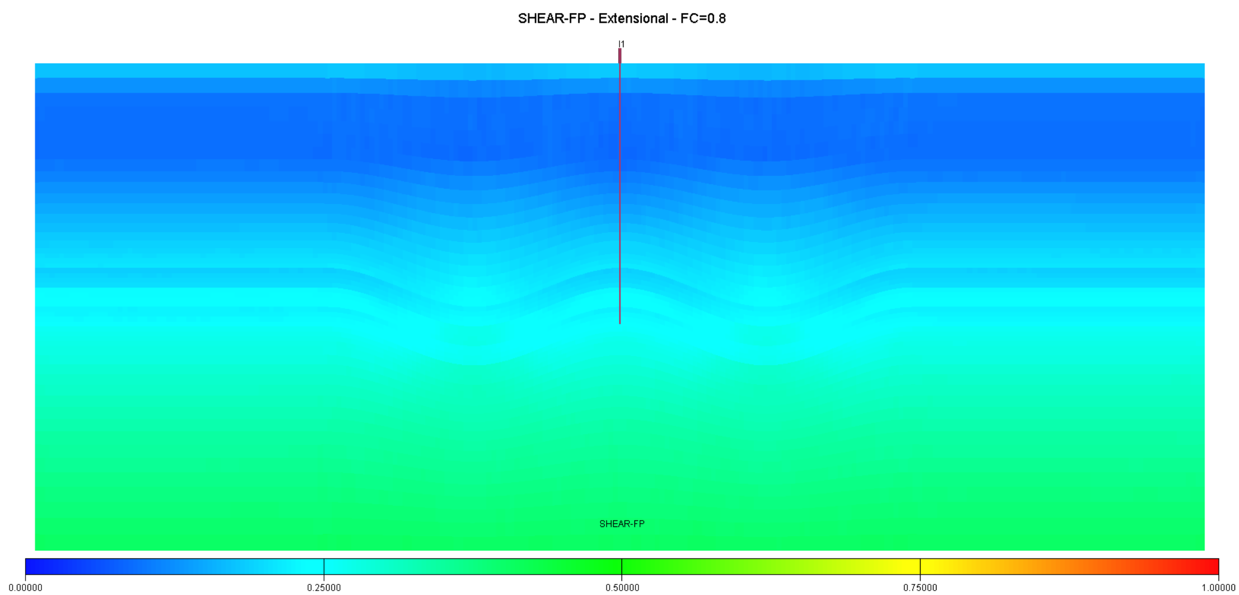

Figure 23 - Initial Shear Fracture Potential - Coefficient of friction = 0.8 – Extensional Model

As shown in these two figures, the initial shear fracture potential in the two models is similar in the model and the shale-sand layers. The two models show the same pore pressure distribution after five years of CO_2 injection at the rate of 20kTons/year, which is depicted in Figure 4.

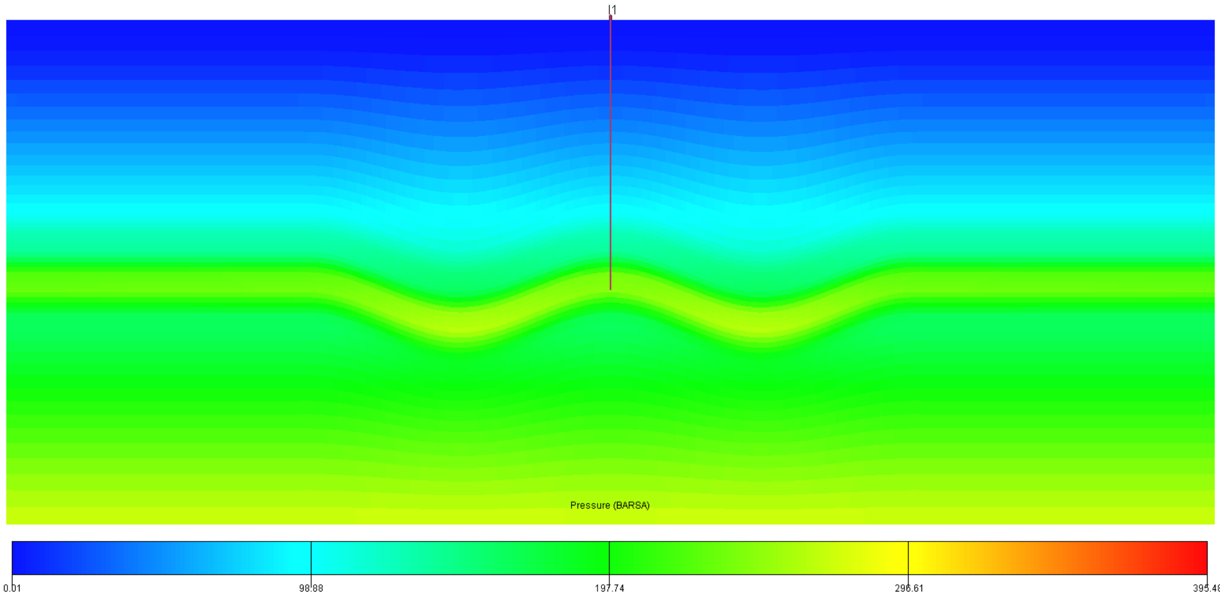

Figure 24 - Pore pressure distribution in bar in the model after 5 years of injection

The increase in pore pressure will result in new states of stress and new sFP in the model models as shown in Figure 5 and Figure 6. The two models undergo a decrease in shear fracture potential, with sFP at the well bore vicinity decreasing from an initial value of 0.26 to 0.11 after five years of injection for the μ=0.1 model and the μ=0.8 model goes from an initial sFP value of 0.24 to 0.11 after the same period of injection.

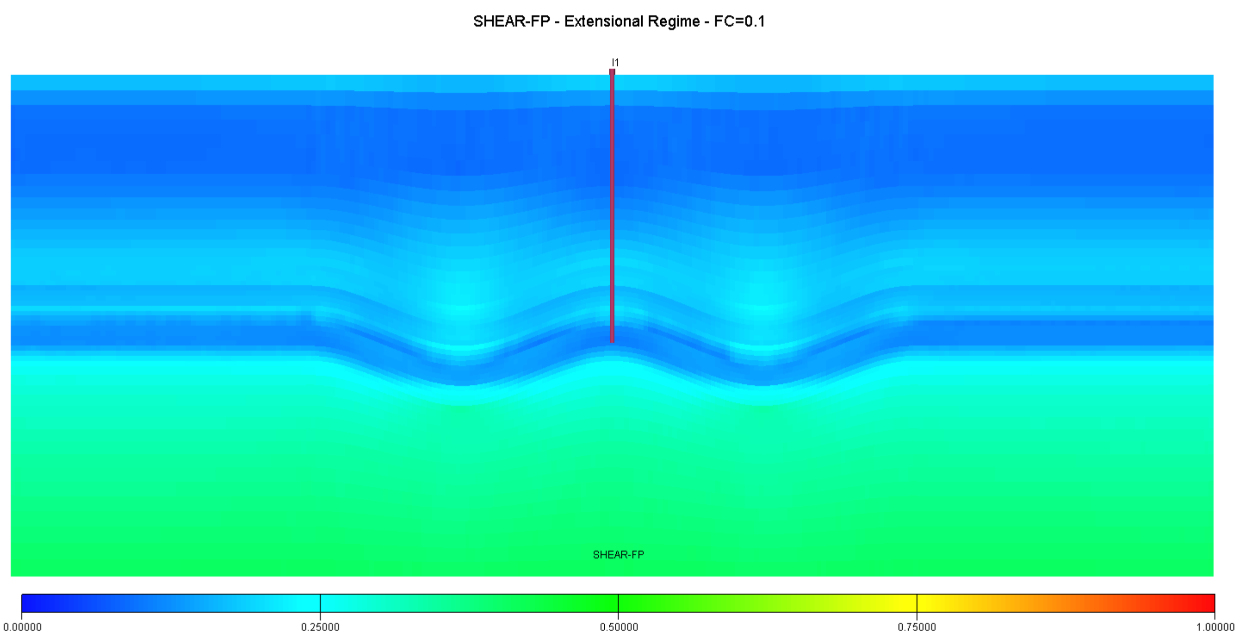

Figure 25 - Shear Fracture Potential after 5 years of injection- Coefficient of friction = 0.1 – Extensional Model

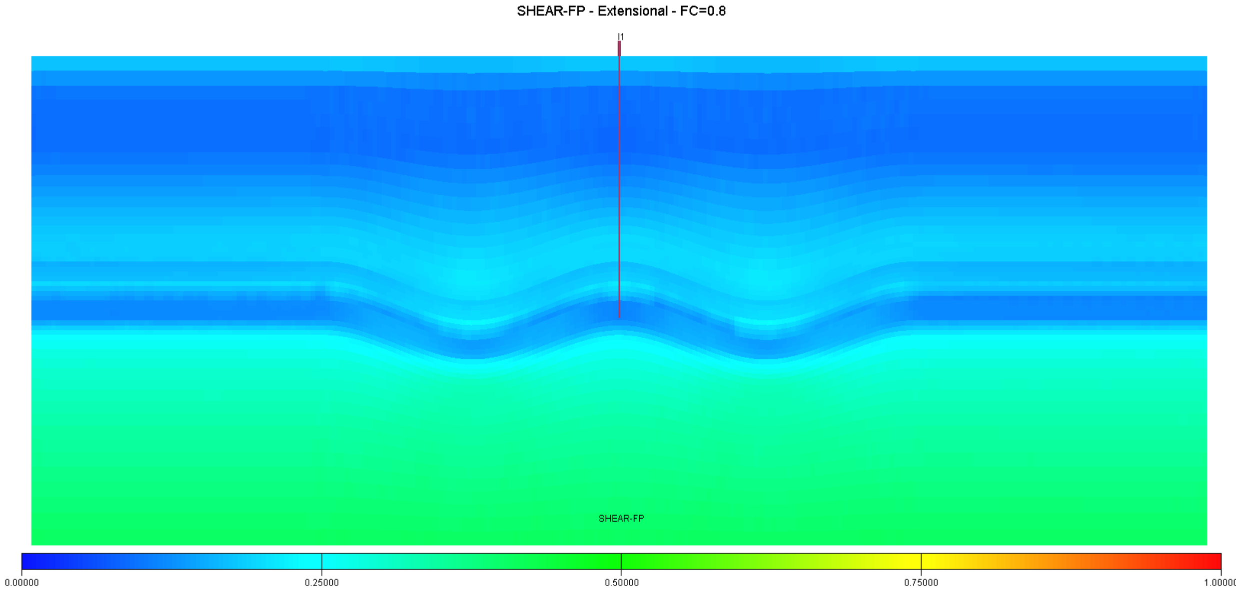

Figure 26- Shear Fracture Potential after 5 years of injection - Coefficient of friction = 0.8 – Extensional Model

The two models show the same overall pore pressure increase after 10 years of injection, as shown in Figure 7. The CO_2 saturation distribution under closed boundary conditions after 10 years of injection is shown in Figure 8. The overall occupancy of the two models is 1.4%. Unlike the compressional regime, no hydraulic fractures are initiated at this point in the models and the two models are safe from shear fracture and tensile fracture formations.

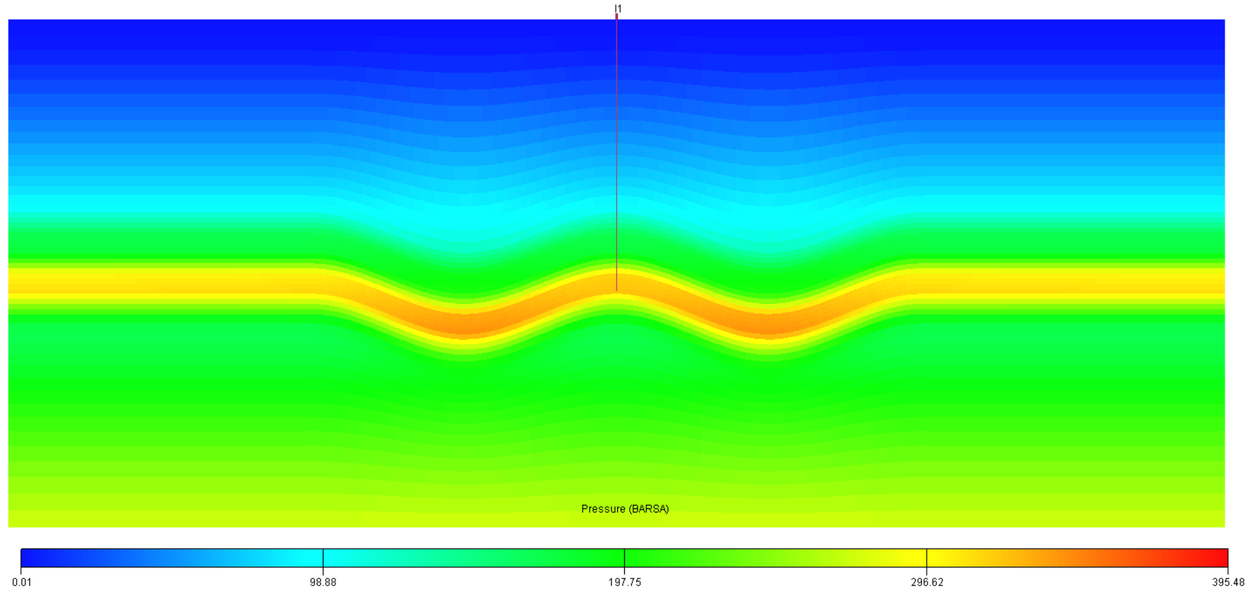

Figure 27 - Pore pressure distribution in bar in the model after 10 years of injection

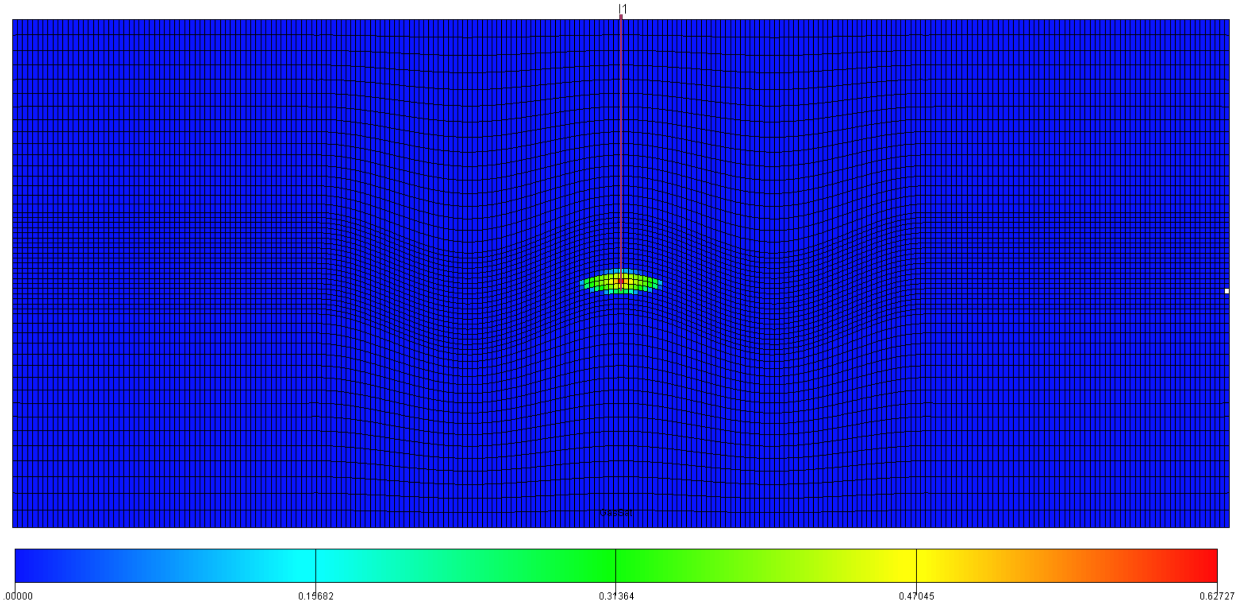

Figure 28 - Saturation of CO2 in the model after 10 years of injection

The two models, show similar behaviors in terms of the shear fracture potential as depicted in Figure 29 and Figure 0 and both are safe in shear fracture potential.

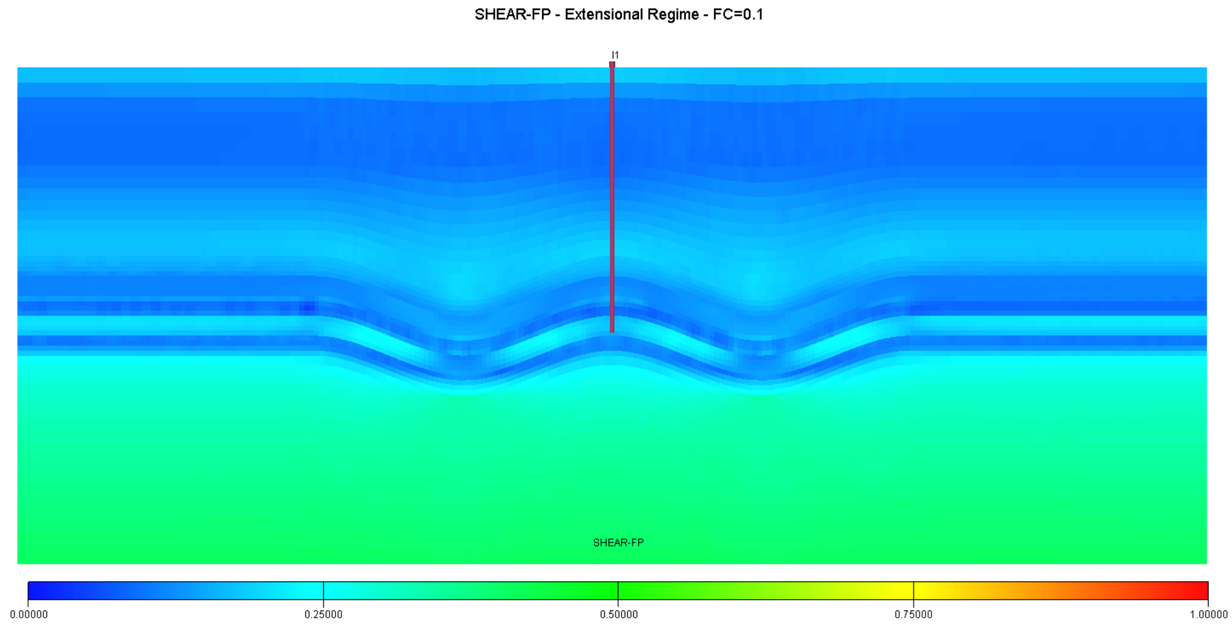

Figure 29 - Shear Fracture Potential after 10 years of injection- Coefficient of friction = 0.1 – Extensional Model

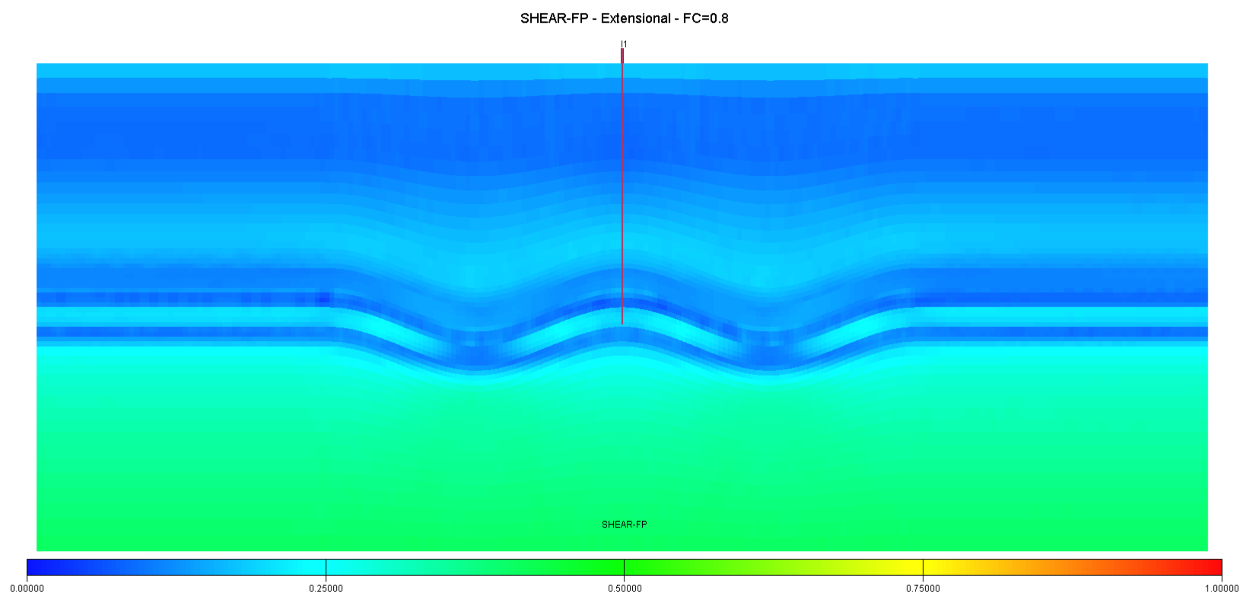

Figure 30 - Shear Fracture Potential after 10 years of injection- Coefficient of friction = 0.8 – Extensional Model

After 15 years of injection, minimum principal stress will get to negative values and tensile fracture potential is assessed from this time on. The shear fracture potential is still less than one in the two models, Figure 1 and Figure 2.

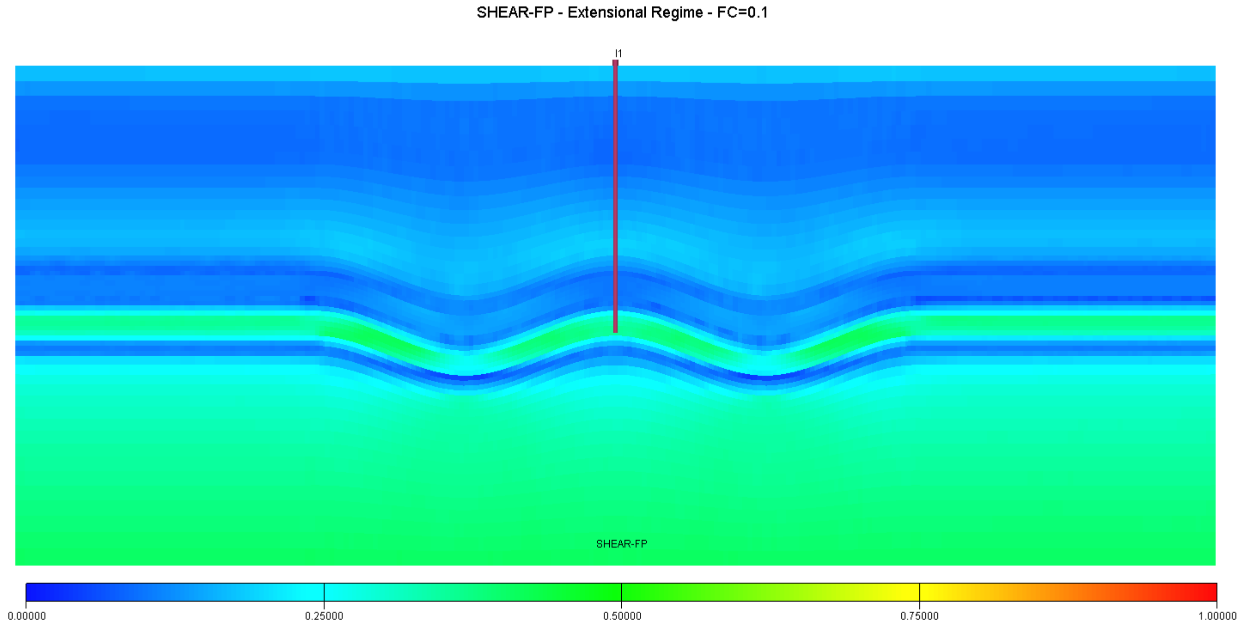

Figure 31 - Shear Fracture Potential after 15 years of injection- Coefficient of friction = 0.1 – Extensional Model

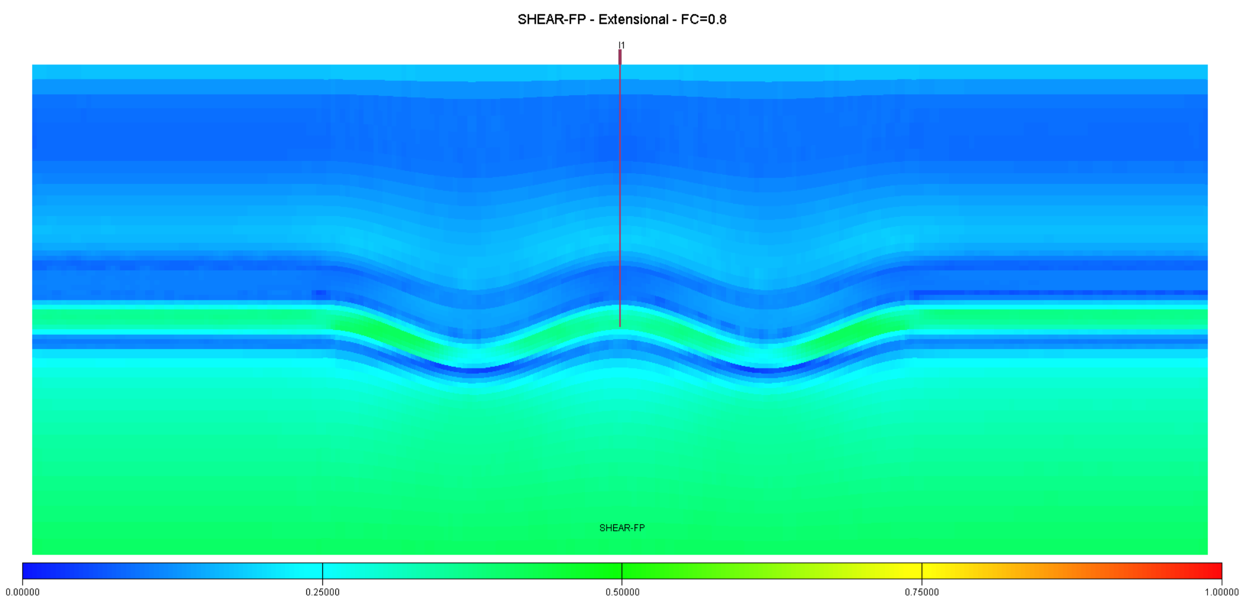

Figure 32 - Shear Fracture Potential after 15 years of injection- Coefficient of friction = 0.8 – Extensional Model

The two models behave exactly the same way in terms of tensile fracture potential, as shown in Figure 3 and Figure 4, however the system is still at safe state of stress in both models.

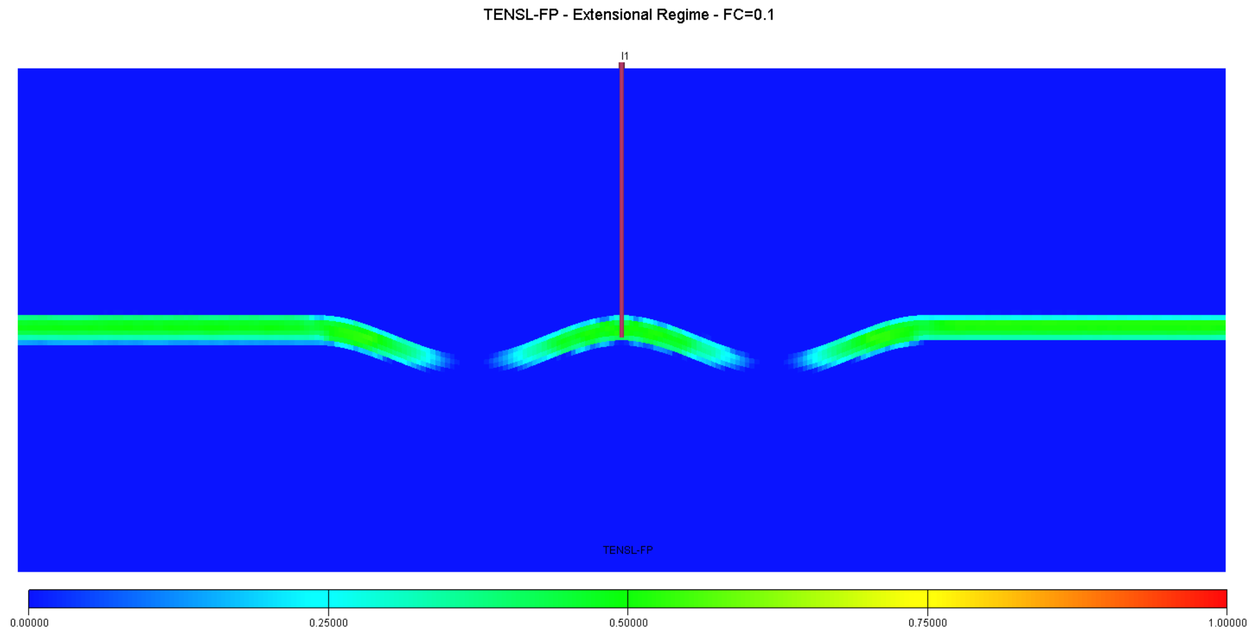

Figure 33 - Tensile Fracture Potential after 15 years of injection- Coefficient of friction = 0.1 – Extensional Model

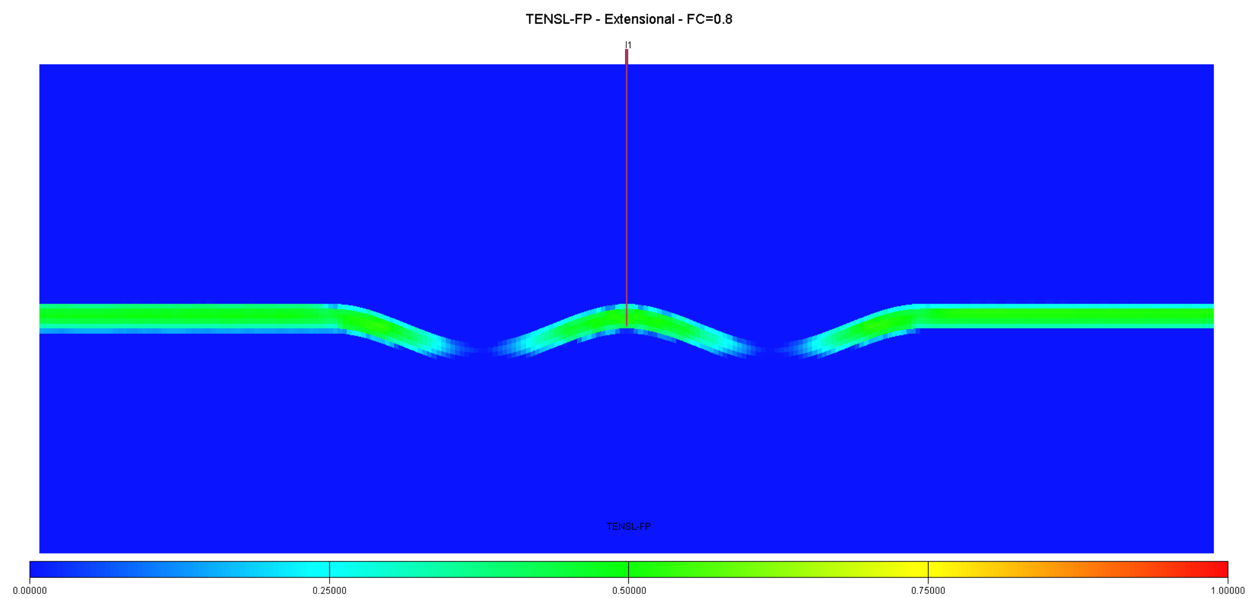

Figure 34 - Tensile Fracture Potential after 15 years of injection- Coefficient of friction = 0.8 – Extensional Model

After 20 years of injection the two models are still at safe state of stress for shear fracture as shown in Figure 5 and Figure 6. As illustrated in Figure 7 and Figure 8, tensile failure is not likely after 20 years of injection and the two models are at a safe state of stress both in terms of shear and tensile failure. The observation that the two models behave similar in terms of shear fracture and tensile fracture denotes that the coefficient of friction does not play an important role under the extensional regime.

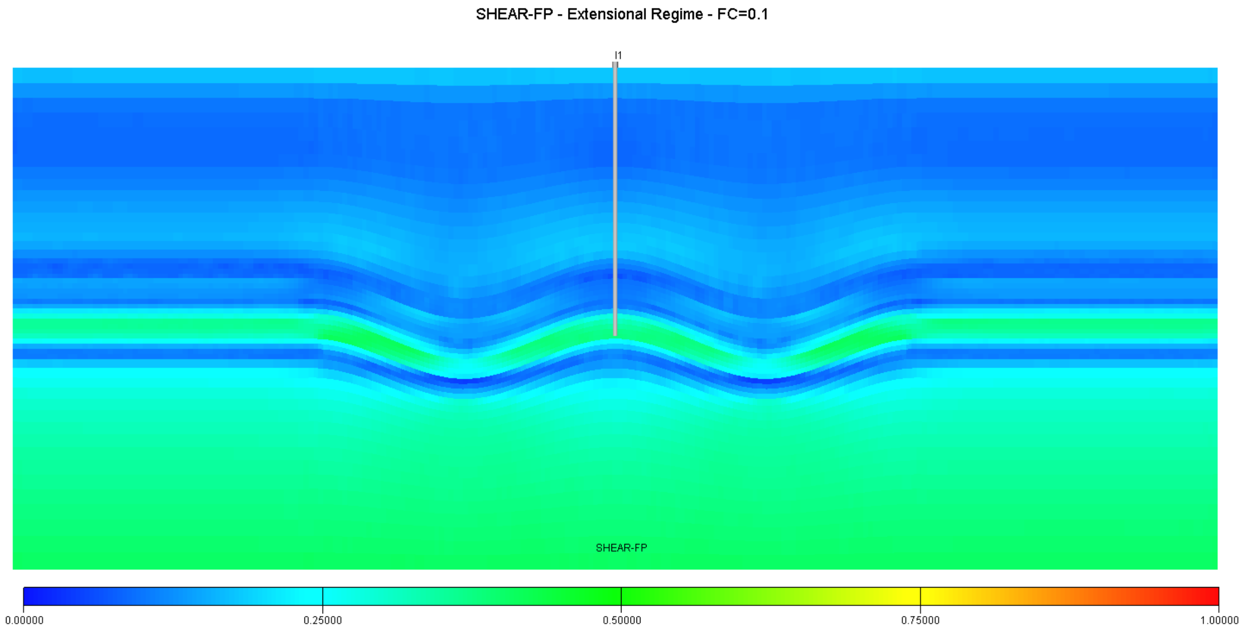

Figure 35 - Shear Fracture Potential after 20 years of injection- Coefficient of friction = 0.1 – Extensional Model

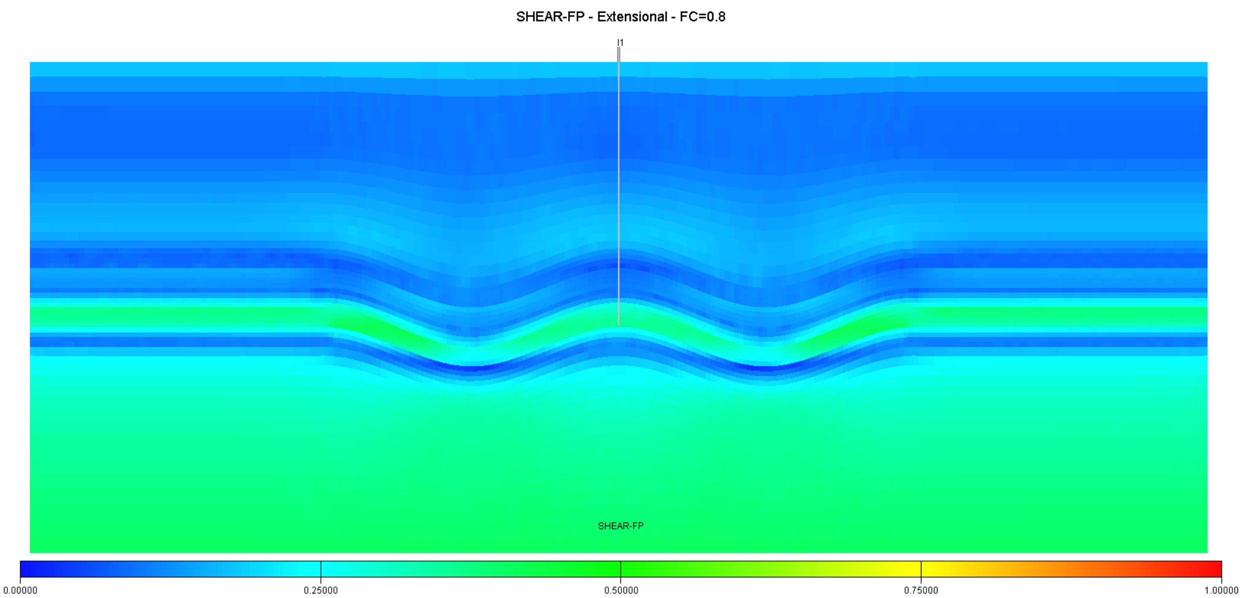

Figure 36 - Shear Fracture Potential after 20 years of injection- Coefficient of friction = 0.8 – Extensional Model

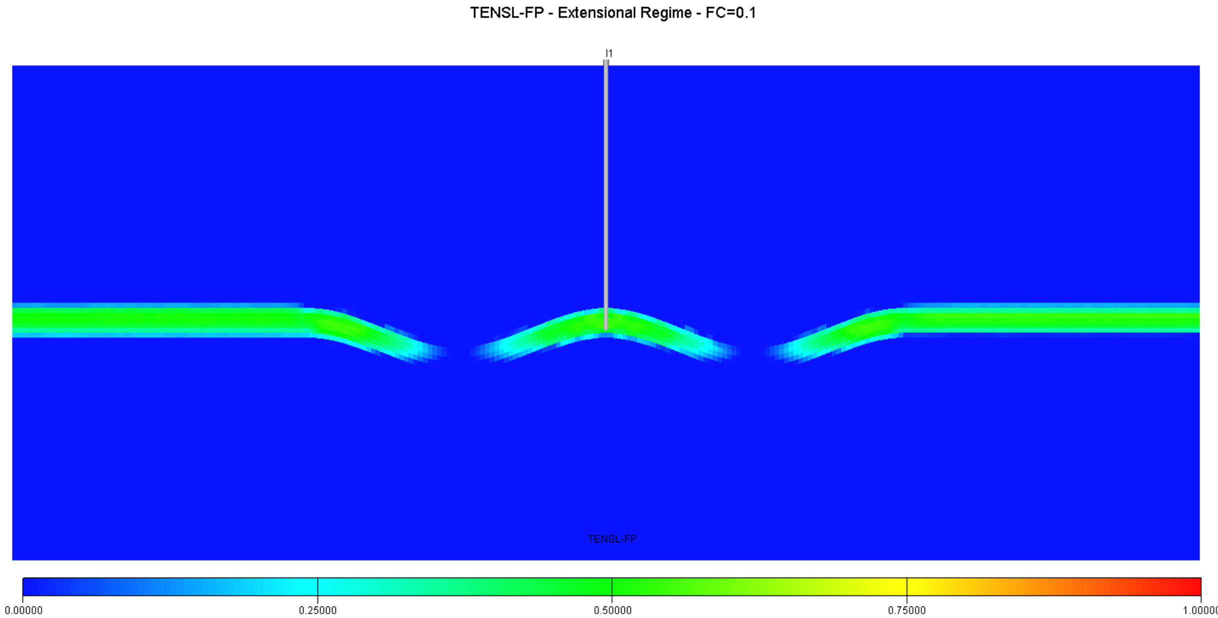

Figure 37 - Tensile Fracture Potential after 20 years of injection- Coefficient of friction = 0.1 – Extensional Model

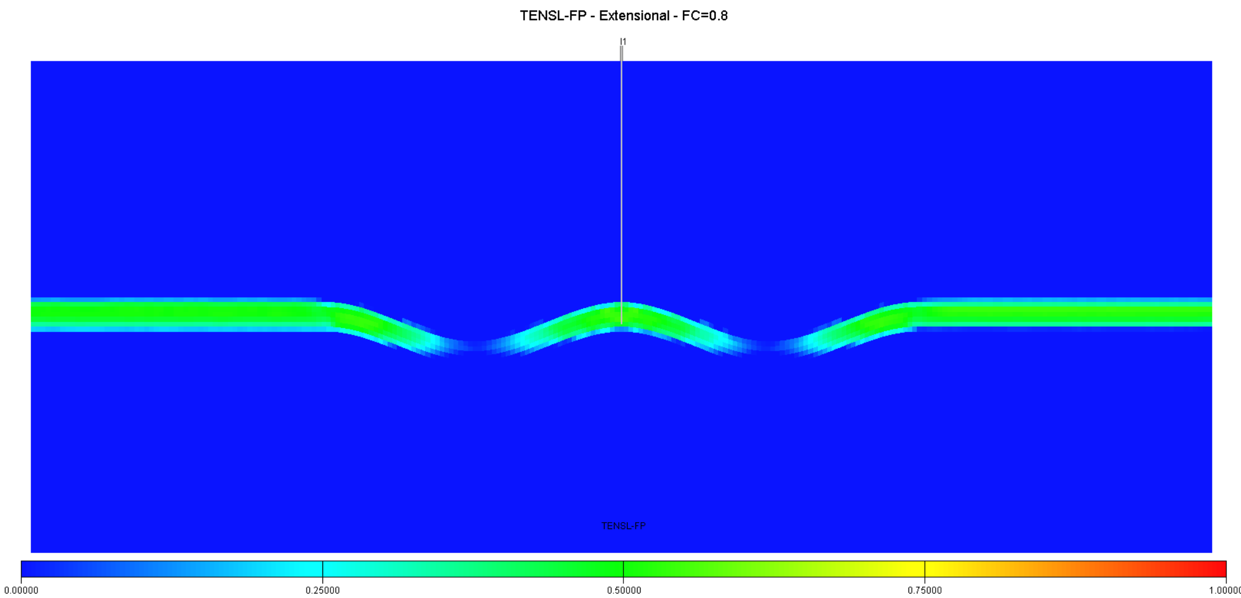

Figure 38 - Tensile Fracture Potential after 20 years of injection- Coefficient of friction = 0.8– Extensional Model

Figure 39 presents the pore pressure distribution in the model after 20 years of injection and Figure 40 shows the saturation of CO_2 after this period of time.

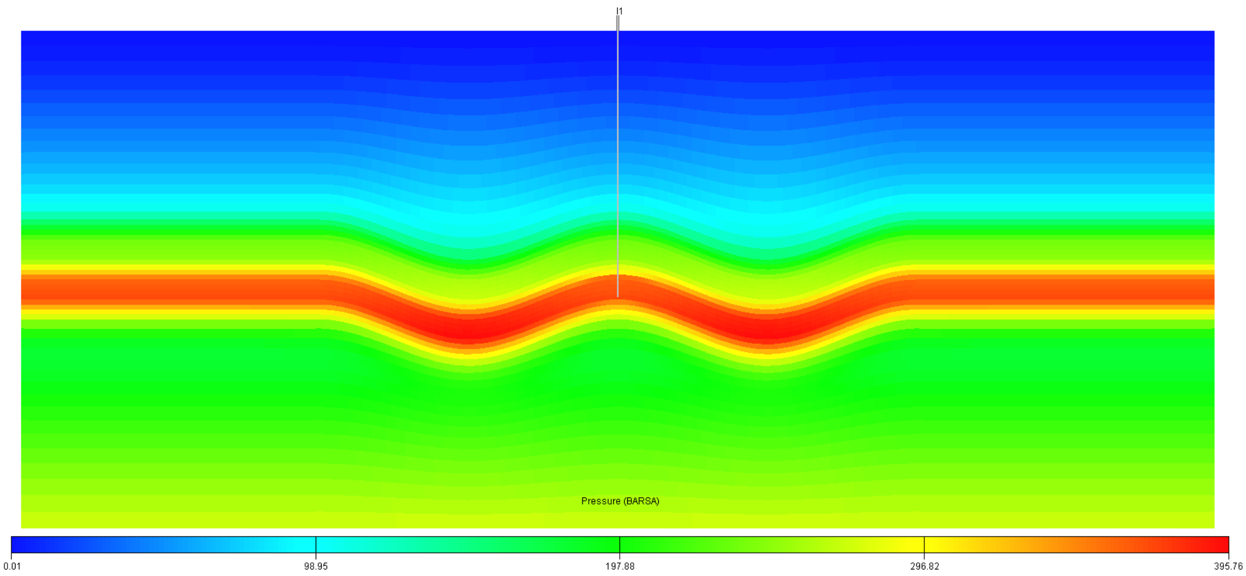

Figure 39 - Pore pressure distribution after 20 years of injection - Extensional Model

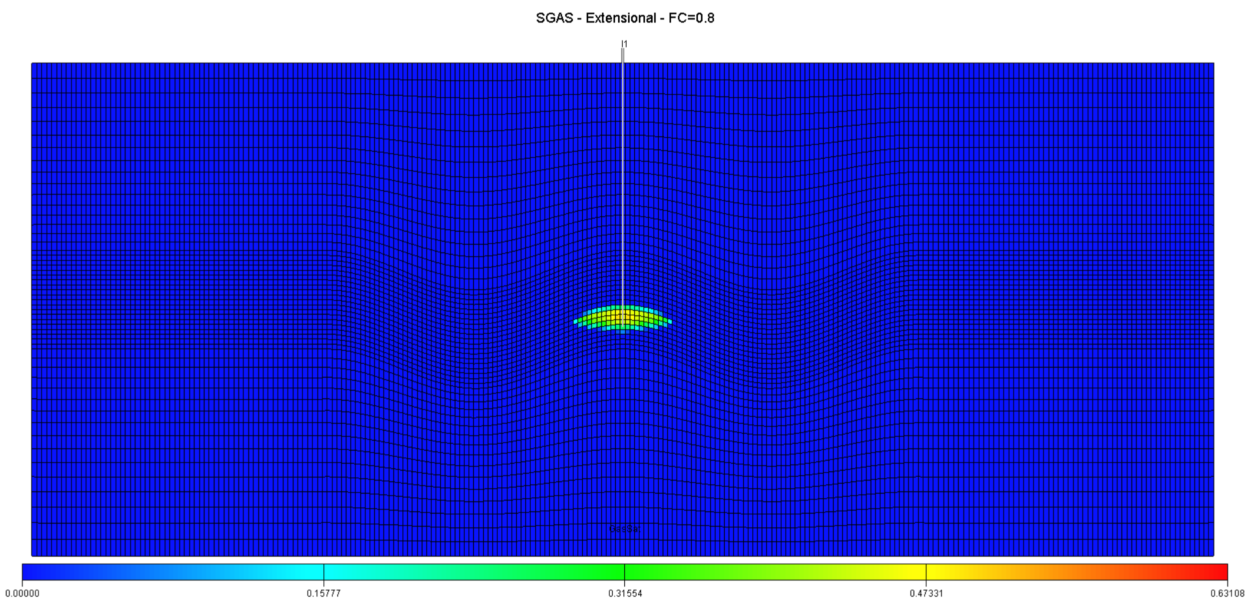

Figure 40 - CO_2 spreading in the reservoir after 20 years of injection - Extensional Model

The evolution of sFP on the two models at the wellbore vicinity, in the caprock and in the far field over the course of 20 years of injection are illustrated in Figure 1, Figure 2 and Figure 3. As illustrated in these figures, the two models undergo a decrease in the sFP for the first ten years of injection and the sFP builds up from ten years up.

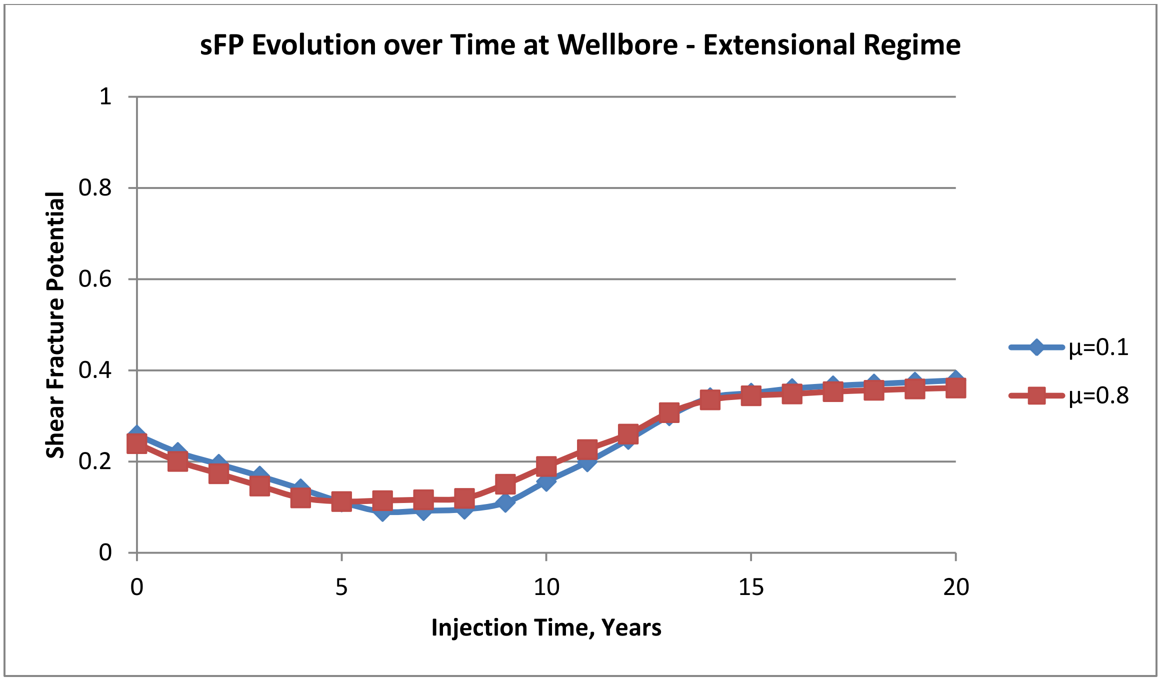

Figure 41 - sFP Evolution over Time at Wellbore - Extensional Regime

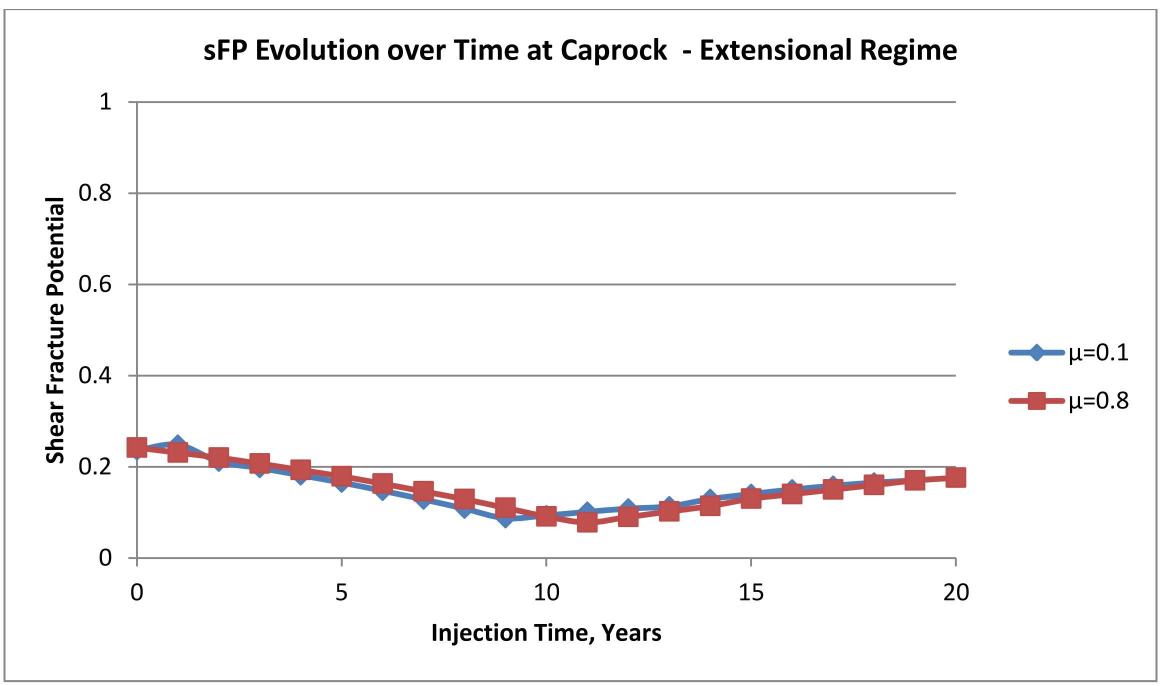

Figure 42 - sFP Evolution over Time at Far Field - Extensional Regime

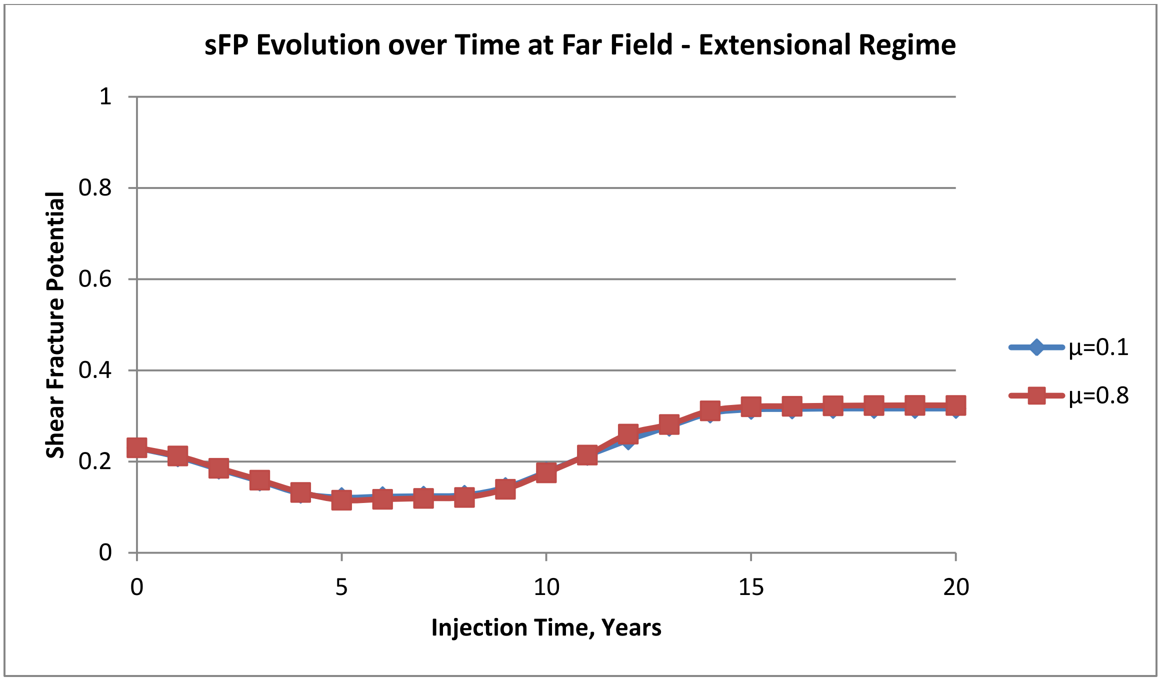

Figure 43 - sFP Evolution over Time at Far Field - Extensional Regime

1.2.4.2.3. Strike Slip Stress Regime

In the strike-slip regime used for this analysis, the minimum principle stress is the minimum horizontal stress which is given by $\sigma_h = 0.8\sigma_v$, the intermediate principle stress is the vertical stress and the maximum principle stress is given by $\sigma_{H,} = 1.2\sigma_v$.

Figure 4 and Figure 5 show the initial shear fracture potential for the anticline with the coefficient of friction of 0.1 and 0.8 between the layers under the strike slip regime respectively.

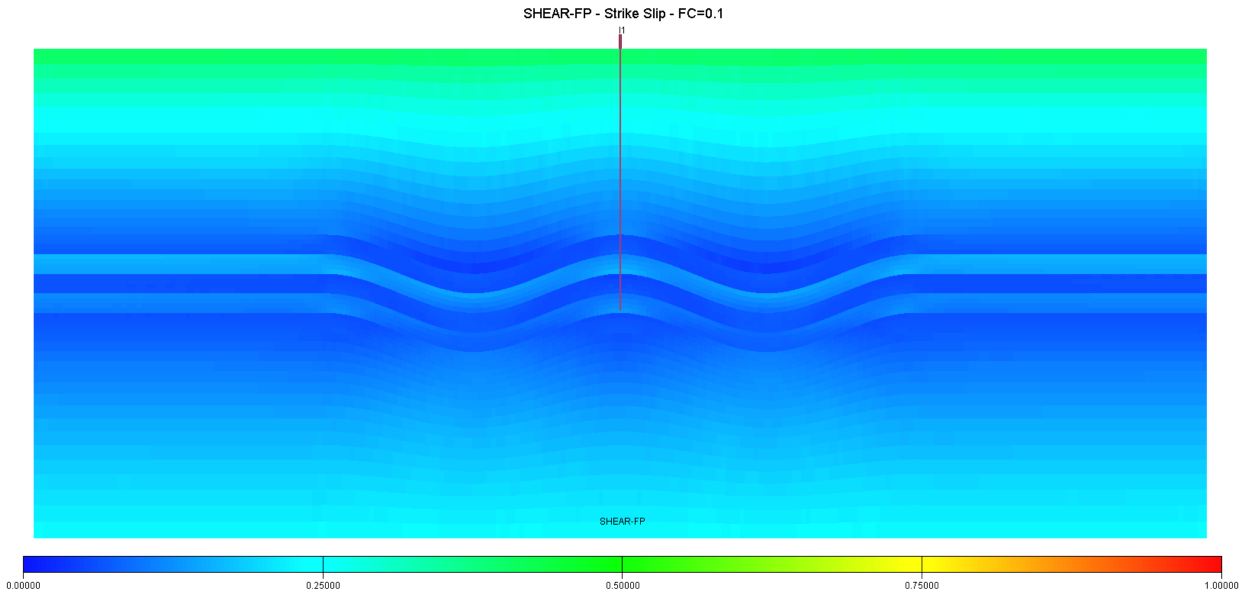

Figure 44 - Initial Shear Fracture Potential - Coefficient of friction = 0.1 – Strike Slip Model

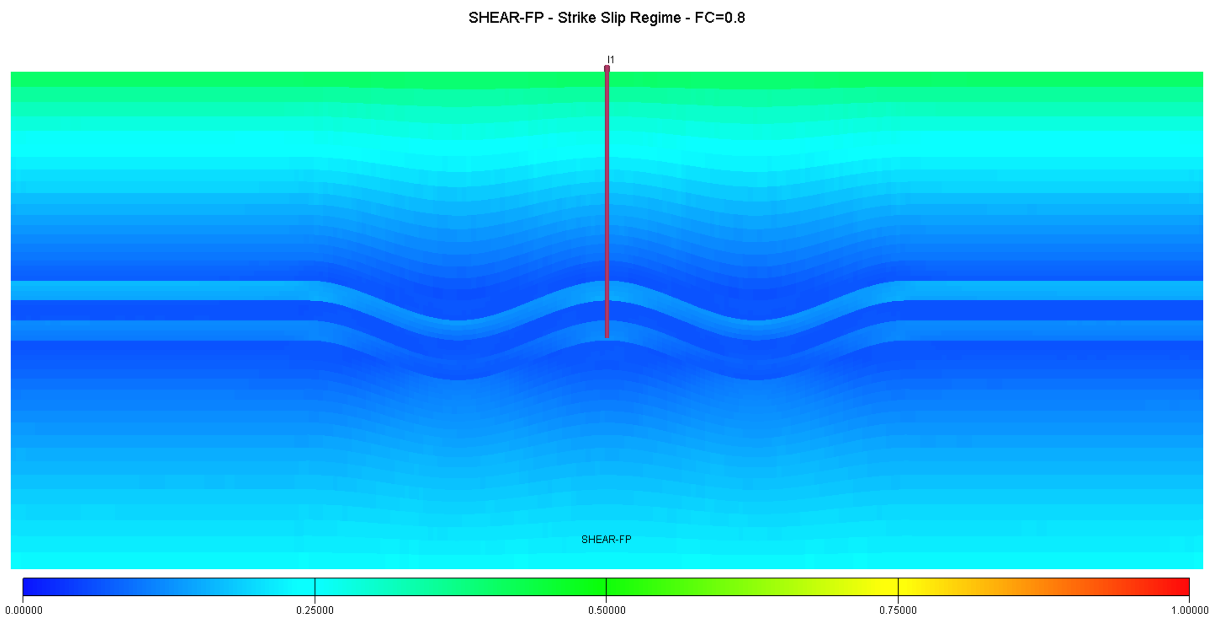

Figure 45 - Initial Shear Fracture Potential - Coefficient of friction = 0.8 – Strike Slip Model

As shown in these two figures, the initial shear fracture potential in the two models is similar in the model and the shale-sand layers. The two models show the same pore pressure distribution after five years of CO_2 injection at the rate of 20kTons/year, which is depicted in Figure 6.

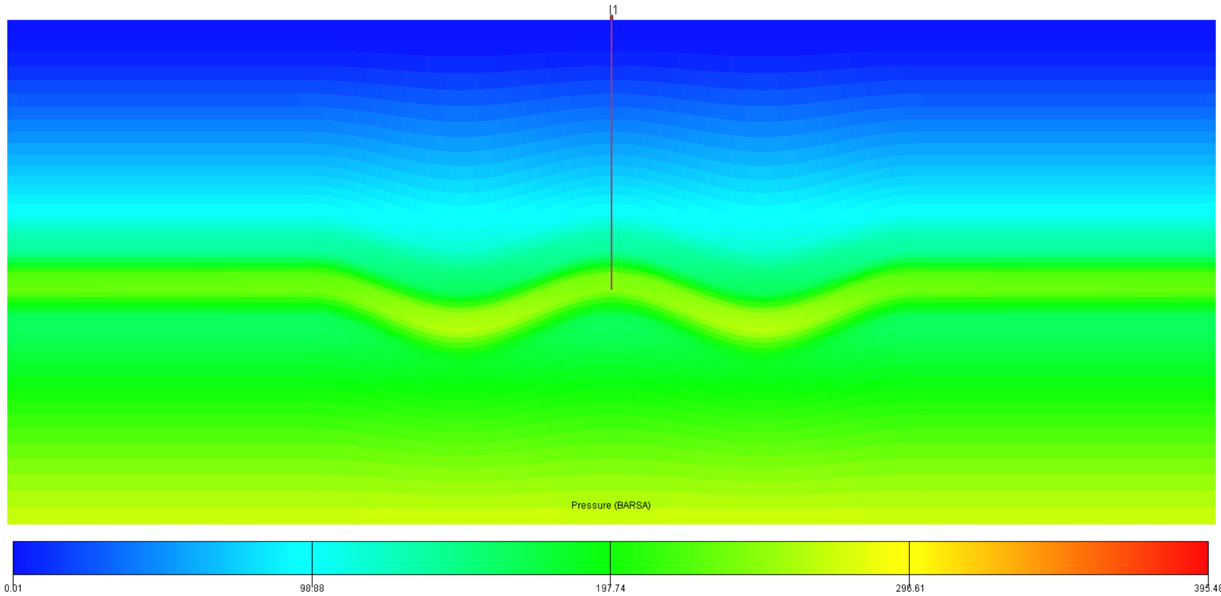

Figure 46- Pore pressure distribution in bar in the model after 5 years of injection

The increase in pore pressure will result in new states of stress and new sFP in the model models as shown in Figure 7 and Figure 8. The two models undergo slight increase in the shear fracture potential, with sFP at the well bore vicinity increasing from an initial value of 0.13 to 0.33 after five years of injection for the μ=0.1 model and the μ=0.8 model goes from an initial sFP value of 0.12 to 0.31 after the same period of injection.

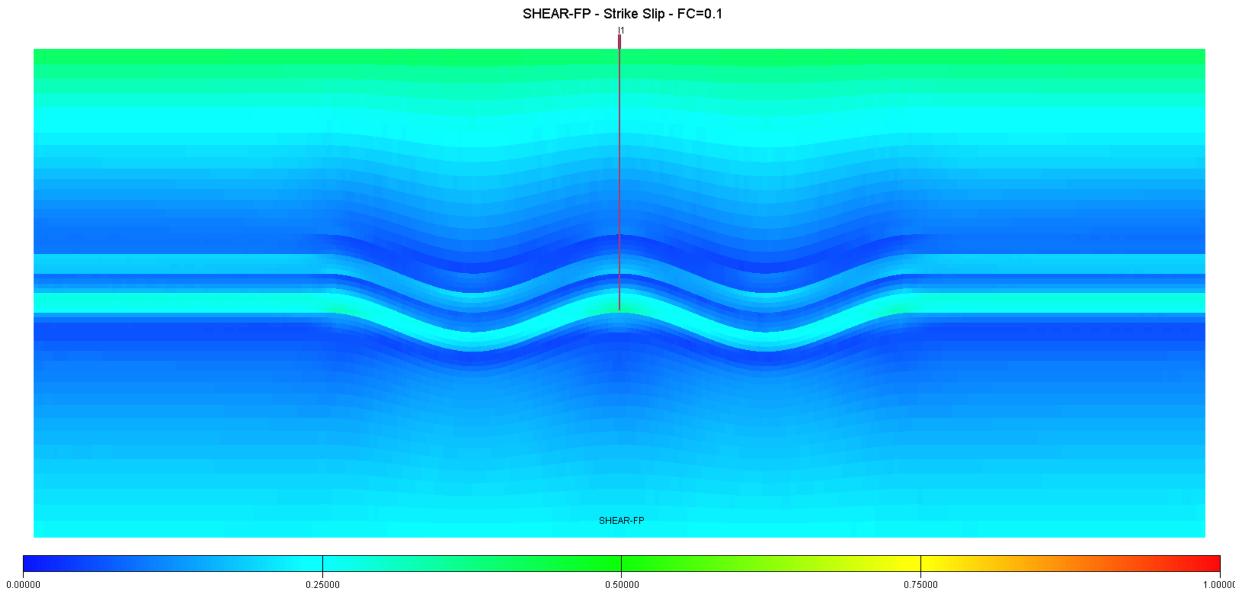

Figure 47 - Shear Fracture Potential after 5 years of injection- Coefficient of friction = 0.1 – Strike Slip Model

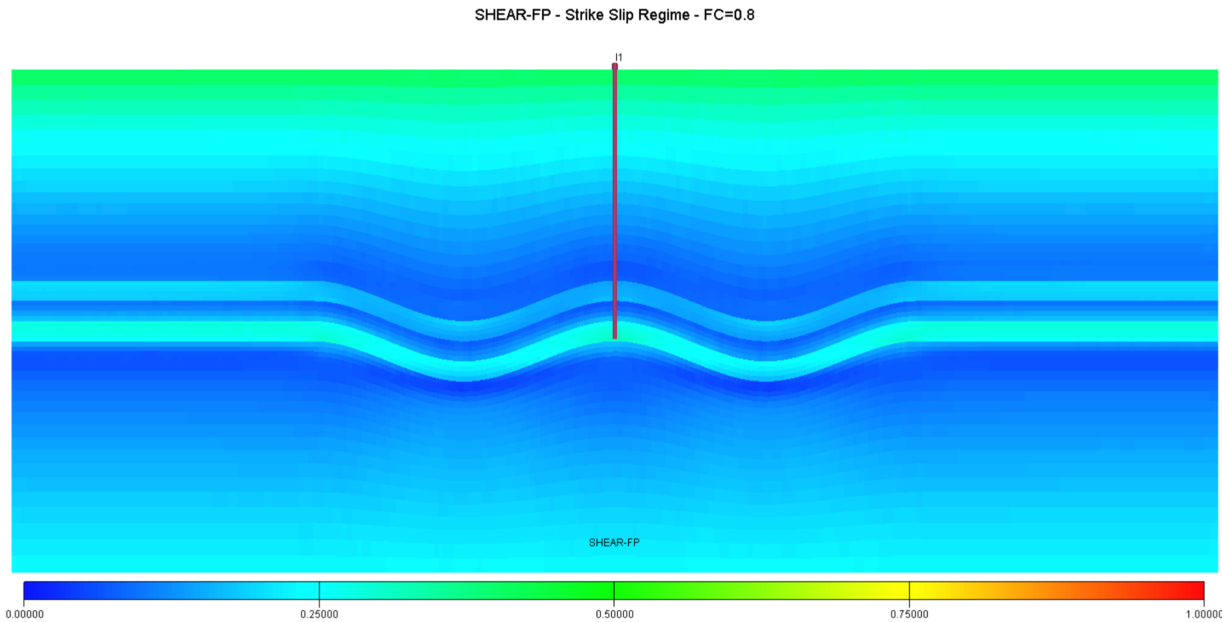

Figure 48- Shear Fracture Potential after 5 years of injection - Coefficient of friction = 0.8 – Strike Slip Model

The two models show the same overall pore pressure increase after 10 years of injection, as shown in Figure 49. The final CO_2 saturation distribution under closed boundary conditions after 10 years of injection is shown in Figure 0. The overall occupancy of the two models is 1.4%. Unlike the compressional regime, no hydraulic fractures are initiated at this point in the models and the two models are safe from shear fracture and tensile fracture formations.

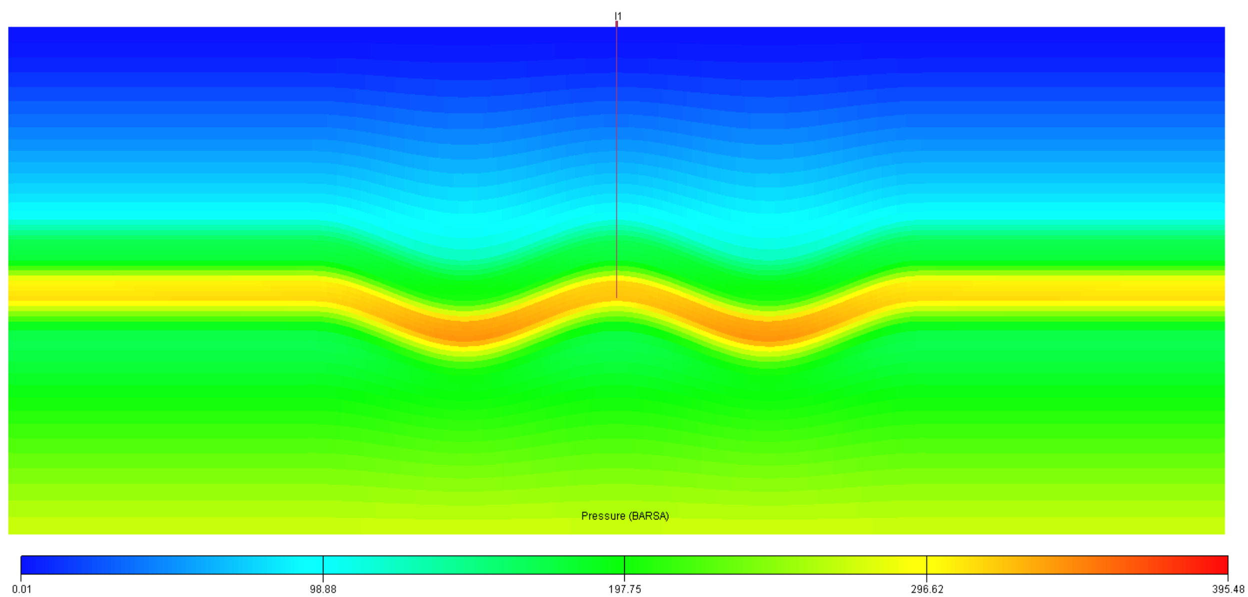

Figure 49 - Pore pressure distribution in bar in the model after 10 years of injection

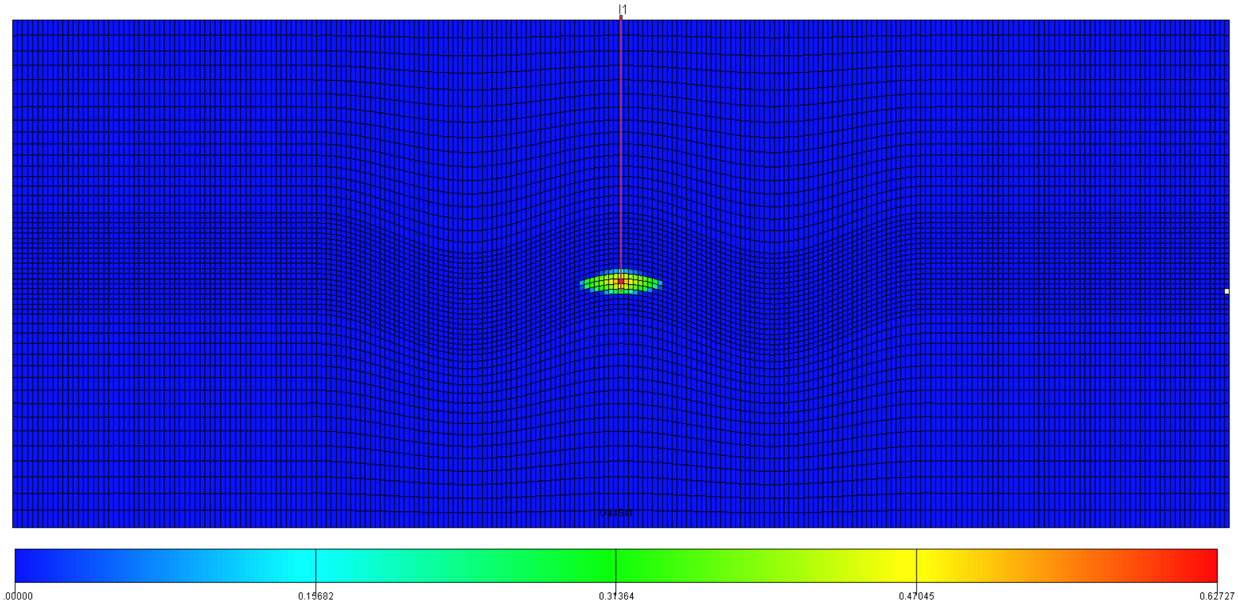

Figure 50 - Saturation of CO2 in the model after 10 years of injection

The two models, show similar behaviors in terms of the shear fracture potential as depicted in Figure 1 and Figure 2 and both are safe in shear fracture potential.

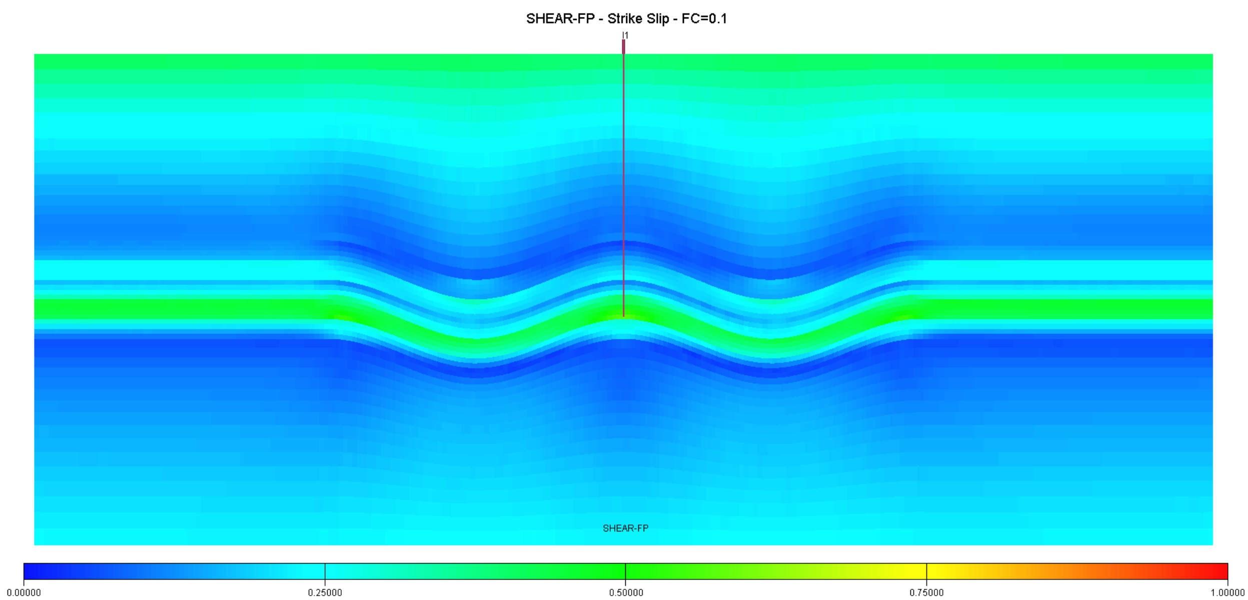

Figure 51 - Shear Fracture Potential after 10 years of injection- Coefficient of friction = 0.1 – Strike Slip Model

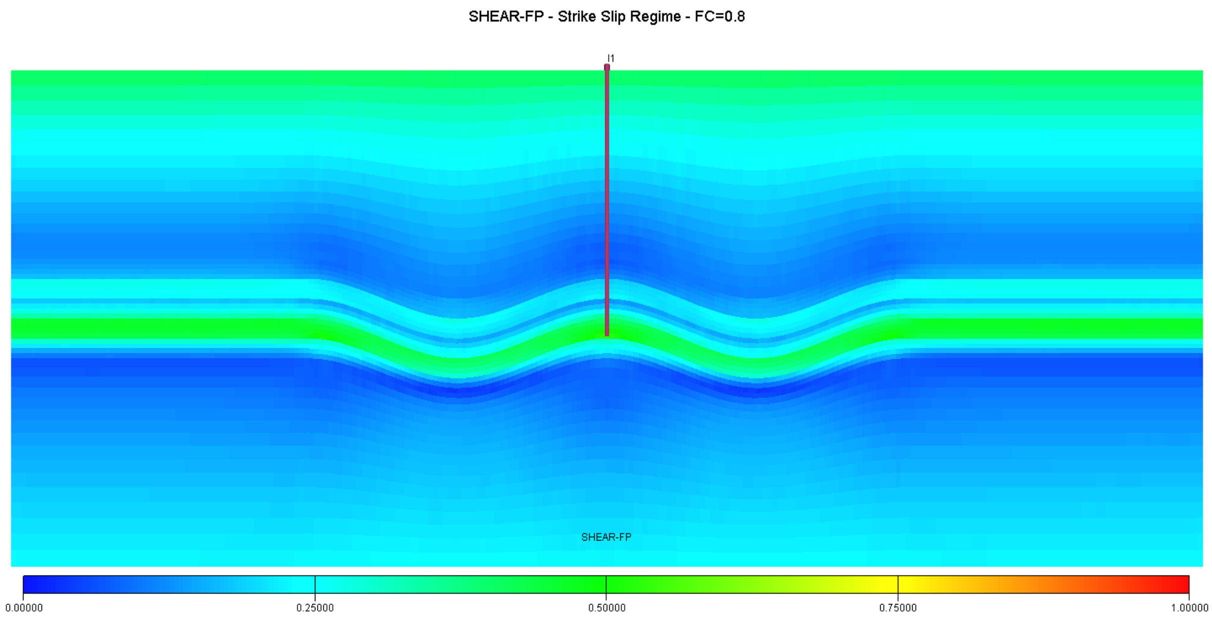

Figure 52 - Shear Fracture Potential after 10 years of injection- Coefficient of friction = 0.8 – Strike Slip Model

As depicted in Figure 3 and Figure 4 the two models do not encounter tensile failure after 10 years of injection, however, tensile failure potential is starting to build up in the two models.

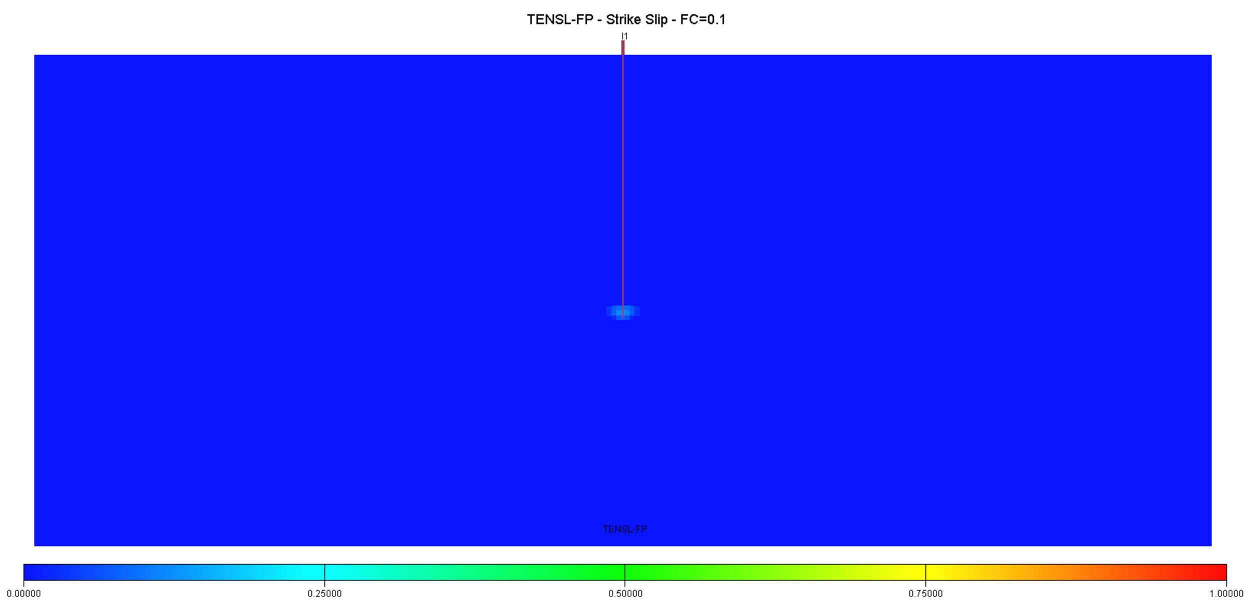

Figure 53 - Tensile Fracture Potential after 10 years of injection- Coefficient of friction = 0.1 – Strike Slip Model

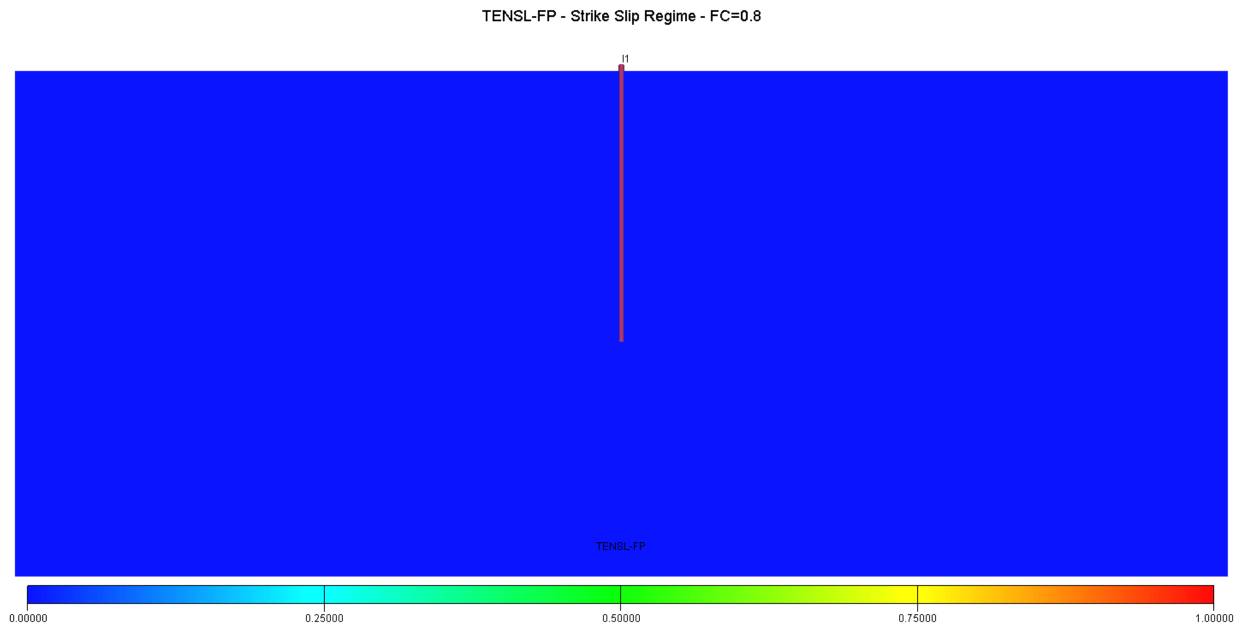

Figure 54 - Tensile Fracture Potential after 10 years of injection- Coefficient of friction = 0.8 – Strike Slip Model

After 20 years of injection, Figure 5 and Figure 6, the two models are still at stable state from the shear failure point of view but they experience tensile fractures in the reservoir layer around the wellbore as illustrated in Figure 7 and Figure 8.

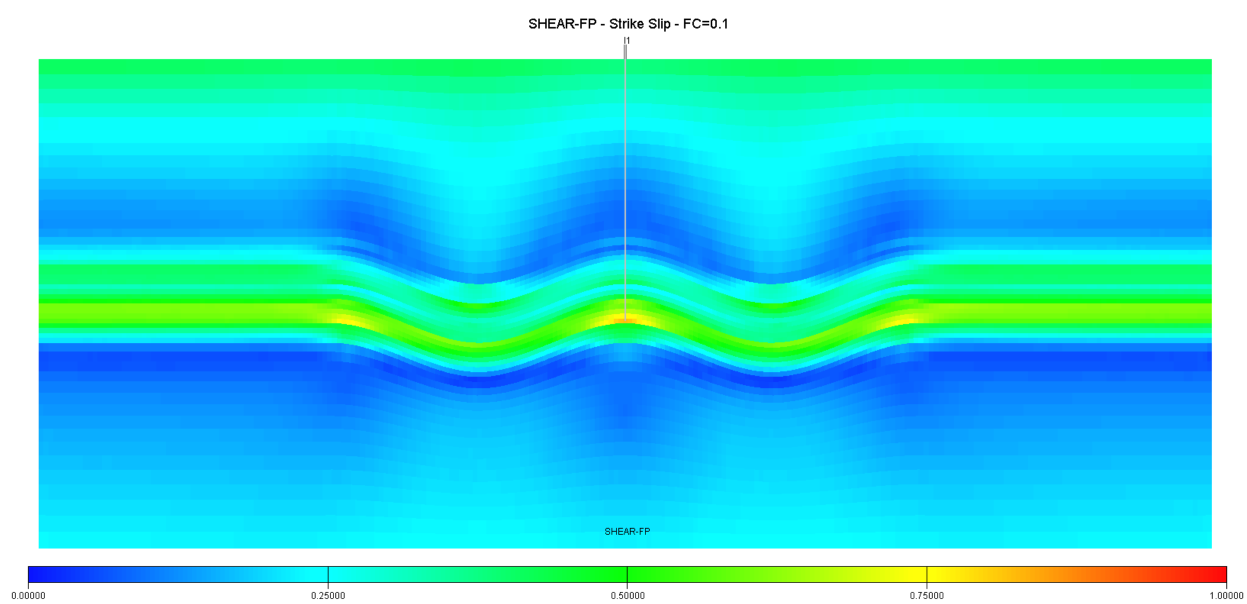

Figure 55 - Shear Fracture Potential after 20 years of injection- Coefficient of friction = 0.1 – Strike Slip Model

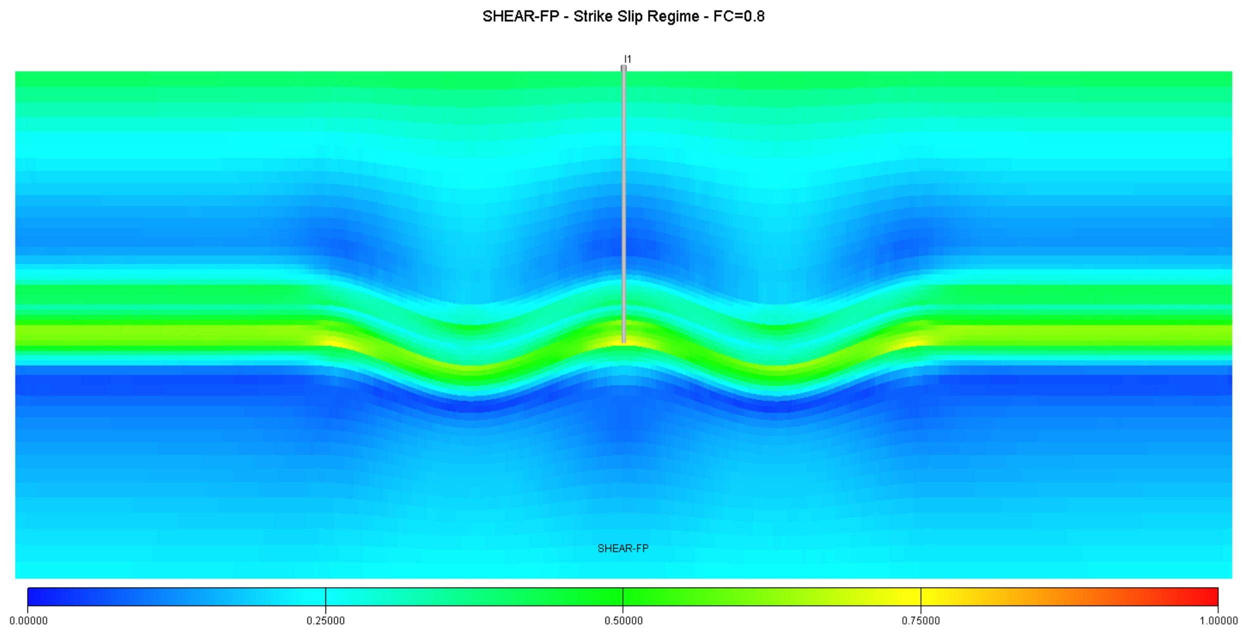

Figure 56 - Shear Fracture Potential after 20 years of injection- Coefficient of friction = 0.8 – Strike Slip Model

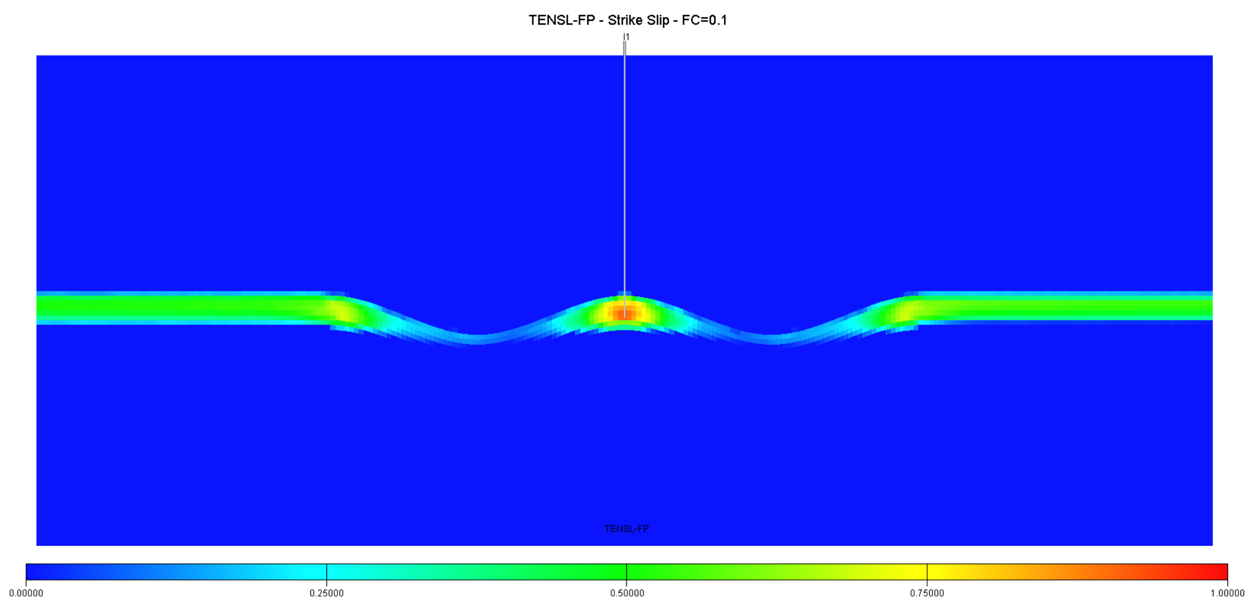

Figure 57 - Tensile Fracture Potential after 20 years of injection- Coefficient of friction = 0.1 – Strike Slip Model

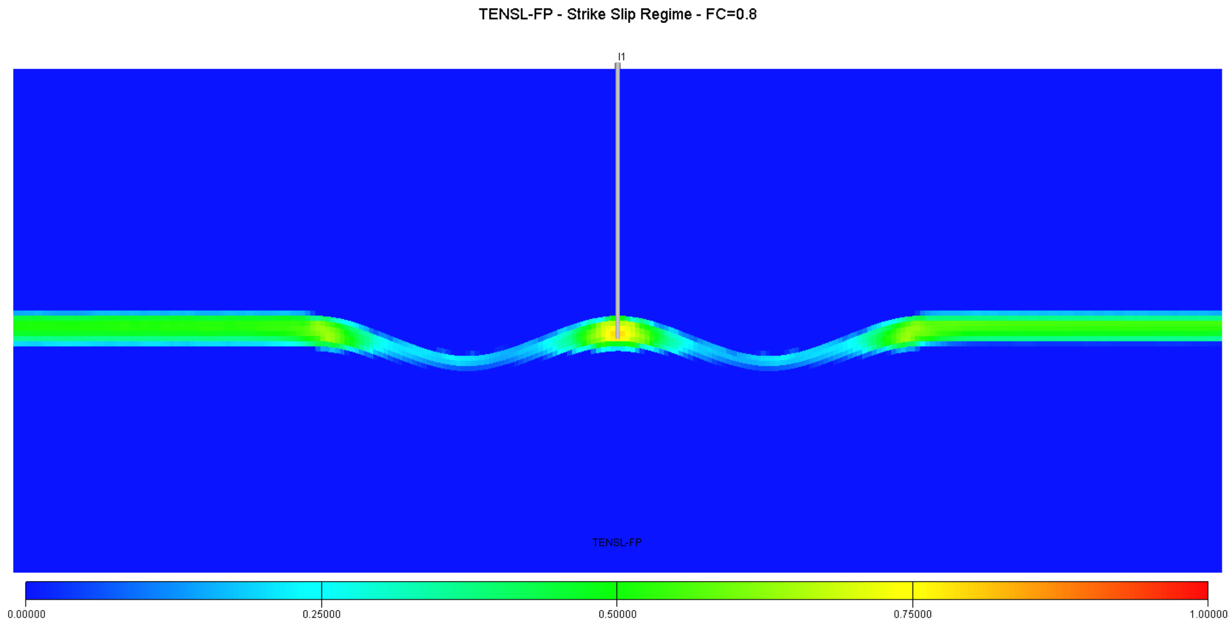

Figure 58 - Tensile Fracture Potential after 20 years of injection- Coefficient of friction = 0.8– Strike Slip Model

Figure 59 presents the pore pressure distribution in the model after 20 years of injection and Figure 0 shows the saturation of CO_2 after this period of time.

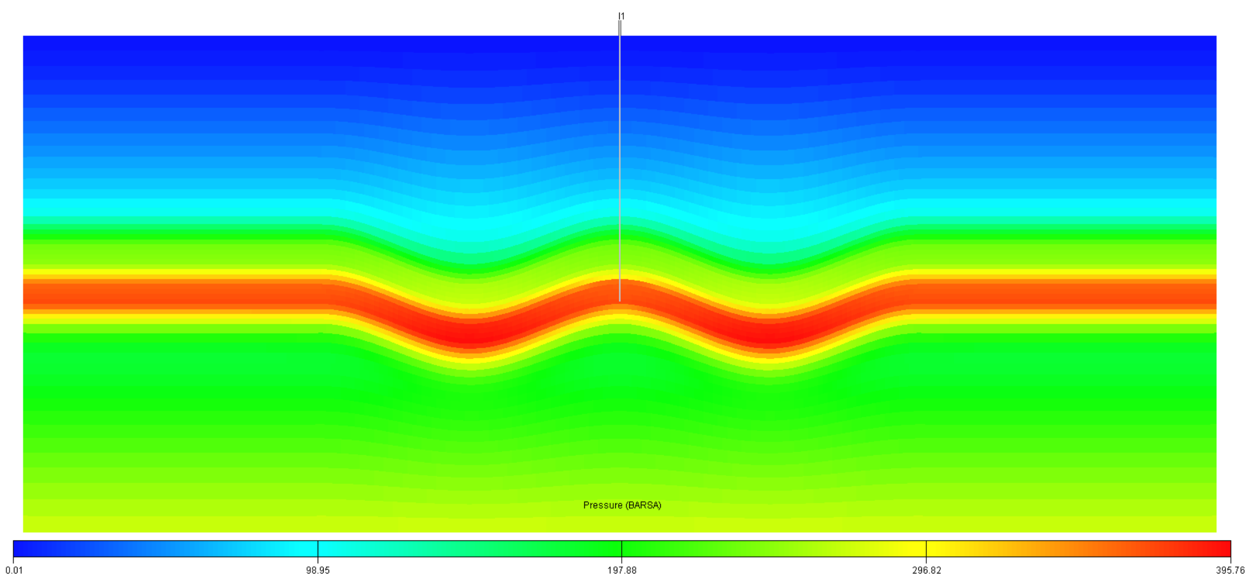

Figure 59 - Pore pressure distribution after 20 years of injection - Extensional Model

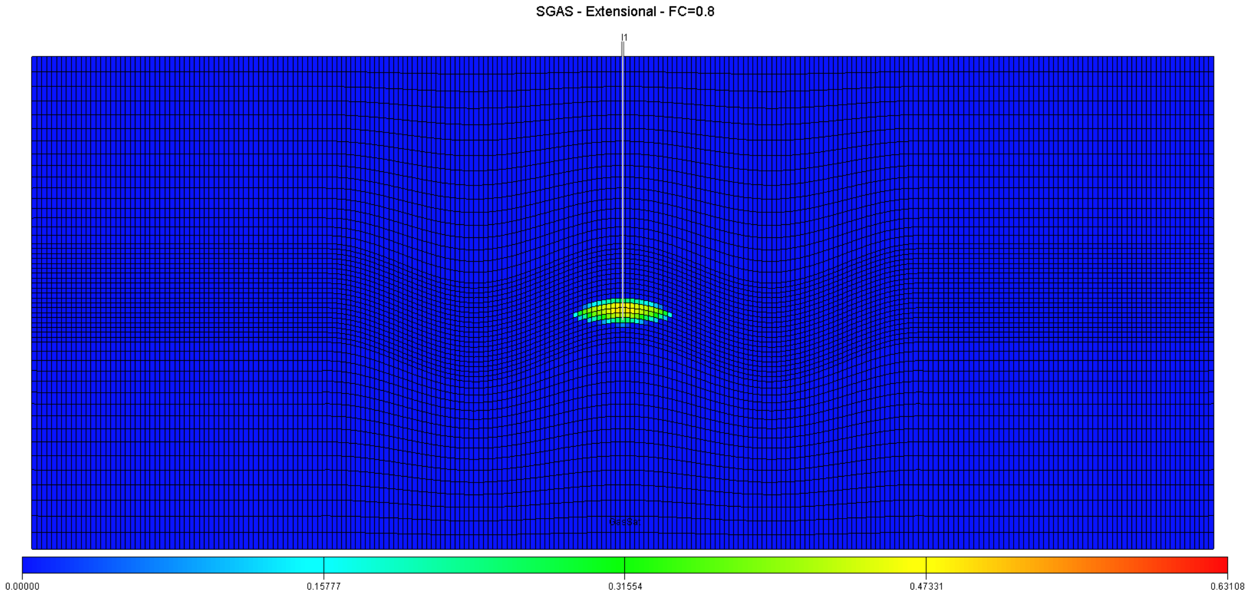

Figure 60 - CO2 spreading in the reservoir after 20 years of injection - Extensional Model

The evolution of sFP on the two models at wellbore vicinity, caprock and the far field over the course of 20 years of injection are illustrated in Figure 3. The sFP trend show a sensitivity to the coefficient of friction, with the 0.1 model observing higher sFP values near the injection location. For the cap rock and the far-field the sFP values are almost identical for both coefficients of friction.

Tensile FP is steadily increased over the injection period and even reaches values of 1 near the injection location in the 0.1 model, however tFP does not reach the caprock which remains stable wih low tFP values (0-0.1).

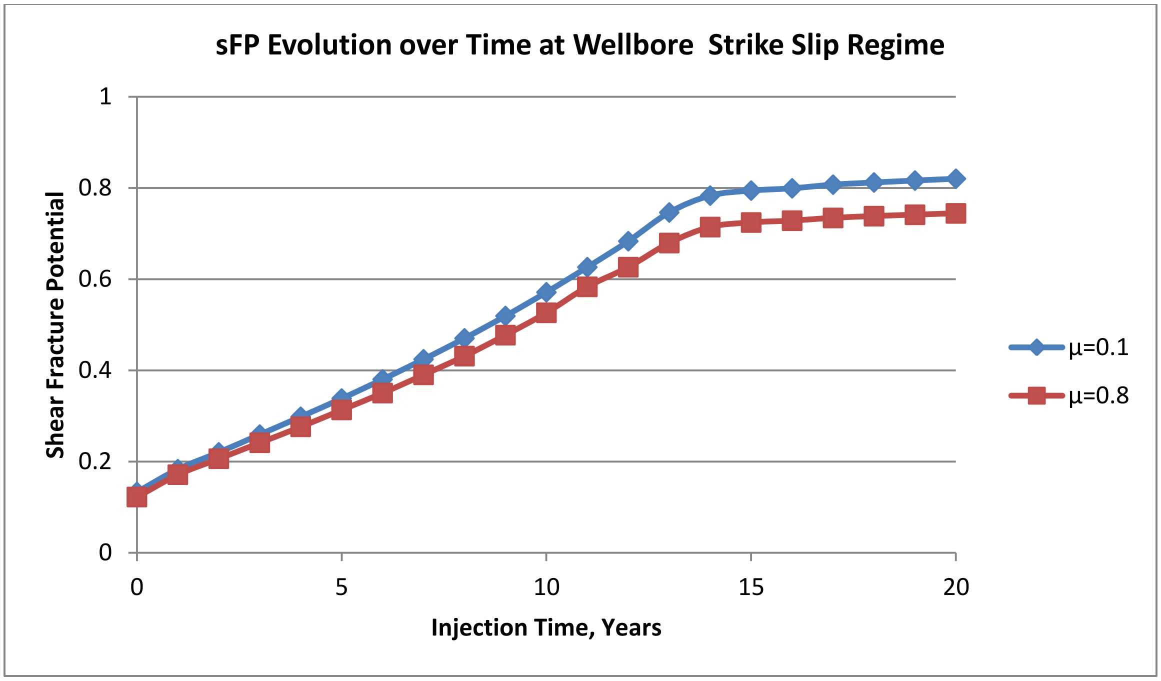

Figure 61 - sFP Evolution over Time at Wellbore - Strike Slip Regime

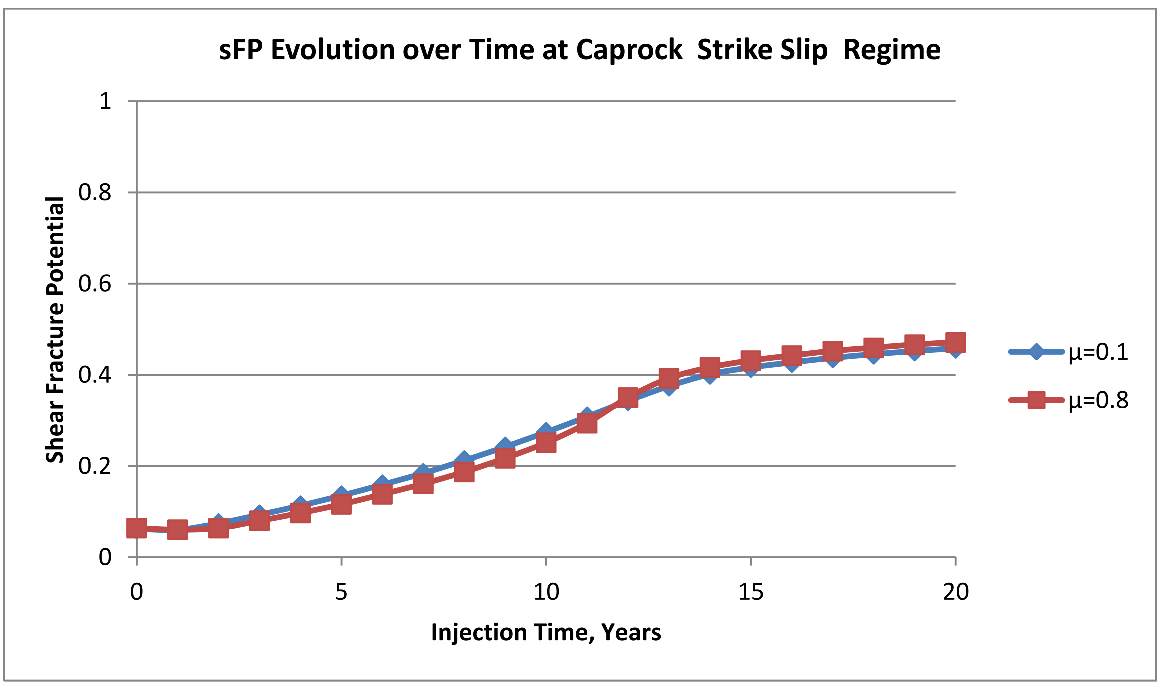

Figure 62 - sFP Evolution over Time at Caprock- Strike Slip Regime

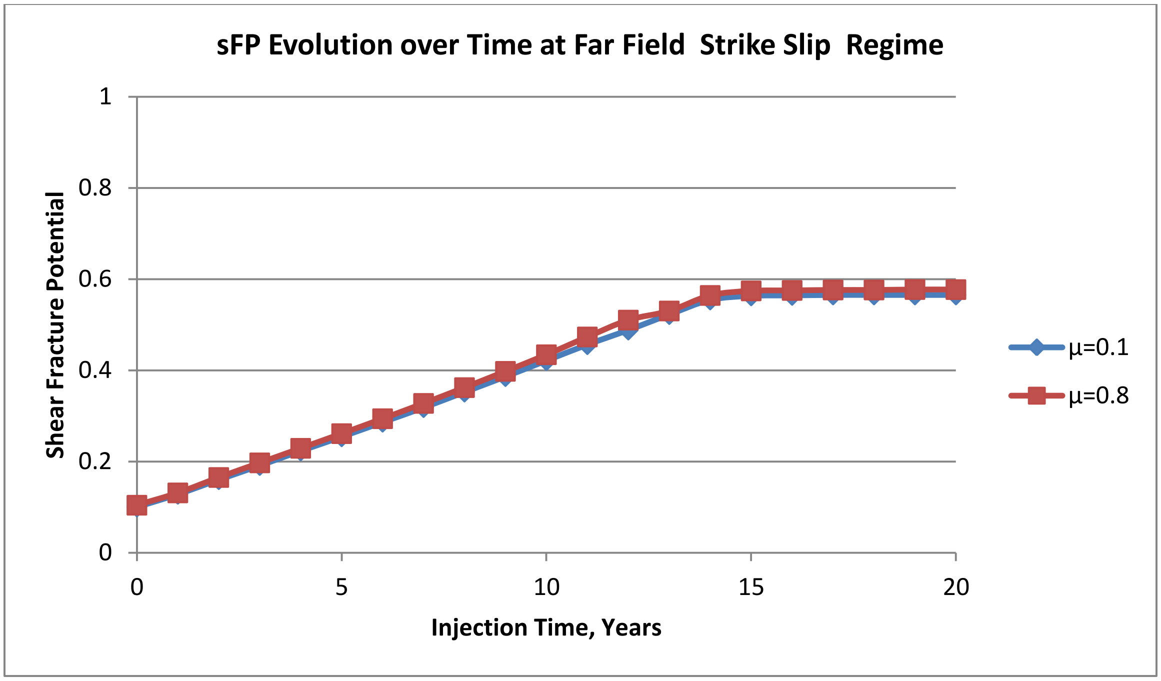

Figure 63- sFP Evolution over Time at Far Field - Strike Slip Regime

1.2.5. Discussion

Estimating and simulating the maximum sustainable pore pressure change, ΔP_c, before optimally oriented fractures are reactivated represents a key component of geomechanical risk analyses for CO_2 injection applications (e.g. Streit and Hillis, 2004; Rutqvist et al., 2007; Cappa and Rutvist, 2011; Paradeis et al., 2012). These analyses become especially relevant when structural trap systems such as anticlines are considered for CO_2 sequestration. Anticline structures have a heterogeneous state of stress whereby the horizontal stresses change rapidly at the top of the crest to the bottom of the crest (Paradeis et al., 2012).

As shown by equations 3-5 simplified analytical solutions based on the principle of pore pressure – stress coupling (Altmann et al., 2010) can be used to calculate the maximum sustainable pore pressure, P_c, prior to CO_2 injection. The results presented show that P_c is strongly dependent on the stress regime and the relative location with respect to the injection location. Based on these calculations different stress regimes result in significant differences between horizontally layered sedimentary basins and anticlines. In this respect the case of horizontally layered basins in an extensional stress regime merits special consideration. If such basins are tectonically relieved the minimum horizontal stress is often determined by the uni-axial strain model (Equation 2; Engelder, 1993). Assuming a typical Poisson's ratio of ν=0.25 and a typical coefficient of friction of μ=0.58 (Zoback, 2007) the state of stress is in exact frictional equilibrium (Figure 64a). Visualizing the effects of pore pressure stress coupling due to CO_2 injection in a Mohr Circle (i.e. following equations 3, 4, and 5; Figure 64b) shows that along the σ_V and σ_H direction ΔP_c is zero and the risk of fluid injection related fault reactivation is eminent. Only an increase of σ_h by a tectonic contribution (Figure 64c) or due to a Poisson's ratio larger than 0.25 (Figure 64d) results in a lower risk of fault reactivation and in conditions suitable for CO_2 sequestration. The state of stress within an anticline structure represents such a condition and the simulation results presented show that CO_2 can be safely injected into an anticline structure over an extended period of time under an extensional stress regime.

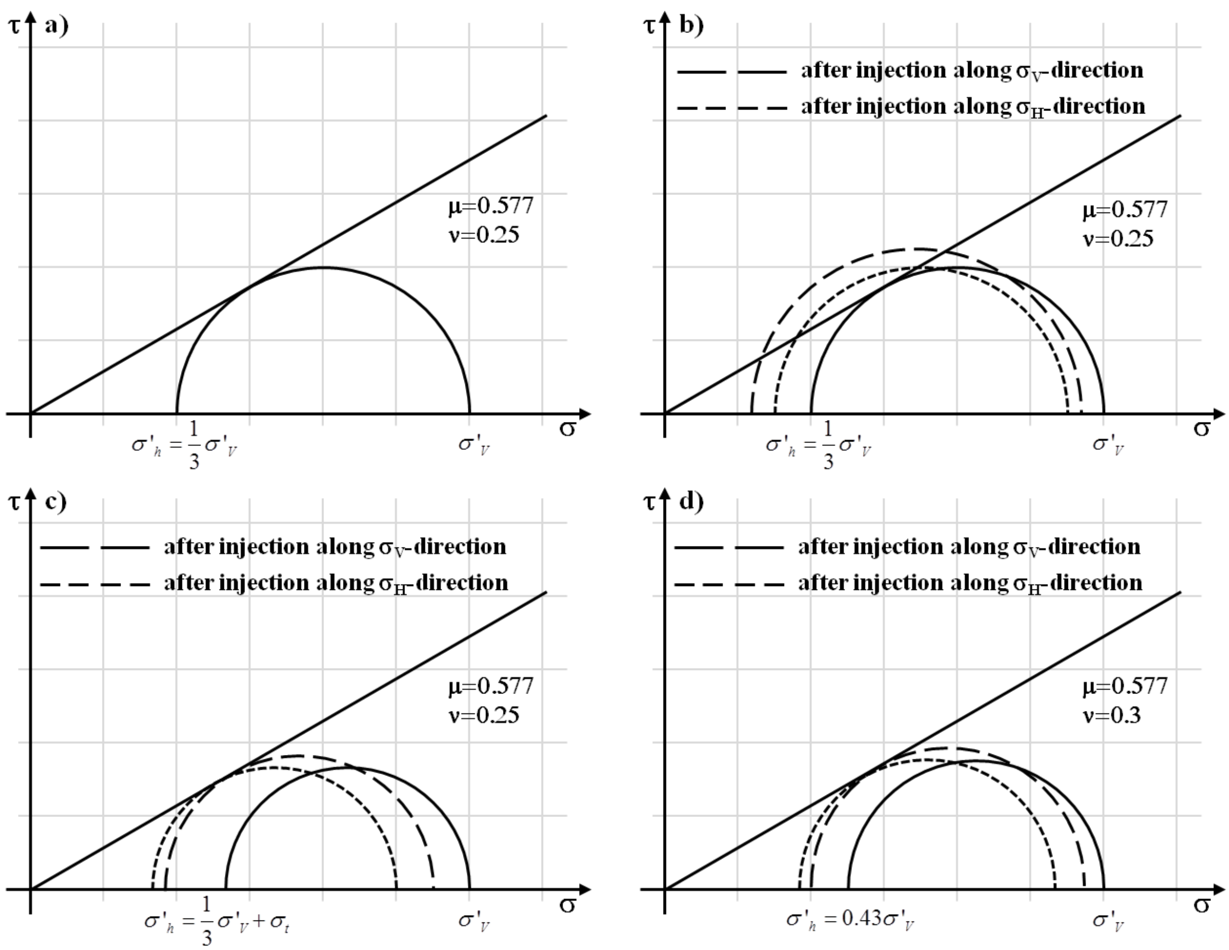

Figure 64: a) Exact frictional equilibrium conditions are encountered for sedimentary basins that are tectonically relaxed and where the horizontal stresses are determined by the uni-axial strain model. b) Fluid injection results in fault

reactivation in tectonically relaxed sedimentary basins. Basins who have a tectonically increased horizontal stress (c) or who have Poissons ratios larger than 0.25 can be subjected to fluid injection.

The results based on the pre-injection analytical estimates (along the vertical direction) are compared to a horizontally layered sedimentary basin at the same depth and the critical pore pressure magnitudes are compared. As shown in Table 13, only for compressional stress regimes horizontally layered basins provide safer conditions (i.e. higher ΔP_{crit} values). For extensional and strike-slip stress regimes anticlines are favorable compared to horizontally layered basins.

Table 13: Critical pore pressure magnitude comparison between generic anticline structures and horizontally layered sedimentary basin models.

	Extensional	Strike Slip	Compressional
Hor. Layered Basin	0 MPa	7.41MPa	58.9 MPa
Anticline model	2 MPa	18.5 MPa	15 MPa

Another aspect of anticline stress heterogeneity results in differences of the maximum sustainable pore pressure, ΔP_c, in the vertical direction across the layer. These differences in ΔP_c have to be carefully considered as the reservoir is not characterized by a single value for ΔP_c, contrary to horizontally layered sedimentary basins. If anticline structures are characterized by flexural slip folding and the bedding interfaces are characterized by a frictional surface, stress heterogeneities between reservoir and cap rock are amplified. The results presented in this study show that a low inter-bedding coefficient of friction effectively decouples the layers mechanically whilst a larger coefficient of friction represents a stronger coupling. This decoupling results in significant stress differences at the crest of the anticline and hence different ΔP_{crit} values between the top of the injection layer and the bottom of the overlaying cap rock. The pre-injection results show that for extensional and strike-slip stress regimes the reservoir layer can sustain a larger ΔP_c than the bottom of the cap rock. With the extensional stress regime displaying the overall lowest ΔP_c magnitudes the influence of the inter-bedding friction coefficient becomes important. The lower the coefficient of friction for the bedding interface the larger the difference in ΔP_c between reservoir and cap rock layers. This observation implies that seal integrity and thus the permeability difference between reservoir layer and cap rock are crucial parameters that have to be ensured.

The pre-injection risk assessment for the compressional stress regimes shows that ΔP_c is higher in the cap rock than in the reservoir. This represents the most favorable conditions as fractures in the reservoir rock can be reactivated, thus increasing infectivity, whilst the cap rock remains stable.

The results based on the simplified analytical derivations (i.e. using long-term limits) show that they are useful to obtain a quick 1st order estimate on P_c prior to injection to estimate fault reactivation risk. Furthermore, for the specific location along the crest of the anticline the influence of specific geological parameters such as the inter-bedding friction coefficient can be demonstrated. It is clear that the true nature of pore pressure - stress coupling is much more complex (Altmann et al., 2010). In order to include the spatial and temporal relationships coupled numerical analyses involving all physical processes are necessary.

It should be noted that due to the licensing (ECLIPSE) problems at Missouri S&T in the final 2 project quarters of the project only fracture generation results have been calculated and analyzed for the coupled simulations and thus cannot be compared to the analytical estimates based on fracture reactivation. The results for fracture reactivation would show an overall increased risk for failure and the applied parameter of fracture potential.

The results show that the stress regime has a significant influence on the geomechanical risk assessment. As expected from pore pressure stress coupling theory, the compressional stress regime results in increasing differential stresses and the risk for shear failure is evident. The results also show that pore pressure-stress coupling is dependent on the direction and distance to the injection point. The results for the compressional regime show that FP increases at a higher rate in the lateral direction from than injection well than in the vertical direction. On the other hand the extensional stress regime exhibits the safest conditions and within the 20 year injection period modeled neither tensile nor shear failure is observed.

Furthermore, the more compressional the stress regime, the larger is the difference between the models with a different inter-bedding plane coefficient of friction. The compressional stress regime exhibits a much lower ΔP_c magnitudes for low friction coefficients. This result is confirmed as shown by the pre-injection estimate (Figure 5a).

The results presented over a 20 injection period result only show elevated geomechanical risks for the compressional stress regime. However, with shear fracture potential steadily increasing in the strike slip regime and tensile fracture potential increasing in the extensional regime, a longer injection period is necessary. Model runs for a 50 year injection period and longer are recommended to analyze for similar case studies. It is important to note that whilst the anticline structures investigated in this study represent generic structures the results presented have shown that stress heterogeneities due to the geometry of a geological structures have an important impact on the resulting geomechanical risks and should not be neglected. Also, whilst the absolute magnitudes of the results of this study are not representative of a “real” geologic structure, the relative importance of geometry, stress regime and inter-bedding friction has been shown and the procedure can be readily applied to a real case study.

1.2.6. Conclusions

The analytical pre-injection estimates together with the coupled simulations have shown and confirmed that the in-situ stress regime is a crucial, if not the most important, factor determining geomechanical risks, for fluid injection applications such as CO_2 sequestration. It is therefore strongly recommended that every case study is based on in-situ stress measurements for a thorough calibration of numerical models used to analyze geomechanical risks.

The coupled simulations for the generic anticline structures have shown that the extensional stress regime represents the overall safest scenario, however is considered the most unlikely as anticlines are compressional structures. The compressional stress regime shows reservoir failure after 20 years of CO_2 injection. Whilst this is considered favorable as failure in the injection layer increases overall injectivity, the caprock is also very close to failure and a longer injection periods would thus require adjustment of the injection parameters. It should be noted again that the coupled modeling result are for fracture generation and fracture reactivation would occur much earlier, enhancing the geomechanical risks, and resulting in shorter safe injection times.

The generic anticline geometries investigated in this study have shown that in addition to the in-situ state of stress the stress heterogeneities associated to the geometry of such structures result in significant differences with respect to sustainable pore pressure magnitudes. For extension and strike slip stress regimes anticline structures should be favored over horizontally layered basin as they feature higher ΔP_c magnitudes. If sedimentary basins are tectonically relaxed and their state of stress is characterized by the uni-axial strain model the basin is in exact frictional equilibrium and fluids should not be injected.

Another important observation from the generic models is the influence of geological parameters such as the inter-bedding friction coefficient. Whilst the influence of this parameter is not important for horizontally layered structures, the geometry of anticline structures results in stress heterogeneities and the coefficient of friction on bedding planes determines the mechanical coupling between different layers. The results have shown that low friction coefficients effectively decouple layers resulting in lower ΔP_c magnitudes, especially for the compressional stress regime.

2. Wellbore Scale Model

2.1. Model Initialization

2.1.1. Introduction

Many applications of wellbore stability analysis, wellbore design, cementing as well as hydraulic fracturing processes rely on an accurate representation of the state of stress in the near-wellbore region. The analytical solution of the borehole stresses for a linear elastic material is given by the well known solution derived by Ernst Gustav Kirsch in 1898. Bradley [1979] and Zhang et al. [2006] further derived the effective wellbore stresses at the borehole wall for an inclined borehole including pore pressure and mud pressure. However, the analytical solution has limitations handling complex formation geometry, material heterogeneities and different rheological models. As computers and commercial numerical software applications have become readily available as a standard engineering tool a variety of borehole stress studies utilize 2D and 3D finite element analysis for solving geomechanical problems associated with borehole failure [Cheng and Dusseault, 1993; Zervos et al., 1998; Gentzis et al., 2009]. It should be noted that numerical modeling methods introduce errors by nature, as they represent an approximation approach [Zienkiewiscz et al. 2006], and often utilize assumptions and simplifications of the physical problem. Thus, a common problem of numerical studies is the validation and calibration to analytical solutions and field data. Since this standard modeling procedure is sometimes not available, care has to be taken with numerical codes to provide an accurate solution before the results can be relied on for interpretation.

For wellbore stress analyses the accuracy of numerical modeling results becomes crucial especially at the wellbore wall where the state of stress changes rapidly and it is therefore recommended to ensure a high quality mesh to obtain accurate results. The optimization of the mesh quality may not be done in every study [Rutqvist et al., 1989; Zahn et al., 2010], and to date only few studies have shown that mesh quality has a significant influence on numerical modeling results in geomechanical applications [Nipp et al., 1987; Grabinsky et al., 1995; Turon et al., 2007]. Grabinsky et al. [1995] studied the impact of different element types providing good quality discretizations for rock excavation scenarios. Turon et al. [2007] showed that results are sensitive to the element size when handling pore cohesive elements in the wellbore fracture zone, and a mesh size as small as 0.5mm in length is necessary to obtain converging solutions. Nipp and McNulty [1987] demonstrated how boundary conditions and element size can affect the accuracy of solutions involving creep around a single borehole in an infinite medium. In summary, these studies support the inference that the discretization parameters of element size, element type, model size and boundary conditions are crucial regarding the accuracy of numerical results.

In this paper we present a general guideline to generate an optimized mesh for wellbore stress analysis of non-inclined wellbores and show how the boundary conditions and discretization parameters of the model can affect the accuracy of the calculated stresses around the wellbore. We use a parametric study on model size, element size, element type and boundary condition application and compare and validate the numerical results to the analytical solution. In the context of a safe mud weight window prediction study for three different stress regimes, we show how errors from non-optimized meshes can lead to a significant under- or over-estimation of the safe mud weight window.

2.1.2. Theoretical Background

a) Analytical Solution for Wellbore Stresses

Before drilling, the state of stress of the rock in the subsurface is in equilibrium and can be represented by the three in-situ principal stresses $\sigma 1$, $\sigma 2$, and $\sigma 3$, which for an Andersonian state of stress, are the vertical stress and two far field horizontal stresses [Pollard and Fletcher, 2005]. During drilling, the borehole rock is removed and the acting loads are to be compensated by the adjacent rock around the wellbore. After redistribution of the stresses, local stress concentrations occur in the close vicinity of the wellbore. The linear elastic solution describing the concentration of radial and tangential stresses around a hole was first derived by Kirsch [1898] in 1898 and extended by Zhang et al. [2006] to account for pore pressure and the fluid pressure in the wellbore. Assuming a constant pore and a Biot's coefficient of 1, the effective stresses around the borehole for a vertical well can be obtained [3]:

$$\sigma_{rr}^{'}=\frac{\left(\sigma_H+\sigma_h-2P_p\right)}{2}\left(1-\frac{R_w^2}{r^2}\right)-\frac{\left(\sigma_H-\sigma_h\right)}{2}\left(1-\frac{4R_w^2}{r^2}+\frac{3R_w^4}{r^4}\right)\cos 2\theta+\left(P_m-P_p\right)\frac{R_w^2}{r^2} \tag{6}$$

$$\sigma_{\theta\theta}^{'}=\frac{\left(\sigma_H+\sigma_h-2P_p\right)}{2}\left(1+\frac{R_w^2}{r^2}\right)-\frac{\left(\sigma_H-\sigma_h\right)}{2}\left(1+\frac{3R_w^4}{r^4}\right)\cos 2\theta-\left(P_m-P_p\right)\frac{R_w^2}{r^2} \tag{7}$$

$$\sigma_{z}^{'}=\sigma_v-P_p-\nu\frac{2R_w^2}{r^2}\left(\sigma_H-\sigma_h\right)\cos 2\theta \tag{8}$$

$$\tau_{r\theta}^{'}=-\frac{\left(\sigma_H-\sigma_h\right)}{2}\left(1+\frac{2R_w^2}{r^2}-\frac{3R_w^4}{r^4}\right)\sin 2\theta \tag{9}$$

where σ'_{rr} , $\sigma'_{\theta\theta}$, σ'_z and $\tau'_{r\theta}$ are the radial stress, hoop stress, vertical stress, and shear stress in the r-θ plane, respectively; σ_H , σ_h , and σ_z are the maximum horizontal, minimum horizontal, and the overburden stress, respectively; R_w is the wellbore radius, and r is the distance from wellbore center; θ is the angle with respect to the direction of σ_H.

At the wellbore wall ($r = R_w$) at θ = 90° or 270°, the hoop stress reaches its maximum and thus compressive failure or borehole breakouts may occur if $\sigma_{\theta\theta}$ is larger than the compressive strength of the rock (Figure 65). Tensile failure occurs at $r = R_w$ at θ = 0° or 180°, when the hoop stress overcomes the tensile strength (Figure 65).

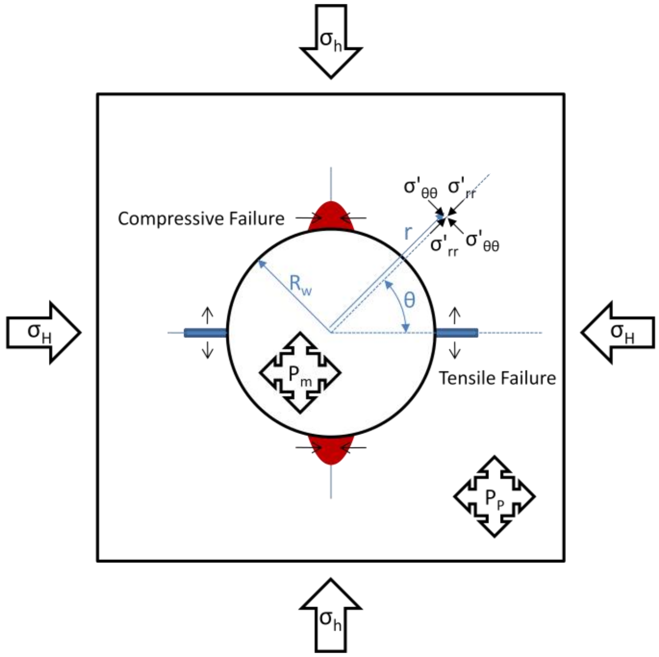

Fig. 65. A vertical wellbore showing the state of stress and potential failure types around the borehole: σ_{rr} is the radial stress, $\sigma_{\theta\theta}$ is the hoop stress, Pp is the pore fluid pressure in the rock formation and Pm is the drilling fluid pressure. Vertical stress σz is along the borehole axis and is not shown in the figure.

b) Failure Criteria

The criterion for tensile failure at the borehole wall is given when the minimum effective principal stress σ'_3 is less than the formation tensile strength T_0:

$$\sigma_3^{'} \leq -T_0 \tag{10}$$

In order to predict compressive rock failure, different failure criteria are commonly applied [McLean and Addis, 1990]. These criteria can be categorized into criteria, where failure is only dependent on the differential stress $\sigma_1 - \sigma_3$, such as the Mohr-Coulomb criterion, or into criteria accounting for a strength dependence of the intermediate principal stress (σ_2), such as the Drucker-Prager or the modified Lade criterion [Zhang et al., 2010].

Studies have shown that the choice of the applied failure criterion has a significant influence on the prediction of the safe minimum mud weight [Ewy, 1999; Nawrocki, 2010; Tran et al., 2010]. It should be noted that for the subsequent analysis the evaluation of an appropriate failure criterion for wellbore stability analysis is beyond the scope of this paper and that the errors introduced by non-optimized meshes result in errors of the numerically determined hoop and radial stresses. For the linear elastic, isotropic analysis applied in this study theses numerical errors are independent from the application of the relevant failure criterion. Thus, for simplicity we chose the Mohr-Coulomb failure criterion as the example of the most conservative criterion [Zhang et al., 2010] for predicting the minimum mud weight to ensure wellbore stability. The Mohr-Coulomb [Coulomb, 1776] failure criterion represents the linear envelope that can be expressed by the normal stress and shear stress on a failure plane:

$$\tau = C_0 + \sigma_n \tan\phi \tag{11}$$

where τ is the shear stress, σ_n is the normal stress, C_0 is the cohesion and φ is the internal friction angle of the rock. When the Mohr circle, defined by σ_1 and σ_3, intersects with the failure envelope, shear failure will occur, and the failure criterion can be expressed in terms of the relation of σ_1 and σ_3 at failure:

$$\sigma_1 = 2C_0 \frac{\cos\phi}{1-\sin\phi} + \frac{1+\sin\phi}{1-\sin\phi}\sigma_3 \tag{12}$$

c) Safe Mud Weight prediction

The safe mud weight window for drilling is defined by the collapse pressure as the lower limit to prevent the onset of breakouts and the breakdown pressure as the upper limit to prevent the onset of tensile failure. In permeable formations mud pressure is required to be higher than the pore fluid pressure to prevent kicks to occur. If the required mud pressure is higher than the collapse pressure, the mud pressure is chosen as the lower limit of the safe mud weight window. Based on the Mohr-Coulomb failure criterion, the collapse pressure can be solved for by utilizing Eq. (13) and the fact that the two Mohr circles have the same mean stress:

$$\frac{\sigma'_{rr} + \sigma'_{\theta\theta}}{2} = \frac{\sigma_3 + \sigma_1}{2} \tag{13}$$

$$\Rightarrow \sigma_3 = \frac{\sigma'_{rr} + \sigma'_{\theta\theta} - 2C_0 \dfrac{\cos\phi}{1-\sin\phi}}{1 + \dfrac{1+\sin\phi}{1-\sin\phi}}$$

P_m, collapse can be solved for by the fact that σ_3 equals to σ'_{rr} added by P_m,collapse (Eq. (14)) or σ_1 equals $\sigma'_{\theta\theta}$ subtracted by P_m,collapse (Eq. (15)):

$$P_{m,collapse} = \sigma_3 - \sigma'_{rr} \quad or \quad \sigma'_{\theta\theta} - \sigma_1 \tag{14}$$

The breakdown pressure is calculated by:

$$\sigma'_{\theta\theta} - P_{m,breakdown} = -T_0$$
$$\Rightarrow P_{m,breakdown} = \sigma'_{\theta\theta} + T_0 \quad (15)$$

2.1.3. Geomechanical Model and Input Data

a) Mapped Meshing Approach

The geometry of a borehole model has been constructed using the commercial pre-processing software package Altair HyperMeshTM. A mapped meshing approach [Mitchell, 1997] was followed to have complete control on the size and shape of the elements. By using this meshing approach, the aspect ratio of the elements around the borehole can be controlled most conveniently. For the borehole geometry, we use a relatively fine circular mesh in the near-wellbore region (Figure 66) which is biased towards the borehole, since the state of stress changes rapidly close to the borehole wall. In the outer sections (the far-field region) we use a coarser mesh since the state of stress should be given by the homogeneous far-field stresses (Figure 66). The near-wellbore region is defined ranging from R_w to $5R_w$ from the borehole center.

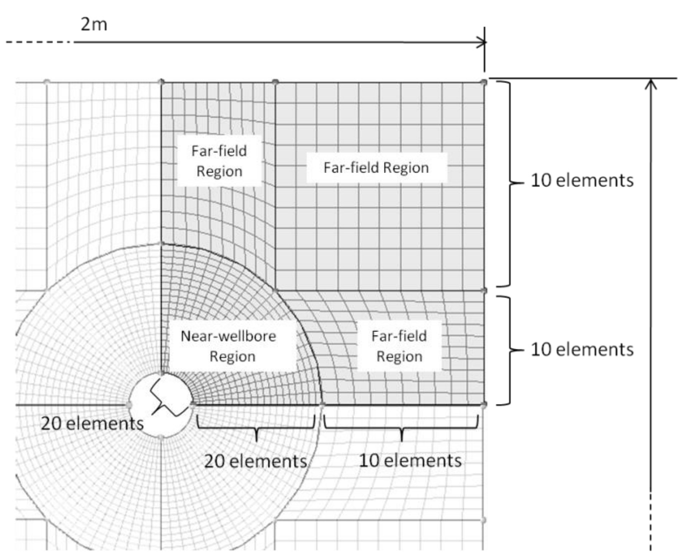

Fig. 66. Mapped meshing approach dividing the model into sections defined as a near-wellbore region and three adjacent far-field regions, with the model size and the mesh density of the base model shown.

b) Initial Model Geometry and Model Input

In order to present a meshing guideline we set up an initial 2D “base model” which has a borehole radius of 0.1m (R_w) and horizontal dimensions of 2m by 2m (Figure 66). The near-wellbore region ranges from the borehole wall (R_w) to the outer circle of the region ($5R_w$); the far-field region ranges from the outer circle of the near-wellbore region ($5R_w$) to the model boundary ($10R_w$). The “base model” mesh consists of 1st order quadrilateral elements. Referring to Figure 66, for the initial circumferential mesh density in the near-wellbore region, 20 elements per quarter circumference are used; for the initial radial mesh density, 20 elements per $4R_w$ distance are used; for the far-field region a radial mesh density of 10 elements per $5R_w$ distance is used. These element densities are representative of commonly regarded good quality meshes [Knupp, 2007], i.e. we have a fine mesh in areas of rapidly changing stresses and the element aspect ratio (optimal is 1) does not exceed 2.55 in the near wellbore region.

The material model is linear elastic, isotropic and homogeneous with a Poisson’s ratio of 0.25 and a Young’s modulus of 5 MPa. The initial far-field stresses are: σ_H = 40 MPa and σ_h = 20 MPa; the fluid pressures are: P_p = 10 MPa and P_m = 15 MPa. The model is solved utilizing 2D plane strain analysis with the commercial Finite Element software package ABAQUS^{TM}.

2.1.4. Modeling Approach

a) Boundary Conditions

The influence of the various meshing parameters on the quality of the results is studied using three types of boundary conditions:

- Displacement boundary conditions: far-field stresses are generated by applying displacements to the model boundary (Figure 67a);
- Stress boundary conditions: far-field stresses are directly applied on the model boundaries (Figure 67b);
- Drilling process simulations: the model geometry before drilling without the wellbore is subjected to an initial state of stress in equilibrium; removal of wellbore elements simulates the drilling process and the stresses subsequently are redistributed (Figure 67c).

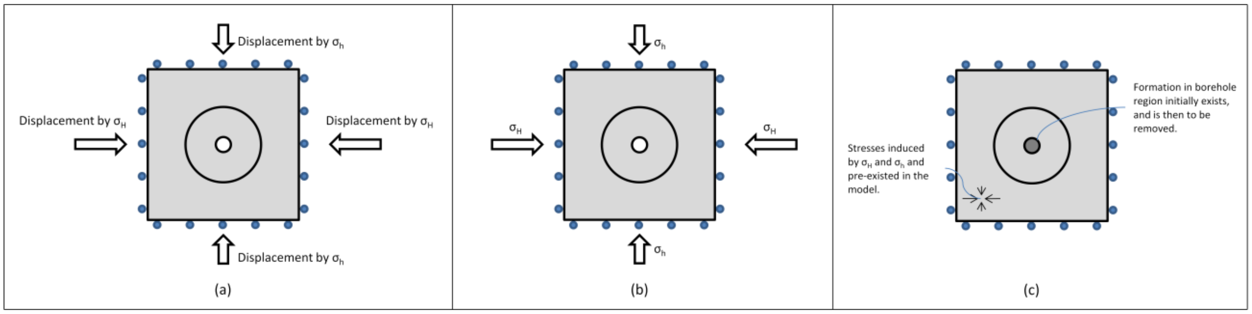

Fig. 67. Three types of boundary conditions: (a) displacement, (b) stress, and (c) drilling process simulation.

b) Parametric Study

Sensitivity analyses are conducted for the following parameters of the model/mesh:

- Model size: wellbore model dimensions.
- Element type: quadrilateral 1^{st} and 2^{nd} order, and triangular 2^{nd} order elements are studied. 1^{st} order triangular elements are not used here because pore pressure cannot be applied for this element in ABAQUS.
- Mesh density
    - mesh density around the circumference of the borehole
    - mesh density along the radial distance

For each parameter the modeled result is compared to the analytical solutions (Eqs. 6 and 7), and the influence of the model parameters is investigated.

2.1.5. Results

2.1.5.1. Displacement Boundary Conditions

a) Comparison of the Base Model to the Analytical Solution

The results for the hoop stress and radial stress for the base model and the analytical solution are shown in Figure 68. At first sight the comparison shows a good agreement. The hoop stress at 0° with respect to σ_H (Figure 68) or the radial stress at 90° matches the analytical solution throughout the model. However, the hoop stress at 90° and the radial stress at 0° show discrepancies. These misfits are especially noticeable at the borehole wall for the hoop and radial stresses at either 0° or 90° (Table 14). The errors have maximum values of -8.23 MPa at the borehole wall for the hoop stress at 90°, and a value of 4.62 MPa for the hoop stress at 0°.

The significance of these numerical errors become obvious when considering that the hoop stress at 90° is related to compressive failure of the wellbore, while the hoop stress at 0° is related to tensile failure of the wellbore. For example, in a 2000 m deep formation, an 8 MPa stress error represents 40% of the hydrostatic pore pressure (around 20 MPa) of water, or it may be equivalent to around 0.5 specific gravity (s.g.) or 4 ppg in terms of mud density. This shows the inherent need to develop a mesh optimization procedure that provides precise results for wellbore models.

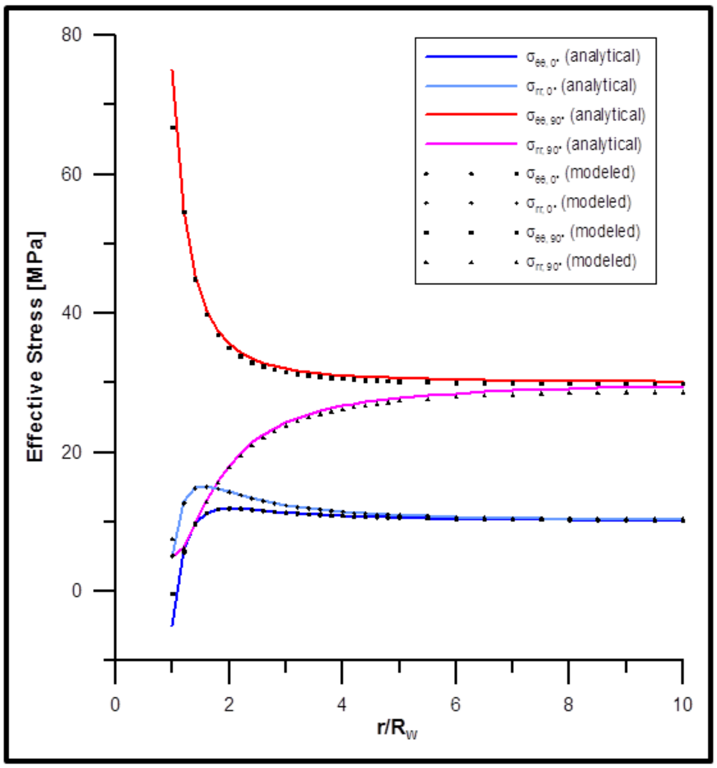

Fig. 68. The modeled results for the base model as compared to the analytical solution.

Table 14. Errors of the effective stresses at borehole wall for the base model.

Numerical Errors at Borehole Wall (MPa)			
$\sigma_{\theta\theta}$ at 0°	σ_{rr} at 0°	$\sigma_{\theta\theta}$ at 90°	σ_{rr} at 90°
4.62	2.58	-8.23	0.10

b) Sensitivity Analysis of the Model Size

For the sensitivity analysis of the model size, in addition to the base model (2m by 2m; i.e. 10x of borehole diameter), models of 1.5m by 1.5m (7.5x of diameter), 3m by 3m (15x of diameter), 4m by 4m (20x of diameter), 10m by 10m (50x of diameter) are investigated.

Choosing the overall model size is the first step when modeling a geometric structure. If the model size is chosen appropriately, the state of stress at the boundary of the model should reach the homogeneous far-field stresses σ_H and σ_h. The sensitivity analysis of the model size shows that the finite element results are affected by the model size, not only as expected for the far-field region but also in the near-wellbore region (Figure 69). This can be seen most clearly for the radial stress at 0° (Figure 69a). The most significant observation is that larger model sizes provide an overall better fit of the model results to the analytical solution. Further, increasing the model size specifically improves the model results for the hoop stress at the borehole wall at 90° (Table 14), which shows the largest error in the base model. However, the errors at the borehole wall do not decrease to a satisfactory degree.

A model with dimensions of at least 15 to 20 times of the borehole diameter produces a result in good agreement with the analytical solutions for the effective stresses, i.e. larger model sizes do not improve the result any further. It should be noted that wellbore failure may occur on the wellbore surface and inside the formation [23], thus the importance of the fitting in the near-wellbore region should not be ignored.

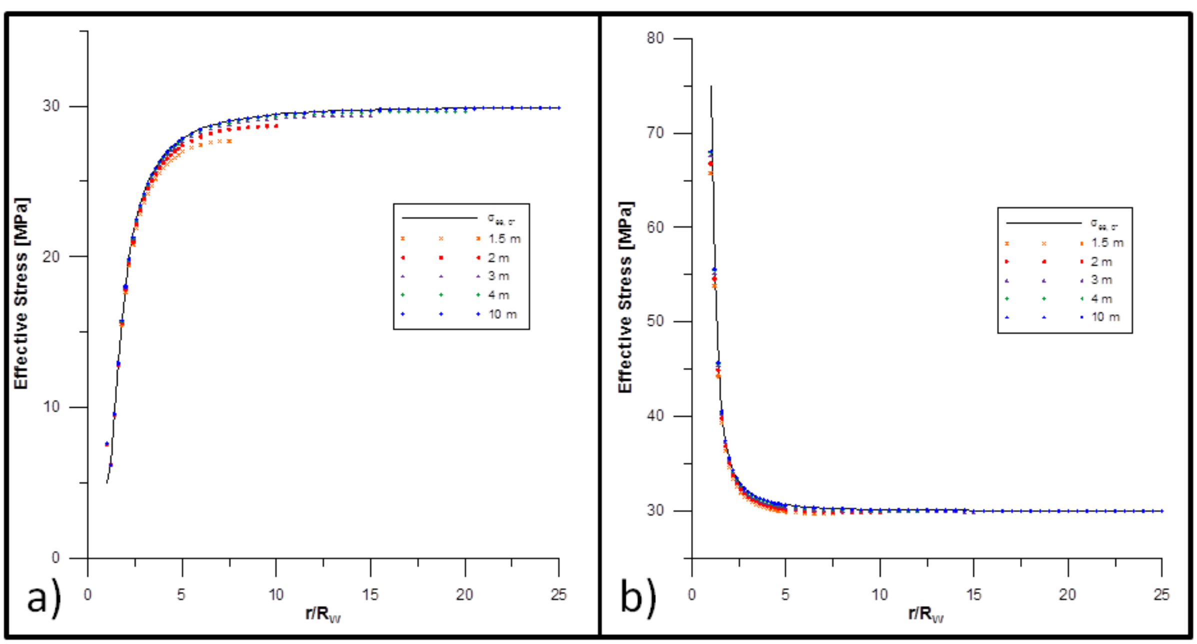

Fig. 69. Influence of model size on the effective stresses at a) σ_{rr} at 0° and b) $\sigma_{\theta\theta}$ at 90° with respect to σ_H. The larger the model size, the smaller become the errors in the near-wellbore and in the far-field region.

Table 15. Sensitivity analysis of the model size using displacement boundary conditions. The base model is highlighted.

Model Size (m)	Numerical Errors at Borehole Wall (MPa)			
	$\sigma_{\theta\theta}$ at 0°	σ_{rr} at 0°	$\sigma_{\theta\theta}$ at 90°	σ_{rr} at 90°
1.75	5.02	2.55	-9.25	0.11
2	4.62	2.58	-8.23	0.10
3	4.38	2.64	-7.37	0.09
4	4.25	2.62	-7.14	0.10
10	4.14	2.63	-6.91	0.09

c) Sensitivity Analysis of the Element Type

For the sensitivity analysis of the element type, 1st (base model) and 2nd order of quadrilateral and 2nd order of triangular elements are studied. 1st order triangular elements are not used here because pore pressure cannot be applied for this element in ABAQUS.

All three types of elements yield very similar results beyond $r/R_w = 2$ (Figure 70). However close to the borehole wall, i.e. $r/R_w = 1$ to 2, quadrilateral 2nd order element and triangular 2nd order element both provide better results than the quadrilateral 1st order element, and the maximum error at the borehole wall can be greatly reduced to around -1.25 (quads) or -0.13 (trias) MPa from -8.23 MPa (Table 16). Although the 2nd order triangular element produces slightly better results than the quadrilateral 2nd order element at the borehole wall, the results from quadrilateral 2nd elements generally have less discrepancies compared to the analytical solution in the region of $r/R_w = 1$ to 2. Thus the quadrilateral 2nd order element should be chosen over triangular 2nd order element to obtain an overall better fitting to the analytical solution.

Table 16. Sensitivity analysis of the element type using displacement boundary conditions. The base model is highlighted.

Element Type	Numerical Errors at Borehole Wall (MPa)			
	$\sigma_{\theta\theta}$ at 0°	σ_{rr} at 0°	$\sigma_{\theta\theta}$ at 90°	σ_{rr} at 90°
1st Quad	4.62	2.58	-8.23	0.10
2nd Quad	0.50	-0.80	-1.25	0.50
2nd Tria	1.11	-0.63	-0.13	0.06

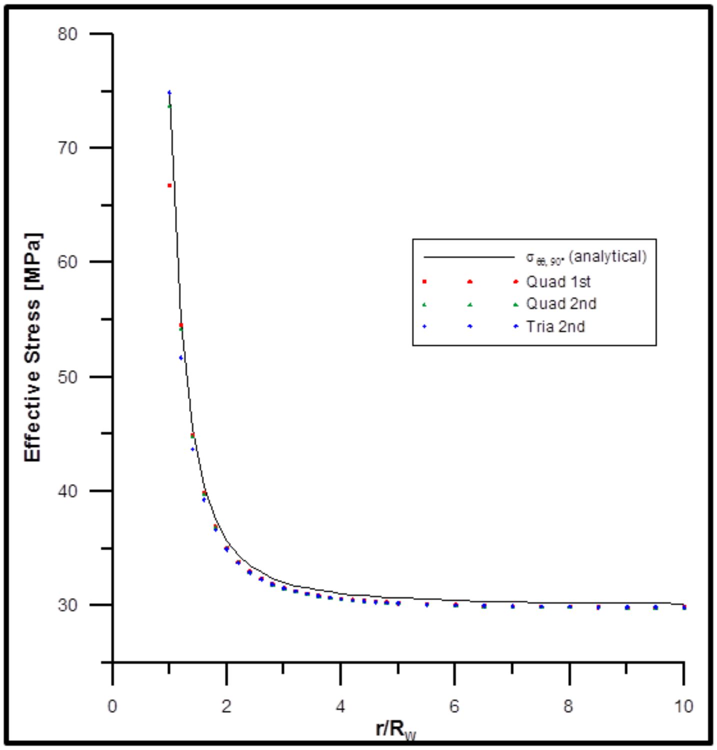

Fig. 70. Influence of element type for the hoop stress at 90°. The choice of 2nd order element greatly increases the accuracy of the modeled result. The 2nd order quadrilateral element is slightly better than the 2nd order triangular element due to the better fitting near the wellbore surface (r/R_w = 1 to 1.5).

d) Sensitivity Analysis of the Mesh Density

For the sensitivity analysis of the mesh density in the near-wellbore region (the base model has a mesh density of 20 elements per quarter wellbore circumference and a mesh density of 20 elements per the radial distance (4 Rw) mesh densities of 10, 30 and 40 elements per quarter wellbore circumference and mesh densities of 10, 30, 40, 50 element per 4Rw radial distance are studied.

A change in the circumferential mesh density has nearly no effects to the model results near the borehole or for the overall fitting of the results in the entire model (Table 17). An increase in mesh density would adversely cause a slightly larger error, resulting from a poorer aspect ratio of the elements due to the elongated shape, if the radial mesh density is fixed.

A change in the radial mesh density significantly alters the model results and by utilizing higher densities significant improvement can be obtained (Figure 71). This becomes most apparent for the hoop stress at 90° where the difference between the model results and the analytical solution decreases from -12.89 MPa for 10 elements to -4.72 MPa for 50 elements (Table 18). Also the difference for the radial stress at 0° decreases from 4.94 MPa for 10 elements to 1.08 MPa for 50 elements (Table 5). The influence of increasing the radial mesh density marginally decreases, and the accuracy of the effective stresses can be only enhanced to some degree by refining the mesh.

Table 17. Sensitivity analysis of the mesh density around the borehole circumference using displacement boundary conditions. The base model is highlighted.

Circum. Density (elements)	Numerical Errors at Borehole Wall (MPa)			
	$\sigma_{\theta\theta}$ at 0°	σ_{rr} at 0°	$\sigma_{\theta\theta}$ at 90°	σ_{rr} at 90°
10	4.80	2.79	-8.39	0.05
20	4.62	2.58	-8.23	0.10
30	4.65	2.56	-8.22	0.13
40	4.65	2.55	-8.22	0.14

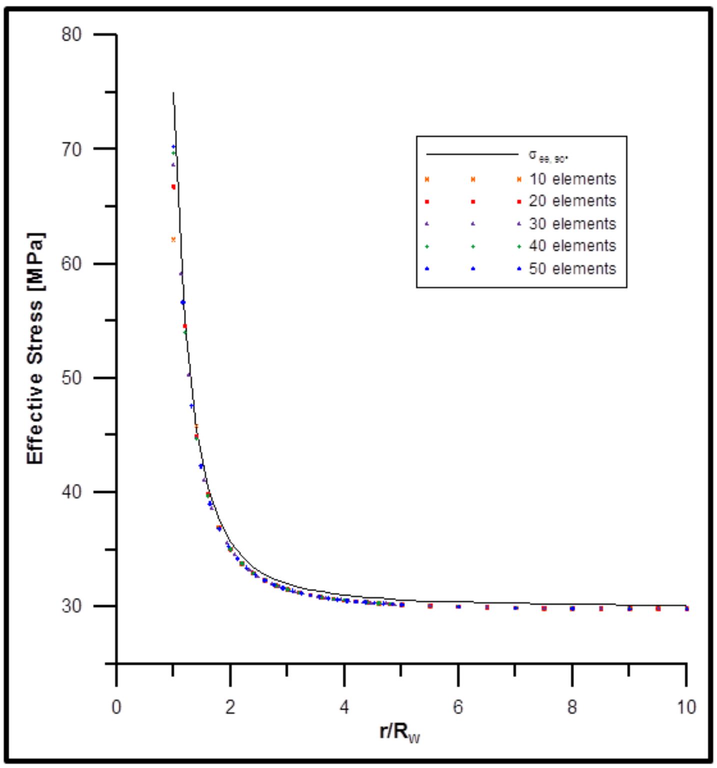

Fig. 71. Influence of the radial mesh density in the near-wellbore region for the hoop stress at 90°.

Table 18 – Sensitivity analysis of the mesh density along the radial distance in the near-wellbore region using displacement boundary conditions. The base model is highlighted.

Radial Density (elements)	Numerical Errors at Borehole Wall (MPa)			
	$\sigma_{\theta\theta}$ at 0°	σ_{rr} at 0°	$\sigma_{\theta\theta}$ at 90°	σ_{rr} at 90°
10	7.12	4.94	-12.89	-0.02

20	4.62	2.58	-8.23	0.10
30	3.58	1.76	-6.31	0.11
40	2.95	1.34	-5.28	0.08
50	2.93	1.08	-4.72	0.07

e) General Meshing Guideline

From the sensitivity study presented for the displacement boundary conditions, a general guideline for meshing and the choice of meshing parameters can be obtained. Finite element meshes of borehole models should:

1) use an appropriate model size to yield a good match to the analytical solution throughout the model;

2) use 2nd order quadrilateral elements to increase the accuracy of effective stresses at the borehole wall;

3) use a finer mesh along the radial distance in the near-wellbore region to further improve the results;

4) use an appropriate mesh density along the borehole circumference to ensure a good aspect ratio of the elements.

2.1.5.2.Mesh Optimization

According to the parametric study and the guideline obtained above, an optimized model is constructed using the following parameters:

- Model size: 4m by 4m, which is 20x the borehole diameter.

- 2nd order quadrilateral element.

- Radial mesh density in the near-wellbore region: 40 elements along the 4Rw distance.

- Circumferential density in the near-wellbore region: 40 elements per quarter wellbore circumference.

Comparing the numerical results from the optimized model to the analytical solution shows a very good agreement (Figure 72). Further the error at the borehole wall is minimized to less than 0.5 MPa (Table 19).

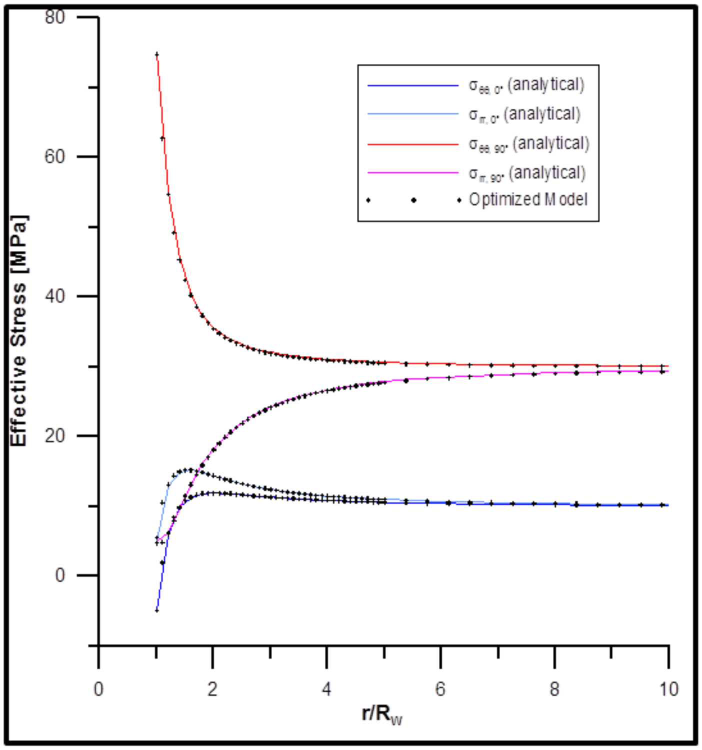

Fig. 72. The modeled results from the optimized model compared with the analytical results.

Table 19. Errors of the modeled results from the optimized model compared to that of the base model.

Model	Numerical Errors at Borehole Wall (MPa)			
	$\sigma_{\theta\theta}$ at 0°	σ_{rr} at 0°	$\sigma_{\theta\theta}$ at 90°	σ_{rr} at 90°
Base	4.62	2.58	-8.23	0.10
Optimized	0.09	-0.29	-0.28	0.50

2.1.5.3. Stress Boundary Conditions and Drilling Simulation Boundary Conditions

The sensitivity analyses for the stress boundary conditions and the drilling process simulation boundary conditions yield very similar results as for the displacement boundary conditions. Therefore, the majority of this data is not repeatedly shown here again. The comparison of the base model case using the three boundary condition scenarios is shown in Figure 73. While the stress boundary conditions seem to provide the best solution at the borehole wall, especially for the hoop stress at 90° (Table 20), the discrepancies at distances larger than $r/R_w = 1.2$ become larger. The mean error and the standard deviation of the error of the hoop stress at 90° between $1.2 \leq r/R_w \leq 2$ for the stress boundary conditions are 1.04 MPa and 0.55MPa, respectively, compared to -0.53 MPa (mean error) and 0.13 MPa (standard deviation) for both displacement boundary conditions and for drilling simulation boundary conditions. Further, the stress boundary conditions show relatively large discrepancies for the sensitivity check on the model size. The hoop stress at 0° at the model boundary does not converge to the far-field stress, and only slightly improves with increasing model size (Figure 74).

Due to the similarity of the sensitivity analysis for all the three boundary conditions the same meshing guideline can be applied and an optimized model according to our suggestion above can be obtained. In the optimized model the results for each boundary condition scenario are improved. In contrast to the base model, after optimization, the displacement boundary conditions and the drilling simulation boundary conditions now yield the smallest errors also at the borehole wall (Table 20) and are thus preferred over the stress boundary conditions. It should be noted that the drilling simulation boundary conditions increase the numerical complexity by their implementation and thus displacement boundary conditions are recommended for wellbore stress analyses.

Table 20. Errors at the wellbore surface for the base model and the optimized model under three boundary conditions.

Model	Numerical Errors at Borehole Wall (MPa)			
	$\sigma_{\theta\theta}$ at 0°	σ_{rr} at 0°	$\sigma_{\theta\theta}$ at 90°	σ_{rr} at 90°
Base				
Displace	4.62	2.58	-8.23	0.10
Stress	3.11	2.71	-5.28	0.05
Drilling Sim	4.67	2.59	-8.23	0.10
Optimized				
Displace	0.09	-0.29	-0.25	-0.50
Stress	0.40	0.30	0.60	0.51
Drilling Sim	0.08	-0.29	-0.25	0.50

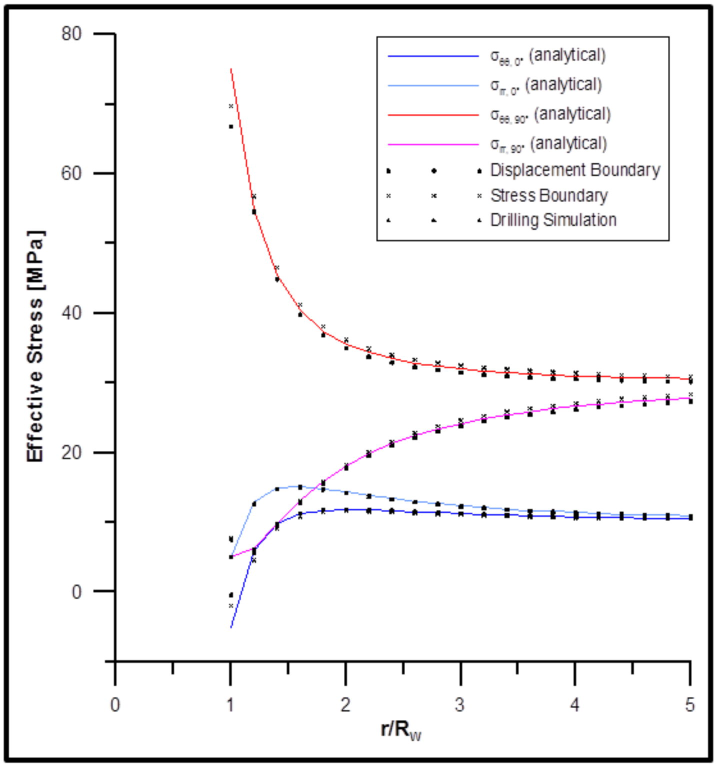

Fig. 73. Base model under three boundary conditions and compared to the analytical solutions.

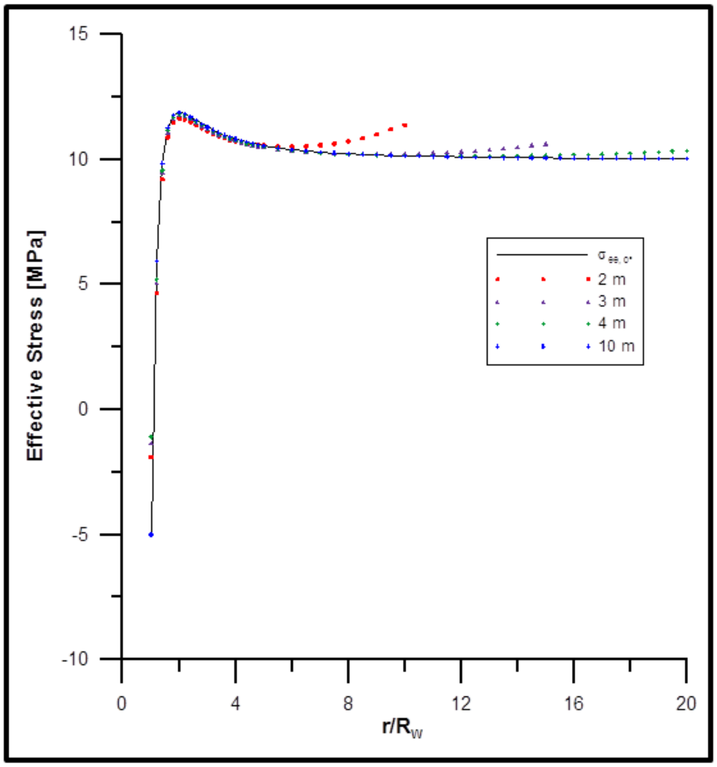

Fig. 74. Hoop stress at 0° for the stress boundary conditions shows a great discrepancy near the model boundary for the base model.

2.1.6. Discussion

2.1.6.1. Models Using the Displacement Boundary Conditions

The numerical study presented in this paper shows that, considering the general availability of numerical modeling tools such as the finite element (FE) method, care has to be taken when these methods are applied for wellbore stress analysis. It is obvious that for the case of a homogeneous, isotropic, linear elastic material the analytical solution provides the accurate solution and numerical analysis is not necessary. However, many applications for wellbore stability or hydraulic fracturing occur in anisotropic rocks (e.g. shale; [24]) or require composite materials (e.g. cementing analysis; [25]) where analytical solutions do not exist. Therefore, numerical wellbore stress analysis for a homogeneous, isotropic, linear elastic material provides an excellent opportunity to test the influence of the various discretization parameters on the existing analytical solution [3] and to provide conclusions for meshing and model optimization requirements for all types of wellbore stress analyses. A variety of studies have shown that the accuracy of results of FE studies are highly dependent on discretization approaches and parameters [26, 27, 28]. Even if errors of the modeled results are within 1 to 3 MPa [10], these should be taken seriously, otherwise the subsequent study based on the modeled results might be questionable.

Our study shows that the most prominent improvement on the accuracy of the modeled result is obtained by using 2nd order elements. The -8.23 MPa error of the hoop stress at 90° in the base model using the displacement boundary is decreased to around 1 MPa by merely changing the element type with other modeling parameters fixed, and at no cost to the increase of the numbers of the elements, although more nodes are used. In the sensitivity analysis, the increase of radial mesh density in the near wellbore region the error is reduced to around 5 MPa, and its influence marginally diminishes. Thus choosing 2nd order elements has the highest priority before the increase of mesh density.

In the context of the significance of the numerical errors, it should be noted that the FE method inherently introduces errors as it is a method of approximation [8]. This becomes most evident when comparing the stress results at the borehole wall, where the numerical model yields the largest error. One has to understand that the FE method calculates stresses at the element integration point [29], which is situated inside the element (Figure 75) and thus cannot reproduce the absolute exact result at free surfaces like the borehole wall. To compare FE model stresses to the analytical solution the element stresses from the integration points have to be extrapolated to the nodal coordinates (Figure 75). This procedure generally provides very accurate agreements for nodes attached to 4 elements but at the free surface of the borehole wall an error is introduced. Here, the stress changes rapidly and the stress at this node is extrapolated from the two integration points inside the formation only. This extrapolation will always return a non zero stress value for the radial stress (if no fluid pressure is applied) and thus cannot obey the rule that normal stresses do not exist at a free surface.

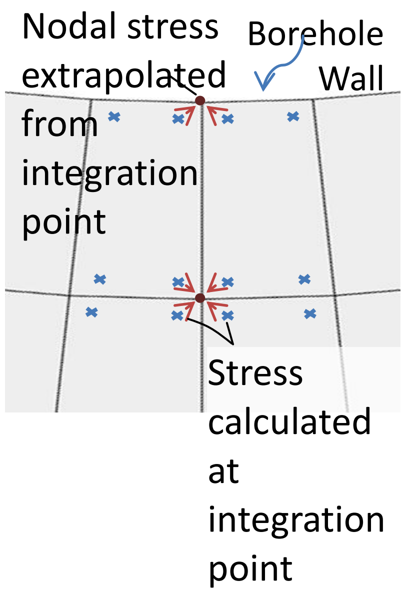

Fig. 75. Stresses are calculated at the element integration points [29]. When stresses are extrapolated to nodal positions a greater error is introduced especially near the borehole wall.

2.1.6.2.Comparisons of the Models for the Different Boundary Conditions

The displacement and drilling simulation boundary conditions produce almost identical results and yield smaller errors than the stress boundary conditions. Since the drilling simulation boundary conditions require an additional initial pre-stressing procedure, displacement boundary conditions are considered sufficient for wellbore stress analyses if there is no specific need for simulating the drilling process.

2.1.6.3.Implications for Safe Mud Weight Prediction

In order to demonstrate the significance of the numerical errors for wellbore stability applications we predict the safe mud weight window for the base model, the optimized model, and for the analytical solution under three different stress regimes: normal or extensional faulting (NF), strike-slip (SS) faulting, and compressional or reverse faulting (RF) regime. It should be noted again that the evaluation of an appropriate failure criterion for wellbore stability analyses is beyond the scope of this paper and that each failure criterion is affected differently by the numerical errors. We use the Mohr-Coulomb failure criterion as the most conservative [16] criterion for this analysis to point out the general implications for wellbore stability.

The magnitudes of the horizontal stresses are based on a vertical well at 2000 m depth with a hydrostatic pore pressure of 19.62 MPa (i.e. using a pore fluid density of 1g/cm^3) and an overburden stress of 44.15 MPa (i.e., using an overburden rock density of 2.25 g/cm^3). The rock formation is based on a typical sandstone, which has a cohesion of 5.10 MPa, a friction angle of 33° and a Poisson's ratio of 0.25 [30]. Table 21 lists the stress magnitudes for the different regimes applied for the far-filed stresses.

Table 21. State of stress for the different stress regimes applied to the wellbore models.

Stress regime	σ_v (MPa)	σ_H (MPa)	σ_h (MPa)
NF	44.15	35.97	27.80
SS	44.15	52.97	33.11
RF	44.15	66.22	55.18

The numerical results of the hoop and radial stresses at the borehole wall for the base (non-optimized) model and the optimized model presented above are compared to the analytical solution, and the errors for each stress regime are shown in Table 22. Our results for the base model show that for all stress regimes considered the highest errors occur at the locations prone to borehole breakouts, i.e. for the hoop stress at 90° (-6.42 MPa for NF, -10.93 MPa for SS and 10.78 MPa for RF). The stress errors for the radial stress at 0° and 90° and the hoop stress at 0° are less, but still significant. In comparison, the errors obtained from the optimized model are less than 0.65MPa for all locations.

Table 22. Stress errors at borehole wall of the base model and optimized model under the three stress regime.

Model	Numerical Errors at Borehole Wall (MPa)			
	$\sigma_{\theta\theta}$ at 0°	σ_{rr} at 0°	$\sigma_{\theta\theta}$ at 90°	σ_{rr} at 90°
Base				
NF	-1.17	3.38	-6.42	2.36
SS	0.43	5.07	-10.93	2.87
RF	-5.65	6.14	-10.78	4.77
Optimized				
NF	-0.13	0.06	-0.25	0.38
SS	-0.12	-0.05	-0.38	0.65
RF	-0.25	0.20	-0.45	0.63

Table 23. Predicted safe mud weight window using the Mohr Coulomb failure criterion.

Stress Regime	Safe Mud Weight Window (s.g.) Analytical	Base	Optimized
NF	1.26 – 1.55	1.09 – 1.49	1.24 – 1.54
SS	1.76 – 1.83	1.52 – 1.85	1.73 – 1.82

RF	1.99 – 4.19	1.68 – 4.01	1.96 – 4.18

Predicting the safe mud weight window from the modeled results shows that the collapse pressure gradient and the breakdown pressure gradient for the optimized model have a maximum error of -0.03 specific gravity (s.g.) or -0.25 ppg. This error is within the practical limits of mud weight density control.

However, if the safe mud weight window for the base (non-optimized) model is predicted (for all three stress regimes), the errors become significant. For the collapse pressure gradient the model yields a much lower collapse pressure compared to the analytical solution. With errors of -0.17, -0.24, and -0.31 s.g. (or 1.4, 2.0, and 2.6 ppg) for NF, SS, and RF regimes, respectively, this would lead to an over-optimistic prediction for the mud weight. If this error was neglected mud weights causing borehole breakouts might be chosen.

This is most noticeable for the strike-slip regime where vertical wells represent the least stable well direction. For the example case the analytical solution shows that the safe mud weight window is very narrow (1.76 to 1.83 s.g. or 14.67 to 15.23 ppg), while the non-optimized model results predict a mud weight window of 1.57 to 1.85 s.g. or 13.05 to 15.43 ppg. This clearly overestimates the range of actual applicable mud weights and a stable borehole cannot be guaranteed.

The breakdown pressure is determined by the hoop stress at 0°. Though the base model only yields an error of 0.02 s.g. of the breakdown pressure gradient in the slip-strike stress regime, the breakdown pressure for the normal faulting and reverse faulting regime shows significant errors of -0.06 and -0.18 s.g. (or 0.5 and 1.5 ppg), respectively. Such errors are of less importance for the reverse faulting regime because the safe mud weight window is rather wide. However, for hydraulic fracturing applications the error accounts for an underestimation of 1.5 ppg of the fracture gradient.

Although only the Mohr-Coulomb failure criterion is used in the wellbore stability analysis, this study shows that the choice of boundary conditions and meshing parameters has crucial implications to the applications of wellbore stress analyses.

2.1.7. Conclusions

The use of finite element analysis in geomechanics provides an excellent tool for complex problems where analytical solutions do not exist. For the case of wellbore stress analyses the accuracy of the numerical results at the borehole wall and in its direct vicinity ensures the applicability of these results to wellbore stability, wellbore design, and cementing analyses, as well as hydraulic fracturing processes.

Our study shows that boundary conditions and meshing parameters, i.e. model size, element type and mesh density in the near-wellbore region, have a significant influence on the accuracy of results and if not appropriately chosen, the effective stresses in the near-wellbore region show significant errors (as high as 11 MPa) when compared to the analytical solution. This misfit shows the inherent need to conduct a mesh optimization for numerical wellbore stress analyses to minimize the errors. For 2D wellbore stress analyses, displacement boundary conditions provide the best fit to the analytical solution for both the near-wellbore region and the far-field. The use of 2nd order quadrilateral elements and a relatively fine mesh in the near-wellbore region are of first priority to obtain accurate results. Further, the overall model size has to be chosen carefully.

With the meshing guideline presented in this study, a good match to the analytical solution throughout the model can be obtained and the error at the borehole wall and in the near-wellbore region can be minimized. It is expected that this general modeling technique also applies to more complex models. If discretization parameters are not optimized, the modeled results are of question and the subsequent analysis should not be relied on.

This conclusion becomes evident for the case of an exemplary wellbore stability analysis in this study. Predicted safe mud weight windows from a non-optimized model for three different stress regimes show differences of up to -0.24 s.g. or 2.6 ppg compared to the analytical solution. For the cases presented this may specifically lead to a significant misinterpretation of the minimum usable mud weight and borehole collapse may result.

2.2. Wellbore Stability Analysis

2.2.1. Pressure Window

The pressure window used for this analysis consists of three unique curves. The first of these curves is the pore pressure. Pore pressure is the pressure exerted by trapped water molecules in the pores of the rock. For the purposes of this study the pore pressure is considered to be hydrostatic and is calculated using the following equation:

$$p_p = \int_0^z \rho_w g d_z \tag{16}$$

where ρ_w is the density of water; g is the acceleration due to gravity; and z is the depth of interest.

The other two curves used to define the pressure window are the collapse pressure (shear failure) and the fracture gradient (tensile failure). The collapse pressure is the minimum pressure which must be maintained in the wellbore before the onset of borehole collapse. It is reached when the hoop stress reaches the compressive strength of the rock. The collapse pressure is determined by using a Mohr-Coulomb failure criterion and the assumption that the mean stress is constant at any one point in the wellbore. The fracture gradient is the maximum pressure which can be sustained in the wellbore before the surrounding rock begins to undergo tensile failure (fractures). Tensile failure occurs when the hoop stress in the wellbore is less than the tensile strength of the rock. Both types of failure can be detrimental to the drilling of a well so a thorough knowledge of the pressure window is important.

2.2.2. Vertical Wellbores

The reservoir scale Finite Element Model (FEM) has been used to determine the placement of three vertical wellbores for the different stress regimes. The wellbores in question were placed at the crest of the anticline, the base of the anticline, and the limb of the anticline (Figure 76).

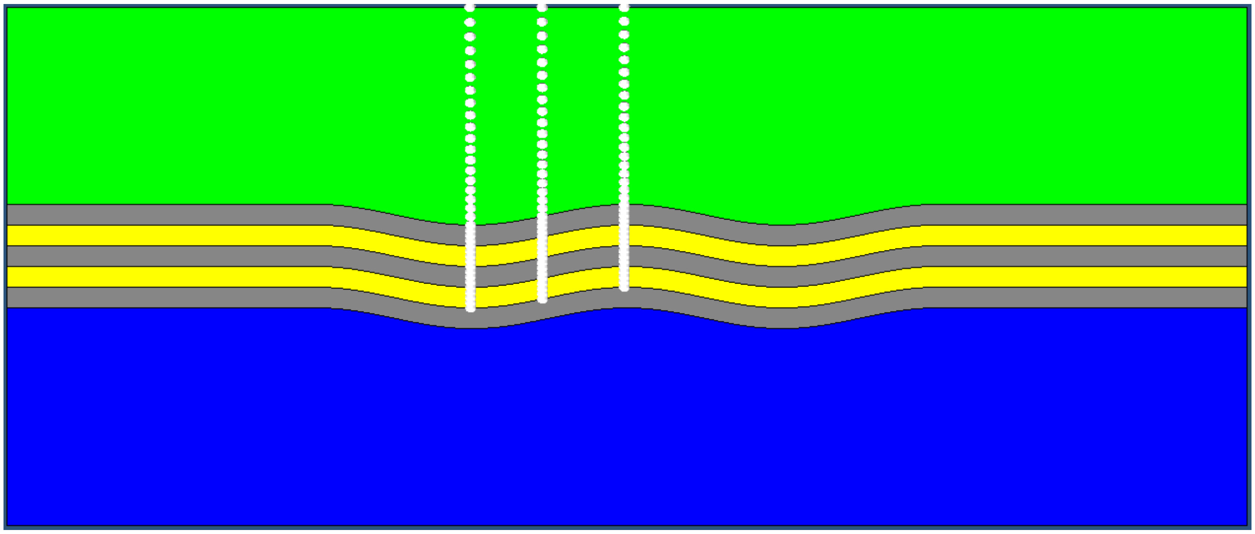

Figure 76: 3D Vertical Well locations (cross sectional view).

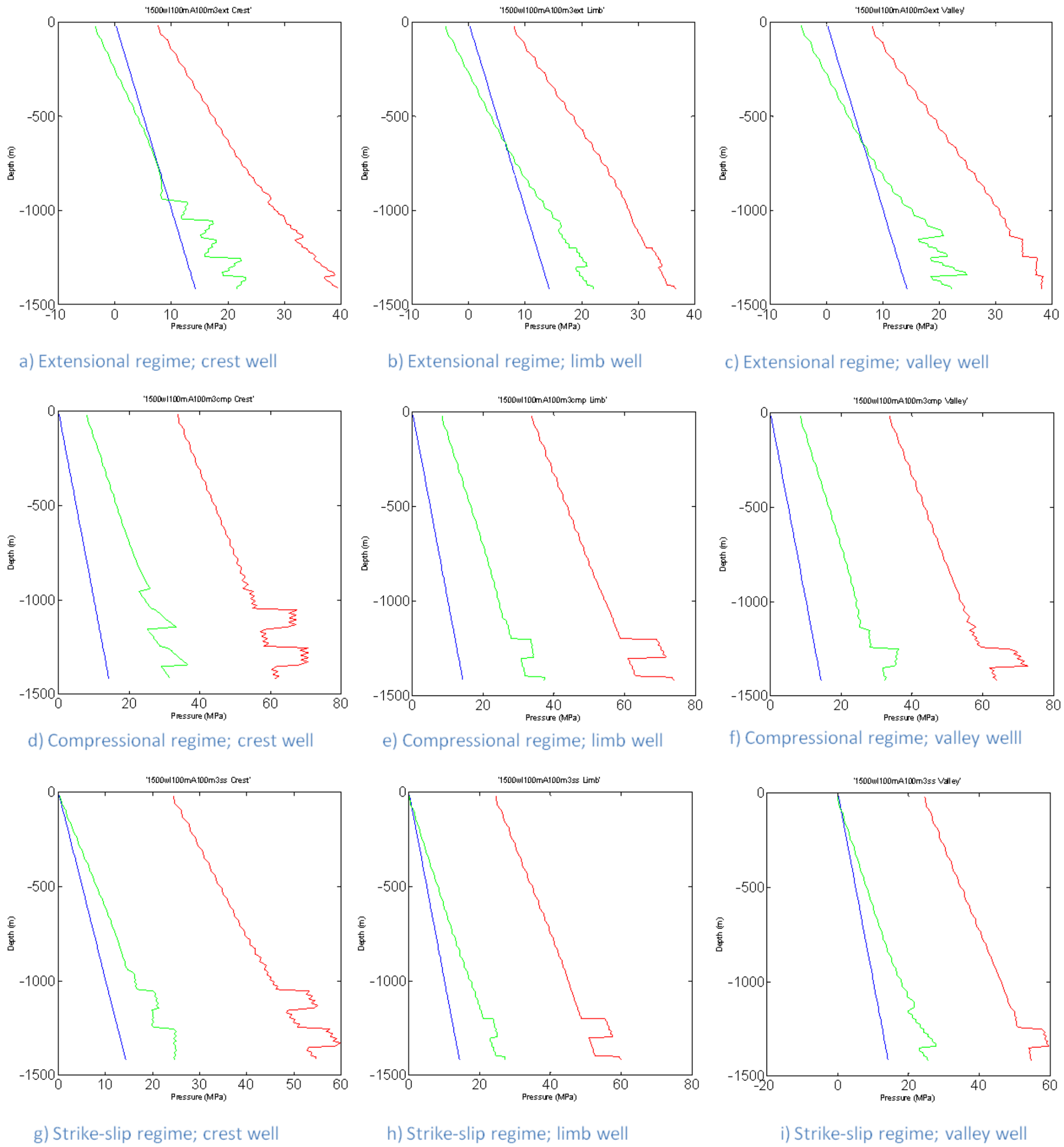

a) Extensional regime; crest well
b) Extensional regime; limb well
c) Extensional regime; valley well
d) Compressional regime; crest well
e) Compressional regime; limb well
f) Compressional regime; valley welll
g) Strike-slip regime; crest well
h) Strike-slip regime; limb well
i) Strike-slip regime; valley well

Figure 77: Mud pressure windows for vertical well locatoions for the various stress regimes.

Data is extracted at each node along this path and is then used to calculate a pressure window based on the Mohr-Coulomb failure criterion. The red line in Figures 77a-i represents the fracture pressure, the green line the collapse pressure and the blue line the pore pressure. Figures 77a, 77b, and 77c show the pressure windows of each vertical wellbore location (i.e. limb, crest and synform of the anticline structure) for the extensional stress regime. For each wellbore the pressure window exhibits the same general shape, with only slight deviation when entering the reservoir layer. For this regime the pressures at the bottom of the wellbore differ by about 10MPa.

Figures 77d, 77e, and 77f show the pressure windows of each wellbore for the compressional stress regime. In general the compressional regime shows a much larger mud window compared to the extensional models.

Figures 77g, 77h, and 77i show the pressure windows of each wellbore for the strike-slip stress regime. The pressure window is similar to the compressional regime, however at the crest location the strike sip stress regime shows the overall widest pressure window.

As an initial conclusion vertical wells are safe to drill for the generic anticline models. However to provide more general wellbore stability criteria applicable for more complex scenarios deviated wellbores of type I & II wells are additionally investigated. Type I inclined wellbores become relevant as the trajectory has an increased surface area with the injection layer thus increasing infectivity. A more detailed description and the numerics of these well types are given in Appendix 2.

2.2.3. Deviated Wellbores

A deviated wellbore is any wellbore which does not lie entirely along the vertical axis [2]. Deviated wellbores are defined by an angle of inclination (i) and an azimuthal angle (α) (Figure 78). The angle of inclination is the deviation of the wellbore from the vertical axis and ranges from 0^o-90^o. The azimuthal angle is the direction of the borehole axis with respect to north. The azimuth ranges from 0^o-360^o where 0^o is north and the angle increases clockwise [7, 9].

Two unique types of well profiles will be tested in this study (Figure 79). A Type I well profile consists of a vertical well section that extends downwards from surface until it reaches the kickoff point [KOP]. Once the KOP is achieved the well enters a build section until the final inclination angle is achieved. The well then holds this angle until it reaches the target. A Type II well profile consists of a vertical section down to the KOP. After the KOP is reached the well extends into a build section until it reaches the desired inclination angle. Once the desired inclination angle is obtained, the angle will be held until the well reaches a desired length. At this length, the well enters a drop section (drop off point; DOP) until it reaches the reservoir or another hold section.

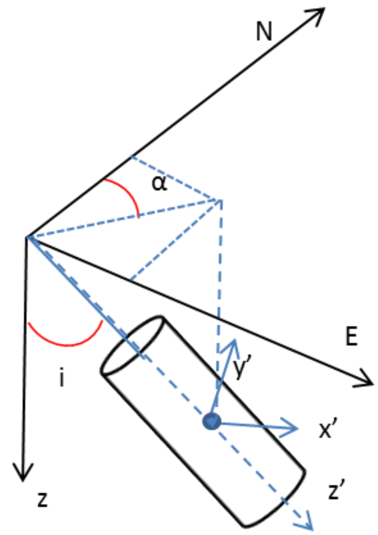

Figure 78. Orientation of wellbore coordinate system. The azimuth is measured from North toward the East, and the angle of inclination is measured from the vertical to the new wellbore axis.

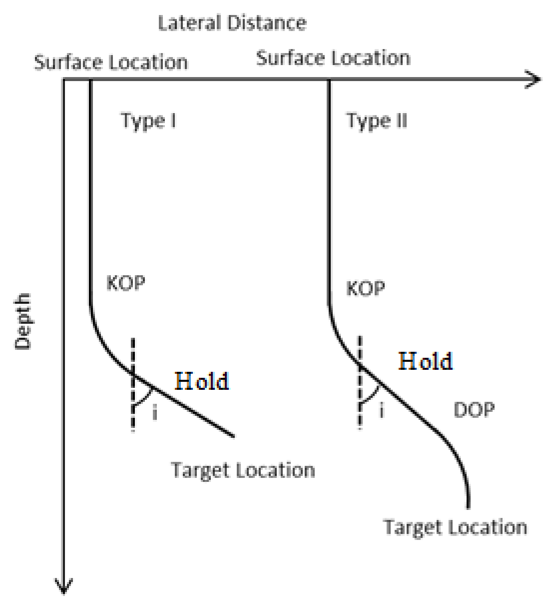

Figure 79. Graphic representation of Type I and Type II well profiles showing KOPs, DOPs, surface locations, target locations and inclination angles (i). When the inclination angle is constant, the well is in a hold.

2.2.4. Wellbore Stresses for Arbitrary Well Orientations

The drilling process results in a redistribution of the stresses and local stress concentrations result in the close vicinity of the wellbore. The equations describing the radial and tangential (hoop) stress distribution for a vertical well were initially derived by Kirsch [19] and extended to include pore pressure and pressure in the wellbore by Zhang et al. [20]. In order to resolve the borehole state of stress for an arbitrarily oriented wellbore it is convenient to define a coordinate system (x', y', z') using inclination and azimuth for a certain point along the well path. In the new coordinate system the z' axis coincides with the wellbore axis, the x' axis acts toward the bottom side of the wellbore, and the y' axis acts horizontally in the plane perpendicular to the wellbore axis (Figure 78).Using this coordinate system the stress tensor (eq. 17) can be transformed using the following transformation matrix [13]:

$$\mathbf{D} = \begin{bmatrix} -\cos(\alpha)\cos(i) & -\sin(\alpha)\cos(i) & \sin(i) \\ \sin(\alpha) & -\cos(\alpha) & 0 \\ \cos(\alpha)\sin(i) & \sin(\alpha)\sin(i) & \cos(i) \end{bmatrix} \tag{17}$$

In order to obtain the stress tensor for the new coordinate system the following operation must be performed [13]:

$$\sigma'_w = D\sigma'_{ij}D^T = \begin{bmatrix} \sigma_{x'x'} & \sigma_{x'y'} & \sigma_{x'z'} \\ \sigma_{x'y'} & \sigma_{y'y'} & \sigma_{y'z'} \\ \sigma_{x'z'} & \sigma_{y'z'} & \sigma_{z'z'} \end{bmatrix} \tag{18}$$

where σ_w is the wellbore stress tensor and D^T is the transpose of the transformation matrix.

From the new wellbore stress tensor (σ_w) the effective stresses at the wellbore wall can be calculated.

$$\sigma'_{\theta\theta} = \sigma_{z'z'} - 2(\sigma_{x'x'} - \sigma_{y'y'})\cos 2\theta + 4\sigma_{x'y'}\sin 2\theta - \Delta P \tag{19}$$

$$\sigma'_{rr} = \Delta P \tag{20}$$

$$\sigma'_{zz} = \sigma_{z'z'} - 2v(\sigma_{x'x'} - \sigma_{y'y'})\cos 2\theta + 4v\sigma_{x'y'}\sin 2\theta \tag{21}$$

$$\tau'_{\theta z} = 2(\sigma_{y'z'}\cos\theta - \sigma_{x'z'}\sin\theta) \tag{22}$$

where $\sigma'_{\theta\theta}$ is the effective hoop stress, θ is the angle around the wellbore, ΔP is the difference between pore pressure and the mud pressure, σ'_{rr} is the effective radial stress, and υ is the Poisson's ratio.

From equations 19-22 the principal stresses around the wellbore can be calculated:

$$\sigma'_{tmax} = \frac{1}{2}[\sigma_{zz} + \sigma_{\theta\theta} + \sqrt{(\sigma_{\theta\theta} - \sigma_{zz})^2 + 4\tau_{\theta z}^2}] \tag{23}$$

$$\sigma'_{tmin} = \frac{1}{2}[\sigma_{zz} + \sigma_{\theta\theta} - \sqrt{(\sigma_{\theta\theta} - \sigma_{zz})^2 + 4\tau_{\theta z}^2}] \tag{24}$$

$$\sigma'_{rr} = \Delta P \tag{25}$$

2.2.5. Wellbore Stability Analysis: Setup

The previously described 3D Finite Element Model (FEM) has been used to plan the placement of a group of Type I deviated wellbores. The wells are placed in a circular pattern with an angle of 30^o separating each of the wells. Figure 80 below shows the layout of these wells. The purpose of this group of wells is to determine which well would provide the most stable conditions (i.e. best mud weight window for all sections) based on the stress information from the FEM. If the best drilling location can be identified using FEMs as a pre-drilling risk assessment tool, significant amounts of money and time could be saved. Initially for this wellbore trajectory optimization procedure the extensional stress regime model with a reservoir thickness of a 100m and a inter-bedding coefficient of friction of μ=0.3 is chosen.

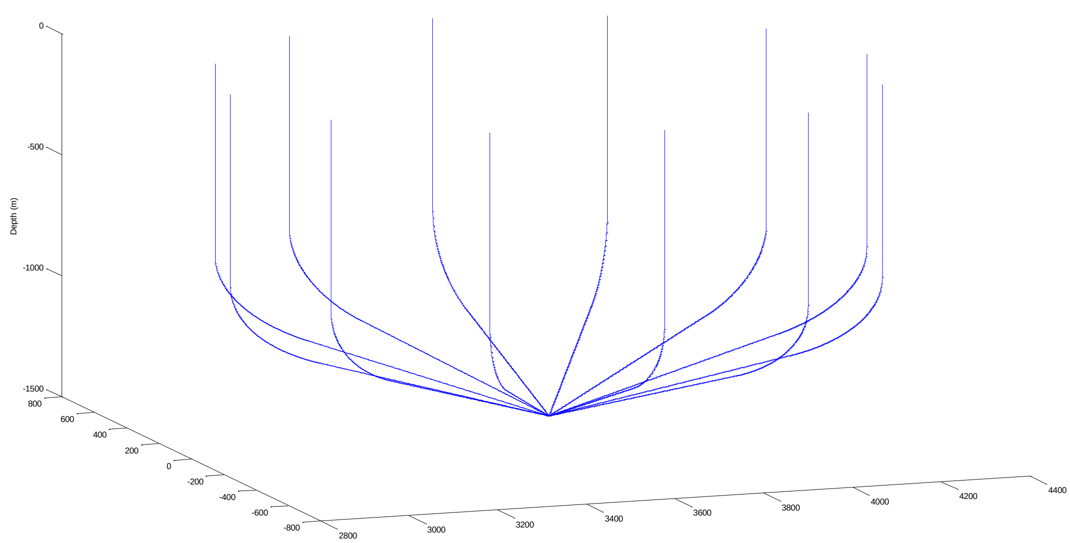

Figure 80: Circular Group of wells created for processing.

For the stress extraction routine along the well path a MATLABTM script is written to perform all calculations required to process all of the data from the FEM. The first calculations in the file construct the path of one well, which can then be translated in order to form the other wells in the group. For this current project, the well created has a true vertical depth of 1415m, a kick off point at a depth of 800m, a build-up rate of 15^o/100m, and a horizontal distance traveled of

718m. All of the other wells have the same initial data as this well, but are shifted 30° from one another (Figure 80). Once all of the wells are created, the file will then use the coordinate and stress data and extract a cylinder of data which encompasses all of the wells; i.e. all stress data not containing a well path is discarded. This step is necessary to significantly cut down computation time. Figure x shows the created smoothed well paths (blue) and the matched data wells (red). It should be noted here that the angle for the well deviation is taken from the smooth trajectory (Figure 81, blue line) and the stress input is taken from the nearest node (Figure 81, red line). By having new wells which have the exact coordinates as nodes in our model, we are then able to export all of the stress data at those coordinates for post processing.

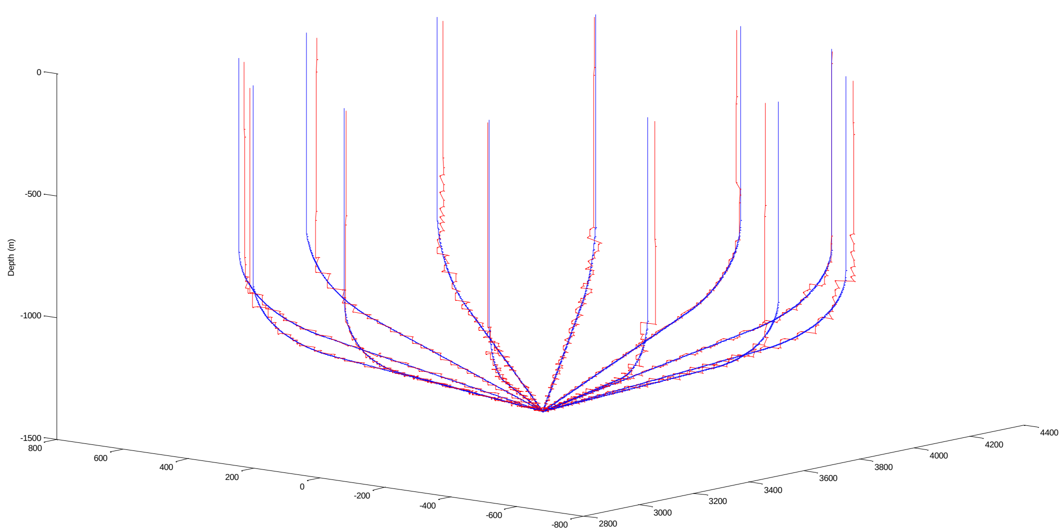

Figure 81: Both created and matched data wells.

Extracting all of the stress tensors at each node of our well from the FEM, we then use the previously reported method of stress transformation to transform the stress tensors from the geographic system to the system of each of our wellbores. A difference is made concerning the definition of the azimuth used. For this portion of the projected, we have defined the azimuth to be the angle of the well measured clockwise from geographic North. The figure below shows how the azimuth has been defined.

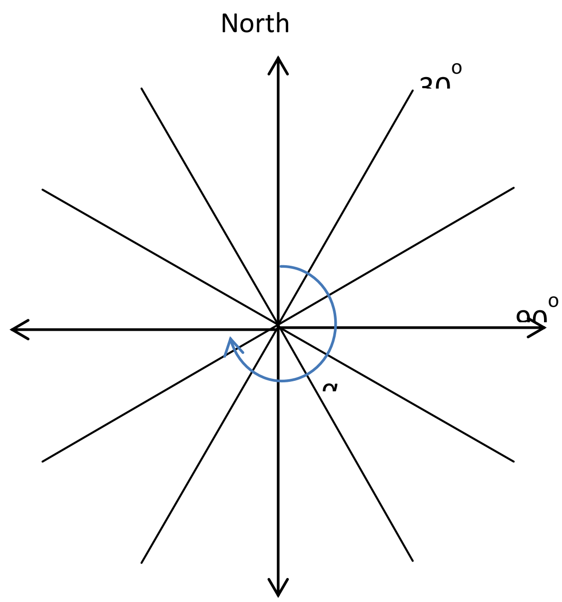

Figure 82: Definition of azimuth.

With all of the stress tensors and coordinate data, mud weight windows can be constructed for each of the wells.

The reservoir scale 3D Finite Element Models [FEM] have been used as the geometry for the placement of a group of Type I deviated wellbores. Based on the respective state of stress optimal drilling trajectories need to be found to ensure stable wellbore conditions for the CO2 injection phase. Conventional wellbore stability predictions and assessment is based on the assumption that the vertical and horizontal stresses are principal stresses. Once these stresses are determined and estimated for a well path, stereographic projection plots are used to determine the well orientation (azimuth and inclination) which provides the optimal conditions for wellbore stability (i.e. optimal mud weight window conditions; Zoback, 2007). The disadvantage of these methods is that only specific depths are considered and based on these locations an optimal drilling direction is proposed. The anticline models of this study in contrast show that vertical and horizontal stresses are not principal stresses at all locations within the model. Therefore wellbore trajectories have to be based on the full stress tensor data in complex geologic geometries. The full stress tensor can be readily supplied by the finite element models used in this study. The extraction of the stress tensor at a proposed well trajectory enables to assess wellbore stability for the entire well path.

In order to determine and assess the most stable well trajectory for the anticline geometries in this study, the proposed wells were placed in a circular pattern with an angle of 30^{o} separating each of the wells. Table 24 shows the input data which was used to create the 15 well paths. This study is independent of well inclination changes. The procedure to create the wells was given in the progress report for quarter 3. Figure 81 above shows the layout of these wells (blue) and the matched data from the model (red). The purpose of defining a circle of wells is to determine which well represents the most stable conditions within the respective state of stress.

2.2.6. Wellbore Stability Analysis: Model Validation

A simplified FEM has been setup to validate and verify the wellbore trajectory calculation and pressure window calculation procedure. The model is a simple block model which was used to perform a statistical analysis of the MATLABTM script file. The purpose of the analysis is to compare the stresses and mud pressures calculated for the wellbore trajectories to the analytical solution. The model setup is shown below in Figure 83. This model is in a simple all sandstone block in an extensional stress regime where the vertical stress is the maximum principal stress and the two horizontal stresses are equal in magnitude and are the intermediate and minimum principal stresses. For this model the pore pressure is hydrostatic. Two well paths, one vertical and one with an inclination of 45 degrees from horizontal, were created in order to perform the analysis. The values used in the analysis of these wells are in Table 24 below.

Table 24. Input data for the validation model vertical and deviated well path.

Model Data for Vertical Well										
Solution Type	Depth (m)	S11 (Mpa)	S22 (Mpa)	S33 (Mpa)	S12 (Mpa)	S13 (Mpa)	S23 (Mpa)	Pp (Mpa)	Azimuth (°)	Inclination (°)
Analytical	2500	40.29	40.29	61.31	0	0	0	24.53	0	0
MATLAB	2490	40.14	40.14	61.08	~0	~0	~0	24.44	0	0
Model Data for Deviated Well										
Solution Type	Depth (m)	S11 (Mpa)	S22 (Mpa)	S33 (Mpa)	S12 (Mpa)	S13 (Mpa)	S23 (Mpa)	Pp (Mpa)	Azimuth (°)	Inclination (°)
Analytical	2500	40.29	40.29	61.31	0	0	0	24.53	30	45
MATLAB	2490	40.14	40.14	61.08	~0	~0	~0	24.44	30	44.99

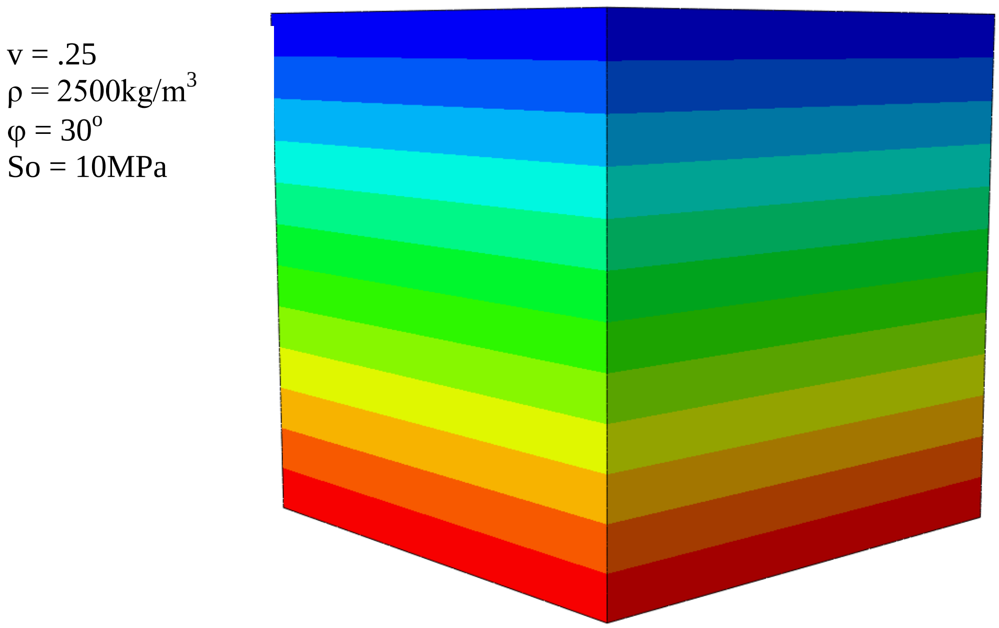

Figure 83. Validation model setup and rock strength parameters.

The results from the statistical analysis of the validation model are shown below in Table 25. These results show that the results from the analytical solution and the results from the FEM are in a good agreement. In both cases the percent of error introduced is under one percent, which shows that the results obtained through these methods are accurate and comparable to the analytical solution. A larger amount of error may be encountered in models where the element density is not high enough to obtain close matches of the experimental well path. The percent of error is also higher in the deviated well due to the addition of the stress transformation from the geographic coordinate system to the borehole coordinate system, but still less than 1%.

Table 25. Results of the Statistical analysis of Model 1.

Model Data for Vertical Well								
Results					Statistics			
Solution Type	$S_{\theta\theta}'$ (MPa)	S_{rr}' (MPa)	Pmin (MPa)	Pmax (MPa)	% Error $S_{\theta\theta}'$	% Error S_{rr}'	% Error Pmin	% Error Pmax
Analytical	31.4	8.39	32.92	61.00	0.00	0.24	0.03	0.25
MATLAB	31.4	8.37	32.81	60.85				
Model Data for Deviated Well								
Results					Statistics			
Solution Type	$S_{\theta\theta}'$ (MPa)	S_{rr}' (MPa)	Pmin (MPa)	Pmax (MPa)	% Error $S_{\theta\theta}'$	% Error S_{rr}'	% Error Pmin	% Error Pmax
Analytical	21.02	14.97	39.5	50.55	0.19	0.27	0.03	0.34
MATLAB	20.98	15.01	39.61	50.38				

2.2.7. Wellbore Stability Analysis: Stress Regimes

For the wellbore stability analysis of the generic anticline structure three different stress regimes have been investigated: extensional [Model 2], compressional [Model 3], and strike-slip [Model 4]. In each of these models 15 well locations were created and analyzed. The geometry and rock parameters used in Models 2, 3, 4, 5, and 6 are shown in Figure 4. Models 2, 3, and 4 were all created with a coefficient of friction of 0.3 on the rock contact surfaces.

Two additional models were created in order to test the influence of inter-bedding friction in the pressure windows. Each of these models was created using the same anticline geometry as models 2, 3, and 4, but the only stress regime which was tested was the compressional regime. The coefficients of friction were tested are 0.1 [Model 5] and 0.8 [Model 6].

2.2.7.1. Extensional Stress Regime

The 15 pressure windows which were created from Model 2 are compiled in Appendix 3.1. By using the pressure windows and the knowledge of the intermediate principal stress direction, the optimal drilling directions can be determined for this model. The intermediate principal stress direction is usually the least safe drilling direction because the differential stress is the largest. Figure 84 below shows a visualization of the intermediate stress direction for Model 2.

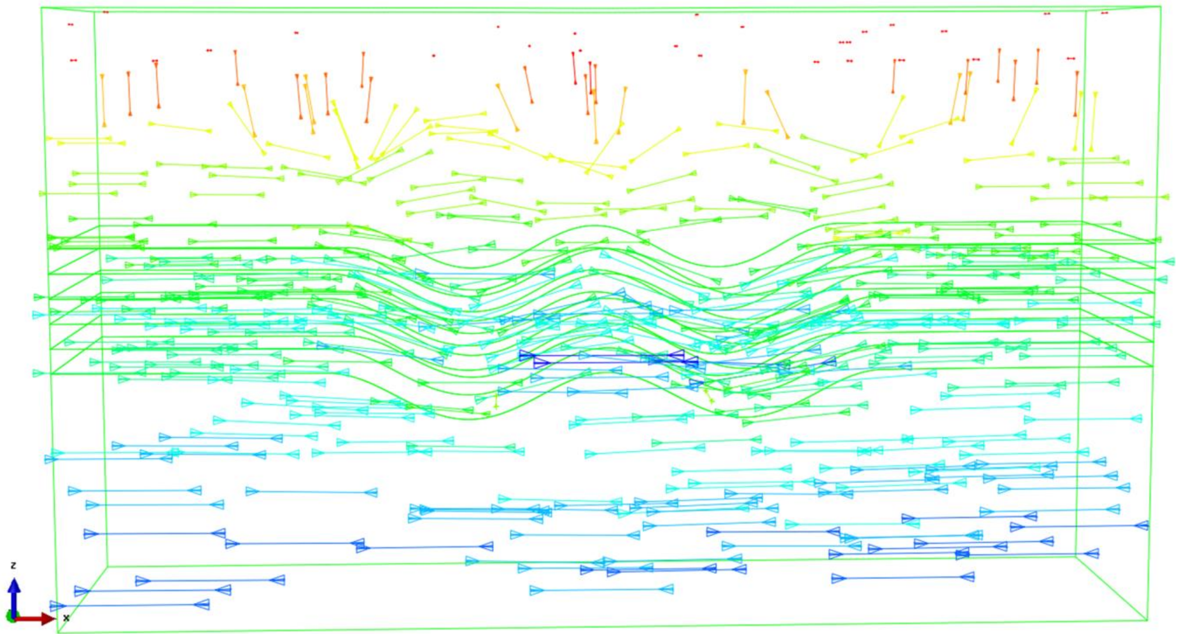

Figure 84. Intermediate stress direction in Model 2.

From Figure 84 the least safe drilling direction in this stress regime is highly influenced by the geometry and boundary conditions. At the surface of the model the least safe direction is on the y axis, but then changes to the vertical direction after about 100m. The least safe direction at the reservoir would be a completely horizontal well along the x axis. The same trends can be seen from the figures in Appendix 3. The smallest sections of the pressure windows are at the surface where the pore pressure has become the minimum safe mud weight for drilling. If the windows are examined as a whole, with the target as the main point of interest, it can be seen that as the azimuthal angle approaches either 90 or 270 degrees the pressure window narrows more than it does at other angles. By inspection it can be seen that as the azimuthal angle approaches angles of either 0 or 180 degrees the pressure window gets wider. Figure 85a below shows the pressure window at an azimuth of 0 degrees, while Figure 85b shows the pressure window at an azimuth of 90 degrees. In all of the pressure window figures given in this report the blue line is pore pressure, the green line is the collapse pressure, and the red line is the fracture gradient.

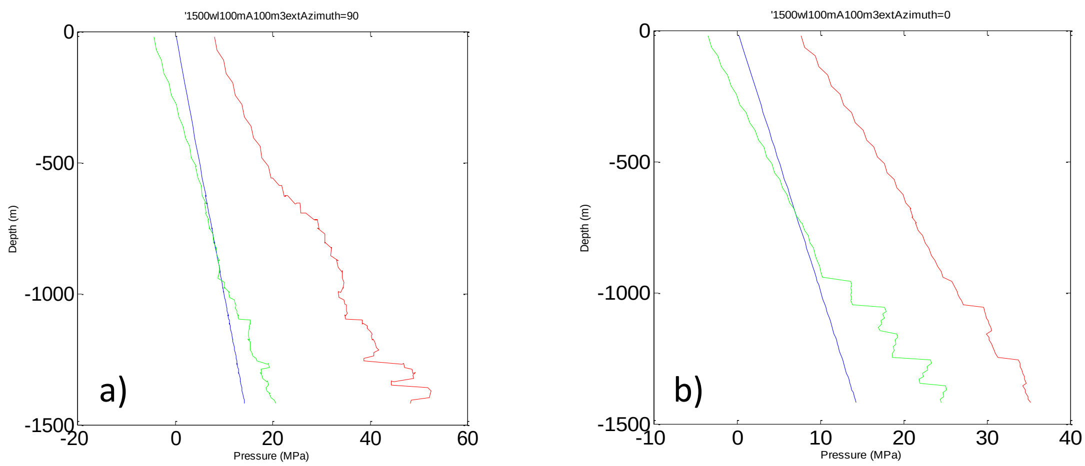

Figure 85: Pressure window for Azimuth = $0^o$and 90^o.

Figure 85a represents the best and Figure 85b the least favorable drilling directions for Model 2. The pressure window at 0 degrees is wider and at a steeper angle, which will lessen the amount of casing points needed. It should be noted that both wells can be drilled safely, however the costs associated to casing will be different. The minimum casing points which a well at 0 degrees could be safely drilled with is 2, while it would take at least 3 if not 4 casing points to drill a well at an azimuth of 90 degrees. If drilling were to be done in this Model the best direction would either be at 0 or 180 degrees, but there may still be slight drilling problems near the surface where all of the wells would be vertical and would be being drilled in least safe drilling direction. Wells drilled in directions of 90 or 270 degrees should be avoided in this Model.

2.2.7.2.Compressional Stress Regime

The resulting pressure windows for Model 3 have been compiled in Appendix 3.2. Figure 86 below shows the intermediate principal stress direction for Model 3 which does not change throughout the length of the wells which are used in this analysis. The intermediate stress direction is at a constant path along the y axis until the base layer of the model where the stress is along the z axis.

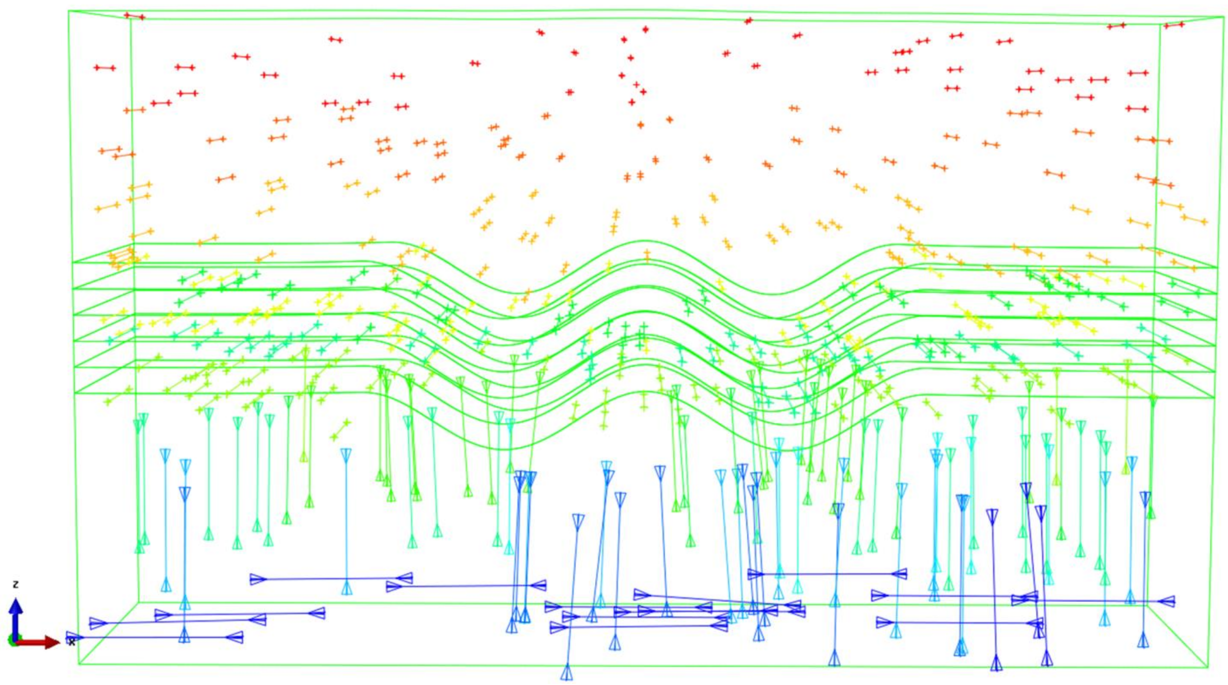

Figure 86. Intermediate principal stress direction for Model 3.

For Model 3 the vertical stress is not the intermediate stress near the surface or in the reservoir, therefore vertical wells and the vertical portion of deviated wells are much safer than they were in Model 2. The pore pressure does never become the minimum pressure for safe drilling. All of the pressure windows for this model are relatively safe and the slope of the pressure lines indicates that all wells could potentially be drilled with only 1 or 2 casing points.

By inspection of figures B1-B15 in Appendix 3 it can be seen that wells with an azimuth of 0 or 180 degrees, while still representing stable drilling conditions) represent the least favorable drilling orientations. The fracture gradient in these wells narrows significantly towards the collapse pressure causing a much smaller pressure window. As the well paths azimuths move closer to 90 and 270 degrees the fracture gradient increases causing a larger pressure window and a safer drilling scenario. If drilling a well in this Model, the azimuths of 90 and 270 degrees would be the preferred well orientation. The extra space in the pressure window allows for easier drilling, and these wells could be drilled with fewer casing points as opposed to wells drilled along the other azimuths.

Figure 86a shows the pressure window for a well drilled along an azimuth of 0 degrees, while Figure 86b shows the pressure window for a well drilled along an azimuth of 90 degrees. From these figures it can be seen that the well with an azimuth of 0 degrees represents the more favorable drilling direction.

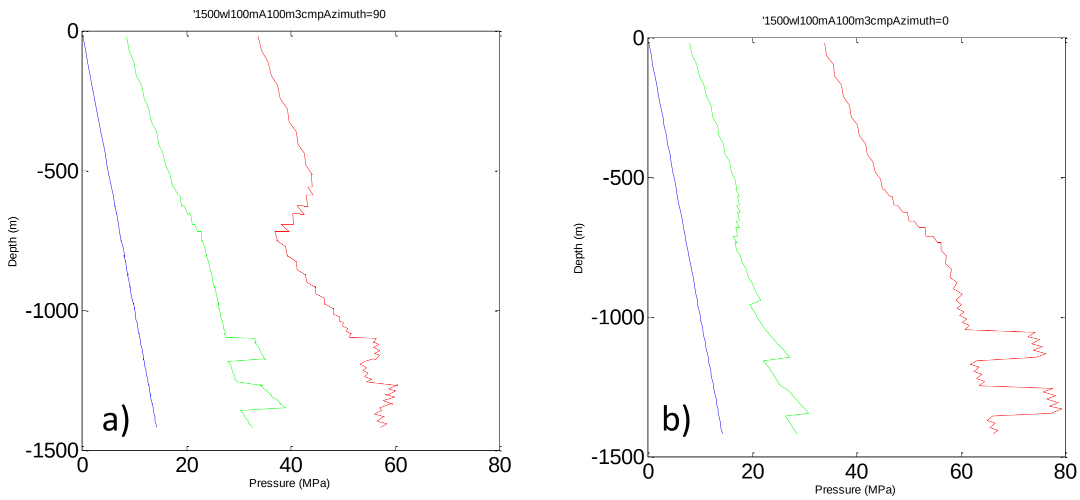

Figure 86. Model 3 Pressure Window for Azimuth = 0^o and 90^o.

2.2.7.3.Strike-Slip Regime

The pressure window figures for Model 4 are displayed in Appendix 3.3. Figure 87 below shows the intermediate principal stress direction for this Model. The intermediate principal stress for this Model is similar to the intermediate principal stress direction from Model 3. A strike slip regime for the whole model would result in an intermediate stress direction in the vertical direction, but the boundary conditions were set up, such that the strike-slip stress regime is occurring only in the reservoir layer. Above the reservoir layer, the stress regime is compressional. Figure 87 shows the vertical direction to be the intermediate principal stress direction in the reservoir layer, and in most of the area surrounding the reservoir layer.

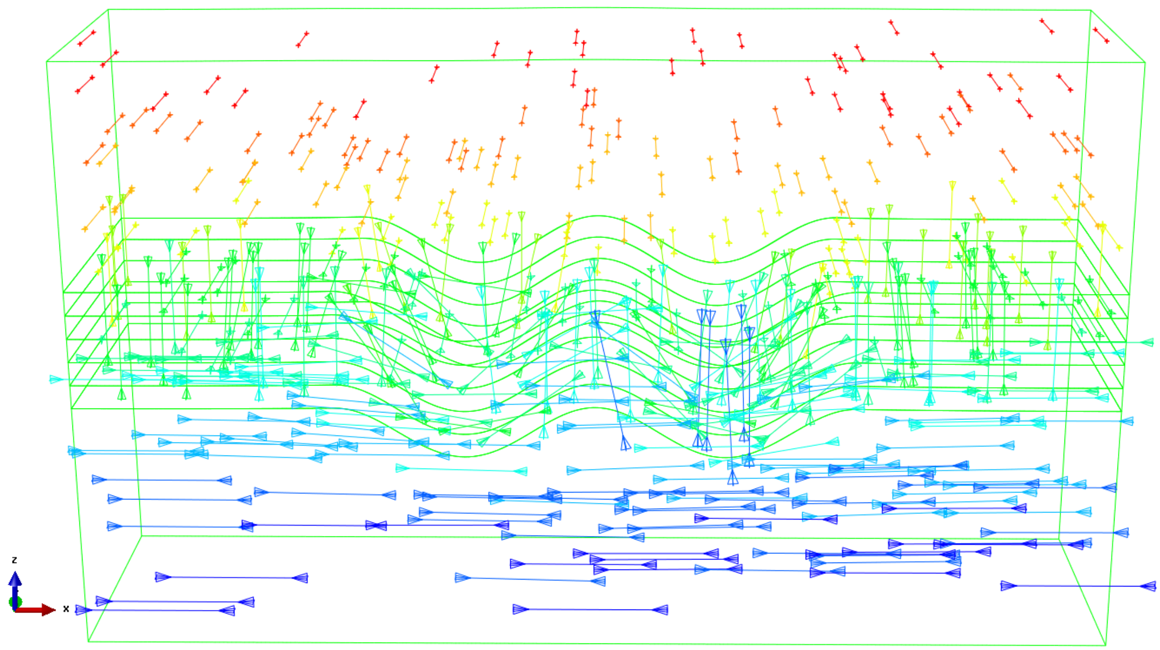

Figure 87. Intermediate principal stress direction for Model 4.

Comparing the 3 different stress regimes, the strike-slip regime for Model4 shows the least influence by the intermediate principal stress direction changes. The stress direction changes in this model only cause a change of 1-2MPa in the pressure windows. It still does hold true that the narrowest pressure windows are at azimuths of 0 and 180 degrees which is the intermediate principal stress direction. However, because the change is so slight the inferred differences for preferred drilling conditions are minute. For this model it may even be most appropriate to drill a vertical well through the crest of the reservoir section. In any pure strike-slip model this would most likely not be true because the vertical direction should be the least favorable to drill. Figure 88a shows the pressure window for a well drilled with an azimuth of 0 degrees, and Figure 88b shows the pressure window for a well drilled with an azimuth of 90 degrees. There is only a very slight difference in these pressure windows caused by the influence of the well azimuth.

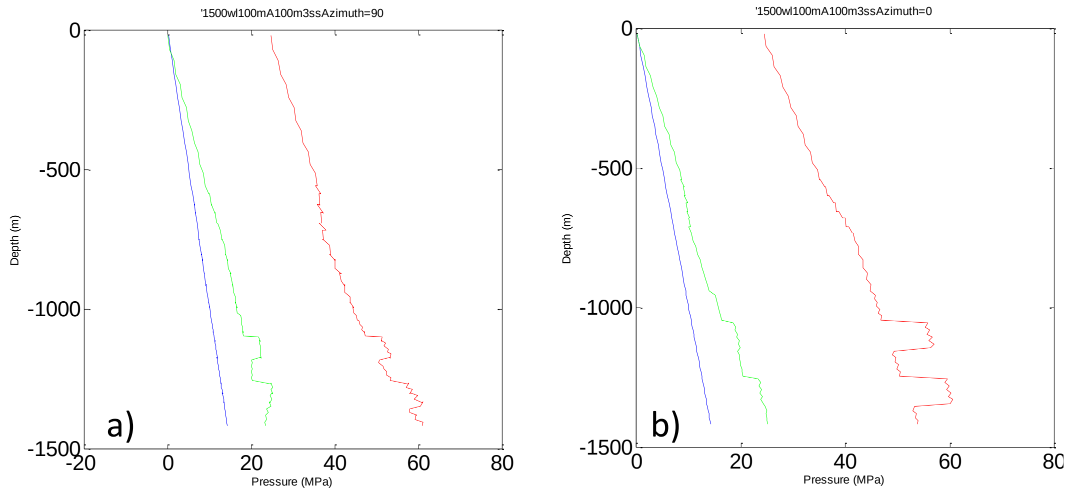

Figure 88. Model 4 Pressure window for Azimuth = 0^o and 90^o.

2.2.7.4.Influence of inter bedding friction

The inter-bedding coefficient of friction shows a significant influence on reservoir rock and cap rock stability. To show the influence of the inter-bedding coefficient of friction on the wellbore stresses and the resulting wellbore pressures the compressional regime for coefficients of friction of 0.1 (Model 6) and 0.8 (Model 7) is investigated. Because the coefficient of friction is only changed between rock layers there is not much of a change in the pressure window except at these locations. Figure 89a shows the pressure window for Model 6 at an azimuth of 0 degrees. Figure 89b shows the pressure window for Model 6 at an azimuth of 90 degrees. These azimuths were chosen because they were the least favorable and safest pressure windows for Model 3 respectively.

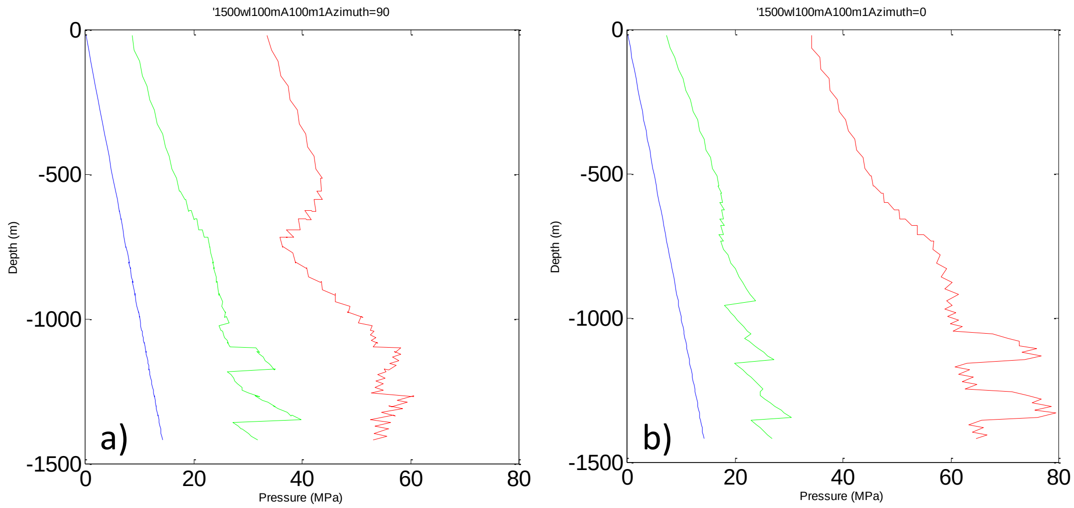

Figure 89. Model 6 Pressure Window for Azimuth = 0^o and 90^o for μ=0.1.

Comparison of Figure 86 with Figure 89 shows that there are only very slight differences due to changing the coefficient of friction to 0.1. The only noticeable change is a slight change in shape of the collapse pressure curve where the sandstone and shale contact layers are located (roughly 1100m – 1400m). Other than this slight shape change there was no difference in the magnitudes of the stresses.

Shown below are Figures 90a and 90b which are the pressure windows for Model 7 at azimuths of 0 and 90 degrees respectively. There are some changes at the sandstone shale interfaces, but the changes are not as noticeable as they are in Model 6. From Models 6 and 7 it can be concluded that the coefficient of friction between rock surfaces has a greater impact for low coefficients than for higher coefficients.

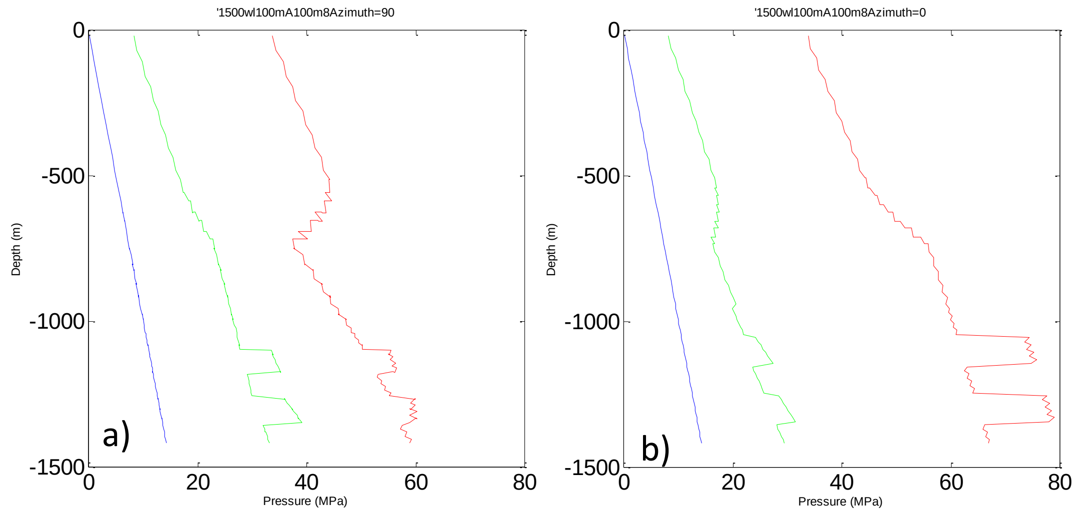

Figure 90. Model 7 Pressure Window for Azimuth = 0^o and 90^o.

2.2.8. Conclusions

The results for the wellbore stability analysis have shown that while vertical wells have proven to be stable for all three stress regimes, a procedure has been developed that can be readily applied to prospective case studies with more complex material models and geometries. The procedure provides accurate results as proven by the validation model.

The procedure developed provides mud pressure window calculation for inclined wellbores of type I wells. These wellbore types, especially type I wellbores with a horizontal hold section, are relevant for CO_2 sequestration applications, as horizontal wells have an increased surface area inside the reservoir and thus feature increased injectivity. As predicted by Kirsch's analytical solution the in-situ stress regime has significant impact on stable drilling directions, whereby the direction of the intermediate principal stress represents the least stable direction. This procedure developed becomes of relevance when applied to case studies where the principal stresses are not given by σ_V, and $\sigma_{h,H}$. In order to further improve the resulting wellbore stability analysis a wellbore trajectory optimization procedure is necessary to account for scenarios where the vertical stress is not a principal stress.

2.3. Wellbore Trajectory Optimization

2.3.1. Introduction

Wellbore trajectory planning plays an important role in the development and optimization of any petroleum field. The placement of a wellbore may not only influence the amount of hydrocarbons contacted, but will also influence the ease at which a well is drilled [1, 2], its long-term integrity [2] and affect hydraulic fracture stimulations [3]. With the advent of new drilling techniques, the enhanced accuracy during the drilling process and the ability to drill various types and shapes of wells has resulted in an demand and understanding of wellbore trajectory planning [4, 5, 6]. Stable wellbore conditions with respect to mechanical failure are a function of the geometrical trajectory within the 3D state of stress [1]. Wellbore stability can be predicted by determining safe mud pressures preventing either borehole breakdown or collapse [1, 2, 4, 5, 6, 7, 8, 9]. Thus, a thorough knowledge of the in-situ stresses in the subsurface and how they change during the life of a petroleum field is a crucial input parameter for planning stable wellbores.

Most wellbore trajectory planning studies [1, 2, 3, 8, 9, 10, 11, 12, 13] assume an Andersonian state of stress (ASoS) [14], where one principle stress is vertical; a common observation in the Earth's crust [7, 15]. Implicitly this assumption excludes many scenarios where complex geologic conditions, such as heavily faulted or folded regions, areas subjected to salt dome intrusion, and any shallow regions where unconsolidated rock is encountered, imply that the SoS is not Andersionian and that shear stresses have to be considered [7, 10, 16]. When drilling in regions where the stress tensor may be rapidly changing, an inclination or azimuth change of 5o of the wellbore trajectory may result in a significant change in the stress magnitudes acting on the wellbore wall. Assuming an ASoS also introduces a potentially misleading symmetry between drilling directions. In an ASoS the conditions for the stable mud pressure window in any azimuthal combination, which are 180o offset from each other, will be equal at the same inclination. With the addition of shear stresses this is no longer true.

Another limitation of wellbore trajectory studies is the utilization of stereographic projections to predict the safe mud pressure window [7, 13, 17, 18]. Stereographic projections enable visualization of the full range of effects that inclination and azimuth have on the mud pressure window. Unfortunately, these projection plots are only valid for a specific depth. Rapidly changing stresses with depth could imply different conditions/orientations for a stable wellbore and the overall stability of a wellbore trajectory cannot be studied in a continuous way.

In this paper we present a methodology for wellbore trajectory planning/optimization which implements the complete stress tensor obtained from a numerical mechanical earth model

(MEM). This enables analysis of an arbitrary state of stress and precludes the simplification of assuming an ASoS. Stereographic projections predicting stable wellbore orientations at certain locations (starting at the target location in the reservoir) are used to find a suitable and stable overall wellbore trajectory. The continuous stress data from the numerical model is extracted along that planned well trajectory and the safe mud pressure window can be predicted for well trajectories of different well types. The methodology described in this paper has been applied to stresses extracted from a synthetic MEM of an offshore field in the Gulf of Mexico [GOM] and best-fit wellbore trajectories and mud pressure windows are presented.

2.3.2. Theoretical Background

2.3.2.1. Stress in the Subsurface

At any point in the subsurface the state of stress is described by the stress tensor, σ_{ij}, often assumed to consist of the vertical and two horizontal principal stresses. This so called Andersonian state of stress (ASoS) represents a common observation from stress measurements in the Earth's crust [7, 15]. If complex geologic conditions result in a non-ASoS the stress tensor for effective stresses takes the form of:

$$\boldsymbol{\sigma'}_{ij} = \begin{bmatrix} \sigma_{xx} - Pp & \sigma_{xy} & \sigma_{xz} \\ \sigma_{xy} & \sigma_{yy} - Pp & \sigma_{yz} \\ \sigma_{xz} & \sigma_{yz} & \sigma_{zz} - Pp \end{bmatrix} \quad (26)$$

Based on the stress tensor at any point the state of stress at a borehole of arbitrary orientation can be calculated following equations 18-22 as presented above.

2.3.2.2. Failure Criteria and Safe Mud Pressure

In order to determine the safe mud pressure window, i.e. to determine collapse and breakdown pressure, a combined Griffith-Mohr-Coulomb failure criterion is used. The procedure to calculate breakdown and collapse pressures is described in detail by Lee et al. [21] and is exactly followed here. Calculations of inclination/azimuthal wellbore stability (IAWBS) using stereographic projections are used to calculate mud pressures (either breakdown or collapse) for all combinations of azimuths and inclinations [13].

It should be noted that several studies have shown that the choice of the failure criterion used has a significant influence on the prediction of the safe minimum mud pressures [22, 23, 24]. The Mohr-Coulomb failure criterion is chosen for this study due to its simplicity and slightly more conservative character for predicting the collapse pressure [7, 8]. However, the methodology for wellbore trajectory planning presented in this paper can be applied using any failure criterion and thus investigation of the impact of different failure criterions is beyond the scope of this paper.

For this study the rock properties required to calculate failure are assumed to be constant throughout the volume. Cohesion, So, tensile strength, T_o, friction angle, ø, and Poisson's ratio, ν are given values of 10MPa, 5MPa, 30o, and 0.3 respectively. Clearly this is not the case in a real world situation, where these parameters would change along the well trajectory, just as the stresses are in these illustrative examples.

2.3.3. Application

3D numerical MEMs represent an excellent tool to simulate the state of stress in complex geologic environments [25, 26, 27, 28]. When calibrated against existing stress measurements numerical MEMs are capable of predicting realistic stress magnitudes and provide a continuous 3D data field of the state of stress. This stress field can then be used to determine the optimal well path to a specific target location.

In the approach presented here, the 3D state of stress at a target location for a specific well path is extracted from the numerical MEM and stereographic projections are used at each evaluation location to determine the collapse pressure, P_c, the fracture gradient, P_{bd}, and the pressure difference, $P_{diff}=P_{bd}-P_c$, for all possible combinations of azimuths and inclinations. The optimal angles for azimuth and inclination are determined by the largest pressure difference between breakdown and collapse pressure. In other words, the full range of inclination/azimuthal mud pressure windows is obtained at each location along the proposed well and then collapsed into a single parameter (P_{diff}) that can be optimized for. If the surface location of the drilling rig is fixed (e.g. pad or template based drilling) the following procedure can be used to find optimal well inclinations and KOP locations. If the surface location of the rig is flexible, the procedure can be used to find both optimal drilling azimuths (i.e. surface location) and inclinations.

For the methodology presented here, all stereographic projections contain the P_{diff} data calculated for every combination of azimuth and inclination. The stereographic projections display each data point on a polar plot with the azimuth being the angle around the circle (0^o being North and increasing toward the East), and inclinations plotted as concentric circles of varying radii.

Locations with larger P_{diff} values have wider mud pressure windows, and are assumed to define safer drilling directions.

2.3.3.1.Surface Location Fixed

For situations where the surface location is fixed, the azimuth and the lateral distance of the well are also pre-determined. Based on the state of stress at the target location optimal drilling inclinations for the well path approaching the target location can be found. The lateral length of the well then determines whether a Type I or Type II well is considered (Figure 91). If the angle α in Figure 91 is smaller than the optimal angle to enter the target location a Type II well is chosen. If the angle α in Figure 3 is larger than the optimal angle, a Type I well is chosen.

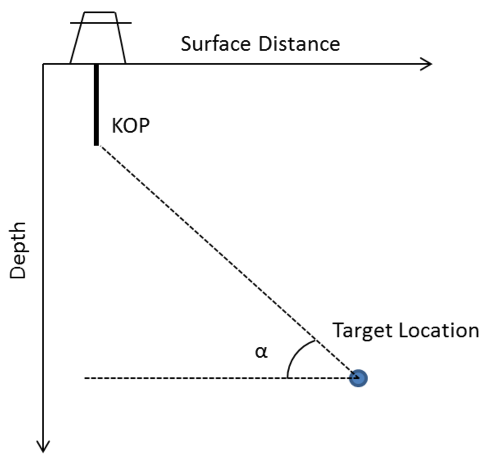

Figure 91. Graphical depiction of the angle α.

For both cases the vertical section below the rig is analyzed using stereonet plots to find a suitable (i.e. safe) KOP. From the KOP the lateral distance to the target location is divided into equal intervals and at each interval stereonet plots at five depths are analyzed to determine safe conditions for the hold angle (see Figure 79, 92) and for Type II wells to find a suitable DOP.

With a basic layout of safe azimuth and inclination combinations at specific depths, the virtual well paths are constructed. Using a nearest neighbor approach the stress tensors are mapped onto the well path are extracted (Figure 93) and a continuous mud pressure window for the entire well is calculated (Figure 94).

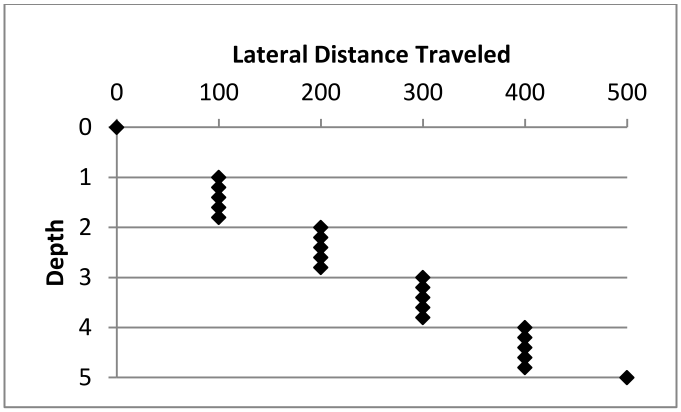

Figure 92. Generic representation of how the locations of stereonet projections are chosen between the KOP and target location. Each diamond represents the location of a single calculation.

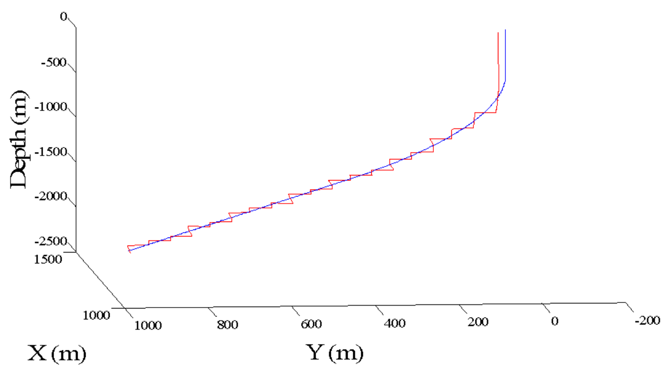

Figure 93. Graphical representation of the stress tensors mapped on the well. The smooth blue line is the calculated well path, while the jagged red line is made from the locations of the nodes extracted from the MEM.

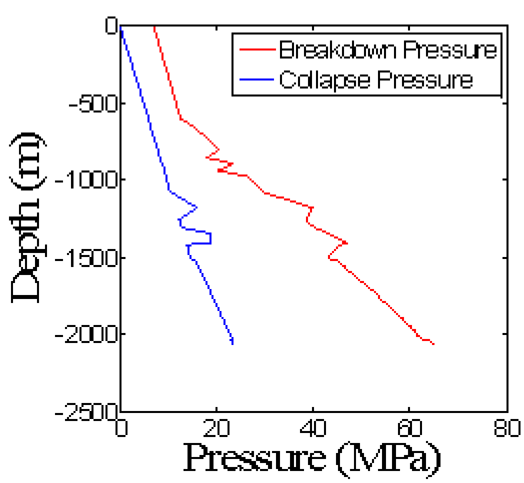

Figure 94. Example mud pressure window where the breakdown pressure is used as the maximum allowable pressure, and the collapse pressure is used as the minimum allowable pressure.

2.3.3.2.Surface Location Flexible

If the surface location of the drilling rig is flexible we assume that Type I wells (including vertical wells) are preferred over Type II wells [29]. Using the optimal azimuth and inclination determined previously at equi-distant intervals (see Figure 92) the safe conditions for the hold angle and KOP are determined. The workflow is summarized and presented in Figure 95.

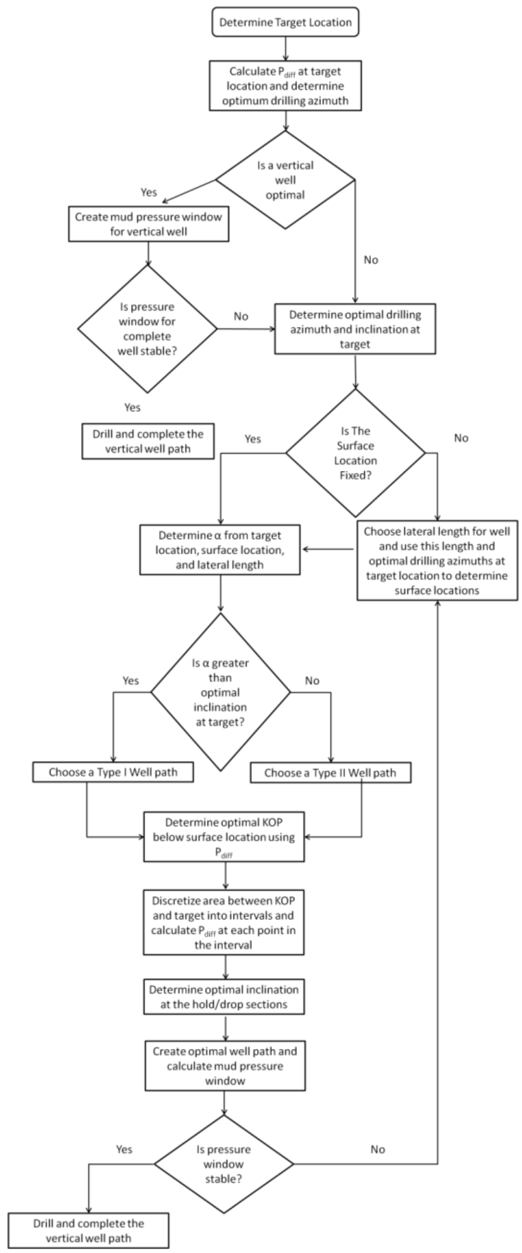

Figure 95: Schematic diagram of wellbore trajectory planning/optimization workflow followed in this study.

2.3.4. Results of the Case Study

The methodology described above has been applied to stress tensors extracted from a synthetic MEM representative of an actual “3 way against salt” field in the deep water Gulf of Mexico. The geologic scenario results in a state of stress which is non-Andersonian and varies considerably both laterally and vertically.

For this study a common target location in the center of the model is chosen for all wells tested. The surface location is assumed to be flexible; therefore, all possible azimuth angles are tested. A lateral reach of 1,000m is chosen based on the size of the numerical model.

Assessment of an arbitrary well path, in this case vertical, is the first step for finding an optimized wellbore trajectory Stereonet projections at selected depths and a continuous mud pressure window are presented in Figure 96. Both stereonet projections and the mud pressure window show the highly varying conditions of the vertical well path. Although the overall conditions suggest a stable well, the vertical trajectory is considered unpractical. To maintain wellbore stability a total of 4 casing sections have to be used. Furthermore, the pressure window between 1600m and 2100m narrows to less than 5MPa. In order to circumvent these complications, a deviated well path is designed for this area.

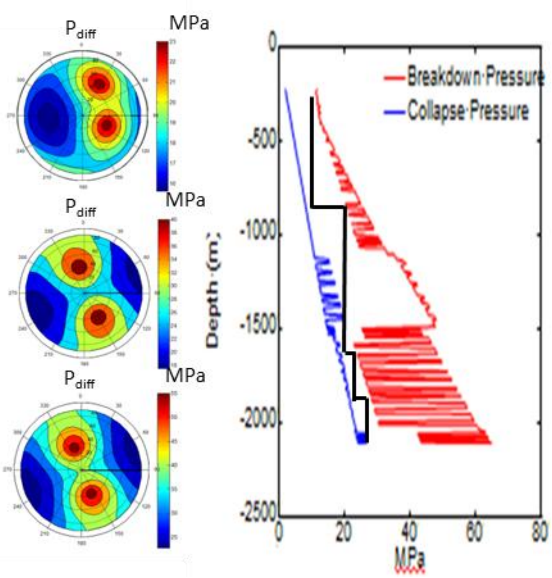

Figure 96. Three stereonets along a vertical path above the target location are shown above. The first was taken at a depth of 600m, the second at 1500m, and the third at 2100m.The plot on the right is a mud pressure window from a vertical well located at the target location where the solid black lines indicate casing sections.

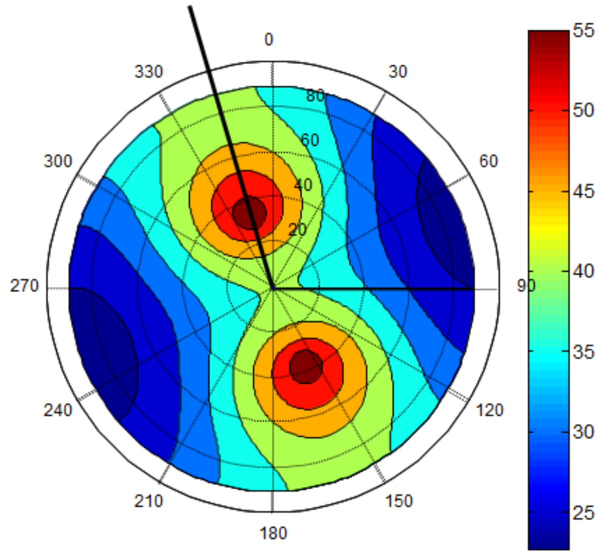

Figure 97. Stereonet projection of the P_{diff} at the target location. The solid black line denotes the azimuth of optimal drilling. The solid red line shows the azimuth of the un-optimized well path.

In order to determine an optimized, stable deviated wellpath, a stereonet projection of P_{diff} at the target location is used to define the optimum drilling azimuth and inclination angle (Figure 97).

The optimal drilling direction at the target location is shown as the solid black line in Figure 97. This line lies at an azimuth of 345^o, with the optimal inclination being approximately 35^o-45^o. With the optimal drilling direction at the target location being determined, and with the lateral length of the well chosen, the surface location of the well can be found. Using this surface location as a starting point, 20 stereonet projections of P_{diff} at varying depths below the surface location are used to determine the optimal KOP (Figure 98). The depth of stereonet B is chosen as the most suitable depth for the KOP. At this depth the optimal azimuth and inclination angles determined for the target location (345° and 45°) also result in the largest P_{diff} compared to the other depths. As can be seen in stereonets C and D (Figure 98) P_{diff} decreases in the direction of optimal drilling azimuth.

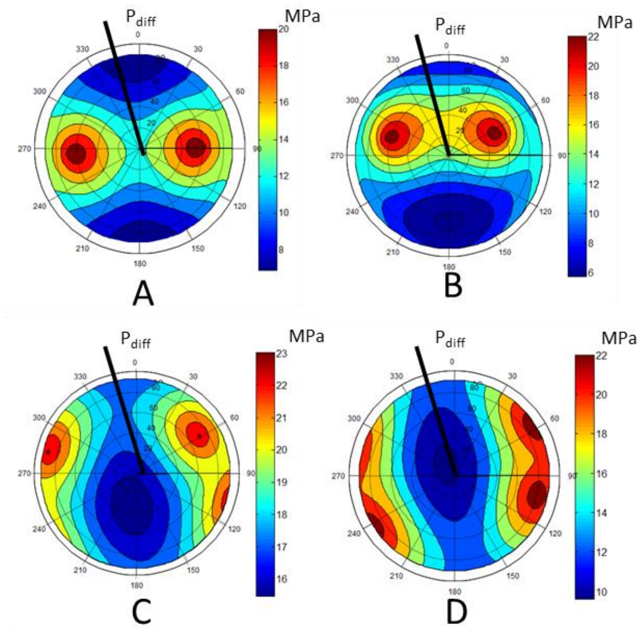

Figure 98. Stereonet projections of P_{diff} along a vertical line below the surface location. Stereonet A is at a depth of 450m, stereonet B at 500m, stereonet C at 550m, and stereonet D is at a depth of 600m.

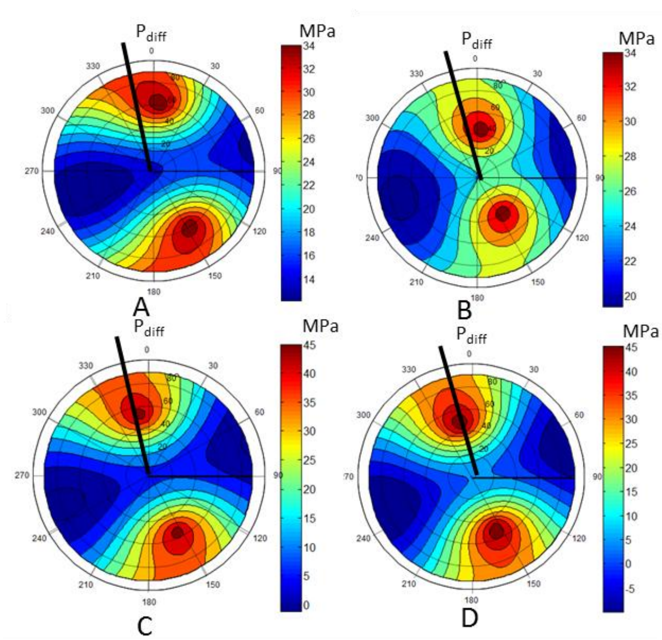

Figure 99. Stereonet projections of P_{diff} along the hold section of the optimized well path. The depth is decreasing from A-D.

Following the geometry in Figure 91 the angle α is determined as 57°. Thus, a Type I well profile is chosen to be the preferred well shape. In order to ensure stable conditions for the “hold” section (for the chosen azimuth and inclination) of the well path, the distance between the target location and the KOP is discretized into ten 100m intervals (following the methodology of Figure 92). At each interval 5 depths are analyzed using stereonet projections. Figure 99 shows four stereonet projections which are intersected by the well path at lateral intervals of 200m (Figure 100).

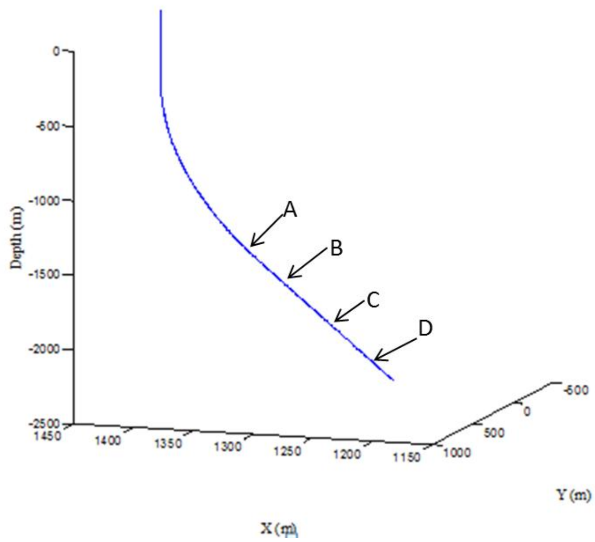

Figure 100. Approximate locations for the given stereonet projections on the proposed well path.

The stereonets displayed in Figure 99 show that the chosen azimuth and inclination do not represent the most optimized combination at the beginning of the hold section. However, as the well extends deeper into the subsurface the stress orientations are changing such that the optimal azimuth and inclination converge to the previously determined optimized combination at the target location.

With all of the necessary components to build a Type I well path tested, the well trajectory can be constructed and placed in the numerical MEM. By extracting the stress data from the synthetic Gulf of Mexico MEM along the well path the continuous mud pressure window can be created (Figure 101). Compared to the vertical well the mud pressure window is much wider (i.e. the wellbore is more stable) and fewer casing points have to be set.

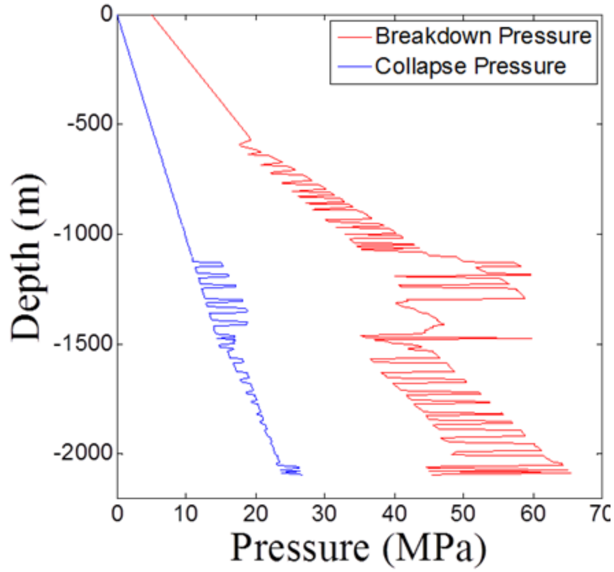

Figure 101. Mud pressure window for the optimized well trajectory.

For the purpose of comparison, an un-optimized, worst-case scenario well path is also presented. This well is created using the same Type I trajectory and inclination angle as the optimized well path, but was placed along an azimuth of 60^{o}. As seen in Figure 97, a well placed along this azimuth is not preferentially oriented and has a much narrower mud pressure window when compared to the optimized well path (Figure 102). Furthermore, at specific depths, the breakdown pressure and the collapse pressure lines cross indicating unstable drilling conditions which cannot be resolved by mud weight adjustments.

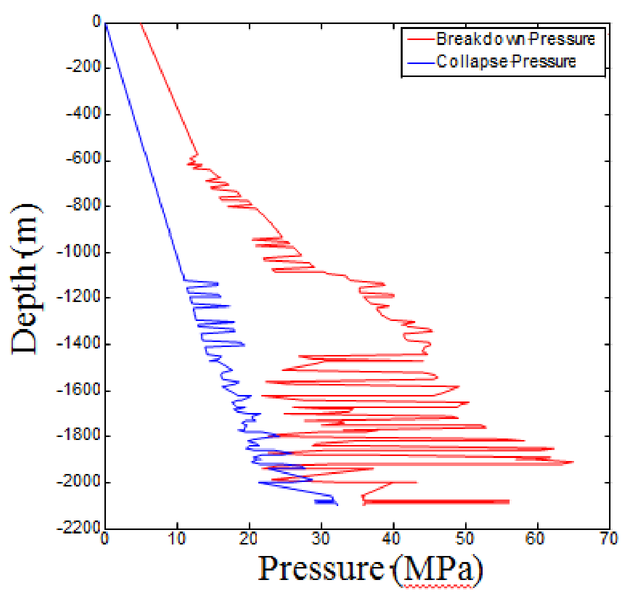

Figure 102. Mud pressure window from an un-optimized well path with an azimuth of 60^o and an inclination of 45^o.

2.3.5. Summary And Conclusions

Wellbore stability represents a crucial field in the development of hydrocarbon exploration and production. Instable wells, amongst others, cause reduced drilling performance, lost circulation, stuck bottom hole assembly, well work-over costs, and at worst can lead to a total collapse and a loss of the wellbore. A thorough geomechanical analysis in the planning stage of a well can significantly reduce these risks. A large number of 'conventional' wellbore trajectory planning studies utilize 1D MEMs to predict the reservoir state of stress and rock strength parameters from wireline logging measurements and hydraulic minifrac tests. Based on these data sets a mud pressure window for the logged well can be obtained. If unstable conditions occur, stereographic projections are utilized to find more optimal drilling azimuths and inclinations for different wells in the same field [7, 17, 18]. While this approach proves successful and valid for a large number of case studies it utilizes the inherent assumption of an Andersonian state of stress (ASoS) and thus is not valid for cases where complex geologic structures violate this assumption.

For such scenarios 3D numerical MEMs have proven to be an excellent tool for continuous spatial stress prediction. 3D MEMs of hydrocarbon fields are calibrated against stress measurements and predict realistic stress magnitudes [25]. Based on 3D numerical MEMs the methodology presented in this paper represents a valuable work process to optimize wellbore trajectories in the planning stage of a well. Assumptions on the state of stress are not necessary as the 3D MEM provides the complete stress tensor at any location in the model. The methodology is based on most general mathematical description and thus enables all possible scenarios of azimuth, inclination and surface rig location for multiple well types along the entire trajectory of the well path. The methodology can also be applied for any failure criterion.

The case study results show that if applied to a scenario with a highly varying state of stress a significant improvement of wellbore stability conditions can be achieved. In comparison to a vertical well the proposed well trajectory has a significantly wider mud pressure window also resulting in a reduction of casing points.

Although neither stereographic projections nor mud pressure windows alone can produce optimal wellbore trajectory results, the combination of the two can be a powerful tool for predicting optimal drilling directions. The presented methodology however, still utilizes significant ‘human’ effort for analyzing stereonets at various locations of a deviated well path. As the 3D MEM provides all necessary input data, the next step for the presented methodology is to find an automatic process to find an optimal well trajectory for a given target location.

3. Overall Concluding Remarks and Accomplishments

In this ARRA training project 4 graduate students (3MS, 1PhD) have been employed and been trained in numerical modeling of CO_2 sequestration applications.

In contrast to the majority of numerical modeling studies for CO_2 sequestration applications this project does not employ horizontally layered basin models but focuses on a set of generic anticline structures. Anticline structures are the most prominent structural trap for mature hydrocarbon reservoirs and hence represent prime targets for CO_2 sequestration sites. The geometry of an anticline induces stress heterogeneities which in turn result in differences when geomechanical risks such as fracture reactivation are analyzed. As a major conclusion, if geometry information is available (i.e. 3D seismic), numerical models should not be simplified to horizontally layered basins. The results of the pre-injection risk assessment on maximum sustainable pore pressures based on finite element analysis and the results of the coupled fluid flow – geomechanical analysis have shown that the prevailing stress regime is the most important input parameter for geomechanical models. It is therefore recommended that every geomechanical study utilized for CO_2 sequestration case studies is calibrated by stress measurements such as mini-frac tests.

Furthermore, these stress heterogeneities are emphasized when inter-bedding friction is considered. This study has shown that low friction results in an effective mechanical decoupling between adjacent beds and thus lower pore pressures can be sustained (i.e. for the compressional stress regime).

If only fluid flow processes are considered the project results show that the fluid flow boundary conditions are the most important parameter and huge differences are observed between open and closed fluid systems. It is recommended that further research is conducted in order to develop methods to quantify this crucial parameter.

On the borehole scale a methodology has been established to setup and optimize numerical models in order to minimize errors. The results of the FE models on the reservoir scale have been used to perform a wellbore stability analysis and to find stable drilling directions for the anticline structures. While vertical wells have proven to be stable for all three stress regimes, a procedure has been developed that can be readily applied to prospective case studies with more complex material models and geometries. The procedure developed provides mud pressure window calculation for inclined wellbores of type I wells. The methodology developed represents a process to optimize wellbore trajectories in the planning stage of a well. Assumptions on the state of stress are not necessary as the 3D FEM provides the complete stress tensor at any point in the model. The methodology is based on the general mathematical description and thus enables all possible scenarios of azimuth, inclination and surface rig location for multiple well types along the entire trajectory of the well path. The case study results show that if applied to a scenario with a highly varying state of stress a significant improvement of wellbore stability conditions can be achieved.

As an overall conclusion the various numerical modeling techniques and analyses applied in this project have shown that geometrical heterogeneities of the reservoir/injection layer have significant influences on CO_2 injection parameters. Whilst this project employed generic anticline geometries and the results do not reflect an actual case study, the methodologies developed in this project can be readily applied to any case study.

References

Aadnoy, B.S.. U. of Stavanger, and A.K. Hansen. 2005. Bounds on In-Situ Stress Magnitudes Improve Wellbore Stability Analyses. SPE Journal. June: 115-120.

ABAQUS Analysis User's Manual V6.10. Chapters 4.1.3 and 25.1.3. ABAQUS, Inc. Dassault Systèmes.

Al-Ajmi, A.M., and R.W. Zimmerman. 2009. A new well path optimization model for increased mechanical borehole stability. J. Pet. Sci. Eng. 69: 53-62.

Al-Ajmi, A.M., U. Sultan Qaboos, and R.W. Zimmerman. 2006. Stability Analysis of Deviated Boreholes Using the Mogi-Coulomb Failure Criterion, With Applications to Some Oil and Gas Reservoirs. In IADC/SPE Asia Pacific Drilling Technology Conference and Exhibition, Bangkok, Thailand, 13-15 November 2006. SPE 104035-MS.

Altmann. J.B, Mueller, T.M., Mueller, BI.R., Tingay, M.R.P., and Heidbach, O., 2010. Poroelastic contribution to the reservoir stress path. International Journal of Rock Mechanics & Mining Sciences, 47, pages 1104-13.

Amirlatifi, A., Eckert, A., Nygaard, R. and B. Bai. 2011. Estimation of reservoir uplift, seismicity and failure likelihood during CO2 injection through coupled reservoir simulation. Paper CSUG/SPE 148946-PP presented in Canadian Unconventional Resources Conference, Calgary, Canada, 15–17 November 2011.

Amirlatifi, A., Eckert, A., Nygaard, R. and B. Bai. 2011. Prediction of caprock fractures during CO2 sequestration by coupled modeling in complex geological fields. In preceedings of tenth annual conference on carbon capture and sequestration, Pittsburgh, USA, 2-5 May 2011.

Amirlatifi, A., Eckert, A., Nygaard, R., Bai, B., Liu, X., Paradeis, M., 2012. Role of Geometrical Influences of CO2 Sequestration in Anticlines, in: 46th US Rock Mechanics / Geomechanics American Rock Mechanics Assosiaction Symposium. Chicago, IL, p. ARMA 12–255.

Bachu, S., Gunter, W.D. and E.H. Perkins. 1994. Aquifer disposal of CO2: hydrodynamic and mineral trapping. Energy Conversion and Management, 35 (4): 269-279.

Barton, C., M. D. Zoback, and D. Moos, 1995. Fluid flow along potentially active faults in crystalline rock, Geology. 23: 683–686.

Barton, C.A. and Moos, D., Peska, P., and Zoback, M.D. 1997. Utilizing Wellbore Image Data to Determine the Complete Stress Tensor: Application to Permeability Anisotropy and Wellbore Stability. The Log Analyst. 38:6.

Biot, M. 1941. General Theory of Three Dimensional Consolidation. J. of Applied Physics. 12:155-164.

Birkholzer, J.T., Zhou, Q. and C.F. Tsang. 2009. Large-scale impact of CO2 storage in deep saline aquifers: a sensivity study on pressure response in stratified systems. Int. J. of Greenhouse Gas Control 3: 181-194

Bourgoyne, A.T. Jr., K.K. Millheim, M.E. Chenevert, and F.S. Young Jr. 1986. Applied Drilling Engineering. Volume 2. SPE textbook series.

Bradley, W.B. 1979. Failure of inclined boreholes. J. Energy Resour. Technol. 101: 232-239.

Brudy, M., M.D. Zoback, K. Fuchs, F. Rummel, and J. Baumgärtner. 1997. Estimation of the complete stress tensor to 8km depth in the KTB scientific drill holes: Implications for crustal strength. J. of Geoph. Res. 102(B8): 18,453-18,475.

Buchman, T.J., G. Peters, and P.T. Connolly. 2008. Recent faulting in the Upper Rhine Graben (Germany): a 3D finite element approach to predict fault reactivation. In 42nd U.S. Rock Mechanics Symposium and 2nd U.S.-Canada Rock Mechanics Symposium, San Francisco, CA, 29 June – 2 July.

Byerlee, J. 1978. Friction of rocks. Pure and Applied Geophysics. 116: 615-626.

Cappa, F. and J. Rutqvist. 2011. Modeling of coupled deformation and permeability evolution during fault reactivation induced by deep underground injection of CO2. Int. J. of Greenhouse Gas Control. 5: 336-346.

Chen, G., M.E. Chenevert, M.M. Sharma, and M. Yu. 2003. A study of wellbore stability in shales including poroelastic, chemical, and thermal effects. Journal of Petroleum Science and Engineering. 38: 167-176.

Cheng, H., and M.B. Dusseault. 1993. Development and application of a fully-coupled two-dimensional finite element approach to deformation and pressure diffusion around a borehole. Journal of Canadian Petroleum Technology. 32: 28-38.

Cooper, G.A. 1994. Directional Drilling. Scientific American. 270(5): 82-87.

Coulomb, C.A. 1776. Essai sur une application des regles des maximis et minimis a quelquels problemesde statique relatifs, a la architecture. Mem. Acad. Roy. Div. Sav. 7: 343-387.

Craupner, B. J., Li, D. and S. Bauer. 2011. The coupled simulator Eclipse-OopenGeoSys for the simulation of CO2 storage in saline formations. J. Energy Procedia 4: 3794-3800

Dean. R.H., Gai, X., Stone, C.M. and S.E. Minkoff. 2006. A Comparison of Techniques for Coupling Porous Flow and Geomechanics. SPE J. 11 (1):132-140.

Eckert, A., 2007: 3D multi-scale finite element analysis of the crustal state of stress in the Western US and the Eastern California Shear Zone, and implications for stress – fluid flow interactions for the Coso Geothermal Field. PhD thesis, Universitaet Karlsruhe.

Eckert, A., and P.T. Connolly. 2004. 2D Finite Element Modelling of Regional and Local Fracture Networks in the Eastern California Shear Zone and Coso Range, California USA. Geothermal Resources Council Transaction. 28: 643-648.

Ehlig-Economides, C. and M.J. Economides. 2010. Sequestering carbon dioxide in a closedunderground volume. J. Pet. Sci. & Tech. 70: 123-130

Engelder T, Fischer MP. Influence of poroelastic behaviour on the magnitude of minimum horizontal stress, Sh, in overpressured parts of sedimentary basins. Geology 1994,22:949–52.

Engelder, T. 1992. Stress Regimes in the Lithosphere. Princeton University Press. 9780691085555

Engelder, T., 1993. Stress Regimes in the Lithosphere. Princeton University Press.

Ewy, R.T. 1999. Wellbore-stability prediction by use of a modified Lade criterion. SPE Drilling & Completion. 14: 85-91.

Feng, Y., and Shi, X. 2013. Hydraulic fracturing process: roles of in-situ stress and rock strength. Adv. Mat. Res. 616-618: 435-440.

Fjaer, E., R.M. Holt, P. Horsrud, A.M. Raaen and R. Risnes. 1992. Petroleum Related Rock Mechanics.. 2nd ed. New York: Elsevier B.V.

Freitag, L., M. Jones, and P. Plassman. 1995. An Efficient Parallel Algorithm for Mesh Smoothing. In Proceedings of the Fourth International Meshing Round Table, 1995, 47-58.

Gentzis, T., D. Nathan, and R.J. Chalaturnyk. 2009. A method to predict geomechanical properties and model well stability in horizontal boreholes. International Journal of Coal. 78: 149-160.

Gibbs, J.F., Healy, J.H., Raleigh, C.B. & Coakley, J., 1973. Seismicity in the Rangely, Colorado, area: 1962–1970, Bull. Seism. Soc. Am., 63, p. 1557–1570.

Goodman, H.E., and P. Connolly. 2007. Reconciling Subsurface Uncertainty With the Appropriate Well Design Using the Mechanical Earth Model (MEM) Approach. In 31st Nigeria Annual International Conference and Exhibition, Abuja, Nigeria, 6-8 August.

Grabinsky, M.W., R. Wilson, and A. Zougas. 1995. Practical meshing considerations for finite element analysis of rock engineering problems. In 8th ISRM Congress, Tokyo, Japan, 25-29 September 1995. SPE 8CONGRESS-1995-266.

Gray, K.E., E. Podnos, and E. Becker. 2009. Finite-Element Studies of Near-Wellbore Region During Cementing Operations: Part I. SPE Drilling & Completion. 24: 127-136.

Hillis RR. Coupled changes in pore pressure and stress in oil fields and sedimentary basins. Pet Geosci 2001;7:419–25.

Houseknecht, D.W. and F.G. Ethridge. 1978. Depositional history of the Lamotte sandstone of southeastern Missouri. J. of Sedimentary Petrology 48 (2): 575-586.

http://www.sourcewatch.org/index.php?title=Existing_U.S._Coal_Plants, accessed January 2012.

Inoue, N. 2009. Answers to some questions about the coupling between fluid flow and rock deformation in oil reservoirs. Paper SPE 125760 presented at SPE/EAGE Reservoir Characterization and Simulation Conference, Abu Dhabi, UAE, 19- 21 October 2009.

Islam, M.A., Skalle, P., Al-Ajmi, A.M., and Søreide, O.K. 2010. Stability Analysis in Shale through Deviated Boreholes using the Mohr and Mogi-Coulomb Failure Criteria. In 44th US Rock Mechanics Symposium and 5th U.S.-Canada Rock Mechanics Symposium, Salt Lake City, UT, 27-30 June.

Jaeger JC, Cook NGW, and Zimmerman RW. Fundamentals of Rock Mechanics. 4th edition, Blackwell Publishin, Malden MA, USA, 2007.

Kirsch, G. 1898. Die Theorie der Elastizität und die Bedürfnisse der Festigkeitslehre. Zeitschrift des Vereines Deutscher Ingenieure. 42: 797.

Knupp, P.M. 2000. Achieving finite Element Mesh Quality Via Optimization of the Jacobian Matrix Norm and Associated Quantities. Part I- A Framework for Surface mesh Optimization. Int. J. Numer. Meth. Engng. 48: 401-420.

Knupp, P.M. 2007. Remarks on mesh quality. In 45th AIAA Aerospace Sciences Meeting and Exhibit, Reno, NV, 7-10 January, 2007.

Kongsjorden, H., Karstad, O. and Tore A. Torp. 1998. Saline aquifer storage of carbon dioxide in the Sleipner project. J. Waste Management 17 (5-6): 303-308

Last, N.C., and M.R. McLean. 1996. Assessing the Impact of Trajectory on Wells Drilled in an Overthrust Region. JPT. July: 620-626.

Lee, M., A. Eckert, and R. Nygaard. 2011. Mesh optimization for finite element models of wellbore stress analysis. In 45th US Rock Mechanics/Geomechanics Symposium, San Francisco, CA, 26-29 June.

Li, Q., Bai, Y., Yin, X., & Li, X. 2007. Thermo-hydro-mechanical modeling of CO2 sequestration system around fault environment. In Computational Earthquake Physics: Simulations, Analysis and Infrastructure, Part II . 2585-2593. Birkhäuser Basel.

Li, Q., Z. Wu, and X. Li. 2009. Prediction of CO2 leakage during sequestration into marine sedimentary strata. Energy Conservation and Management. 50:503-509.

Liu, X. 2011. Universal Technique Normalizes and Plans Various Well-Paths for Directional Drilling. In SPE Middle East Oil and Gas Show and Conference, Manama, Bahrain, 25-28 September.

Loizzo, M., Lecampion, B., Bérard, T., Harichandran, A. and L. Jammes, 2009. Reusing O&G Depleted Reservoirs for CO2 Storage: Pros and Cons. Paper SPE 124317-MS presented at SPE Offshore Europe Oil & Gas Conference and Exhibition, Aberdeen, UK, 8-11 September 2009.

McLean, M.R., M.A. Addis. 1990. Wellbore stability: the effect of strength criteria on mud weight recommendations. In SPE Annual Technical Conference and Exhibition, New Orleans, LA, 23-26 September 1990. SPE 20405-MS.

Metz, B., O. Davidson, Bosch. P, Dave. R and L. A.Meyer (eds.). IPCC, 2007: Climate Change 2007: Mitigation of Climate Change. Contribution of Working Group III to the Fourth Assessment Report of the Intergovernmental Panel on Climate Change. Cambridge University Press, Cambridge, United Kingdom and New York, NY, USA.

Metz, B., O. Davidson, H. de Connick, M . Loos, and L. Meyer. 2005. IPCC Special report on carbon dioxide capture and storage. Cambridge University Press.

Mitchell, S.A. 1997. Choosing corners of rectangles for mapped meshing. In Proceedings of the thirteenth annual symposium on Computational geometry, New York, NY, 1997. 87-93.

Muller B, Altmann JB, M ¨ uller TM, Weisshardt A, Shapiro SA, Schilling F, Heidbach O. Tensor character of pore pressure-stress coupling in reservoir depletion and injection. 72nd EAGE Conference, Barcelona, 2010. Extended abstracts F045.

Nawrocki, P.A. 2010. Critical wellbore pressures using different rock failure criteria. In International Symposium - 6th Asian Rock Mechanics Symposium, New Delhi, India, 23-27 October 2010.

Nicholson, C., E. Roeloffs, and R. L. Wesson. 1986. The northeastern Ohio earthquake of 31 January 1986: was it induced? Seismological Society of America.

Nipp, H.-K, E.G. McNulty. 1987. Effects of mesh size and boundary conditions on creep analysis of rock salt. In The 28th U.S. Symposium on Rock Mechanics, Tucsan, AZ, 29 June - 1 July 1987.

Paradeis, M., Eckert, A. and X. Liu. 2012. Influences of Anticline Reservoir Geometry on Critical Pore Pressures Associated with CO2 Sequestration. Paper ARMA 12-319, to be presented in 46th US Rock Mechanics Geomechanics Symposium, Chicago, USA, 24-27 June 2012.

Peska, P., and M.D. Zoback. 1995. Compressive and tensile failure of inclined well bores and determination of in situ stress and rock strength. J. of Geo. Res. 100(B7): 12,791-12,811.

Pettersen, O. 2006. A predictor for accelerated coupled rock mechanics and reservoir simulation. In proceedings of 10th European Conference on the Mathematics of Oil Recovery, Amsterdam, Netherlands, 4-7 September 2006.

Pollar, D.D. and R.C. Flectcher. 2005. Fundamentals of Structural Geology. Cambridge University Press.

R. J. Gibbs. 1973. Mechanisms of Trace Metal Transport in Rivers. Science. 180: 71-73 .

Rahim, Z., A.A. Al-Kanaan, H.A. Al-Anazi, and M.S. Ahmed. 2012. Successful drilling of lateral wells in minimum horizontal stress direction for optimal fracture placement. Oil & Gas J. 110(12): 74-82.

Rutqvist, J. and C-F. Tsang, 2002. "A study of caprock hydromechanical changes associated with CO2-injection into a brine formation." Environmental Geology, 42, 296-305.

Rutqvist, J., J. Birkholzer, and C.-F. Tsang. 2006. Modeling of geomechanical processes during injection in a multilayered reservoir-caprock system and implications on site characterization. In Proceedings of the International Symposium on Site Characterization for CO2 Geological Storage, Berkeley, 20-22 March 2006.

Ruqvist, J., Birkholzer, J., Cappa, F. and C.F. Tsang. 2007. Estimating maximum sustainable injection pressure during geological sequestration of CO2 using coupled fluid flow and geomechanical fault-slip analysis. J. of Energery Conversion and Management 48: 1798-1807

Rutqvist, J., J. Birkholzer, and C.-F. Tsang. 2008. Coupled reservoir-geomechanical analysis of the potential for tensile and shear failure associated with CO2 injection in multilayered reservoir-caprock systems. Int. J. of Rock Mechanics and Mining Sciences. 45: 132-143.

Rutqvist, J. and F. Cappa. 2011. Modeling of coupled deformation and permeability evolution during fault reactivation induced by deep underground injection of CO2. Int. J. of Greenhouse Gas Control. 5: 336-346.

Rutqvist, J., P. Digby, and O. Stephansson. 1989. Simulation of borehole breakouts with a damage material model. In ISRM International Symposium, Pau, France, 30 August - 2 September 1989.

Samier, P. and S.D. Gennaro. 2007. Pratical iterative coupling of geomechanics with reservoir simulation. Paper SPE 106188, presented at SPE Reservoir Simulation Symposium, Houston, USA,26-28 February 2007.

Sanz, P.F., Pollard, D.D., Allwardt, P.F., and Borja, R.I., 2008. Mechanical models of fracture reactivation and slip on bedding surfaces during folding of the asymmetric anticline at Sheep Mountain, Wyoming. Journal of Structural Geology, vol. 30, no. 9, pp. 1177-1191.

Schutjens, P.M.T.M., J.R. Snippe, H. Mahani, J. Turner, J. Ita, and A.P. Mossop. 2012. Production-Induced Stress Change in and Above a Reservoir Pierced by Two Salt Domes: A Geomechanical Model and Its Applications. SPE Journal. March: 80-97.

Settari, A. and F.M. Mourits, 1998. A coupled reservoir and geomechanical simulation system. Paper SPE 50939. SPE J. 3 (3): 219-226.

Settari, A., and Walters, D. 2001. Advances in coupled geomechanical and reservoir modeling with applications to reservoir compaction. Spe Journal, 6(3), 334-342..

Sibson, R.H., 2003. Brittle failure controls on maximum sustainable over-pressure in different tectonic stress regimes. Bulletin American Society of Petroleum Geology, v.87, p. 901-908.

Smart, K. J., Ferrill, D. a., & Morris, A. P. 2009. Impact of interlayer slip on fracture prediction from geomechanical models of fault-related folds. AAPG Bulletin, 93(11), 1447–1458.

Streit, J. and R. Hillis. 2004. Estimating fault stability and sustainable fluid pressure for underground storage of CO2 in porous rock. Energy. 29: 1445-1456.

Taberner. C., Cartwright, L. and T. Xu. 2009. Injection of supercritical CO2 into deep saline carbonate formations, predictions from geochemical modling. Paper SPE 121272 presented at SPE EUROPEC/EAGE Annual Conference and Exhibition, Amsterdam, Netherlands, 8-11 June 2009.

Tan, Q., J. Deng, and B. Yu. 2013. Study on Borehole Stability of Unconsolidated Sandstone in Depleted Reservoir. Adv. Mat. Res. 616-618: 720-725.

Teufel, L.W., Rhett, D.W., and Farrell, H.E., 1991. Effect of reservoir depletion and pore pressure drawdown on in situ stress and deformation in the Ekofisk Field, North Sea. In: Roegiers, Editor, Rock Mechanics as a Multidisciplinary Science, Balkema Rotterdam, ISBN 906191194X, p. 63-72.

Thomas, L.K., Chin, L.Y., Pierson, R.G. and J.E. Sylte. 2003. Coupled Geomechanics and Reservoir Simulation. SPE J. 8 (4): 350-358.

Tran, D. Shrivastava, V. Nghiem, L. and B. Kohs. 2009. Geomechanical risk mitigation for CO2 sequestration in saline aquifers. Paper SPE 125167 presented in SPE Annual Technical Conference and Exhibition, New Orleans, USA, 4-7 October 2009.

Tran, D., Nghiem, L., Shrivastava, V., Kohse, B., 2010. Study of geomechanical effects in deep aquifer CO2 storage, in: 44th US Rock Mechanics Symposium. ARMA, Salt Lake City, UT.

Tran, M. H., and Y.N. Abousleiman. 2010. The impacts of failure criteria and geological stress states on the sensitivity of parameters in wellbore stability analysis. In 44th U.S. Rock Mechanics Symposium and 5th U.S.-Canada Rock Mechanics Symposium, Salt Lake City, UT, June 27 - 30, 2010.

Turon, A., C.G. Davila, P.P. Camanho, and J. Costa. 2007. An engineering solution for mesh size effects in the simulation of delamination using cohesive zone models. Journal of Engineering Fracture Mechanics. 74, 1665-1682.

Twiss, R.J., and Moores, E.M., 1992. Structural Geology.Freeman and Company, New York.

Twiss, R.J and E.M. Moores. 2007. Mechanics of Natural Fractures and Faults. In Structural Geology, 2nd ed. New York: W.H. Freeman and Company, 231-264.

Van der Meer, L. G. H. and J. D. van Wees. 2006.Limitations to Storage Pressure in Finite Saline Aquifers and the Effects of CO2 Solubility on Storage Pressure. Paper SPE 103342 presented at the SPE Annual Technical Conference and Exhibition, San Antonio, Texas, 24-27 September.

Verdon, J.P, J.M. Kendall, D.J. White, and D.A. Angus. 2011. Linking microseismic event observations with geomechanical models to minimize the risks of storing CO2 in geological formations. Earth and Planetary Science Letters. 305: 143-152.

Vidal-Gilbert, S., J.-F.Nauroy, and E. Brosse, 2008. 3D geomechanical modeling for CO2 geologic storage in the Dogger carbonates of the Paris Basin. Int. J. Greenhouse Gas Control, V.3, Issue 3, p. 288-299.

Wesson, R.L. and C. Nicholson. 1987. Earthquake Hazard Associated with Deep Well Injection. Prepared by the U.S. Geological Survey. Open-File Report 87-331.

Wiprut, D. and M.D. Zoback. Constraining the full stress tensor in the Visund field, Norwegian North Sea: Application to wellbore stability and sand production. Int'l. J. Rock Mech. & Mining Sci., v. 37, pp. 317-336, 2000.

Yamamato, K., M. Tamura, N. Goto. 2006. Borehole instability analysis in an anisotropic and heterogeneous shale formation. In IADC/SPE Asia Pacific Drilling Technology Conference and Exhibition, Bangkok, Thailand, 13-15 November 2006. SPE 103883-MS.

Yang, X., L. Zhiyuan, H. Zhang, Q. Xiong, and H. Liu. 2012. An analysis on wellbore collapse of open hold completion in carbonate formation. Appl. Mech. And Met. 220-223: 150-156.

Zahn, M.N., L.C. Coelho, L. Landau, and J.L.D. Alves. 2010. Numerical study on wellbore stability analysis consindering volumetric failure. Mecánic Computacional. 29: 8837-8858.

Zare-Reisabadi, M.R., A. Kaffash, and S.R. Shadizadeh. 2012. Determination of optimal well trajectory during drilling and production based on borehole stability. J. of Rock Mech. And Min. Sci. 56: 77-87.

Zavattieri, P. 1996. Optimization Strategies in Unstructured Mesh Generation. International Journal for Numerical Methods in Engineering. 39: 2055-2071.

Zervos, A., P. Papanastasiou, and J. Cook. 1998. Elastoplastic finite element analysis of inclined wellbores. In SPE/ISRM Rock Mechanics in Petroleum Engineering, Trondheim, Norway. 8 - 10 July 1998. SPE/ISRM 47322.

Zhang, J., M. Bai, and J.-C. Roegiers. 2003. Dual-porosity poroelastic analyses of wellbore stability. International Journal of Rock Mechanics and Mining Sciences. 40: 473-483.

Zhang, J., W.B. Standifird, K. Adesina, and G. Keaney. 2006. Wellbore stability with consideration of pore pressure and drilling fluid interactions. In the 41st U.S. Symposium on Rock Mechanics, Golden, CO, 17 - 21 June, 2006.

Zhang, L., P. Cao, and K.C. Radha. 2010. Evaluation of rock strength criteria for wellbore stability analysis. International Journal of Rock Mechanics and Mining Sciences. 47: 1304-1316.

Zhou, Q., Birkholzer, J. T., Tsang, C.F. and J. Rutqvist. 2008. A method for quick assessment of CO2 storage capacity in closed and semi-closed saline formations. Int. J. of Greenhouse Gas Control 2: 626-639.

Zienkiewicz, O.C., R.L. Taylor, and J.Z. Zhu. The finite element method: its basis and fundamentals. 6th ed. Butterworth-Heinemann.

Zoback, MD. Reservoir Geomechanics. Cambridge University Press, New York, 2007.

Zweigel, P. and L. Heill. 2003. Studies on the likelihood for caprock fracturing in the Sleipner CO2 injection case. In Saline Aquifer CO2 Storage Project.

Appendix

1. Critical pore pressure derivation: Pore Pressure Stress Coupling

Based on Rudnicki's (1986) solution of continuous fluid injection Altmann et al. (2010) showed that pore pressure - stress coupling, i.e. the ratio of $\Delta\sigma_{ij} / \Delta P$, is a complex function of space and time and has tensor character. This means that all components of the principal stress tensor are affected by changes in pore pressure, contradictory to the previous concept described by Engelder and Fischer (1994) and Hillis (2001). The complex nature of the pore pressure - stress coupling function can be simplified by considering the long term limits. When $t \to \infty$, the coupling ratios for the radial and tangential stress components with respect to the injection location in a principal stress coordinate system (Figure 103) can be derived. For the radial stress the coupling ratio matches Engelder and Fischers' (1994) solution without using any of their assumptions (Altmann et al., 2010; Mueller et al., 2010):

$$\lim_{t\to\infty} \frac{\Delta\sigma_{rad}(\vec{x},t)}{\Delta \mathrm{P}(\vec{x},t)} = \alpha \frac{1-2\nu}{1-\nu} \tag{27}$$

For the tangential stress the coupling ratio is given by (Altmann et al., 2010; Mueller et al., 2010):

$$\lim_{t\to\infty} \frac{\Delta\sigma_{\tan}(\vec{x},t)}{\Delta \mathrm{P}(\vec{x},t)} = \frac{1}{2} \alpha \frac{1-2\nu}{1-\nu} \tag{28}$$

Based on these long term limits the effective principal stress tensor after a change in pore pressure, ΔP, can be calculated (Mueller et al., 2010). If the effective state of stress prior to fluid injection/depletion is given by the radial effective stress, σ'_{rad}, and the tangential effective stress, $\sigma'_{\tan}$, a pore pressure change, ΔP, due to fluid injection results in the new effective stresses $\overline{\sigma}'_{rad}$ and $\overline{\sigma}'_{\tan}$.

$$\overline{\sigma}'_{ij} = \begin{pmatrix} \sigma'_{rad} + \alpha \frac{1-2\nu}{1-\nu}\Delta P - \Delta P & 0 & 0 \\ 0 & \sigma'_{rad} + \frac{1}{2}\alpha \frac{1-2\nu}{1-\nu}\Delta P - \Delta P & 0 \\ 0 & 0 & \sigma'_{rad} + \frac{1}{2}\alpha \frac{1-2\nu}{1-\nu}\Delta P - \Delta P \end{pmatrix} \tag{29}$$

These long term limits become especially relevant for subsurface engineering applications such as CO_2 sequestrations which are interested in how much pore pressure change is sustainable over long times.

A.1. Maximum Sustainable Pore Pressures for Different Stress Regimes

Based on long term limits the maximum sustainable pore pressures, P_c, for fault reactivation is derived with respect to the different stress regimes (i.e. extensional, strike-slip and compressional). For the derivation the Mohr-Coulomb failure criterion for cohesion-less fault reactivation is used.

$$\sigma_1 - P_c = \frac{1-\sin\phi}{1+\sin\phi}(\sigma_3 - P_c) \tag{30}$$

This can be rearranged in terms of the effective stresses, $\overline{\sigma}'_{1/3}$, after a pore pressure change ΔP at the critical (i.e. maximum sustainable) pore pressure P_c.

$$\overline{\sigma}'_1 = \frac{1+\sin\phi}{1-\sin\phi}\overline{\sigma}'_3 \tag{31}$$

Which, when $\Delta P=(P_c-P)$ is introduced in equation 6 and pore pressure stress coupling (for tangential stresses) is considered, is equal to:

$$\sigma_1 - P + \frac{1}{2}\alpha\frac{1-2\nu}{1-\nu}(P_c - P) - (P_c - P) = \frac{1-\sin\phi}{1+\sin\phi}\left[\sigma_3 - P + \frac{1}{2}\alpha\frac{1-2\nu}{1-\nu}(P_c - P) - (P_c - P)\right] \tag{32}$$

For the following derivations we introduce $a = \frac{1-\sin\phi}{1+\sin\phi}$ and solve equation 7 for P_c for the various stress regimes. Due to the nature of pore pressure stress coupling P_c is derived for different locations along the principal axis coordinate system (Figure x; after Altmann et al., 2010). In order to discuss implications for failure the according differential stress after a pore pressure change is also derived. For the following derivations we assume that the principal stresses are given by the vertical stress σ_V and the two horizontal stresses σ_h and σ_H. The derivation are given for the a general case involving principal stresses σ_1, σ_2 and σ_3. To obtain results for the specific stress regimes the according order of the principal stresses has to be used. I.e. for a compressional stress regime $\sigma_1=\sigma_H$ and $\sigma_3=\sigma_V$.

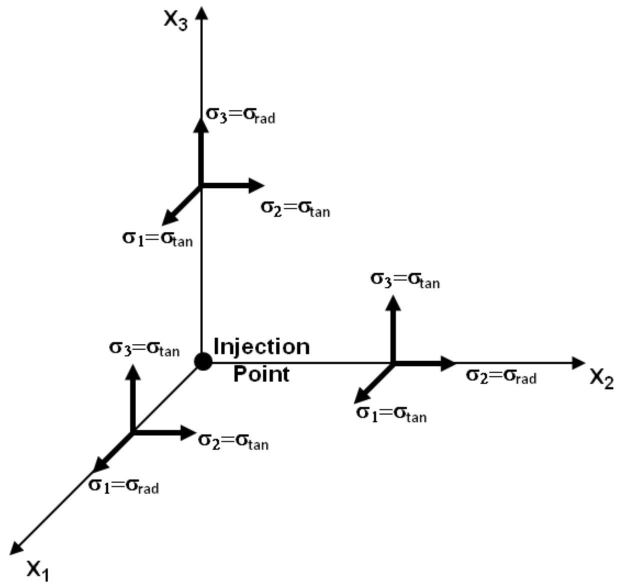

Figure 603: Coordinate system and location of injection point in the origin for the derivation of pore – pressure stress coupling equations.

a) **Along σ_3-direction:** according to Figure 103 and equation 4, σ_3 then represents the radial principal stress and σ_1 a tangential principal stress. The Mohr-Coulomb criterion is then given by:

$$\bar{\sigma}'_1 = a\bar{\sigma}'_3 \tag{33}$$

Which including $\Delta P=(P_c-P)$ becomes:

$$\sigma_1 - P + \frac{1}{2}\alpha\frac{1-2\nu}{1-\nu}(P_c - P) - (P_c - P) = a\left[\sigma_3 - P + \alpha\frac{1-2\nu}{1-\nu}(P_c - P) - (P_c - P)\right] \tag{34}$$

Solving this equation for P_c results in:

$$P_c = \frac{1}{\alpha\dfrac{1-2\nu}{1-\nu}(1/2 - a) - (1-a)}\left[a\sigma_3 - \sigma_1 - \alpha\frac{1-2\nu}{1-\nu}P(a - 1/2)\right] \tag{35}$$

The resulting differential stress, $\sigma_d = \bar{\sigma}'_1 - \bar{\sigma}'_3$, is then given by:

$$\sigma_d = \sigma_1 - P + \frac{1}{2}\alpha\frac{1-2\nu}{1-\nu}\Delta P - \Delta P - \left[\sigma_3 - P + \alpha\frac{1-2\nu}{1-\nu}\Delta P - \Delta P\right] \tag{36a}$$

$$\sigma_d = \sigma_1 - \sigma_3 - \frac{1}{2}\alpha\frac{1-2\nu}{1-\nu}\Delta P \tag{36b}$$

b) **Along σ_2-direction:** according to Figure x and equation 4, both σ_1 and σ_3 represent tangential principal stresses. The Mohr-Coulomb criterion including $\Delta P=(P_c-P)$ becomes:

$$\sigma_1 - P + \frac{1}{2}\alpha\frac{1-2\nu}{1-\nu}(P_c - P) - (P_c - P) = a\left[\sigma_3 - P + \frac{1}{2}\alpha\frac{1-2\nu}{1-\nu}(P_c - P) - (P_c - P)\right] \tag{37}$$

Solving this equation for P_c results in:

$$P_c = \frac{1}{(1-a)\left[\frac{1}{2}\alpha\frac{1-2\nu}{1-\nu} - 1\right]}\left[a\sigma_3 - \sigma_1 - \left(\frac{1}{2}\alpha\frac{1-2\nu}{1-\nu}\right)(a-1)P\right] \tag{38}$$

The resulting differential stress, $\sigma_d = \bar{\sigma}'_1 - \bar{\sigma}'_3$, is then given by:

$$\sigma_d = \sigma_1 - P + \frac{1}{2}\alpha\frac{1-2\nu}{1-\nu}\Delta P - \Delta P - \left[\sigma_3 - P + \frac{1}{2}\alpha\frac{1-2\nu}{1-\nu}\Delta P - \Delta P\right] \tag{39a}$$

$$\sigma_d = \sigma_1 - \sigma_3 \tag{39b}$$

c) **Along σ_1-direction:** according to Figure x and equation 4, σ_1 then represents the radial principal stress and σ_3 a tangential principal stress. The Mohr-Coulomb criterion including $\Delta P = (P_c - P)$ becomes:

$$\sigma_1 - P + \alpha\frac{1-2\nu}{1-\nu}(P_c - P) - (P_c - P) = a\left[\sigma_3 - P + \frac{1}{2}\alpha\frac{1-2\nu}{1-\nu}(P_c - P) - (P_c - P)\right] \tag{40}$$

Solving this equation for P_c results in:

$$P_c = \frac{1}{\alpha\frac{1-2\nu}{1-\nu}(1-a/2) - (1-a)}\left[a\sigma_3 - \sigma_1 - \left(\alpha\frac{1-2\nu}{1-\nu}\right)(a/2-1)P\right] \tag{41}$$

The resulting differential stress, $\sigma_d = \bar{\sigma}'_1 - \bar{\sigma}'_3$, is then given by:

$$\sigma_d = \sigma_1 - P + \alpha\frac{1-2\nu}{1-\nu}\Delta P - \Delta P - \left[\sigma_3 - P + \frac{1}{2}\alpha\frac{1-2\nu}{1-\nu}\Delta P - \Delta P\right] \tag{42a}$$

$$\sigma_d = \sigma_1 - \sigma_3 + \frac{1}{2}\alpha\frac{1-2\nu}{1-\nu}\Delta P \tag{42b}$$

2. Wellbore types

Excel spreadsheets have been created in order to plot the wellbore trajectories for this project. We will be investigating two of the four of the major well profiles; Type I and Type II. With these spreadsheets and starting coordinates for our well from the Hypermesh™ models, we can then use Matlab™ to do a binary search of the data and find the closest Hypermesh™ data points to that of our well trajectories. Once we have matched the data we can then use those data points to create our pressure windows for the new well trajectories.

The excel sheets work by breaking up each section of the well into smaller parts and then connecting them in the last step to create a full well profile. The wells are typically broken into a vertical section, a build section, and a hold section. The Type II well also has the added drop section and can even possess a second hold section where necessary. Each of the Excel spreadsheets is operated in the same way. There is a small input section where the necessary data is placed and once changed the well profile plot and the output data will change in real time. The figure below shows a representative sketch of each type of well path.

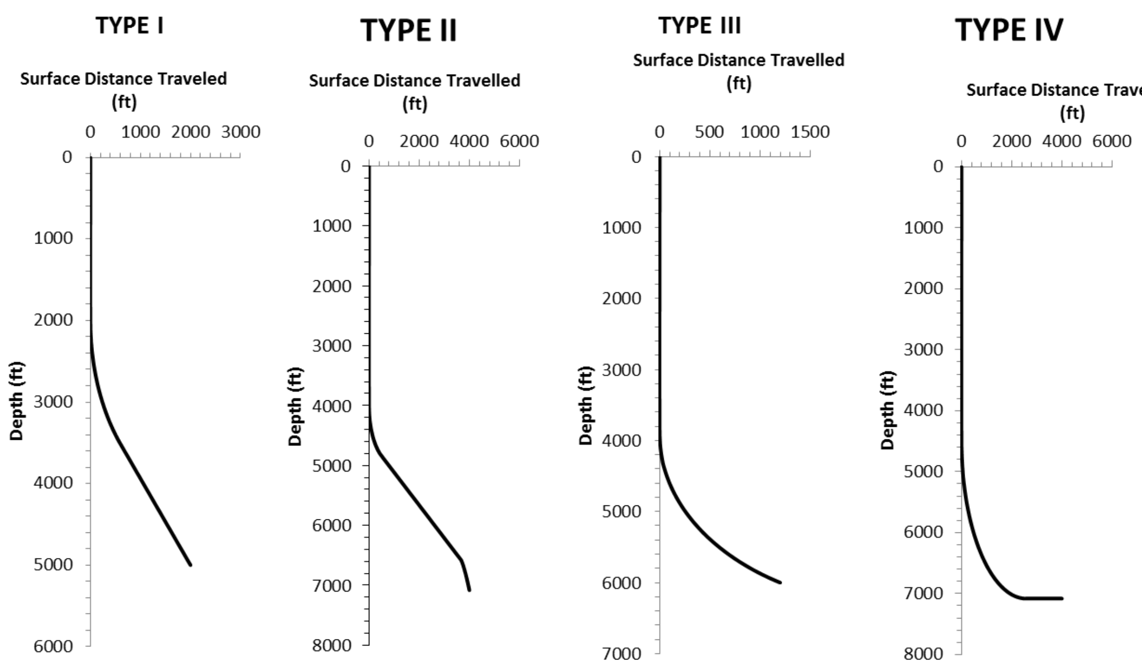

Figure 4. Four typical well types.

a) Type I Well Profile

A Type I well profile consists of a vertical well section that extends down until it reaches the kickoff point. Once the kickoff point is achieved the well will go into a build section until it is at the final inclination angle. The well will then hold this angle until it reaches total depth. This well type will most likely be the most commonly used well profile for this project.

The equations that are used in the Excel spreadsheet to calculate a Type I well are listed below along with their associated variables.

$$\tan k = \frac{r - \Delta x}{D_{TD} - D_{KOP}}$$

$$\sin j = \frac{r}{\sqrt{(r - \Delta x)^2 + (D_{TD} - D_{KOP})^2}}$$

$$i = j - k$$

$$r = \frac{D_{EOB} - D_{KOP}}{\sin i}$$

$$L_{DC} = \frac{2\pi i(D_{EOB} - D_{KOP})}{360 \sin i}$$

$$BUR = \frac{18000}{\pi r}$$

$$L_{HOLD} = \frac{D_{TD} - D_{EOB}}{cosi}$$

$$D_{EOB} = D_{KOP} + rsini$$

$$\Delta x_{EOB} = r(1 - cosi)$$

$$MD_{TD} = D_{KOP} + \frac{2\pi ri}{360} + \frac{D_{TD} - D_{KOP} - rsini}{cosi}$$

$$i_{dx} = \cos^{-1}\left(1 - \frac{dx}{r}\right)$$

$$dy = rsin(i_{dx})$$

$$dMD = \frac{i_{dx} 2\pi r}{360}$$

i = maximum inclination angle (degrees)
Δx = horizontal displacement (ft)
Δx_{EOB} = horizontal displacement at end of build (ft)
D_{TD} = true vertical depth (ft)
MD_{TD} = measured depth at total depth of well (ft)
D_{KOP} = depth of the kick off point (ft)
r = radius of curvature (ft)
L_{DC} = arc length of curve (ft)
L_{HOLD} = length of hold section (ft)
BUR = build up rate (degrees per 100 ft)
dx = incremental change in x direction (ft)

i_{dx} = incremental change in i (degrees)
dy = incremental change in y direction (ft)
d_{MD} = incremental change in MD (ft)

b) Type II Well profile

A Type II well is one in which there is a vertical section down to a kick off point. After the kick off point the well will go into a build section until it reaches a desired inclination angle. Once the desired inclination angle has been obtained, that angle will be held until the well reaches a desired length. At the desired length, the well will then go into a drop section until it reaches the reservoir. A Type II well requires target coordinates, surface coordinates, true vertical depth of target, depth of the kick off point, a build-up rate, and drop off rate, a depth of the drop off point, and a final inclination angle.

The equations that are used in the Excel spreadsheet to calculate a Type II well are listed below along with their associated variables.

$$r_1 = \frac{18000}{\pi\varphi_1}$$

$$r_2 = \frac{18000}{\pi\varphi_2}$$

$$D_{EOB} = D_{KOP} + r_1 \sin i_1$$

$$\Delta x_{EOB} = r_1(1 - \cos i_1)$$

$$\tan j = \frac{r_1 + r_2}{\sqrt{PS}}$$

$$\tan k = \frac{\Delta x - r_1 - r_2 \cos i_2 - (D_{TD} - D_{EOD}) \tan i_2}{D_{EOD} - D_{KOP} + r_2 \sin i_2}$$

$$i_1 = \tan^{-1} j + \tan^{-1} k$$

$$MD_{TD} = MD_{EOD} + \frac{D_{TD} - D_{EOD}}{\cos i_2}$$

$$PS = \sqrt{(D_{EOD} - D_{KOP} + r_2 \sin i_2)^2 + (\Delta x - r_1 - r_2 \cos i_2 - (D_{TD} - D_{EOD}) \tan i_2)^2 - (r_1 + r_2)^2}$$

$$MD_{EOH} = MD_{EOB} + PS$$

$$D_{EOH} = D_{EOB} + PS \cos i_1$$

$$\Delta x_{EOH} = \Delta x_{EOB} + PS \sin i_1$$

$$MD_{EOB} = D_{KOP} + \frac{2\pi r_1 i_1}{360}$$

With:

r_1 = radius of curvature of build (ft)
r_2 = radius of curvature of drop (ft)
φ_1 = build up rate (degrees per 100 ft)
φ_2 = drop off rate (degrees per 100 ft)
i_2 = final inclination angle (degrees)
i_1 = inclination angle (degrees)
D_{EOB} = depth to end of build (ft)
Δx_{EOB} = horizontal displacement to end of build (ft)
MD_{EOB} = measured depth at end of build (ft)
D_{EOH} = depth at end of hold (ft)
Δx_{EOH} = horizontal displacement to end of hold (ft)
MD_{EOH} = measured depth at end of hold (ft)
MD_{TD} = measured depth at true vertical depth (ft)

3. Wellbore stability analysis results

3.a. Extensional Stress Regime

In all of the figures below the blue line is pore pressure, the green line is the formation breakdown pressure, and the red line is the fracture gradient.

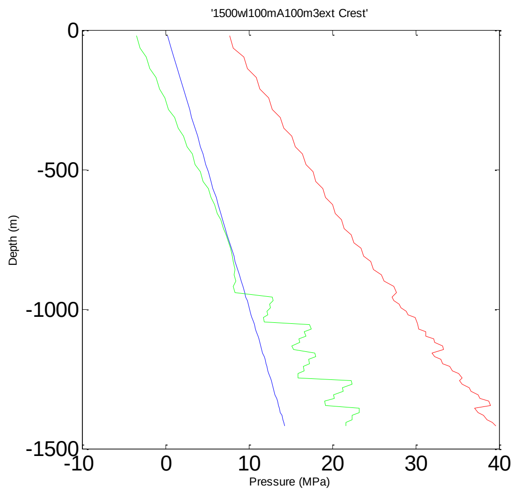

Figure A1. Crest well pressure window.

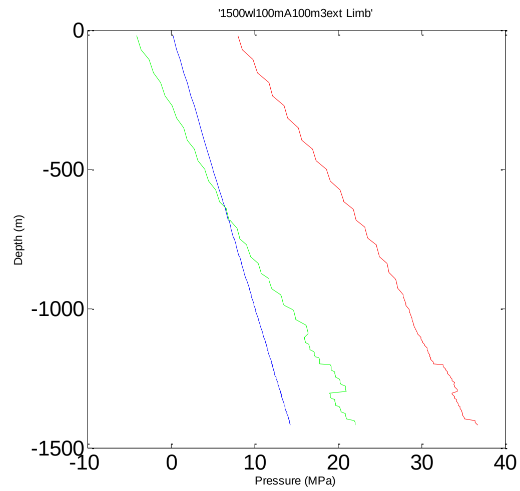

Figure A2. Limb well pressure window.

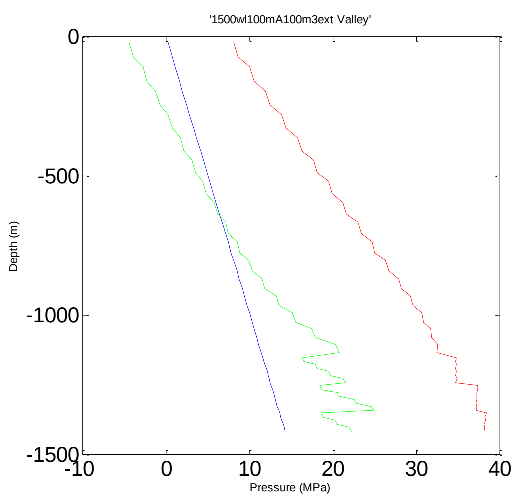

Figure A3. Valley well pressure window.

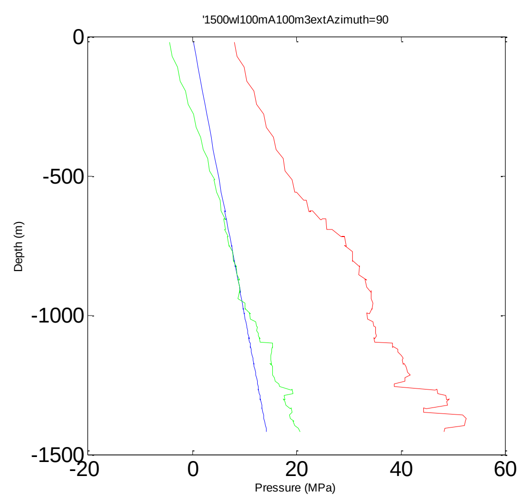

Figure A4. Pressure window for Azimuth $= 0^{o}$.

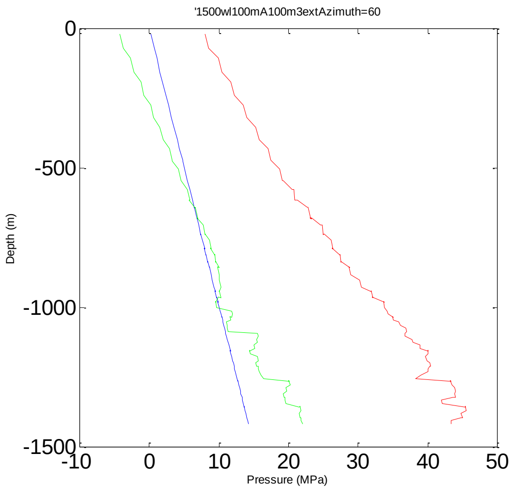

Figure A5. Pressure window for Azimuth = 30°.

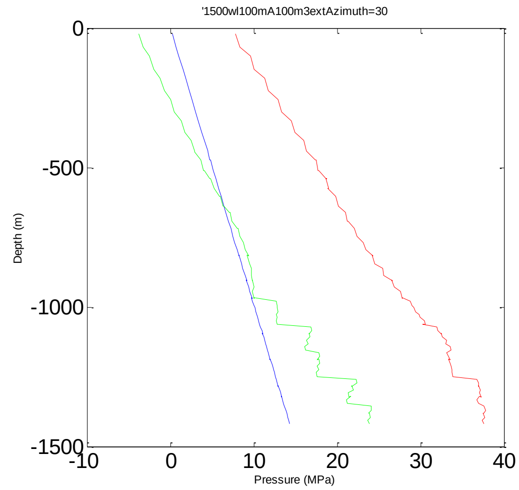

Figure A6. Pressure window for Azimuth = 60°.

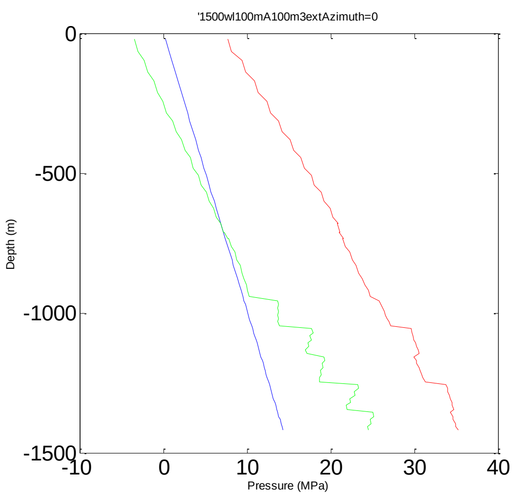

Figure A7. Pressure window for Azimuth = 90°.

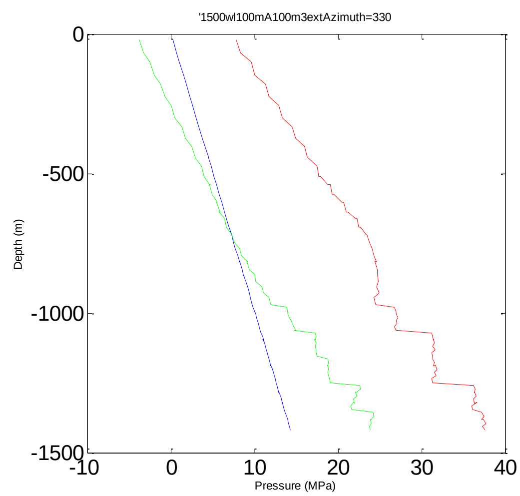

Figure A8. Pressure window for Azimuth = 120°.

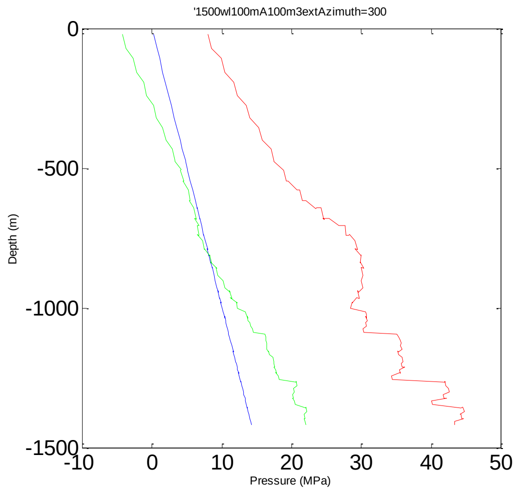

Figure A9. Pressure window for Azimuth = 150°.

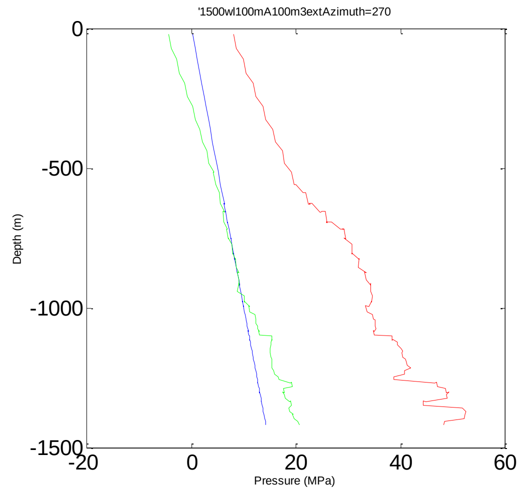

Figure A10. Pressure window for Azimuth = 180°.

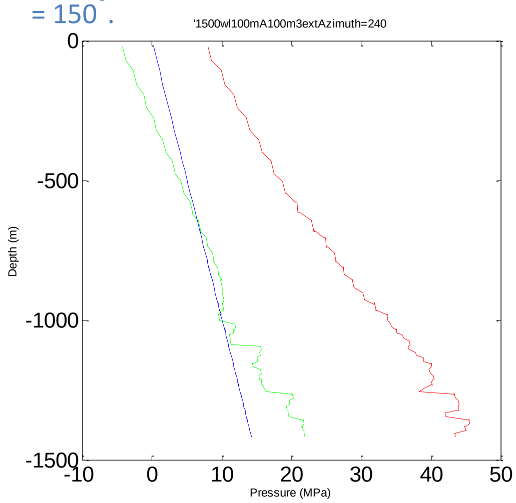

Figure A11. Pressure window for Azimuth = 210°.

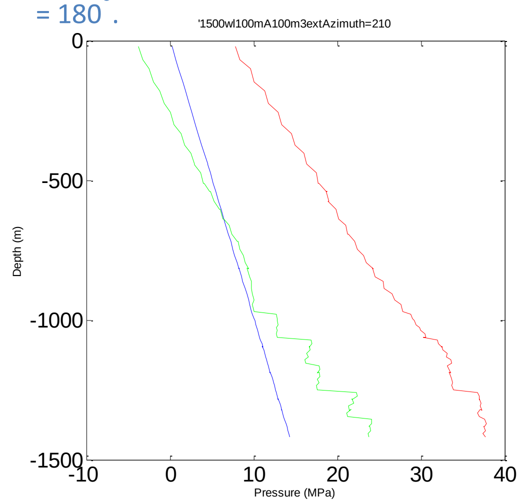

Figure A12. Pressure window for Azimuth = 240°.

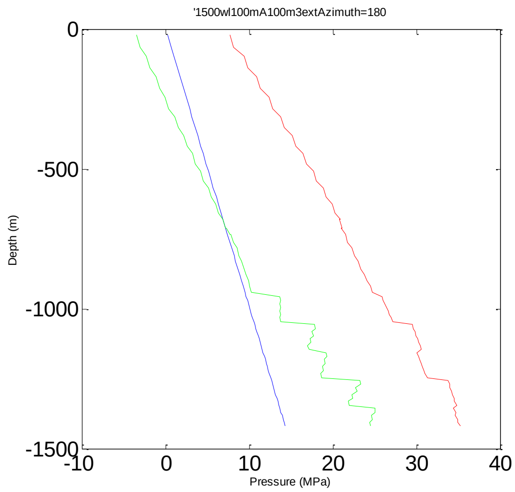

Figure A13. Pressure window for Azimuth = 270°.

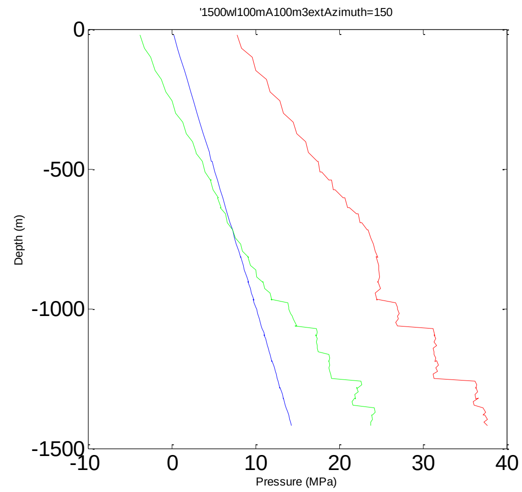

Figure A14. Pressure window for Azimuth = 300°.

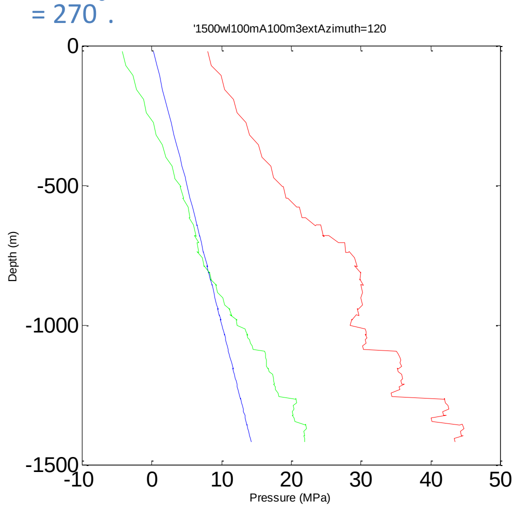

Figure A15. Pressure window for Azimuth = 330°.

3.b. Compressional Stress Regime

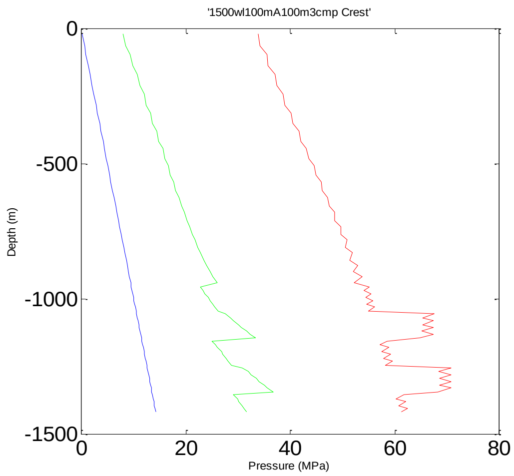

Figure B1. Crest well pressure window.

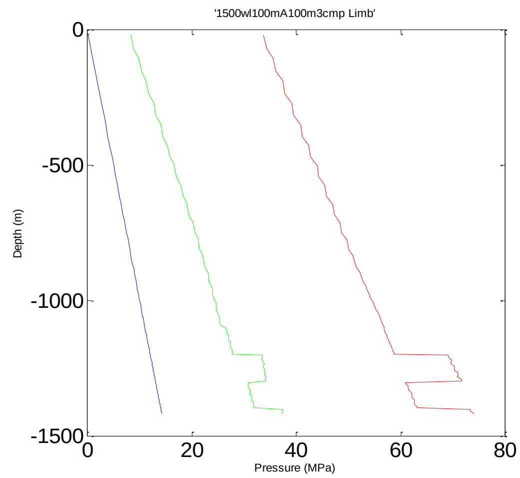

Figure B2. Limb well pressure window.

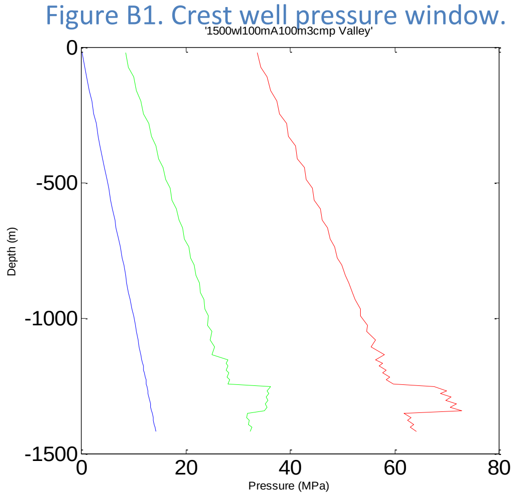

Figure B3. Valley well pressure window.

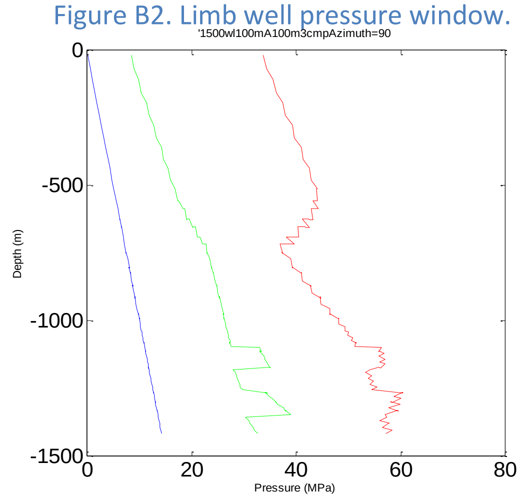

Figure B4. Pressure Window for Azimuth = 0^{o}.

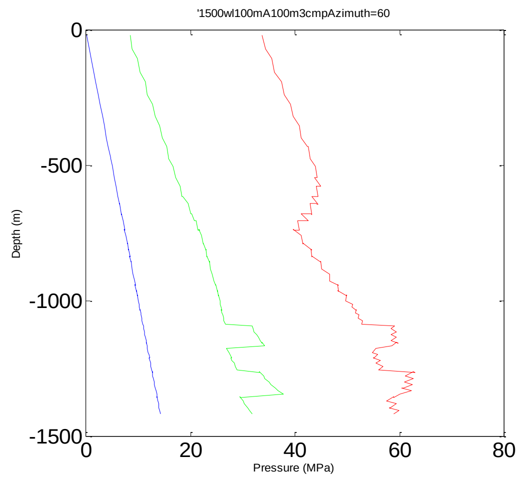

Figure B5. Pressure Window for Azimuth = 30°.

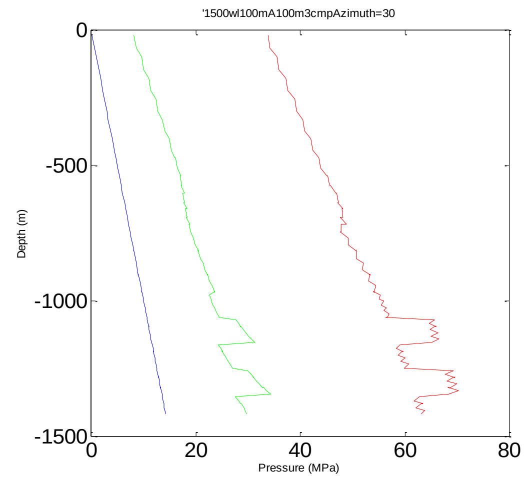

Figure B6. Pressure Window for Azimuth = 60°.

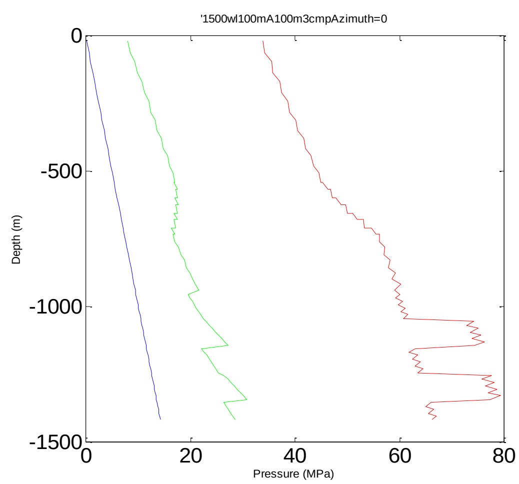

Figure B7. Pressure Window for Azimuth = 90°.

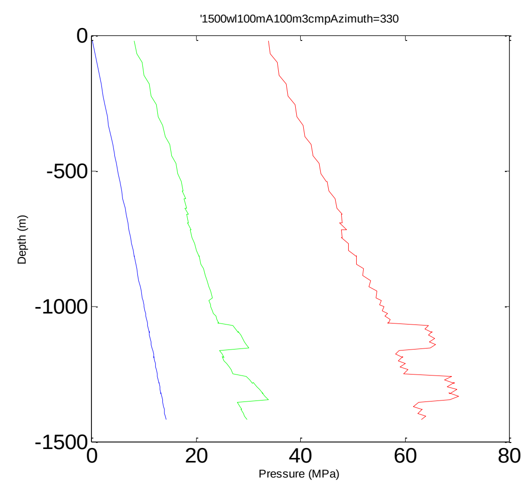

Figure B8. Pressure Window for Azimuth = 120°.

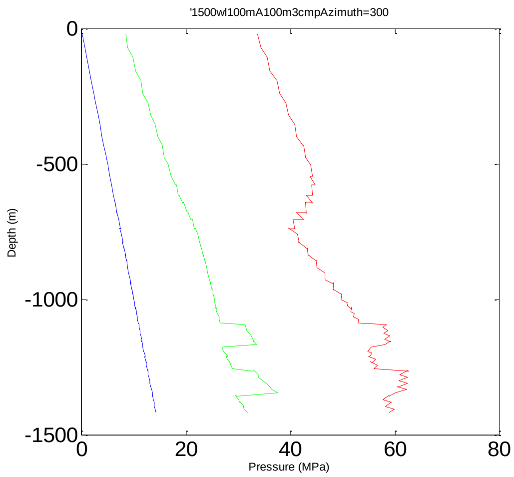

Figure B9. Pressure Window for Azimuth = 150^{o}.

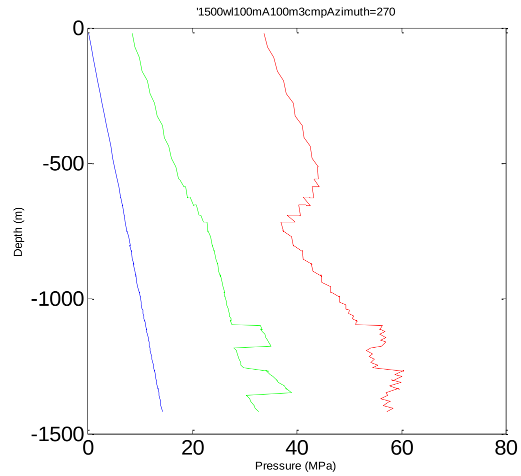

Figure B10. Pressure Window for Azimuth = 180^{o}.

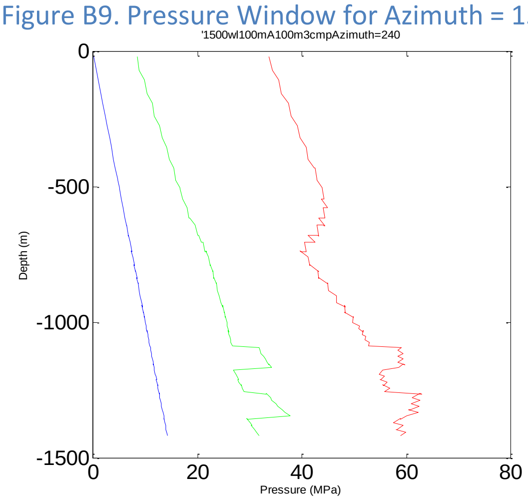

Figure B11. Pressure Window for Azimuth = 210^{o}.

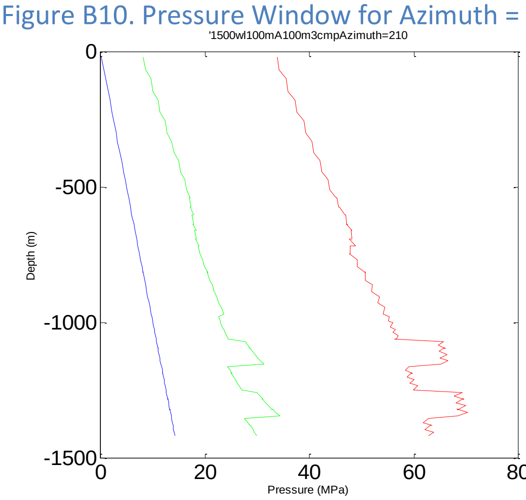

Figure B12. Pressure Window for Azimuth = 240^{o}.

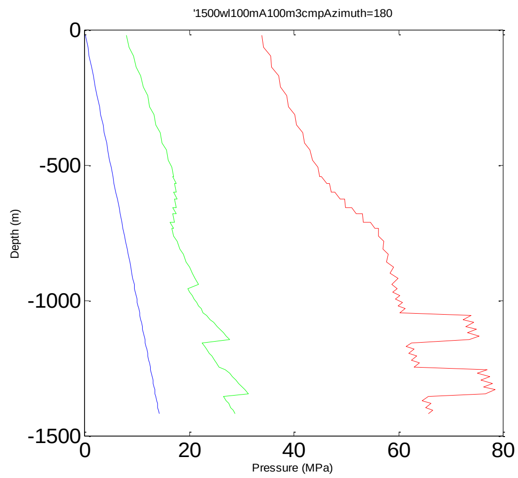

Figure B13. Pressure Window for Azimuth = 270°.

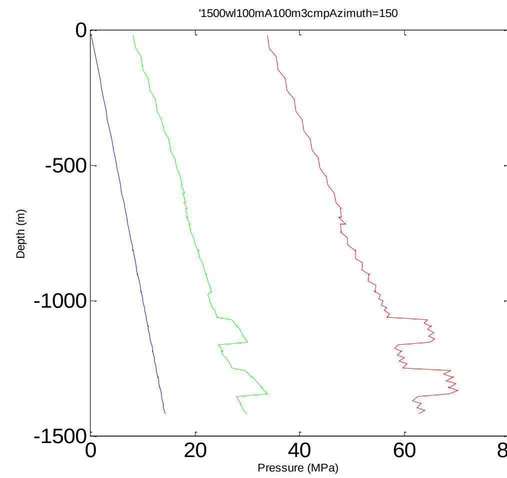

Figure B14. Pressure Window for Azimuth = 300°.

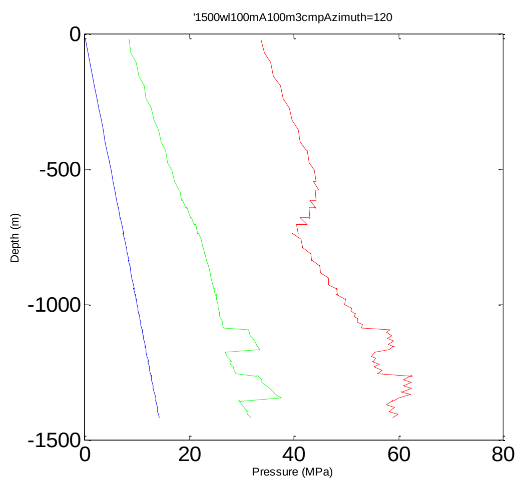

Figure B15. Pressure Window for Azimuth = 330°.

3.c. Strike-Slip Stress Regime

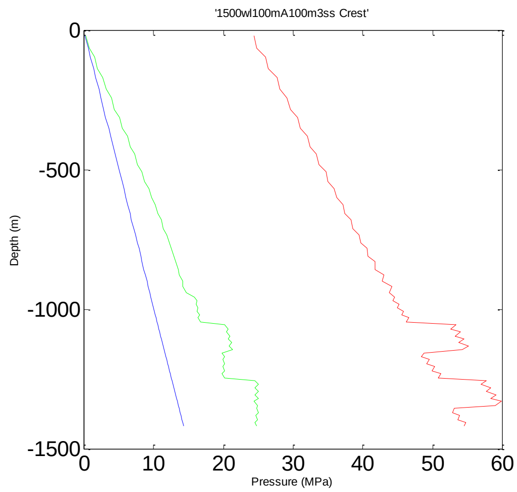

Figure C1. Crest well pressure window.

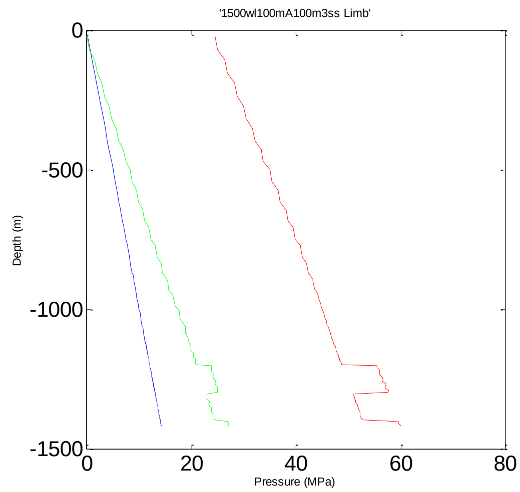

Figure C2. Limb well pressure window.

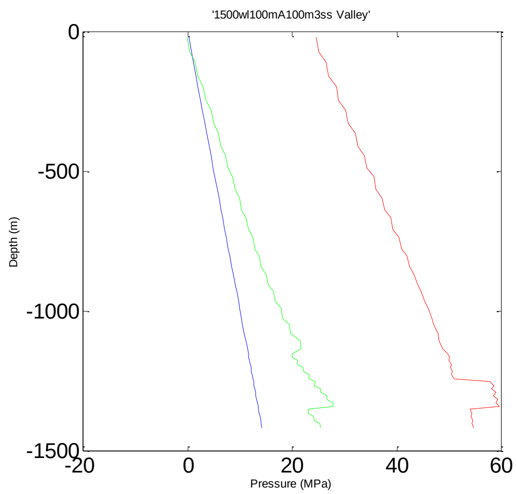

Figure C3. Crest well pressure window.

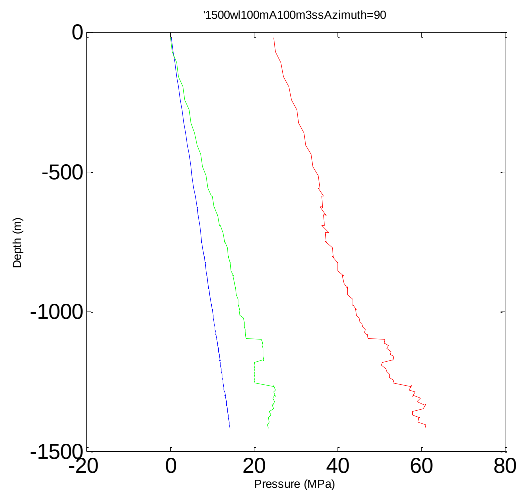

Figure C4. Pressure window for Azimuth $= 0^{o}$.

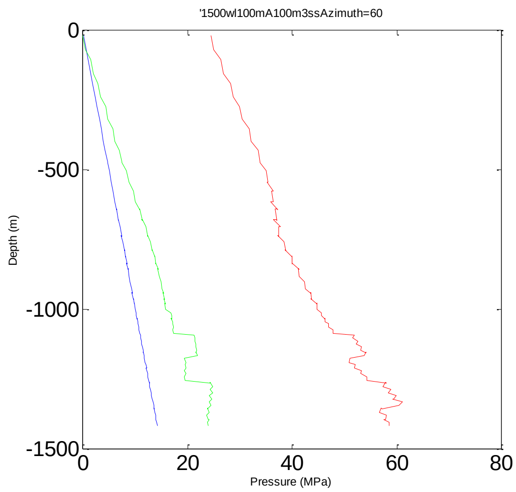

Figure C5. Pressure window for Azimuth = 30°.

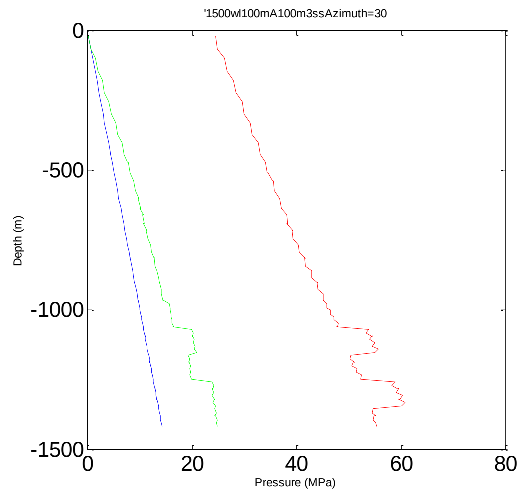

Figure C6. Pressure window for Azimuth = 60°.

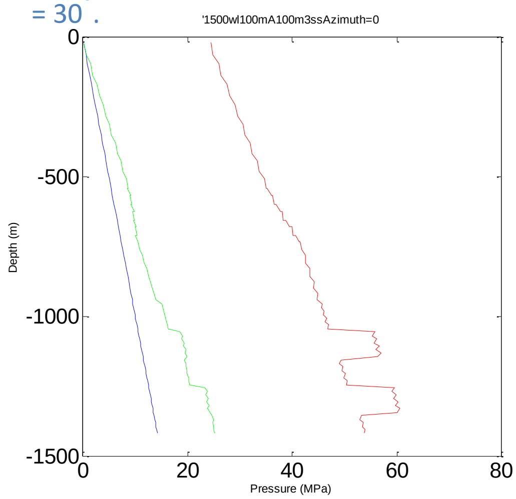

Figure C7. Pressure window for Azimuth = 90°.

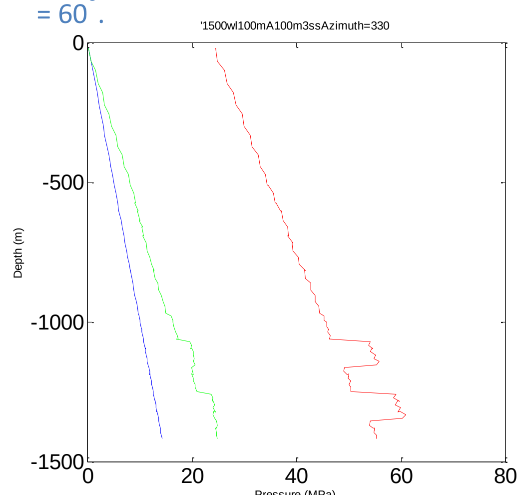

Figure C8. Pressure window for Azimuth = 120°.

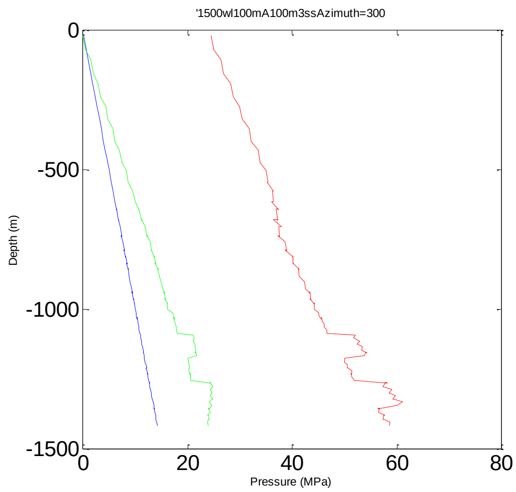

Figure C9. Pressure window for Azimuth = 150°.

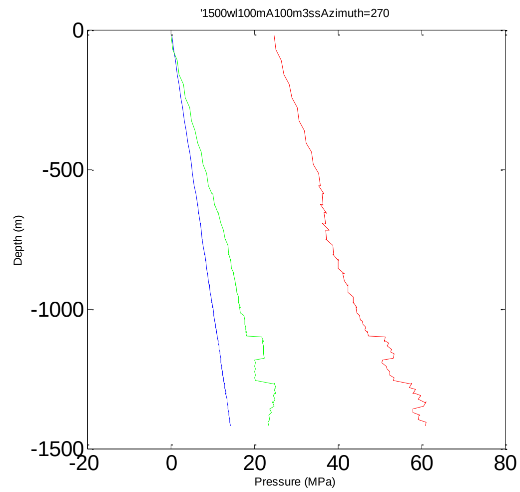

Figure C10. Pressure window for Azimuth = 180°.

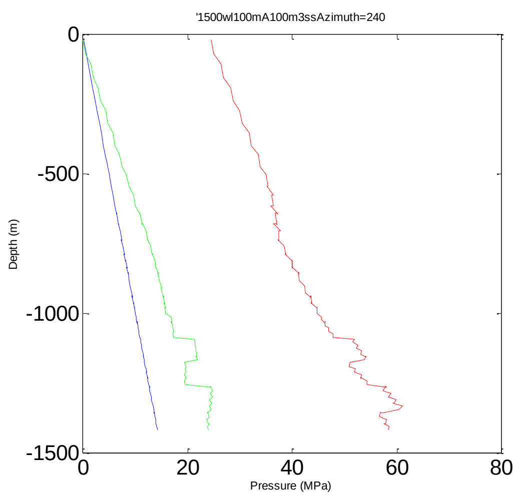

Figure C11. Pressure window for Azimuth = 210°.

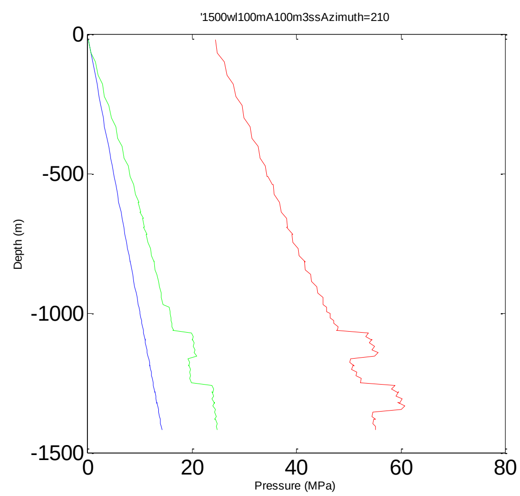

Figure C12. Pressure window for Azimuth = 240°.

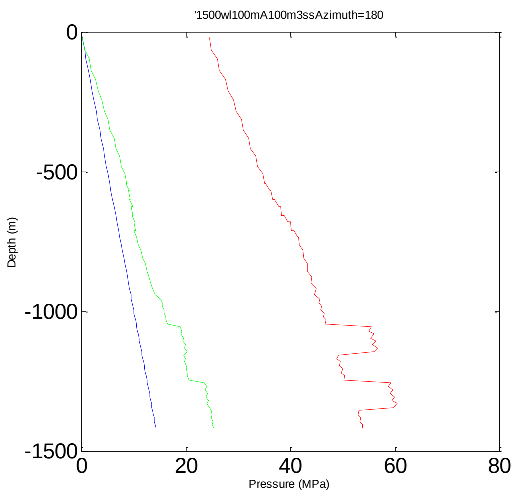

Figure C13. Pressure window for Azimuth = 270°.

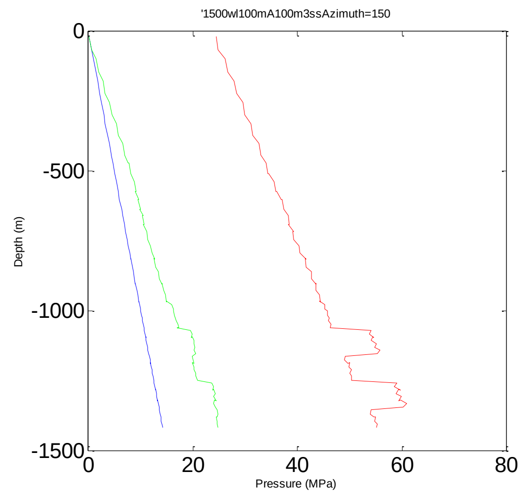

Figure C14. Pressure window for Azimuth = 300°.

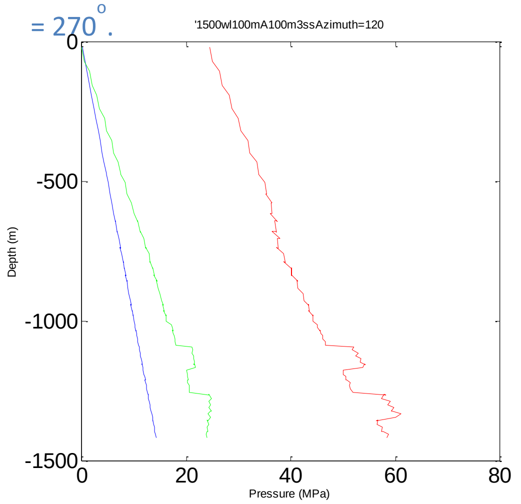

Figure C15. Pressure window for Azimuth = 330°.